

INFORMATION TO USERS

This material was produced from a microfilm copy of the original document. While the most advanced technological means to photograph and reproduce this document have been used, the quality is heavily dependent upon the quality of the original submitted.

The following explanation of techniques is provided to help you understand markings or patterns which may appear on this reproduction.

- 1. The sign or "target" for pages apparently lacking from the document photographed is "Missing Page(s)". If it was possible to obtain the missing page(s) or section, they are spliced into the film along with adjacent pages. This may have necessitated cutting thru an image and duplicating adjacent pages to insure you complete continuity.**
- 2. When an image on the film is obliterated with a large round black mark, it is an indication that the photographer suspected that the copy may have moved during exposure and thus cause a blurred image. You will find a good image of the page in the adjacent frame.**
- 3. When a map, drawing or chart, etc., was part of the material being photographed the photographer followed a definite method in "sectioning" the material. It is customary to begin photoing at the upper left hand corner of a large sheet and to continue photoing from left to right in equal sections with a small overlap. If necessary, sectioning is continued again — beginning below the first row and continuing on until complete.**
- 4. The majority of users indicate that the textual content is of greatest value, however, a somewhat higher quality reproduction could be made from "photographs" if essential to the understanding of the dissertation. Silver prints of "photographs" may be ordered at additional charge by writing the Order Department, giving the catalog number, title, author and specific pages you wish reproduced.**
- 5. PLEASE NOTE: Some pages may have indistinct print. Filmed as received.**

University Microfilms International

**300 North Zeeb Road
Ann Arbor, Michigan 48106 USA
St. John's Road, Tyler's Green
High Wycombe, Bucks, England HP10 8HR**

77-16,976

SILBER, Michael Lawrence, 1943-
MAGNETIC BEHAVIOR OF CURRENT-CARRYING
TYPE-II SUPERCONDUCTING CYLINDERS.

Iowa State University, Ph.D., 1977
Physics, solid state

Xerox University Microfilms, Ann Arbor, Michigan 48106

Magnetic behavior of current-carrying type-II
superconducting cylinders

by

Michael Lawrence Silber

A Dissertation Submitted to the
Graduate Faculty in Partial Fulfillment of
The Requirements for the Degree of
DOCTOR OF PHILOSOPHY

Department: Physics

Major: Solid State Physics

Approved:

Signature was redacted for privacy.

In Charge of Major Work

Signature was redacted for privacy.

For the Major Department

Signature was redacted for privacy.

For the Graduate College

Iowa State University
Ames, Iowa

1977

TABLE OF CONTENTS

	Page
I. INTRODUCTION	1
A. Introductory Remarks	1
B. Historical Review of Superconductivity	3
C. Thermodynamics and Magnetic Quantities	12
D. Critical Currents and Hard Superconductors	16
II. SPIRAL FLUX LINES	54
A. Introductory Remarks	54
B. Qualitative Physical Description	55
C. Differential Equation Between H and ρ	56
D. Flux Line Models	63
E. Model for the Equilibrium Field	68
F. Models for Surface Pinning	75
G. Weak Pinning Limit	77
H. Finite, Nonzero Pinning	117
I. Comparison with Experiment	165
III. SPIRAL COLLAPSE INSTABILITY	190
A. Introduction	190
B. Physical Argument	196
C. Energy and Heat	200
D. Experimental Verification of Collapse Modes	211
E. Modeling Vanadium	217
F. Spiral Collapse in Hypothetical Material	219

IV.	PROGRAMMED CURRENT AND FIELD	245
A.	Introductory Remarks	245
B.	The Fields	245
C.	Instabilities	261
D.	Flux Accumulation and Reduced Quantities	262
V.	CONCLUSIONS AND PROBLEMS FOR FURTHER RESEARCH	264
A.	Standardized Research Procedure	264
B.	The Boundary Condition Problem	265
C.	The Critical Current Problem	265
VI.	BIBLIOGRAPHY	268
VII.	ACKNOWLEDGMENTS	272
VIII.	APPENDIX A. RADIUS OF CURVATURE OF A FLUX SPIRAL	273
IX.	APPENDIX B. LINE TENSION IN VORTEX RING	276
X.	APPENDIX C. DERIVATION OF BESSEL FUNCTION SOLUTION	278

I. INTRODUCTION

A. Introductory Remarks

We are concerned here with the magnetic properties of a specific class of superconductors in a special geometry. The complexity of nonideal superconductors on both microscopic and macroscopic levels requires a deliberately narrow area of study. On a microscopic scale, one looks at the details of flux vortices and their interactions with the defects and irregularities in the metal, while on a larger scale, the average electrodynamic properties of the sample become important. In the end, one hopes to predict the gross magnetic behavior without recourse to microscopic details.

For simplicity, we choose an infinite, round wire of type-II superconductor in a longitudinal field. The wire carries a transport current I_0 , which is regulated independently of the applied field, H_a . After the current and field follow a prescribed path to some final assigned values, we seek to know the resultant flux and current distributions in the wire. In an actual experiment, there are two measurements which are most convenient for this situation. These are the magnetic moment of the specimen and the critical current. The magnetization measurement reveals the nature of the flux distribution, and the critical current measurement reveals the onset of flux line motion, thus indicating the

stability of a given configuration. As a complication, one must carefully define what constitutes a critical current, since the breakdown of superconductivity and the appearance of a longitudinal voltage are not necessarily simultaneous.

In the remainder of this chapter, we present a very terse review of the essential features of superconductivity for the reader who is not very familiar with the field. In particular, we discuss force-free configurations and longitudinal fields in Section D.3. Force-free configurations were first suggested by Bergeron (1) after the experiments of Bergeron et al. (2) and others revealed that longitudinal critical currents are found to be much greater than those measured in transverse fields. The force-free configuration is so named because the local transport current density \vec{J} is parallel to the magnetic flux density \vec{B} , causing the Lorentz force density $\vec{J} \times \vec{B} / c$ to be zero or nearly zero. One of our conclusions shows that the existence of force-free flow depends upon the reversibility of the material and the relative amounts of current and applied field (i.e., the pitch angle of the resultant magnetic field vector at the surface of the sample).

For the most part, however, we concentrate on a nonforce-free model which allows for any arbitrary amount of irreversibility in the material. In our model, irreversibility is accounted for through the description of the critical

current, and the discontinuity between B and H at the surface of the sample. In Chapter IV we generalize the model to account for a more general magnetic history which the specimen has experienced. That is, we give a quasi-static formulation that accommodates any arbitrary sequence in the application of current and longitudinal field up to the final configuration, provided the surface magnetic field increases with time.

B. Historical Review of Superconductivity

1. Zero resistance

The field of knowledge included in the realm of superconductivity is very broad; for a complete and concise survey of the early experiments and phenomenological theories, the reader is referred to the review article by Chandrasekhar (3). Additional background may be obtained from texts devoted exclusively to superconductivity (4-13). It would be useful to review a few of the more important properties of superconductivity here.

The Dutch physicist H. Kamerlingh Onnes discovered superconductivity in 1911 (14) while investigating the electrical resistivity of mercury. Onnes found that the resistance of the sample dropped abruptly to zero at about 4°K and called the phenomenon superconductivity. Since that time, many more

elements and compounds have been found to be superconductors.

The characteristic, although not fundamental, feature of a superconductor is the sudden disappearance of dc electrical resistance below some well-defined temperature, denoted T_c . At this time, most physicists believe that the resistance of a superconductor is truly zero, and not merely some very small finite number. Recent experiments (15) have confirmed that it is no larger than 10^{-23} ohm-cm. Superconductors also respond to magnetic fields, a sufficiently high field being capable of quenching a superconductor back into the normal state. Because magnetic effects vary greatly with sample geometry and the direction of the applied field, we confine our attention to long cylindrical samples immersed in uniform magnetic fields, applied parallel to the cylinder axis. In this situation, there are two basic types of superconductor, defined by their magnetic behavior. For a type-I superconductor at a temperature T below T_c , the critical value of the quenching field, H_c , approximates the following rule:

$$H_c = H_0 [1 - (T/T_c)^2] \quad , \quad (1.1)$$

where H_0 is the critical field at zero degrees Kelvin. The other kind of superconductor, called type-II, has a gradual transition to the normal state occurring over a finite span of field intensity. The upper and lower limits of the transi-

tion fields are called H_{c2} and H_{c1} , respectively. Type-II superconductors will be discussed in more detail later.

Understanding of superconductivity is further complicated by the existence of so-called nonideal materials. These substances exhibit irreversible behavior in the presence of changing magnetic fields, so that the state of a sample is history-dependent. Irreversible effects are attributed to the phenomenon of pinning, whereby inhomogeneities, point defects, impurities, and other metallurgical irregularities impede the motion of flux lines through the material.

The thermodynamic nature of the superconducting transition is obscured in nonideal materials. However, in 1933 Meissner and Ochsenfeld (16) discovered that an ideal type-I superconductor totally excludes magnetic flux, with the exception of a thin surface layer. That is, such superconductors behave like perfect diamagnets. In ideal type-I materials, the onset of diamagnetic behavior is independent of the order in which the temperature and field are varied. Thus, for a sample already immersed in a magnetic field, lowering the temperature below T_c will cause the sudden exclusion of flux from the sample. Similarly, lowering the applied field below H_c for a sample already below the zero-field critical temperature would cause the sudden expulsion of flux. Interestingly enough, one can show that the property

of zero resistance alone is insufficient to guarantee a Meissner effect. It appears that a Meissner effect implies superconductivity, and not conversely. The behavior of B versus H for an ideal type-I cylinder in a longitudinal field is shown in Figure 1.

For type-I cylindrical specimens in transverse fields, and for bulky shapes such as spheres and ellipsoids, higher magnetic fields lead to the formation of the intermediate state. This phase is characterized by intermixed zones of superconducting and normal material, wherein all flux passing through the sample is confined to the normal zones, and all superconducting regions remain flux-free. The intermediate state results from the demagnetizing effect of the sample shape, which causes an enhancement of the magnetic flux density around the equatorial zones. Thus, while the applied field may be less than H_c , the local field in certain places may exceed H_c , driving those regions into the normal state.

A type-I cylinder in a longitudinal field exhibits a Meissner effect up to the critical field H_c . Above H_c , the sample reverts to the normal state. In contrast, a type-II material exhibits a Meissner phase only up to a field $H_{c1} < H_c$. Above H_{c1} , magnetic flux penetrates the cylinder, but at a lower density than the applied field.

The penetration of flux becomes complete only at a higher field $H_{c2} > H_c$. For fields above H_{c2} , a macroscopic

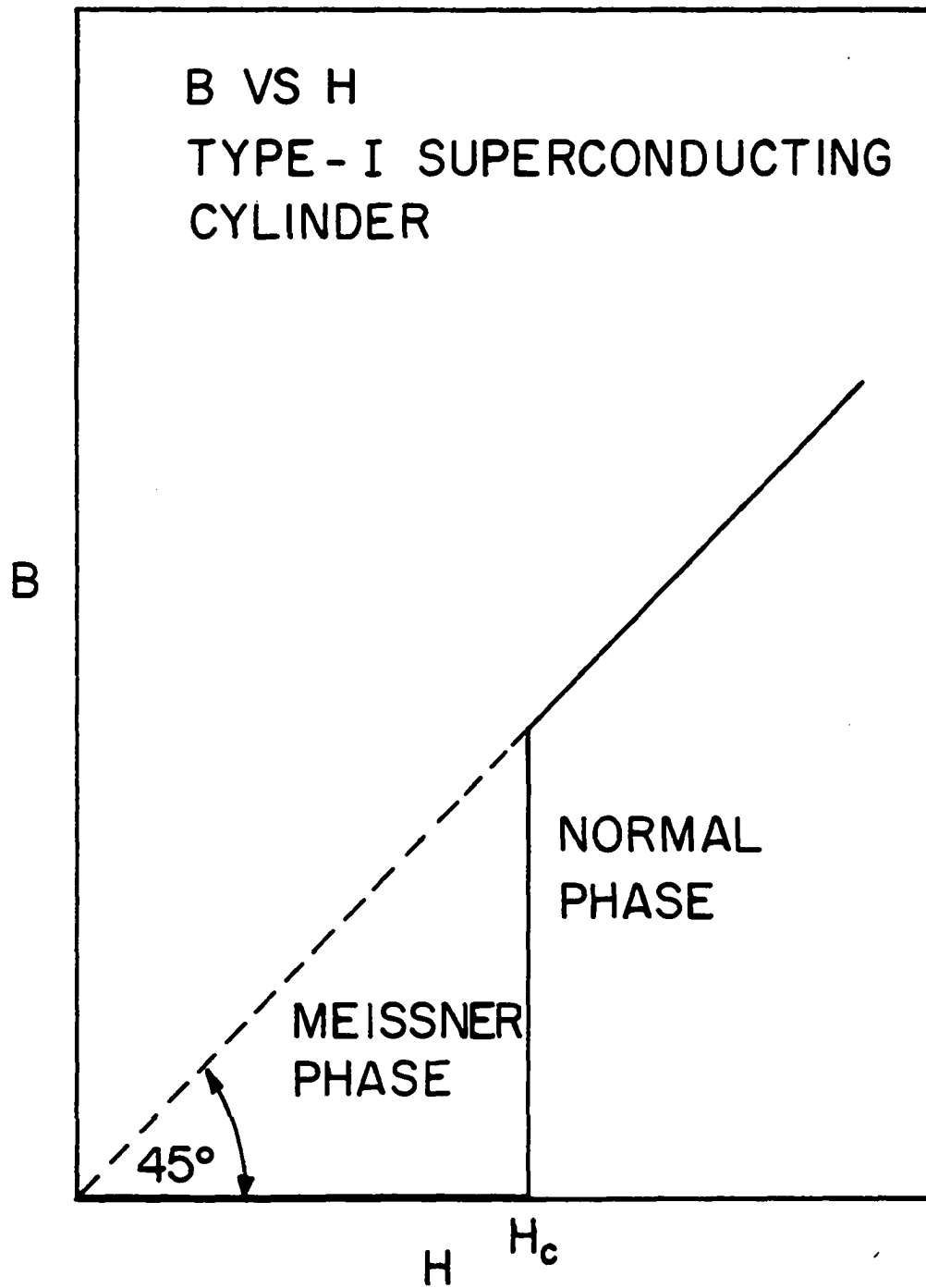


Figure 1. Magnetic flux density B inside an ideal type-I superconducting cylinder, as a function of the applied field H

sample does not show any flux expulsion, and the internal flux density B is equal to the applied field H . While the bulk of the material no longer shows zero dc resistance above H_{c2} , there does exist a thin surface sheath which is superconductive up to an applied field denoted H_{c3} . Typically, H_{c3} is about 70% greater than H_{c2} , while H_{c2} can vary from H_{c1} up to several orders of magnitude above H_{c1} , depending upon the material. In much of what follows, we will be concerned with the region between H_{c1} and H_{c2} , which is called the vortex state. (Sometimes the vortex state is called the Shubnikov phase, after the Russian experimentalist who first discovered evidence for its existence.) The behavior of B versus H for an ideal type-II cylinder in a longitudinal field is shown in Figure 2.

The precise way in which a superconductor breaks down into normal and superconducting zones is related to the free energy cost of the zone boundaries. For type-II materials the interface energy is negative, favoring the creation of a finely divided mixture of normal and superconducting zones, with a maximum of interface area. The size of the smallest possible unit must be consistent with quantum mechanics, and what actually appears (in the vortex state) is an array of isolated bundles of flux, called flux vortices, or fluxoids, each containing one quantum of magnetic flux. The experiments of Deaver and Fairbank (17) and Doll and Nabauer (18)

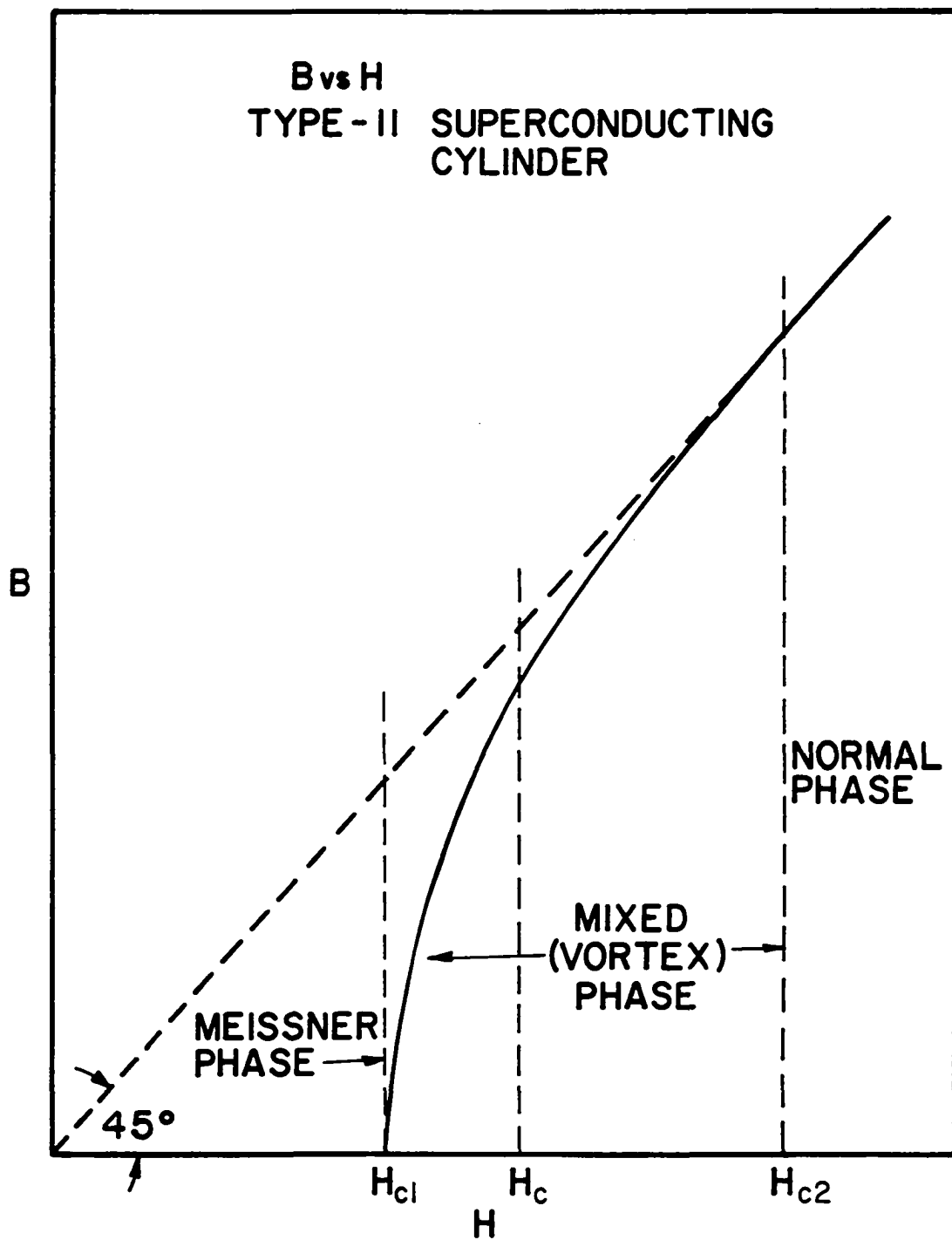


Figure 2. Magnetic flux density B inside an ideal type-II superconducting cylinder, as a function of the applied field H

have shown that the flux quantum ϕ_0 is equal to $hc/2e$, where h is Planck's constant, c is the speed of light, and e is the magnitude of the electronic charge. In the cgs system of units, this is equivalent to 2.07×10^{-7} gauss-cm².

The phenomenological theory of Ginzburg and Landau (19) and its extension by Abrikosov (20) were great advances in our understanding of type-II superconductors. In briefly describing the vortex state, we use some terminology from these theories.

Referring to the flux vortex model illustrated in Figure 3, the approximate magnetic radius of the vortex is given by the parameter λ , and the zone of reduced super-electron density has a radius approximately equal to ξ . The Ginzburg-Landau theory defines a parameter κ (kappa) as the ratio λ/ξ , and shows that κ is of critical importance in describing the properties of a superconductor. One of the results of their theory is that when κ exceeds $1/\sqrt{2}$, the material has a negative surface energy, and so is of the type-II variety. Kappas less than $1/\sqrt{2}$ indicate a positive surface energy, and so describe a type-I superconductor. The parameter λ is called the penetration depth, and is an approximate measure of the depth of penetration of magnetic flux into a superconductor. Typically, λ is on the order of hundreds of Angstroms. The parameter ξ is called the coherence length. The coherence length is difficult to define

MODEL OF A FLUXOID

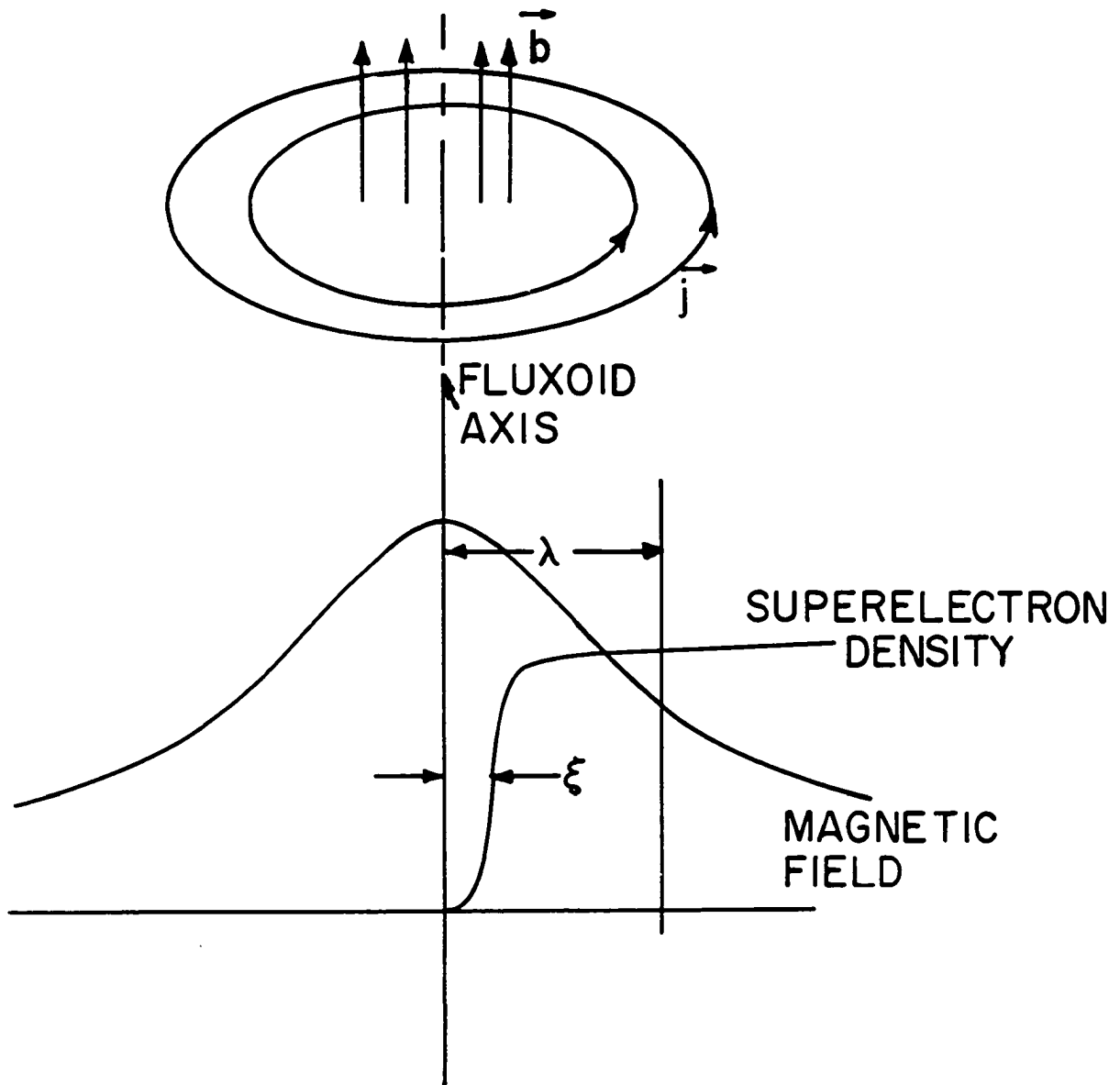


Figure 3. Model of a quantized fluxoid, showing the relative magnitudes of λ and ξ

without going into the details of the microscopic theory. For our purposes, we need only consider the Ginzburg-Landau parameter κ , rather than λ and ξ explicitly.

Figure 4 shows an ideal magnetization curve for a long cylindrical type-II superconductor, with an applied field parallel to the axis. The slope in the Meissner phase is unity, which derives from the electromagnetic relation,

$$\vec{B} = \vec{H} + 4\pi\vec{M} \quad , \quad (1.2)$$

with \vec{B} identically zero in the bulk of the cylinder. The area under the magnetization curve, divided by 4π , is equal to $H_c^2/8\pi$, the free energy difference per unit volume between the superconducting and normal states. For a type-II material, this serves as a definition of the thermodynamic critical field H_c , which is intermediate in value between H_{c1} and H_{c2} .

C. Thermodynamics and Magnetic Quantities

In defining the electromagnetic quantities as they will be used here, we follow the convention of DeGennes (10) and others and, except where explicitly noted, employ Gaussian units.

On a local level, we define the local magnetic flux density \vec{b} , which is related to the local current density \vec{j} through Ampere's law,

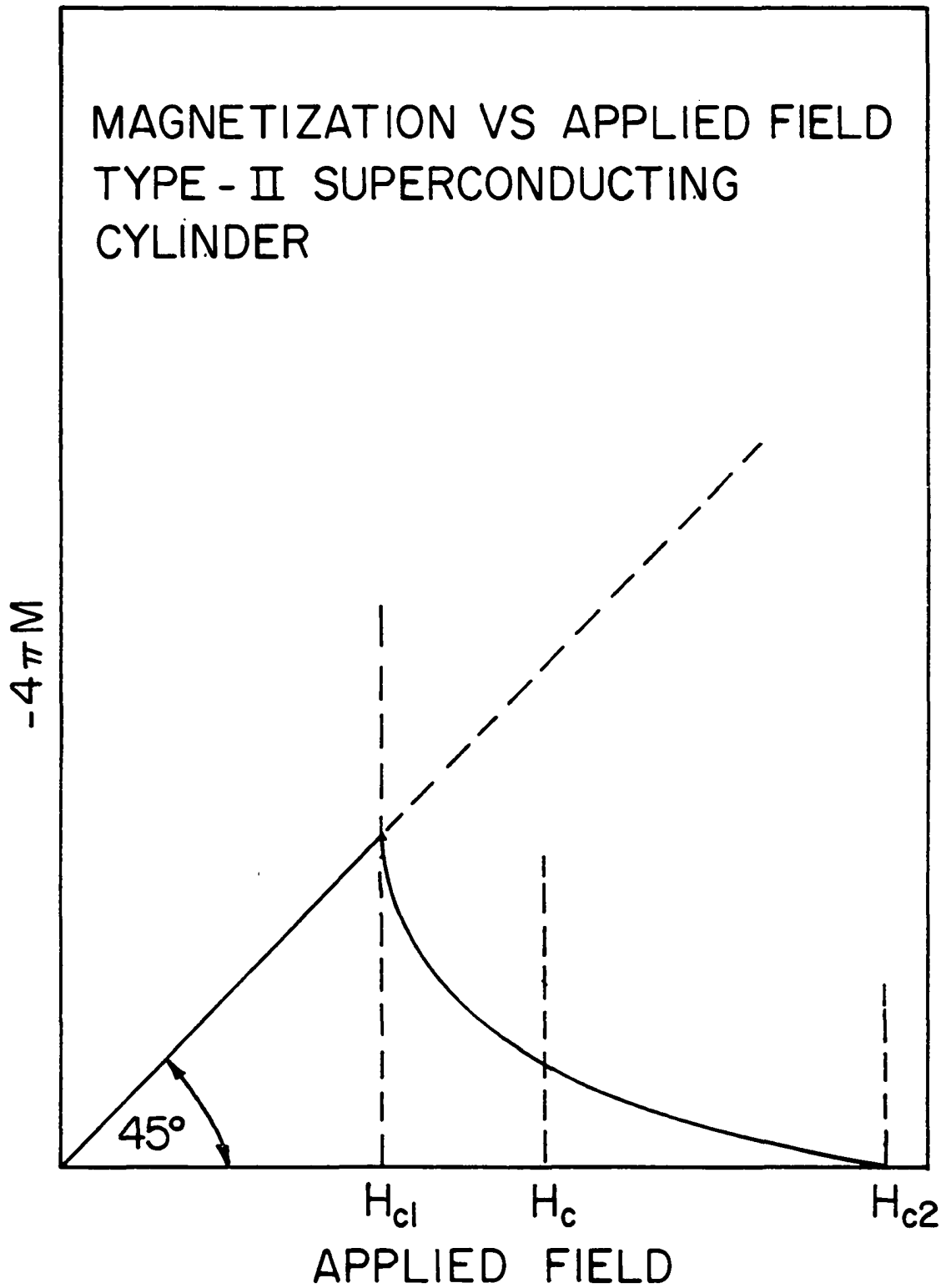


Figure 4. Magnetization curve for an ideal type-II superconducting cylinder in an applied field parallel to the cylinder axis

$$\vec{\nabla} \times \vec{b} = \frac{4\pi}{c} \vec{j} \quad . \quad (1.3)$$

Here, the word local implies a quantity which has meaning on a scale small in comparison with the penetration depth λ . Thus, over the space of one flux vortex, we expect wide variations in \vec{b} and \vec{j} .

When dealing with the macroscopic properties of a superconductor, it is more useful to consider averages in the flux density and current density. That is, we are interested in the average flux density over the space of several flux vortices, and call the relevant quantities \vec{B} and $\langle \vec{j} \rangle$. If ϕ_0 is the magnitude of one flux quantum, and if there are N flux vortices perpendicularly intersecting an area S , the average flux density is simply

$$B = N\phi_0/S \quad , \quad (1.4)$$

and the average current density $\langle \vec{j} \rangle$ is related to \vec{B} through

$$\vec{\nabla} \times \vec{B} = \frac{4\pi}{c} \langle \vec{j} \rangle \quad . \quad (1.5)$$

Following Campbell and Evetts (21, p. 15) we next define the thermodynamic magnetic field \vec{H} as

$$H = |\vec{H}| = 4\pi \frac{\partial F(B)}{\partial B} \quad , \quad (1.6)$$

where the direction of \vec{H} is the same as the direction of

\vec{B} , i.e.,

$$\vec{H}/H = \vec{B}/B \quad .$$

The field \vec{H} defined in this way has all the usual electromagnetic properties normally associated with the quantity \vec{H} . In fact, if the Gibbs free energy density is related to the Helmholtz free energy density through the Legendre transformation

$$G = F - BH/4\pi \quad , \quad (1.7)$$

then one can show that the equilibrium condition $(\frac{\partial G}{\partial B})_{T,H} = 0$ is equivalent to Equation 1.7.

Associated with \vec{H} is the thermodynamic current density \vec{J} , where

$$\vec{\nabla} \times \vec{H} = \frac{4\pi}{c} \vec{J} \quad . \quad (1.8)$$

London (12, p. 102) referred to this as the "coarse-grained current density", and Campbell and Evetts (21, p. 19) call it the "transport current density". Actually, it is not in general the density of current fed into the specimen by external sources. Note also that \vec{J} is not in general equal to $\langle \vec{j} \rangle$. Although \vec{J} is difficult to explain in a physical sense, it may be roughly thought of as the current density needed to maintain the gradients in \vec{H} .

D. Critical Currents and Hard Superconductors

1. Critical currents

The magnetic behavior of type-II materials is intimately connected with the behavior of critical currents in these materials. In fact, the topic of critical currents alone comprises an extensive literature; for a thorough review of this subject, the reader is referred to Campbell and Evetts' recent monograph (21).

For our purposes, we shall regard a critical current as the magnitude of current density which is just sufficient to bring about the onset of flux flow. Experimentally flux flow is detected in a cylindrical sample by the appearance of a longitudinal voltage, indicative of a nonzero electric field. Typically, about one microvolt is detectable in the laboratory and is an acceptable standard for the existence of flux flow.

Part of the early difficulties in understanding type-II superconductivity arose because many type-II materials exhibit irreversible behavior in changing magnetic fields. Irreversibility means that these materials cannot be explained thermodynamically, because the final state of the material is history-dependent. Materials of this sort were called "hard superconductors", because usually they were mechanically hard substances. Quite often, irreversible materials are alloys

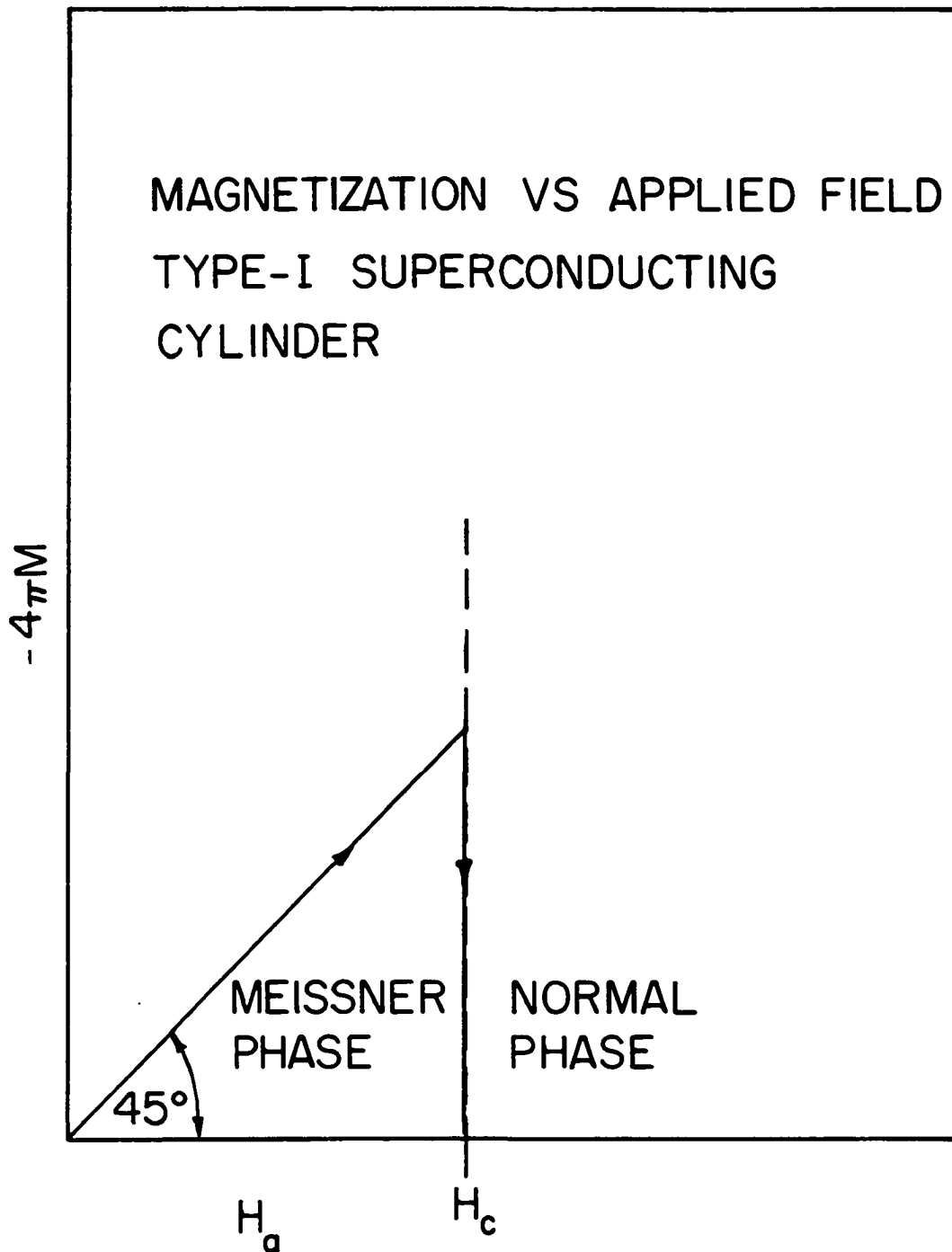


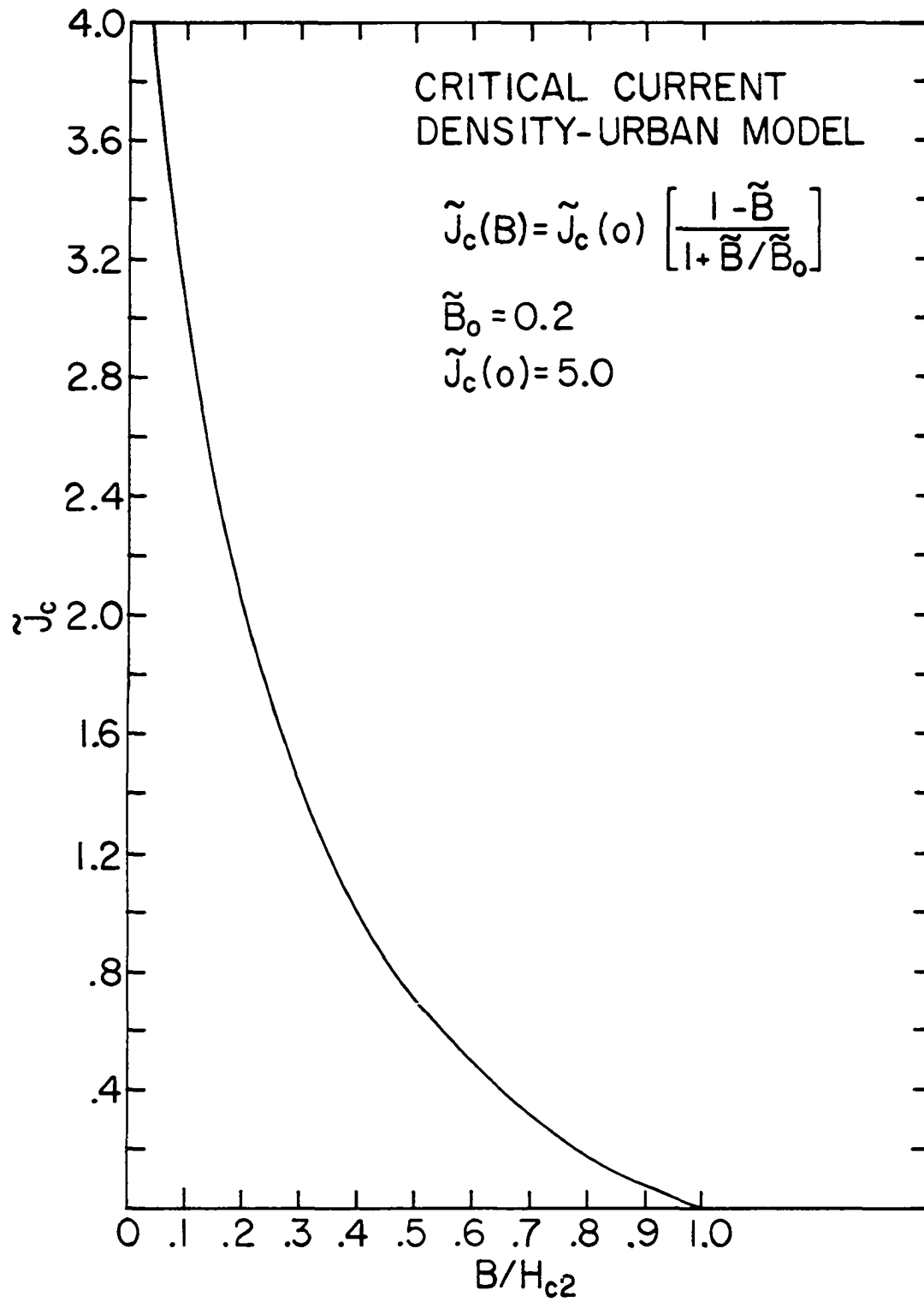
Figure 5. Magnetization curve for an ideal type-I superconducting cylinder in an applied field parallel to the cylinder axis

or otherwise impure metals with short mean free paths, such as Nb_3Sn , NbZr , and V_3Si . In fact, the only known ideal type-II materials are Nb, V, and Tc. In contrast, ideal type-I superconductors are usually very pure substances, such as mercury, tin and lead, and are mechanically soft. Hence, the names soft and hard become synonymous with ideal and non-ideal, respectively. As will be shown, the nonideality of most type-II materials has greatly complicated recent efforts to understand the current and field distributions in cylindrical samples. Later, we will propose a model whereby the history of a sample may be incorporated into a calculation for the magnetic state of the material.

Figure 6 is characteristic of most critical current behavior, when plotted as a function of the magnetic flux density B . As will be made clear later, the exact form of this curve is not primary to our model. That is, $J_c(B)$ appears as an unspecified function which presumably would be known for a specific material. All we require of $J_c(B)$ is that it be single-valued and everywhere finite. Urban (22) has compared various critical current models, and has proposed a new model which better agrees with existing data on Nb-25%Zr wire. Urban gives the empirical expression, in MKSA units,

$$J_c(B) = \alpha_c \cdot \left[\frac{\mu_0 H_{c2} - B}{B_0 + B} \right] , \quad (1.9)$$

Figure 6. Example of idealized critical current behavior according to the Urban model, for a material with moderately strong pinning. \tilde{J}_c is the reduced current density, defined by $\tilde{J}_c = J_c / (cH_{c2}/4\pi a)$, where a is the cylinder radius. $\tilde{B} = B/H_{c2}$ is the reduced magnetic flux density, and $\tilde{B}_0 = B_0/H_{c2}$ is an adjustable parameter which is responsible for the convexity in the shape of the curve



where α_c is a field independent, temperature dependent constant peculiar to a given material, and B_0 is a correction which becomes important at small B . In cgs units, this expression may be written as

$$J_c(B) = J_c(0) \cdot \left[\frac{1 - B/H_{c2}}{1 + B/B_0} \right] \quad (1.10)$$

and has the properties that $J_c(0)$ defines the maximum, and $J_c(H_{c2})$ is zero. Table 1, from Urban's (22) paper, shows some other recent models for $J_c(B)$. Later we will use Equation 1.10 in obtaining numerical solutions for the flux profile across a cylindrical wire.

2. Critical state model

The critical state model due to Bean (23) was a significant breakthrough in explaining the magnetization of hard superconductors. In the discussion which follows, we will take some liberties with Bean's formalism, and maintain a more careful distinction between the fields H and B .

Bean assumed that 1) the critical current density is independent of the magnetic flux density B , and 2) as flux accumulated in the specimen, shielding currents are induced to flow at a maximum value J_c , up to whatever depth is required to shield out the applied field. The field inside a cylindrical superconductor of radius a is obtained from Ampere's law,

Table 1. Critical current models

Source	Functional Form for $J_c(B)$ MKSA units
Bean (23); London (24)	Const. = α
Kim et al. (25)	$\alpha/(B_0 + B)$
Anderson (26); Friedel (27); Silcox and Rollins (28)	α/B
Yasukochi et al. (29)	$\alpha/B^{1/2}$
Irie and Yamafuji (30)	$\alpha/B^{\gamma-1}$
Fietz et al. (31)	$\alpha e^{-B/\beta} + \gamma$
Goedemoed et al. (32)	$\alpha(\mu_0 H_{c2} - B)$
Alden and Livingston (33); Campbell et al. (34); Coffey (35)	$\alpha \left[\frac{\mu_0 H_{c2} - B}{B^{1/2}} \right]$
Urban (22)	$\alpha \left[\frac{\mu_0 H_{c2} - B}{B_0 + B} \right]$

$$\vec{\nabla} \times \vec{H} = \frac{4\pi}{c} \vec{J} \quad , \quad (1.11)$$

which simplifies to

$$\partial H / \partial \rho = \frac{4\pi}{c} J_c \quad , \quad (1.12)$$

and the boundary condition

$$H(a) = H_a \quad , \quad (1.13)$$

where H_a is the applied field. Straight-forward integration yields the field as a function of radius,

$$H(\rho) = H_a + \frac{4\pi}{c} J_c (\rho - a) \quad . \quad (1.14)$$

The penetration radius ρ_p marks the position of the flux front, where the field H must be equal to H_{c1} . Thus,

$$\rho_p = a - \frac{c}{4\pi J_c} \cdot [H_a - H_{c1}] \quad . \quad (1.15)$$

When the flux front reaches the cylinder axis, $\rho_p = 0$ and the applied field has magnitude H^* , so that

$$H^* = \frac{4\pi}{c} J_c + H_{c1} \quad . \quad (1.16)$$

Then Equation 1.15 can be written as

$$\rho_p = a \cdot \left[\frac{1 - H_a/H^*}{1 - H_{c1}/H^*} \right] \quad . \quad (1.17)$$

Kim et al. (36) extended Bean's (23) approach by assuming that J_c depended upon the flux density B . In cylindrical shell specimens of Nb-Zr, they found that the critical state model, altered to the form

$$J_c = \text{const.}/(B_0 + B) \quad , \quad (1.18)$$

yielded screening fields in agreement with their experimental results. Thus, Equation 1.12 yields, in general,

$$H(\rho) = H(a) - \frac{4\pi}{c} \cdot \int_{\rho}^a J_c[B(\rho')] d\rho' \quad . \quad (1.19)$$

It is useful to examine the critical state model for a current-carrying type-II material in the absence of a longitudinal field. We assume that the longitudinal thermodynamic current density J is equal to the critical current density within the region of flux penetration. Then, from Ampere's law, $\vec{\nabla} \times \vec{H} = \frac{4\pi}{c} \vec{J}$, we have

$$\frac{c}{4\pi\rho} \frac{\partial}{\partial \rho}(\rho H_{\theta}) = J_c \quad (1.20)$$

which integrates to

$$H_{\theta}(\rho) = \frac{2\pi}{c} \rho J_c + \frac{1}{\rho} [a H_{\theta}(a) - \frac{2\pi}{c} a^2 J_c] \quad (1.21)$$

where we have assumed J_c to be independent of B .

We define the total transport current through the

cylinder, I_0 , and let $J_0 = I_0/\pi a^2$ be the average current density. Then Ampere's law relates the field at the surface to I_0 via

$$\frac{4\pi}{c} I_0 = 2\pi a H_\emptyset(a) \quad (1.22)$$

so that Equation 1.21 becomes

$$H_\emptyset(\rho) = \frac{2\pi}{c} \rho J_c - \frac{2\pi a^2}{c\rho} [J_c - J_0] \quad (1.23)$$

Dropping the subscript \emptyset and introducing the reduced quantities \tilde{H} , \tilde{J} , and $\tilde{\rho}$ defined by

$$\tilde{H} = H/H_{c2} \quad , \quad \tilde{J} = J/(cH_{c2}/4\pi a) \quad ,$$

and

$$\tilde{\rho} = \rho/a \quad , \quad (1.24)$$

we obtain the reduced form of Equation 1.23:

$$\tilde{H}(\tilde{\rho}) = \frac{1}{2}\tilde{\rho}\tilde{J}_c - \frac{1}{2}[\tilde{J}_c - \tilde{J}_0]/\tilde{\rho} \quad (1.25)$$

Next, we define the penetration radius ρ_p as the inner edge of the flux front. That is, at $\rho = \rho_p$, $H = H_{c1}$ and $B = 0$. Thus, the relationship between $\tilde{\rho}_p$ and \tilde{H}_{c1} is

$$\tilde{H}_{c1} = \frac{1}{2}\tilde{\rho}_p\tilde{J}_c - \rho[\tilde{J}_c - \tilde{J}_0]/\tilde{\rho}_p \quad (1.26)$$

or

$$\tilde{\rho}_p = \tilde{H}_{cl}/\tilde{J}_c + [(\tilde{H}_{cl}/\tilde{J}_c)^2 + 1 - \tilde{J}_o/\tilde{J}_c]^{1/2} .$$

We use the plus sign for the radical, as the negative root would yield a negative ρ_p or a solution where $dH/d\rho$ would be negative. Letting $m = \tilde{H}_{cl}/\tilde{J}_c$ and $q = \tilde{J}_o/\tilde{J}_c$, Equation 1.26 becomes

$$\tilde{\rho}_p = m + [m^2 + 1 - q]^{1/2} \quad (1.27)$$

and Equation 1.25 becomes

$$\tilde{H}(\tilde{\rho}) = \frac{\tilde{H}_{cl}}{2m} [\tilde{\rho} + \frac{q-1}{\tilde{\rho}}] \quad (1.28)$$

Clearly, the penetration radius is a decreasing function of q and has a minimum value of m , which occurs at $q = 1 + m^2$. Thus, for stable solutions we require

$$\tilde{J}_o \leq \tilde{J}_c [1 + m^2] \quad (1.29a)$$

and

$$\tilde{\rho}_p \geq m . \quad (1.29b)$$

These latter results may also be obtained by differentiation of Equation 1.28 and requiring that $dH/d\rho$ be nonnegative at the penetration radius.

As will be explained in the next paragraph, the largest physically meaningful value for $\tilde{\rho}_p$ is unity. The corresponding value for q , i.e., $q = 2m$, is then proportional to the

minimum possible current density consistent with a mixed state condition. Hence, q must lie in the region defined by $2m \leq q \leq 1 + m^2$. In addition, we must now limit q in order to keep $\tilde{H}(\tilde{\rho})$ everywhere less than or equal to unity. It is easy to show that this requirement is met if $q \leq 2m/\tilde{H}_{c1}$. Thus, the permissible values of q are confined to the cross-hatched region of Figure 7, corresponding to

$$2m \leq q \leq \min \left\{ \begin{array}{l} 1 + m^2 \\ 2m/\tilde{H}_{c1} \end{array} \right\} . \quad (1.30)$$

The point where $1 + m^2$ is equal to $2m/\tilde{H}_{c1}$ is given by $m = (1 - k)/\beta$, where

$$\beta \equiv \tilde{H}_{c1} ,$$

and k is related to β through

$$\beta^2 + k^2 = 1 .$$

The above result may in part be verified by considering the notion of the critical radius of a vortex ring. The critical radius ρ_c is defined to be the smallest radius possible before a vortex ring collapses under its own line tension. In Appendix C it is shown that

$$\rho_c = cH_{c1}/4\pi J_c \quad (1.31)$$

Referring to Figure 8, we let ρ_c be the radius of the inner-

Figure 7. Cross-hatched region defines values of m and q necessary to obtain the static mixed state condition, for a current-carrying cylinder in the absence of an applied longitudinal field. $m = \tilde{H}_{cl}/\tilde{J}_c$ and $q = J_o/J_c$, where J_o is the mean current density and J_c is the critical current density. Below the line $q = 2m$, the sample is in the Meissner state. Above the lines $q = 2m/\tilde{H}_{cl}$ and $q = m^2 + 1$, sample reverts to either a flux-flow state or the normal state

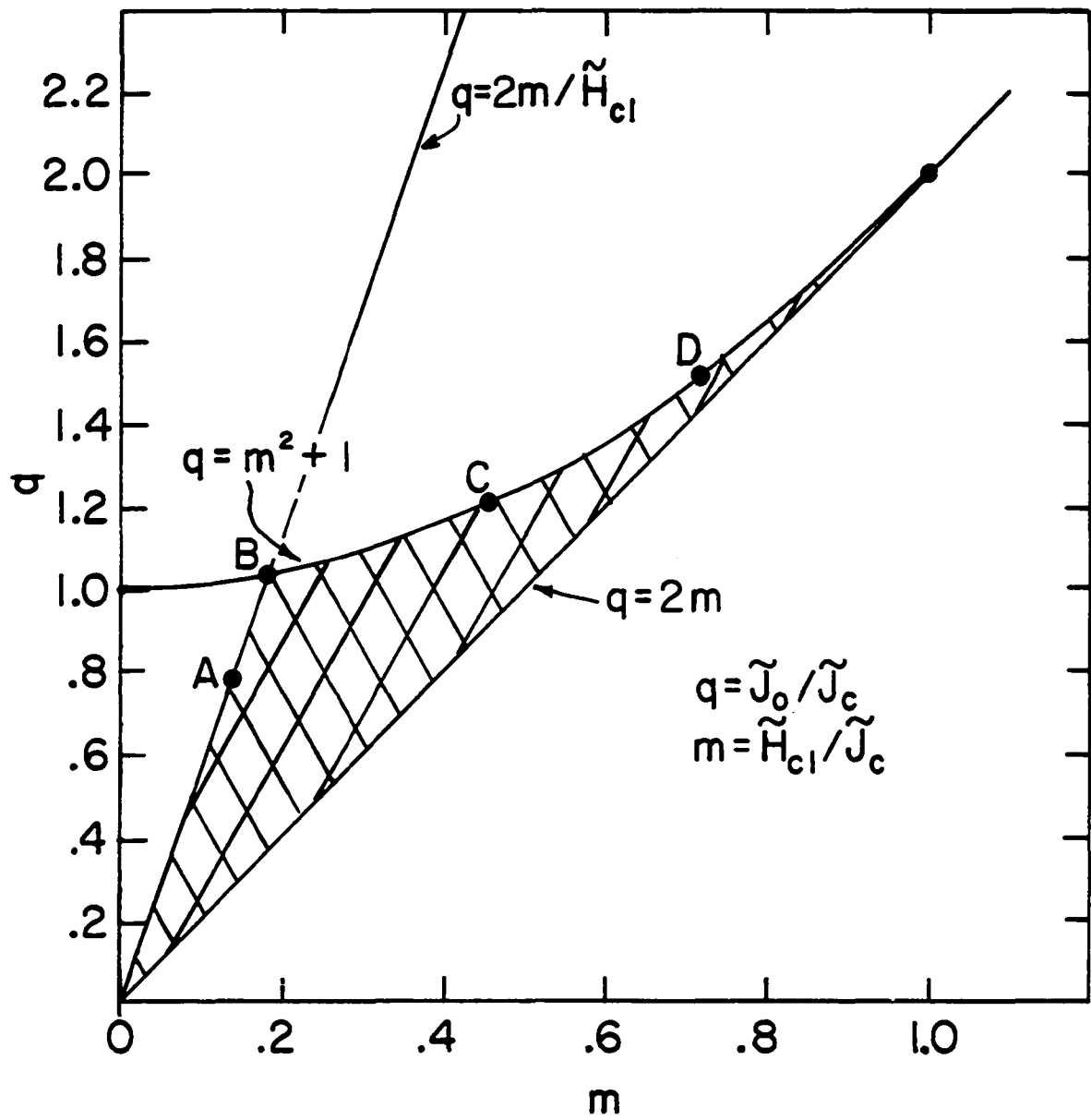
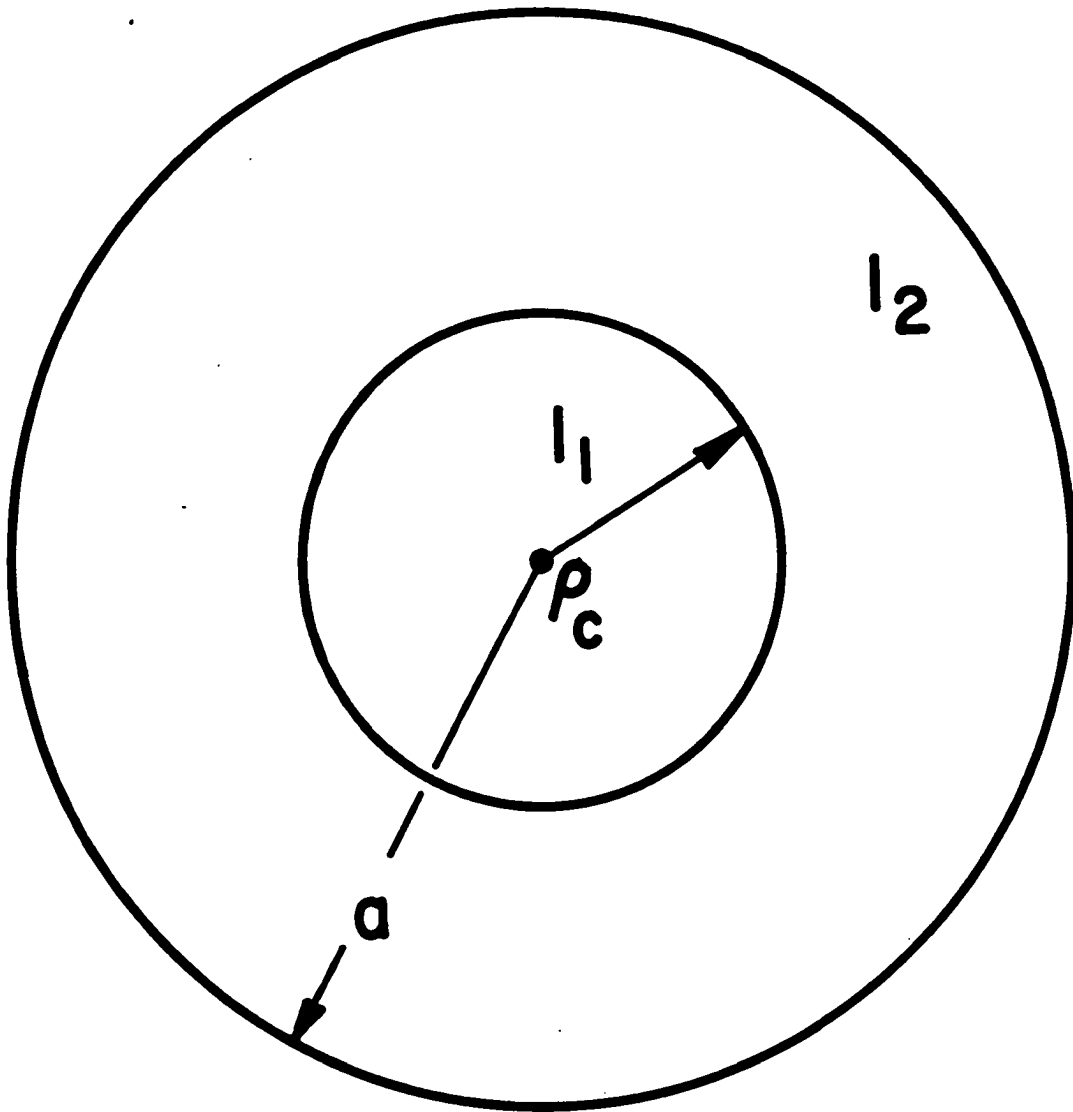


Figure 8. Cross section of type-II cylinder in the current-only situation, showing location of flux front and the distribution of currents. ρ_c represents the flux front, and a is the cylinder radius



most vortex ring. That is, $\rho_p = \rho_c$ and $H(\rho_c) = H_{c1}$. In the region where $0 \leq \rho \leq \rho_c$, the thermodynamic current density is denoted I_1 , and in the region where $\rho_c \leq \rho \leq a$, the current is denoted I_2 . Thus, the total current I_o is

$$I_o = I_1 + I_2 \quad (1.32a)$$

and

$$I_1 = \frac{1}{2}c\rho_c H_{c1} \quad (1.32b)$$

$$I_2 = \pi J_c [a^2 - \rho_c^2] \quad (1.32c)$$

so that

$$I_o = \frac{1}{2}c\rho_c H_{c1} + \pi[a^2 - \rho_c^2]J_c \quad (1.33)$$

and

$$\begin{aligned} J_o &= I_o / \pi a^2 \\ &= c\rho_c H_{c1} / 2\pi a^2 + [1 - (\rho_c/a)^2]J_c \\ &= J_c [1 + \rho_c^2/a^2] \end{aligned} \quad (1.34)$$

In reduced form, this is simply

$$\tilde{J}_o = \tilde{J}_c [1 + \tilde{\rho}_c^2] \quad (1.35)$$

which is the same as Equation 1.29 with m equal to $\tilde{\rho}_c$.

In summary, one may describe the critical state model

by considering the flux profiles which obtain as the magnitude of the surface field is progressively increased from zero. Starting with a sample in the virgin state, subjected to a parallel magnetic field but no current, we observe no flux penetration until the surface field reaches H_{c1} . As the surface field climbs above H_{c1} , flux penetrates progressively deeper into the specimen, with profiles similar to those sketched in Figure 9.

In the current-only case (Figure 7), however, static flux penetration goes no further than $\rho_p = ma$, where $m = \tilde{H}_{c1}/\tilde{J}_c = \tilde{\rho}_c$ is a material-dependent factor, which must be less than one to guarantee a stable mixed state. Should the current density \tilde{J}_0 then exceed the value $(1 + m^2)\tilde{J}_c$, the innermost flux rings collapse under their own line tension, and the sample enters a flux-flow state or reverts to the normal state. We note that the critical current J_c is proportional to the pinning strength of the material. Hence, strong pinning materials would have smaller minimum penetration radii m , and would allow a deeper penetration of flux before breakdown of the mixed state occurred. Figures 10 and 11 are typical H and B profiles for the current-only critical state model in a specimen for which $\tilde{H}_{c1} = 0.25$, selected for the maximum possible current densities allowed at four values of the parameter m . The flux density B obtains from the intrinsic Abrikosov diamagnetism as illustrated

Figure 9. Simplified diagram of Bean-London critical state model, for a material with no surface barrier. $H_1 < H_2 < \dots < H_6$

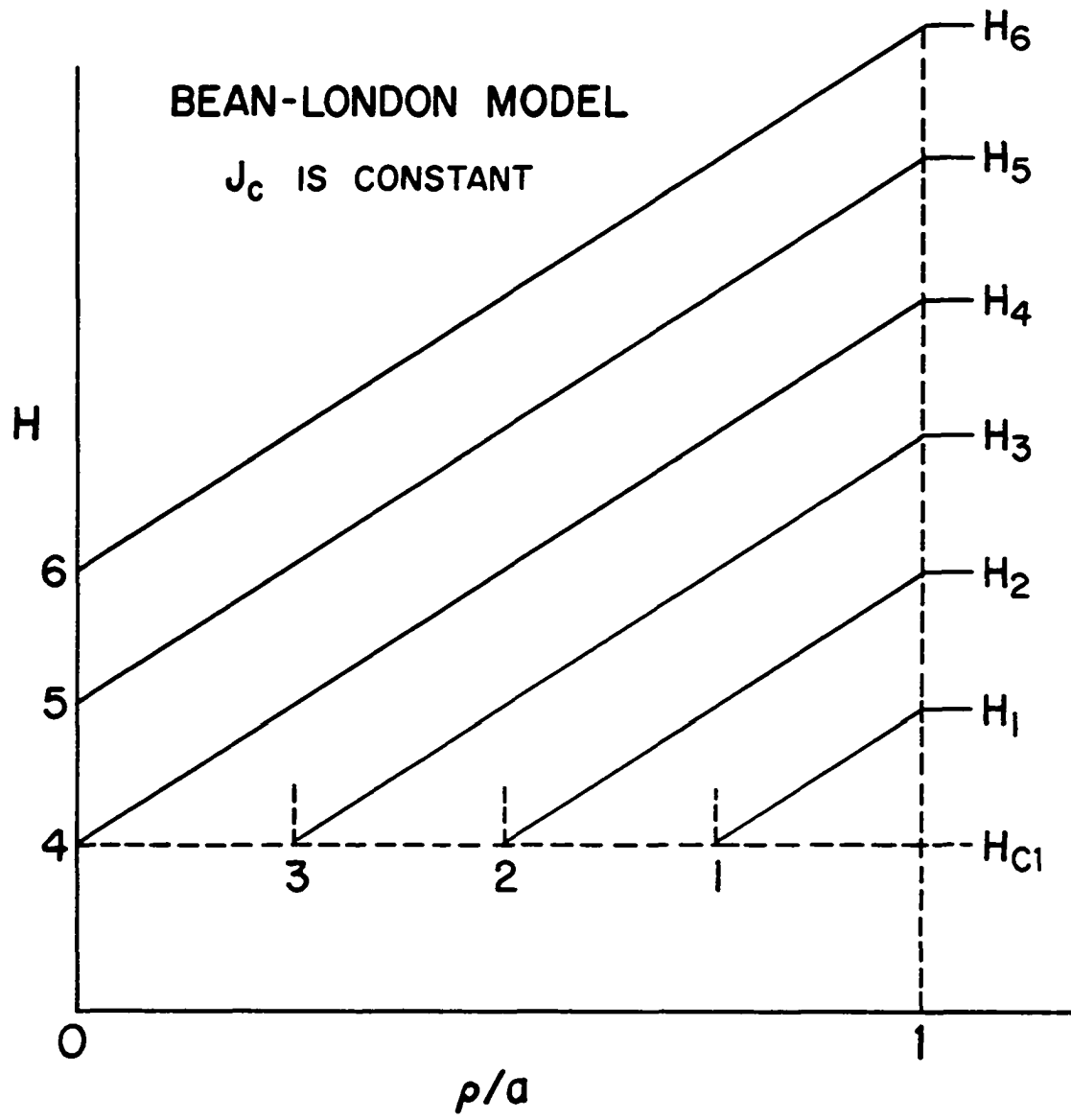
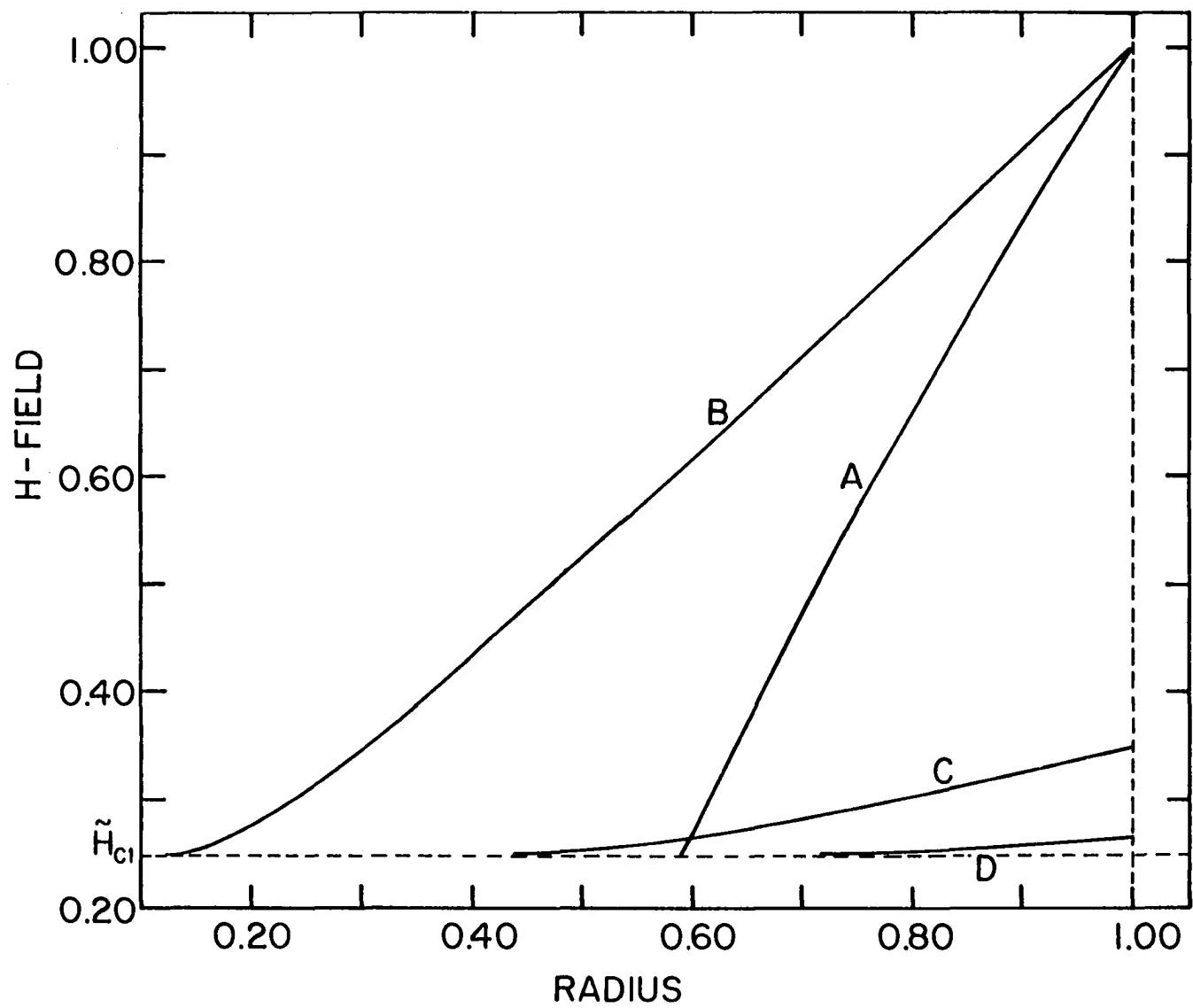


Figure 10. Magnetic field profiles, \tilde{H} versus $\tilde{\rho}$, for type-II cylinder with $\tilde{H}_{c1} = 0.25$ under the conditions corresponding to A, B, C, and D in Figure 7



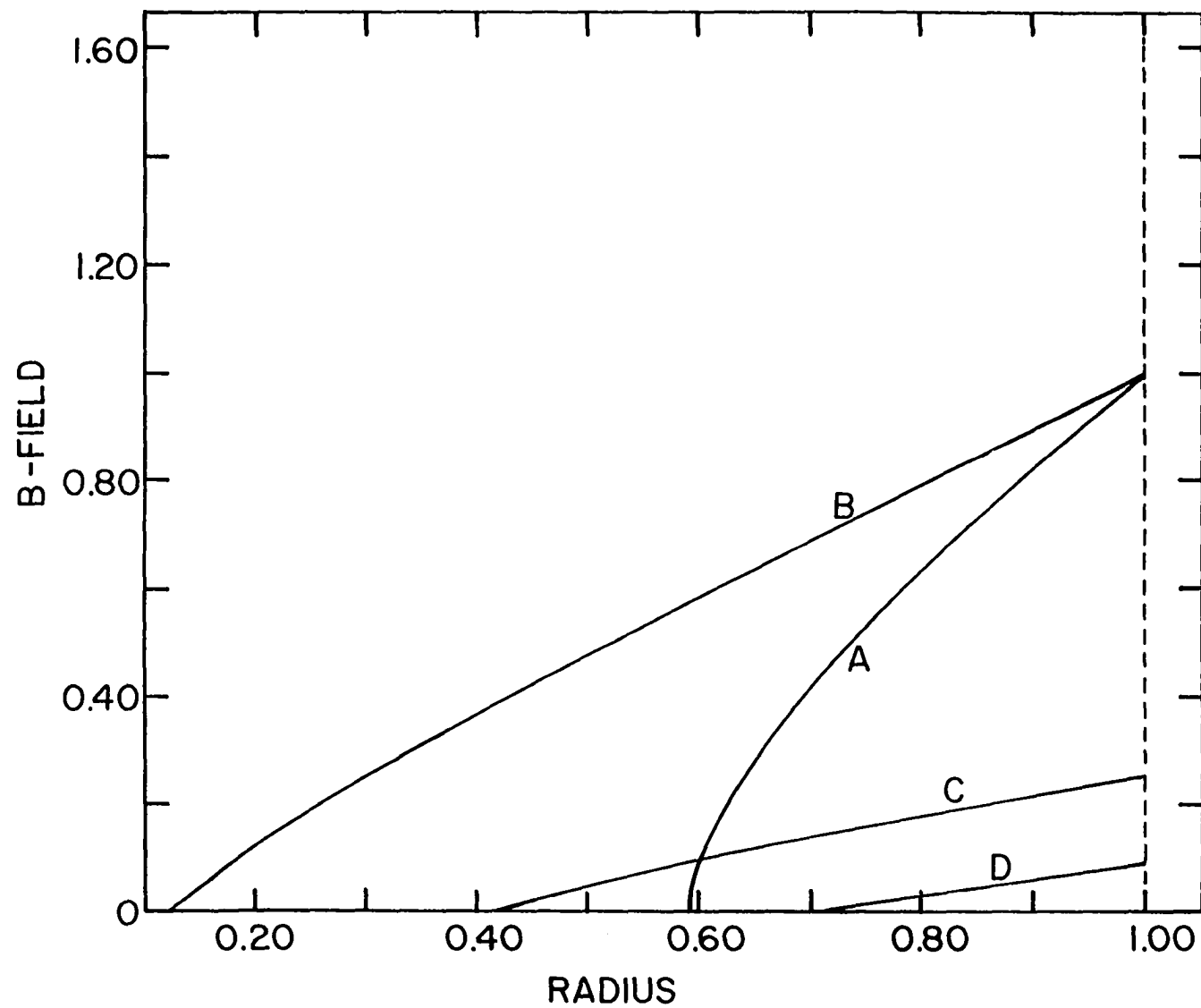


Figure 11. Flux density profiles, \tilde{B} versus $\tilde{\rho}$, corresponding to Figure 10

in Figure 2. The precise form of $B(H)$ used in Figure 11 is not important here; a more complete explanation is given in Section E of Chapter II.

3. Force-free model

In 1963 Bergeron et al. (2) presented measurements of critical currents in commercially available cold-drawn NbZr alloy wires, subjected to longitudinal fields. Their results showed an anomalous hump in the curve of critical current I_c versus applied field, as reproduced in Figure 12. To explain this hump, Bergeron (1) postulated the existence of a helical current flow, which would give rise to a paramagnetic moment. The helical current response was regarded as necessary to minimize the Lorentz forces on the currents. LeBlanc et al. (37) reported paramagnetic moments in cold-worked Nb-25%Zr wire and high purity annealed Nb-50%Ta wire, under experimental conditions similar to those used by Bergeron et al. (2). LeBlanc et al. (37) found rather poor quantitative agreement with Bergeron's force-free model, and regarded force-free fields as probable only in nearly ideal type-II superconductors.

We review here the theory of force-free fields, beginning with an infinite flat slab of type-II superconductor immersed in a field parallel to the surface of the slab. The coordinates describing the geometry are shown in Figure 13.

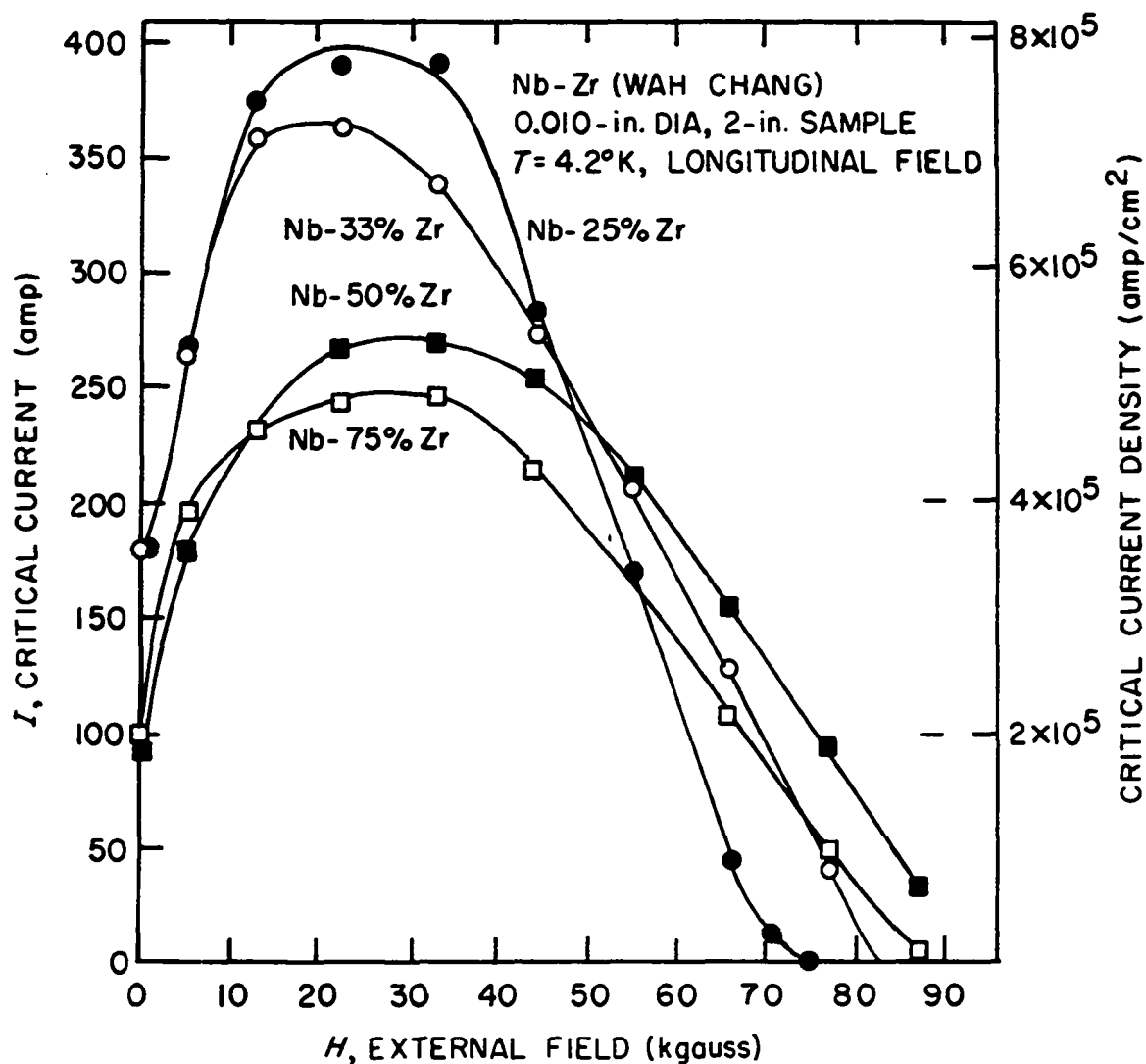


Figure 12. Experimental values of critical current versus external field, from reference 2

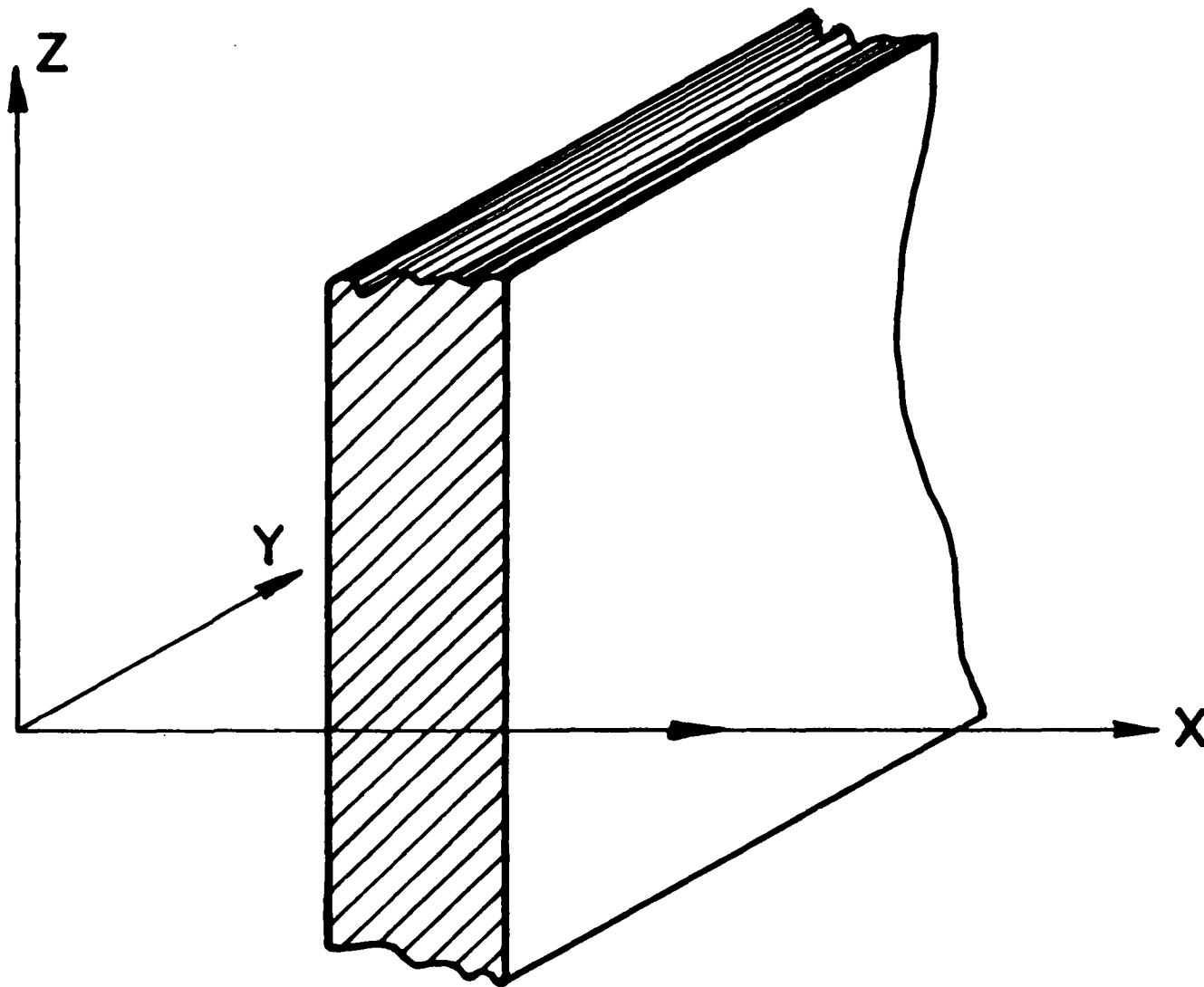


Figure 13. Coordinates for flat slab

We assume that all currents and fields are parallel to the face of the slab, so that the components normal to the faces, i.e., J_x and H_x , are zero. The force-free requirement is expressed as $\vec{J} \times \vec{B}/c = 0$, or, since \vec{H} is parallel to \vec{B} , $\vec{J} \times \vec{H} = 0$. We begin with Ampere's law,

$$\begin{aligned} \vec{J} &= \frac{c}{4\pi} \nabla \times \vec{H} \\ &= \frac{c}{4\pi} \left[-\hat{y} \frac{\partial H_z}{\partial x} + \hat{z} \frac{\partial H_y}{\partial x} \right] \end{aligned} \quad (1.36)$$

where \hat{y} , \hat{z} are unit vectors in those respective directions. The force-free requirement, $\vec{J} \times \vec{H} = 0$, implies that \vec{J} and \vec{H} are parallel, or

$$\vec{J} = f(x) \cdot \vec{H} \quad (1.37)$$

where $f(x)$ is some function of x , to be determined. Arbitrarily, let

$$f(x) = ck(x)/4\pi$$

so that $k(x)$ has units of inverse length. By combining Equation 1.36 and 1.37 we obtain

$$\frac{ck(x)}{4\pi} [H_y \hat{y} + H_z \hat{z}] = \frac{c}{4\pi} \left[-\frac{\partial H_z}{\partial x} \hat{y} + \frac{\partial H_y}{\partial x} \hat{z} \right] \quad (1.38)$$

which yields

$$H_y \frac{\partial H_y}{\partial x} = -H_z \frac{\partial H_z}{\partial x}$$

or

$$\frac{1}{2} \frac{\partial}{\partial x} [H_y^2 + H_z^2] = 0 \quad . \quad (1.39)$$

Since $H^2 = H_y^2 + H_z^2$, Equation 1.39 becomes

$$H \frac{\partial}{\partial x} (H) = 0 \quad (1.40)$$

which demands that either $H = 0$ or that H is everywhere the same. Rejecting the former as trivial, the latter solution allows us to express the components of H parametrically as

$$H_y = H \cdot \sin \alpha(x)$$

$$H_z = H \cdot \cos \alpha(x) \quad (1.41)$$

where $\alpha(x)$ is some arbitrary function of x , subject only to the boundary condition that H_y and H_z be continuous at the surfaces. Using Equation 1.38 together with 1.41 we obtain

$$\begin{aligned} H_y &= -k^{-1}(x) \partial H_z / \partial x \\ &= \frac{H}{k(x)} \sin \alpha(x) \frac{\partial \alpha(x)}{\partial x} \end{aligned}$$

so that

$$\frac{\partial \alpha(x)}{\partial x} = k(x) \quad . \quad (1.42)$$

We see that the magnitude of $k(x)$ determines the amount of

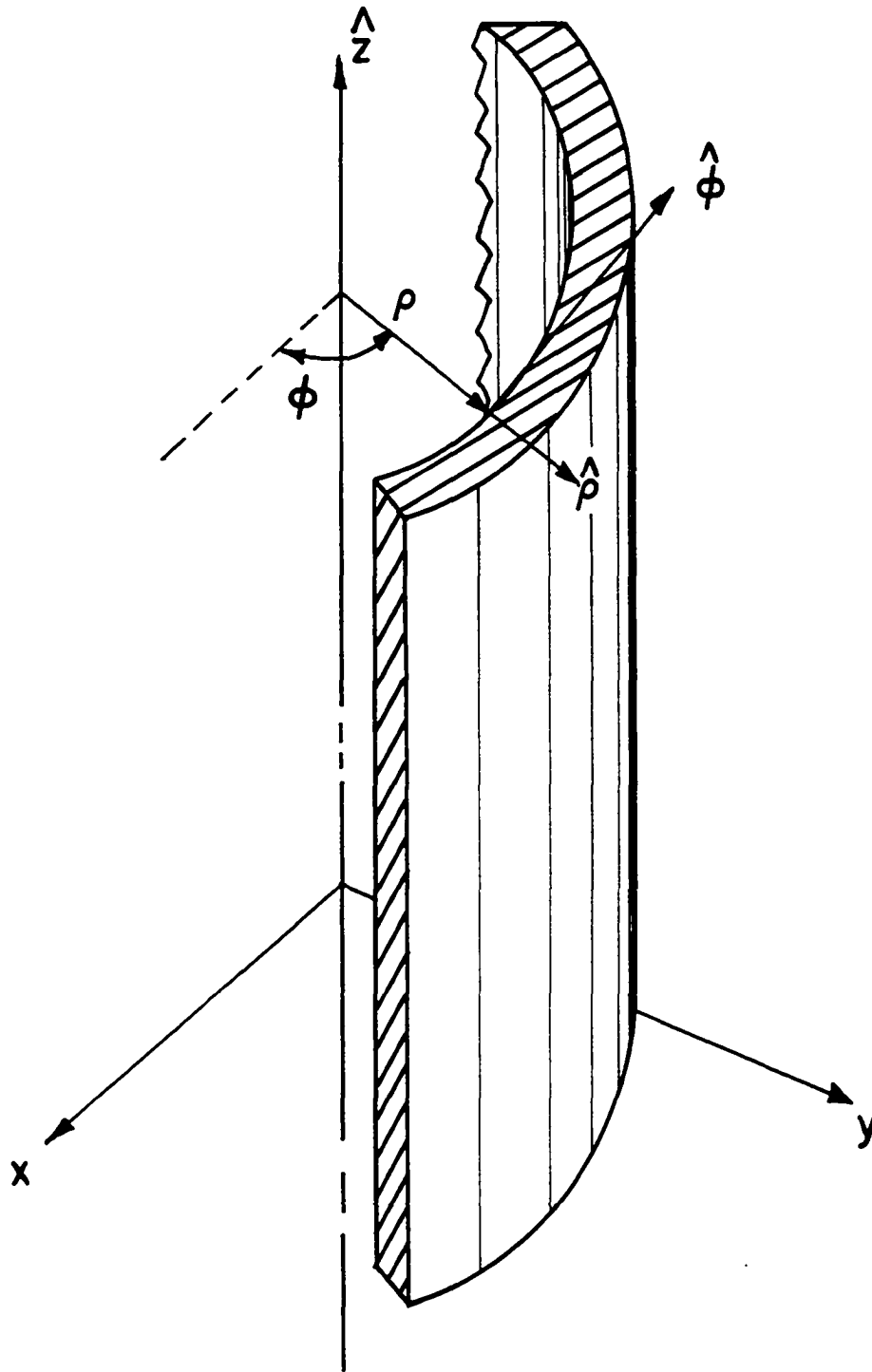
twist which the field undergoes in traversing the thickness of the slab. If $k(x)$ is sufficiently large, it appears possible for the field and current to reverse directions one or more times within the span of the slab thickness.

The flat infinite slab calculation above is easily modified to accommodate the case of a thin cylindrical shell in an axial field. That is, we regard the flat slab as a cylinder with an infinite radius. Referring to Figure 2 we define the word "thin" to mean that the thickness of the cylinder wall is small compared with the radius. It is convenient to switch to cylindrical coordinates $\rho = (x^2 + y^2)^{1/2}$, $\phi = \tan^{-1}(y/x)$, and z , with unit vectors $\hat{\rho} = \hat{x}\cos\phi + \hat{y}\sin\phi$, $\hat{\phi} = \hat{y}\cos\phi - \hat{x}\sin\phi$, and \hat{z} , where the z -axis is coincident with the cylinder axis. (See Figure 14.) We shall assume that \vec{H} has no ϕ -dependence and no z -dependence, but only ρ -dependence. Thus, Equation 1.37 guarantees that \vec{J} will have ρ -dependence only, so that \vec{J} and \vec{H} may be written

$$\begin{aligned}\vec{J}(\rho) &= \hat{\phi}J_{\phi}(\rho) + \hat{z}J_z(\rho) \\ \vec{H}(\rho) &= \hat{\phi}H_{\phi}(\rho) + \hat{z}H_z(\rho) \quad .\end{aligned}\tag{1.43}$$

In cylindrical coordinates the curl of \vec{H} is

$$\vec{\nabla} \times \vec{H} = -\hat{\phi} \frac{\partial H_z}{\partial \rho} + \hat{z} \left[\frac{H_{\phi}}{\rho} + \frac{\partial H_{\phi}}{\partial \rho} \right]\tag{1.44}$$



CYLINDRICAL COORDINATES

Figure 14. Cylindrical coordinates

so that from Ampere's law we obtain

$$J_{\theta} = - \frac{c}{4\pi} \frac{\partial H_z}{\partial \rho} \quad (1.45a)$$

$$J_z = \frac{c}{4\pi} \left[\frac{H_{\theta}}{\rho} + \frac{\partial H_{\theta}}{\partial \rho} \right] \cong \frac{c}{4\pi} \frac{\partial H_{\theta}}{\partial \rho} \quad (1.45b)$$

$$J_{\rho} = 0 \quad (1.45c)$$

where the approximation used in Equation 1.45b is valid in the case of a thin shell where $\frac{H_{\theta}}{\rho} \ll \frac{\partial H_{\theta}}{\partial \rho}$. As before, we may write

$$\vec{J} = \frac{ck(\rho)}{4\pi} \vec{H}(\rho) \quad (1.46)$$

from the force-free requirement, which yields

$$J_{\theta} = \frac{ck(\rho)}{4\pi} H_{\theta} = - \frac{c}{4\pi} \frac{\partial H_z}{\partial \rho}$$

$$J_z = \frac{ck(\rho)}{4\pi} H_z = \frac{c}{4\pi} \frac{\partial H_{\theta}}{\partial \rho}$$

or

$$H_{\theta} = - k^{-1}(\rho) \frac{\partial H_z}{\partial \rho}$$

$$H_z = k^{-1}(\rho) \frac{\partial H_{\theta}}{\partial \rho}$$

$$H_{\rho} = 0 \quad . \quad (1.47)$$

Then, as before, we may define a parametric angle $\alpha = \alpha(\rho)$ such that

$$\begin{aligned} H_{\theta}(\rho) &= H \sin \alpha(\rho) \\ H_z(\rho) &= H \cos \alpha(\rho) \end{aligned} \quad (1.48)$$

and where H is constant. Using arguments presented above, it is easy to show that $\frac{\partial \alpha(\rho)}{\partial \rho} = k(\rho)$, or

$$\alpha(\rho) = \int k(\rho') d\rho' \quad .$$

Equations 1.48 describe a flux spiral whose pitch angle with respect to the z -axis is $\alpha(\rho)$.

We consider next the case of the thick-walled cylinder, where the thickness of the wall is on the same order of magnitude as the radius of the cylinder. The analysis proceeds as before, although the term H_{θ}/ρ may no longer be neglected in Equation 1.44. Thus,

$$\begin{aligned} J_{\theta} &= \frac{ck}{4\pi} H_{\theta} = - \frac{c}{4\pi} \frac{\partial H_z}{\partial \rho} \\ J_z &= \frac{ck}{4\pi} H_z = \frac{c}{4\pi} \left[\frac{H_{\theta}}{\rho} + \frac{\partial H_{\theta}}{\partial \rho} \right] = \frac{c}{4\pi \rho} \frac{\partial}{\partial \rho} (\rho H_{\theta}) \quad . \end{aligned} \quad (1.49)$$

Just as above, there is a wide variety of different force-free configurations possible, corresponding to different radial dependencies of the pitch angle α . An interesting

example to consider is that for which k is constant. Then we may substitute the dimensionless quantity w in place of ρk , giving $k^{-1}d/d\rho = d/dw$, so that Equations 1.47 become

$$H_{\emptyset} = - \partial H_Z / \partial w \quad (1.50a)$$

and

$$H_Z = \frac{1}{w} \frac{\partial}{\partial w} (w H_{\emptyset}) \quad . \quad (1.50b)$$

Substituting Equation 1.50a into 1.50b yields

$$H_Z = - \frac{1}{w} \frac{d}{dw} \left(w \frac{\partial H_Z}{\partial w} \right)$$

or

$$H_Z + \frac{1}{w} \frac{d}{dw} \left[w \frac{\partial H_Z}{\partial w} \right] = 0 \quad (1.51)$$

and substituting Equation 1.50b into 1.50a gives

$$H_{\emptyset} = - \frac{d}{dw} \left[\frac{1}{w} \frac{d}{dw} (w H_{\emptyset}) \right]$$

or

$$H_{\emptyset} + \frac{d}{dw} \left[\frac{1}{w} \frac{d}{dw} (w H_{\emptyset}) \right] = 0 \quad . \quad (1.52)$$

Equations 1.51 and 1.52 are Bessels equations of order zero and one respectively. A Bessel equation of integral order ν has for solutions the Bessel functions of the first and second kinds, $J_{\nu}(w)$ and $Y_{\nu}(w)$, respectively. Thus, a linear combination of $J_{\nu}(w)$ and $Y_{\nu}(w)$ also represents a

solution, and we obtain

$$H_z(w) = aJ_0(w) + bY_0(w) \quad (1.53)$$

$$H_\theta(w) = aJ_1(w) + bY_1(w) \quad (1.54)$$

where the constants a , b may be evaluated from the boundary conditions.

Recently Clem (38) has shown that for any arbitrary functional dependence of the pitch angle $\alpha(\rho)$ upon ρ , one may determine $H(\rho)$ and $k(\rho)$ explicitly, according to

$$k(\rho) = \rho^{-1} \sin\alpha(\rho)\cos\alpha(\rho) + \frac{\partial\alpha(\rho)}{\partial\rho} \quad (1.55)$$

and

$$H(\rho) = H(a) \cdot \exp \left\{ \int_{\rho}^a dr \frac{\sin^2\alpha(r)}{r} \right\} \quad (1.56)$$

where, as in Equation 1.46, \vec{H} , \vec{J} , and \vec{k} are related through

$$\vec{J} = \frac{ck(\rho)}{4\pi} \cdot \vec{H} \quad (1.57)$$

In the special case where $k(\rho)$ is a constant, one may show that

$$\alpha(\rho) = \tan^{-1} [J_1(k\rho)/J_0(k\rho)] \quad (1.58)$$

and

$$H(\rho) = H(0) \cdot [J_0^2(k\rho) + J_1^2(k\rho)]^{1/2} \quad (1.59)$$

which is the well known Bessel function solution (39).

For details of the above solution, see Appendix C.

Figure 15 shows $\alpha(\rho)$ versus $\tilde{\rho}(= \rho/a)$ for several arbitrary values of k (Equation 1.58). Figures 16 and 17 show H and B profiles corresponding to Equation 1.59, where $k(\rho)$ has been assigned several arbitrary values. As was the case with Figure 11, the flux density B obtains from the intrinsic Abrikosov diamagnetism of the mixed state, the model for which appears in Section E of Chapter II.

We will return to the force-free model in the next chapter, after first discussing some general features of spiral flux lines. The origins of Equations 1.55 and 1.56 will be shown there, as well as a phase diagrammatic method to characterize the force-free, or weak pinning state.

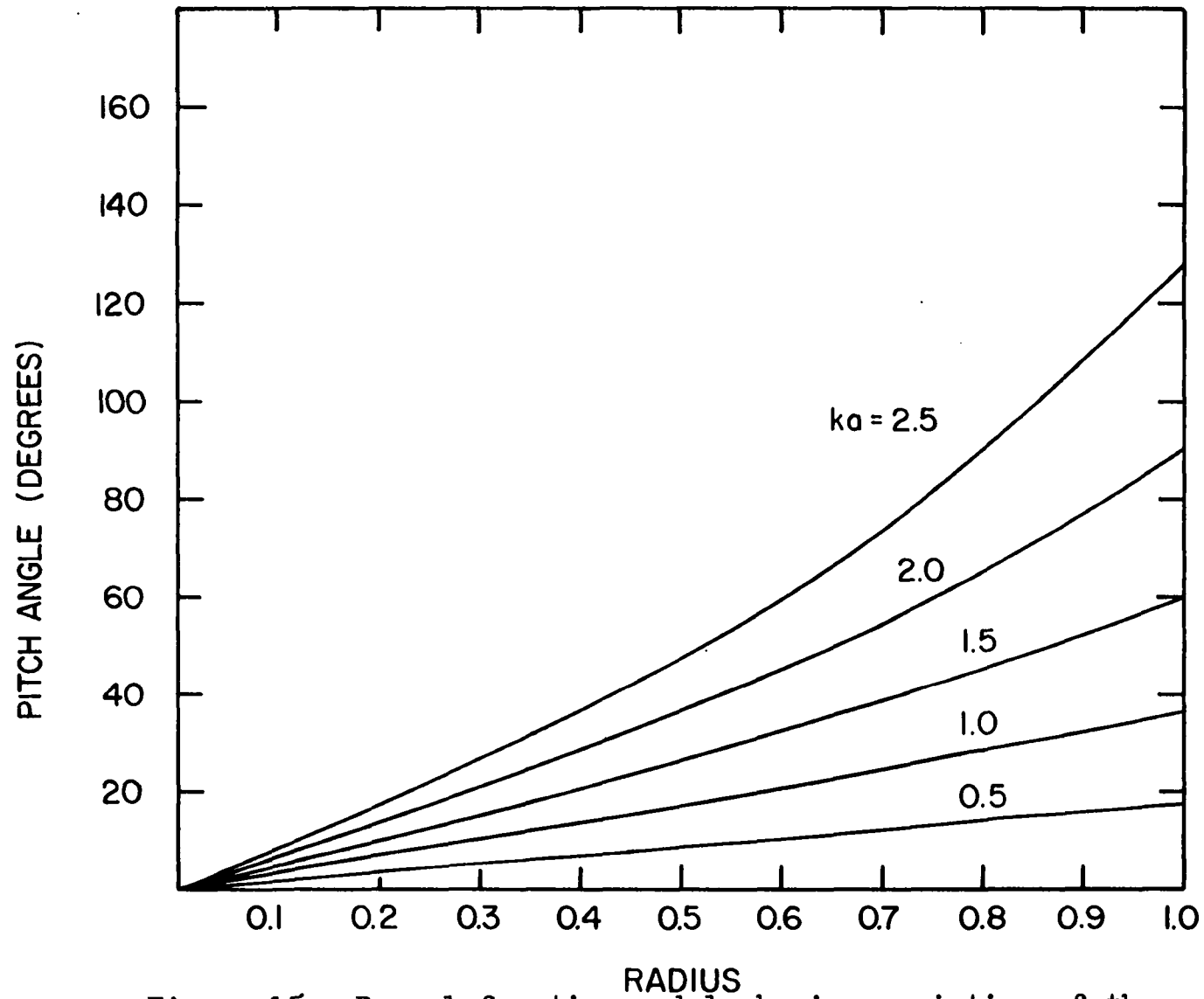


Figure 15. Bessel function model showing variation of the fluxoid pitch angle with radius, α versus $\tilde{\rho} = \rho/a$, for several values of the parameter k

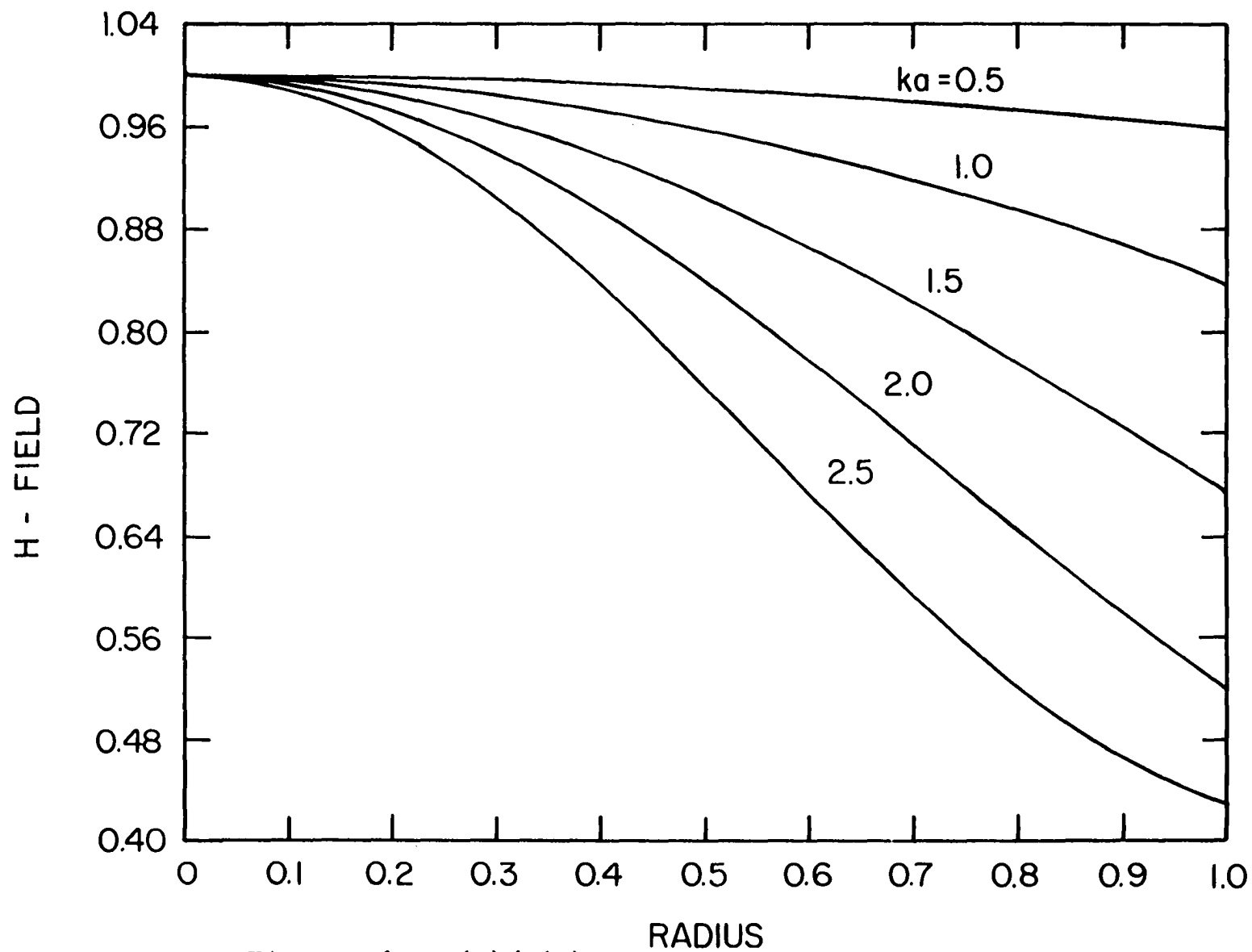


Figure 16. $H(\rho)/H(0)$ versus $\tilde{\rho} = \rho/a$ for Bessel function model, for several values of the parameter k

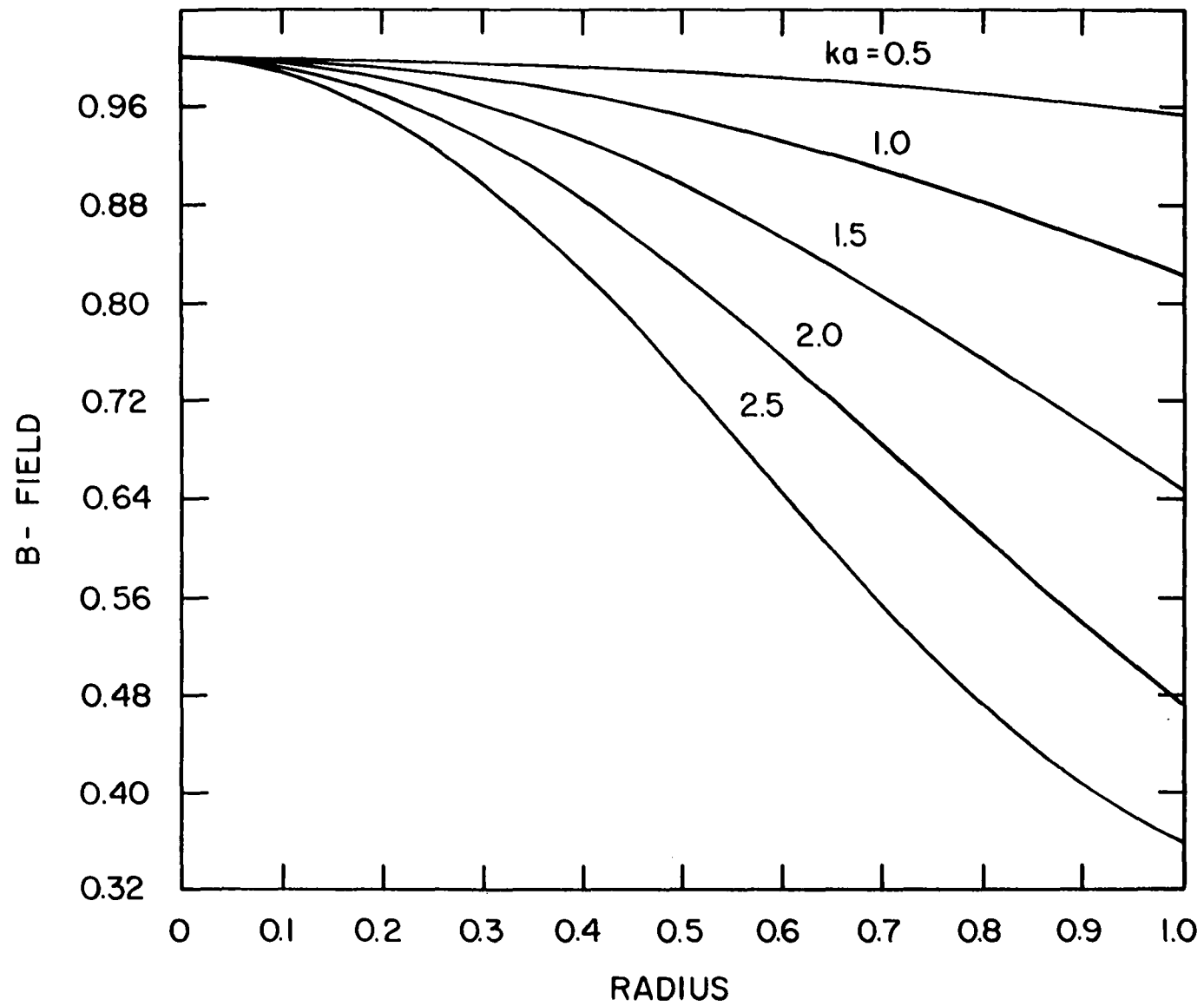


Figure 17. $B(\rho)/B(0)$ versus $\tilde{\rho} = \rho/a$ for Bessel function model, for several values of the parameter k

II. SPIRAL FLUX LINES

A. Introductory Remarks

An excellent review of the literature of current-carrying type-II superconducting cylinders has been given by Timms and Walmsley (39). We wish to propose here a formal statement of the problem of infinite cylinders and a model to describe this behavior. We assume an infinite cylinder of some type-II material, with dimensions large compared with the flux penetration depth λ . For the present, we assume that the cylinder is originally in the virgin state containing no vortices, and that a transport current I and uniform axial field H_a are slowly applied, until some final values H_{af} and I_f are reached. During this time, we require that the ratio I/H_a be maintained constant. We characterize the material in the following way: the Ginzburg-Landau parameter κ is known, along with the upper and lower critical fields H_{c2} and H_{c1} . In addition, we assume that the bulk pinning properties are well described by two parameters, $J_c(0)$ and B_0 , whose precise definitions will be made clear later. Finally, we assume that surface pinning is well described by one parameter, H_g , also to be discussed later. We shall demonstrate that the above information is sufficient to unambiguously describe the resultant state of the system at equilibrium.

B. Qualitative Physical Description

We expect flux to enter the cylinder in the form of quantized fluxoids, each carrying the flux quantum ϕ_0 of magnetic flux. Flux enters at the surface only, and the shape of each fluxoid is a spiral. We describe the fluxoid according to its radial coordinate and its pitch angle with the z-axis. At nucleation, the pitch angle of the fluxoid must correspond to the angle of the resultant surface field, determined by the ratio of transport current to applied axial field.

We define magnetic flux density according to our prior discussion of average and local flux densities. Accordingly, when we refer to the magnetic flux density, we mean the average flux density, which is given the symbol \vec{B} .

Cylindrical coordinates are most suitable, and we use the notation described earlier. The vector direction of a fluxoid, $\hat{\phi}_0$, is given by

$$\begin{aligned}\hat{\phi}_0 &= \frac{B_z}{B} \hat{z} + \frac{B_\phi}{B} \hat{\phi} \\ &= \hat{z} \cos \alpha + \hat{\phi} \sin \alpha\end{aligned}\tag{2.1}$$

where the pitch angle with respect to the z-axis, α , is given by

$$\alpha = \tan^{-1}(B_\phi/B_z) \quad .\tag{2.2}$$

The thermodynamic field \vec{H} points in the same direction as the flux density \vec{B} , so that

$$\vec{H}/H = \vec{B}/B = \hat{\phi}_0 \quad . \quad (2.3)$$

The various trigonometric relations describing the geometry of a fluxoid may be obtained by "unwrapping" the fluxoid, as in Figure 18. We see that the pitch L of a fluxoid is related to the fluxoid radius and pitch angle via

$$\tan\alpha = B_{\phi}/B_z = H_{\phi}/H_z$$

and

$$|\tan\alpha| = 2\pi\rho/L \quad . \quad (2.4)$$

Later, we shall reconstruct this diagram using reduced quantities.

C. Differential Equation Between H and ρ

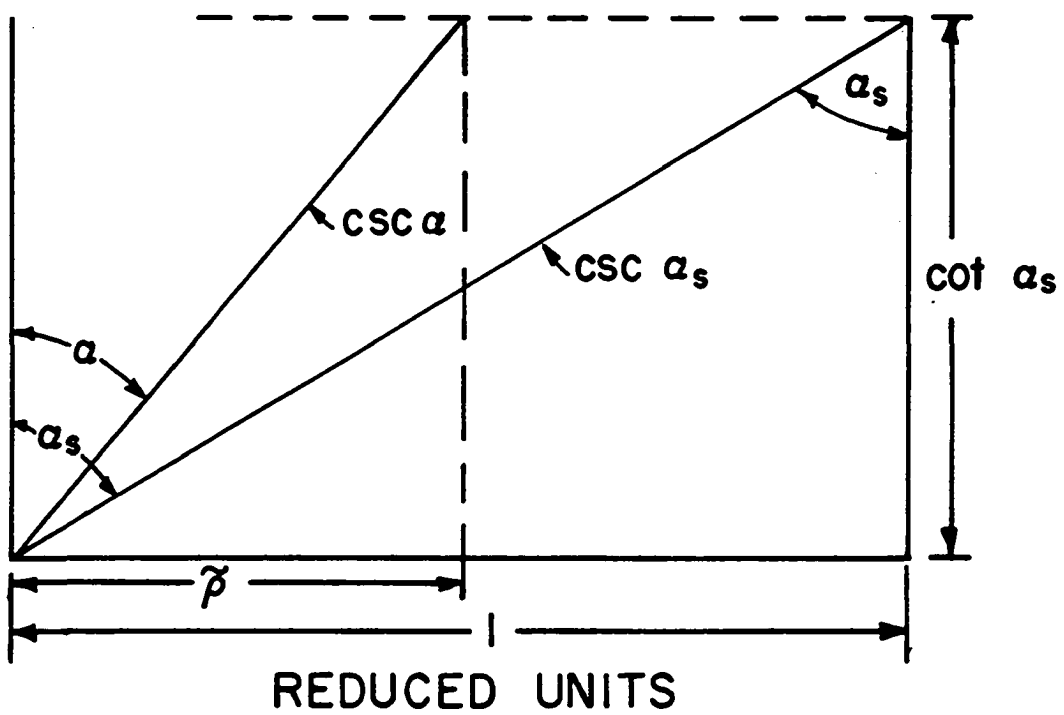
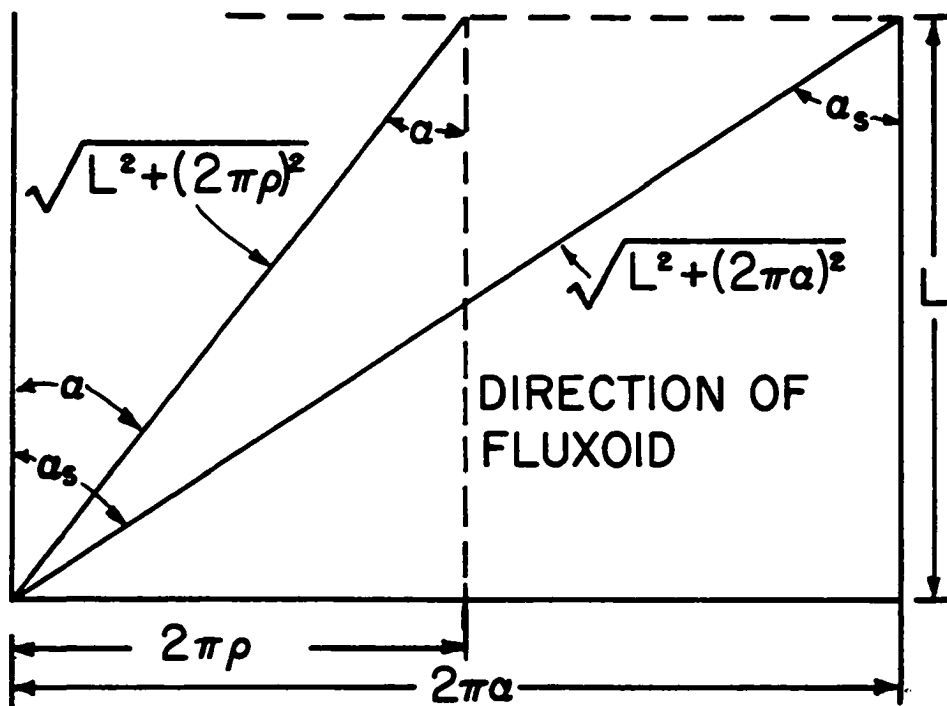
1. Geometrical derivation

We derive here a differential equation linking \vec{H} and ρ . We start with Ampere's law,

$$\vec{\nabla} \times \vec{H} = [4\pi/c] \vec{J} \quad (2.5)$$

and write the fields \vec{H} and \vec{B} as a magnitude times a unit vector,

Figure 18. Geometry describing unwrapped flux spiral.
Lower figure is congruent to upper figure, and
shows reduced dimensions, all lengths being
normalized to $2\pi a = 1$



$$\begin{aligned}
\vec{H} &= H\hat{\phi}_0 \\
\vec{B} &= B\hat{\phi}_0 \quad .
\end{aligned}
\tag{2.6}$$

Then the curl of \vec{H} becomes

$$\begin{aligned}
\vec{\nabla} \times \vec{H} &= \vec{\nabla} \times (H\hat{\phi}_0) \\
&= (\vec{\nabla} H) \times \hat{\phi}_0 + H(\vec{\nabla} \times \hat{\phi}_0) \\
&= -\hat{\phi} \frac{\partial H}{\partial \rho} \cos \alpha + \hat{z} \left[\frac{\partial H}{\partial \rho} \sin \alpha + \frac{H}{\rho} \sin \alpha \right] \quad .
\end{aligned}
\tag{2.7}$$

Next, we write the Lorentz force, \vec{F}_L , according to

$$\vec{F}_L = \vec{J} \times \vec{B} / c
\tag{2.8}$$

and substitute $1/4\pi$ times the right side of Equation 2.7 in place of \vec{J}/c . The result is

$$\begin{aligned}
\vec{F}_L &= \frac{1}{4\pi} (\vec{\nabla} \times \vec{H}) \times \vec{B} \\
&= \frac{1}{4\pi} (\vec{\nabla} \times \vec{H}) \times B\hat{\phi}_0 \\
&= -\hat{\rho} \left[\frac{B}{4\pi} \frac{\partial H}{\partial \rho} + \frac{BH}{4\pi\rho} \sin^2 \alpha \right]
\end{aligned}
\tag{2.9}$$

after some algebra.

We next employ a force balance condition, wherein the Lorentz forces on a fluxoid are balanced by the pinning

forces. The critical pinning force density F_p , a function of B , can be reexpressed in terms of a corresponding critical current density $J_c(B)$ via the expression

$$F_p = J_c(B)B/c \quad (2.10)$$

which should be regarded as the defining equation for J_c . Since in the present geometry the pinning force acts only in a radial direction,

$$\vec{F}_p = \pm F_p \hat{\rho} = \pm [J_c(B)B/c] \hat{\rho} \quad (2.11)$$

When the Lorentz force is balanced by the pinning force, which in the present geometry acts only in the radial direction,

$$\vec{F}_p + \vec{F}_L = 0$$

or

$$\vec{F}_L = \mp [J_c(B)B/c] \hat{\rho} \quad (2.12)$$

Since \vec{F}_p acts opposite to \vec{F}_L , the upper sign in Equation 2.12 applies when vortices are entering the wire, and the lower sign applies in the flux-exiting case. Combining Equations 2.9 and 2.12 yields

$$\pm J_c(B)B/c \hat{\rho} = \hat{\rho} \left[\frac{B}{4\pi} \frac{\partial H}{\partial \rho} + \frac{BH}{4\pi \rho} \sin^2 \alpha \right]$$

so that dividing by B and solving for $\frac{\partial H}{\partial \rho}$, we obtain

$$\frac{\partial H}{\partial \rho} = \pm \frac{4\pi}{c} J_c(B) - \frac{H}{\rho} \sin^2 \alpha \quad . \quad (2.13)$$

This last result may be rewritten as

$$\frac{\partial H}{\partial \rho} = \pm \frac{4\pi}{c} J_c(B) - \frac{H(B)}{R_c(\rho)} \quad (2.14)$$

where $R_c(\rho)$ ($= \rho/\sin^2 \alpha$) may be shown to be the local flux line radius of curvature (see Appendix A).

Equation 2.14 is our fundamental result. To obtain $H(\rho)$ by numerical integration, we need only the functional relations for $J_c(B)$, $H(B)$, and $R_c(\rho)$. Later, it will be shown that $R_c(\rho)$ obtains from the initial surface pitch angle, and the way in which flux line spirals change shape as they move in toward the cylinder axis. The form for $H(B)$ is obtained from an approximation to the Ginzburg-Landau theory, and $J_c(B)$ follows from Urban's model.

2. Thermodynamic connection

Equation 2.14 is closely related to the concept of vortex pressure, which arises because of the gradient in the density of flux vortices. Following DeGennes (10, pp. 83-84), we consider an array of N vortices intersecting perpendicularly to a plane of area S . Let G and F be the Gibbs and Helmholtz free energy densities associated with each vortex, and let γ represent the Gibbs free energy per cm of length, associated with all N vortices. Thus,

$$\gamma = SG$$

and

$$G(B) = F(B) - BH/4\pi \quad . \quad (2.15)$$

The average magnetic flux density throughout the area S is

$$B = N\phi_0/S$$

where ϕ_0 is the flux quantum. Then

$$dB/dS = - N\phi_0/S^2 = - B/S$$

and the magnetic pressure on the vortex array is

$$\begin{aligned} p(B) &= - \left(\frac{\partial \gamma}{\partial S} \right)_N \\ &= - G - S \left(\frac{\partial G}{\partial S} \right) \\ &= -G + B \left(\frac{\partial G}{\partial B} \right) \quad . \end{aligned} \quad (2.16)$$

At equilibrium, $\frac{\partial G}{\partial B} = 0$, so that Equation 2.16 reduces to

$$p(B) = - G(B) \quad . \quad (2.17)$$

We can use this result to show that the gradient in magnetic pressure is proportional to the gradient in H . That is,

$$dp(B)/d\rho = \frac{dp(B)}{dB} \cdot \frac{dB}{dH} \cdot \frac{dH}{d\rho}$$

where

$$dp(B)/dB = - dG(B)/dB$$

$$= \frac{B}{4\pi} \frac{dH}{dB}$$

so that

$$dp(B)/d\rho = \frac{1}{4\pi} B \frac{\partial H}{\partial \rho} \quad . \quad (2.18)$$

Thus, Equation 2.18 could also be expressed as

$$f \equiv dp(B)/d\rho = \pm J_c(B)B/c - BH/4\pi R_c(\rho)$$

where f is interpreted as the force per unit volume on a flux vortex array. Later, in Chapter III, we shall use this result to demonstrate the possibility of an irreversible vortex collapse.

D. Flux Line Models

1. Constant pitch model

Before proceeding further, we need to establish an analytic form for $R_c(\rho)$. That is, we must precisely define the changes which a flux line undergoes as it moves across the cylinder cross section.

In the constant pitch model we assume that the pitch length of a vortex never changes as the vortex moves from the surface toward the axis. The physical argument for this model is that the Lorentz forces and pinning forces act only

radially. Referring to Figure 18, we denote the vortex pitch angle at the surface as α_s , where $-\pi \leq \alpha_s \leq \pi$. Then

$$|\tan \alpha_s| = 2\pi a/L$$

and, for $\rho \leq a$,

$$|\tan \alpha(\rho)| = 2\pi \rho/L \quad (2.19)$$

where L is the pitch of the spiral, and a is the cylinder radius. Thus, $\alpha(\rho)$ and α_s are related through

$$\tan \alpha(\rho) = \frac{\rho}{a} \tan \alpha_s \quad (2.20)$$

The flux line radius of curvature may now be obtained directly from

$$\sin^2 \alpha(\rho)/\rho = \rho/[\rho^2 + (\frac{L}{2\pi})^2]$$

so that

$$R_c(\rho) = \rho + \frac{1}{\rho}(\frac{L}{2\pi})^2 = \rho + \frac{a^2}{\rho} \cot^2 \alpha_s \quad (2.21)$$

In reduced units, the radius of curvature becomes

$$\tilde{R}_c(\tilde{\rho}) = \tilde{\rho} + \frac{1}{\tilde{\rho}} \cot^2 \alpha_s \quad (2.22)$$

We see from Equation 2.21 or 2.22 that for certain special cases, the radius of curvature takes a simple form. In the situation where there is no transport current, α_s is

zero and the vortices are straight with an infinite radius of curvature. When the current is nonzero and the applied field is zero, $\alpha_s = 90^\circ$ and the vortices are closed rings of radius $\rho = R_c(\rho)$. Figure 19 exhibits R_c/a versus $\beta = \rho/a$ for several values of α_s .

2. Constant angle model

In the constant angle model, one assumes that a flux line retains the same pitch angle (with respect to the z-axis) at all radial positions. The basic flaw in this model is the implicit need for vortices to have an axial component of velocity, although all forces on these vortices are purely radial. We therefore regard this model with great skepticism and will make no further references to it.

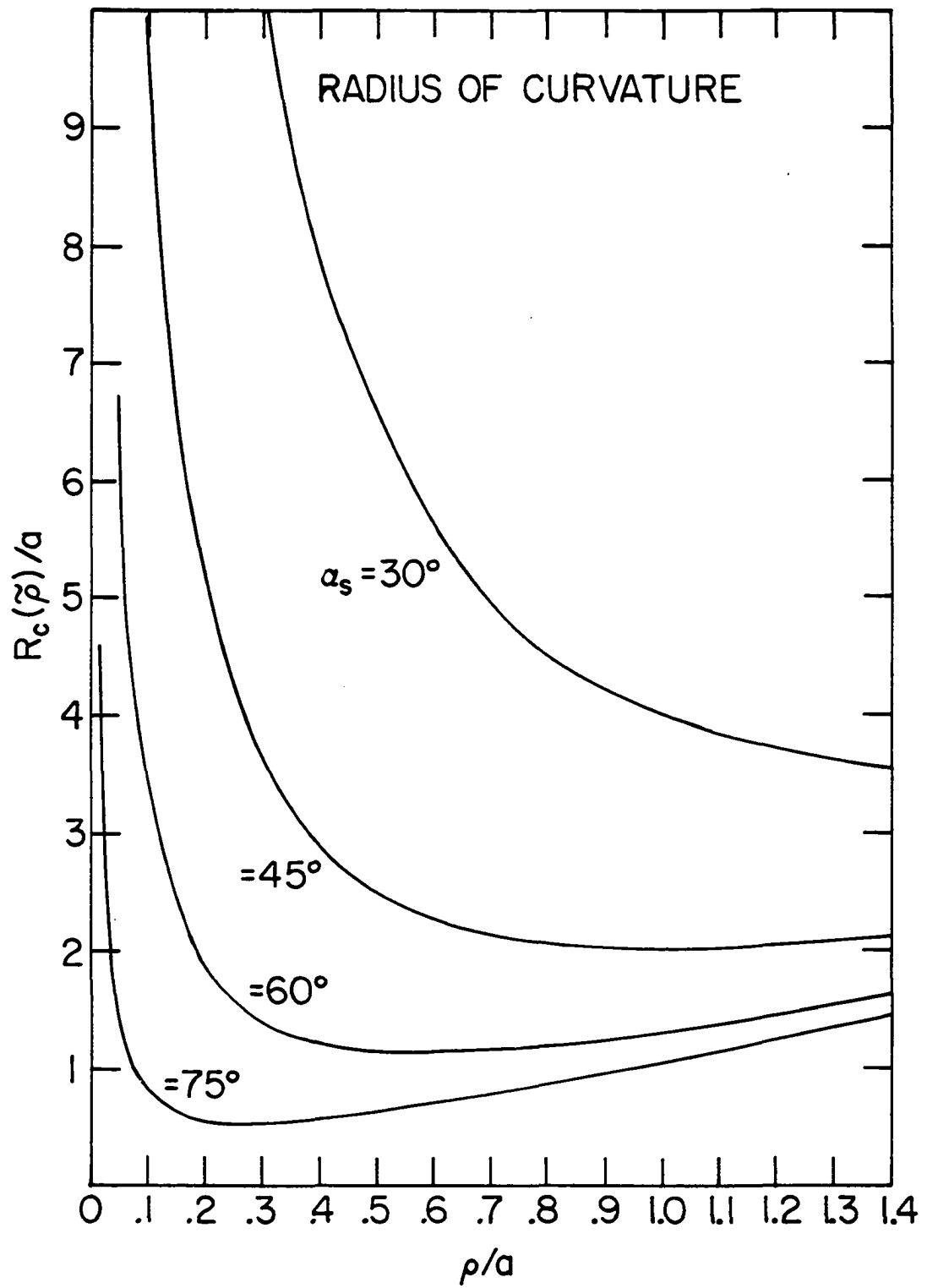
E. Model for the Equilibrium Field

1. Algebraic form

The Ginzburg-Landau theory and more sophisticated theories for the mixed state yield results for $H_{eq}(B)$ that are not expressible in terms of elementary functions. In order to show qualitatively the behavior of $H_{eq}(B)$, it is sufficient to use a simple model for $H_{eq}(B)$ which has the following properties in common with the exact results of theory:

$$H_{eq}(0) = H_{c1} \quad (2.23a)$$

Figure 19. Fluxoid radius of curvature for several values of the surface pitch angle α_s (Equation 2.22). When ρ/a exceeds unity, radius of curvature is virtual concept, since fluxoid does not exist there



$$H_{eq}(H_{c2}) = H_{c2} \quad (2.23b)$$

$$\left. \frac{d}{dB}(H_{eq}(B)) \right|_{B=0} = 0 \quad . \quad (2.23c)$$

The function which we chose was

$$H_{eq}(B) = [k^2 B^2 + H_{c1}^2]^{1/2} \quad (2.24)$$

where the choice $k^2 = 1 - (H_{c1}/H_{c2})^2$ guarantees compliance with the required boundary conditions, Equation 2.23. In reduced units, where all fields are normalized to $H_{c2} = 1$, Equation 2.24 has the very convenient form

$$\tilde{H}_{eq}(\tilde{B}) = H_{eq}(B)/H_{c2} = [\beta^2 + k^2 \tilde{B}^2]^{1/2} \quad (2.25)$$

where

$$\beta = H_{c1}/H_{c2} = \tilde{H}_{c1} \quad ,$$

$$k^2 = 1 - \beta^2 \quad ,$$

and

$$\tilde{B} = B/H_{c2} \quad .$$

2. Helmholtz free energy density

Simple thermodynamics may be used to see how this choice of model for $H_{eq}(B)$ affects the relationships among H_c , H_{c1} , and H_{c2} . Independent of any specific choice for $H_{eq}(B)$, a

thermodynamic analysis shows that the Helmholtz free energy density $F(B)$ has the specific values

$$F(0) = 0 \quad (2.26a)$$

and

$$F(H_{c2}) = H_{c2}^2/8\pi + H_c^2/8\pi \quad (2.26b)$$

The latter expression represents the sum of the field energy density at H_{c2} and the condensation energy density difference between the normal and superconducting states. Integration of our specific model for $H_{eq}(B)$ yields

$$\begin{aligned} F(B) &= \int_0^B \frac{H_{eq}(B') dB'}{4\pi} \\ &= \frac{1}{4\pi} \int_0^B [H_{c1}^2 + k^2 B'^2]^{1/2} dB' \\ &= BH/8\pi + (H_{c1}^2/8\pi k) \ln[(H + kB)/H_{c1}] \end{aligned} \quad (2.27)$$

so that $F(H_{c2})$ is

$$\begin{aligned} F(H_{c2}) &= \frac{H_{c2}^2}{8\pi} + \frac{H_{c1}^2}{8\pi k} \ln\left[\frac{H_{c2}}{H_{c1}}(1+k)\right] \\ &= \frac{H_{c2}^2}{8\pi} + \frac{H_{c1}^2}{8\pi k} \ln\left[\frac{1+k}{\beta}\right] \end{aligned} \quad (2.28)$$

Comparing Equation 2.28 with 2.26b shows that

$$\begin{aligned} H_c^2 &= \frac{H_{c1}^2}{k} \ln\left[\frac{1+k}{\beta}\right] \\ &= \frac{H_{c1}^2}{2k} \ln\left[\frac{1+k}{1-k}\right] \end{aligned}$$

or

$$(H_c/H_{c1})^2 = k^{-1} \tanh^{-1}(k) \quad . \quad (2.29)$$

In the Ginzburg-Landau theory, H_{c2} is related to κ and H_c via

$$H_{c2} = \sqrt{2} \kappa H_c \quad (2.30)$$

so that one may use Equation 2.30 together with Equation 2.29 to show that κ and β are related in this model according to

$$\kappa^2 = k/2\beta^2 \ln\left(\frac{1+k}{\beta}\right) = \frac{k}{2\beta^2 \tanh^{-1}(k)} \quad . \quad (2.31)$$

The Ginzburg-Landau theory, on the contrary, predicts a much more complicated, nonalgebraic relationship between κ and β . Recently, Clem (40) has demonstrated a modified Bessel function model for the relationship between κ and β , which agrees very well with Neumann and Tewordt's (41) exact numerical solutions of the Ginzburg-Landau equations. Figure 20 shows a comparison between Equation 2.31 and Clem's Bessel

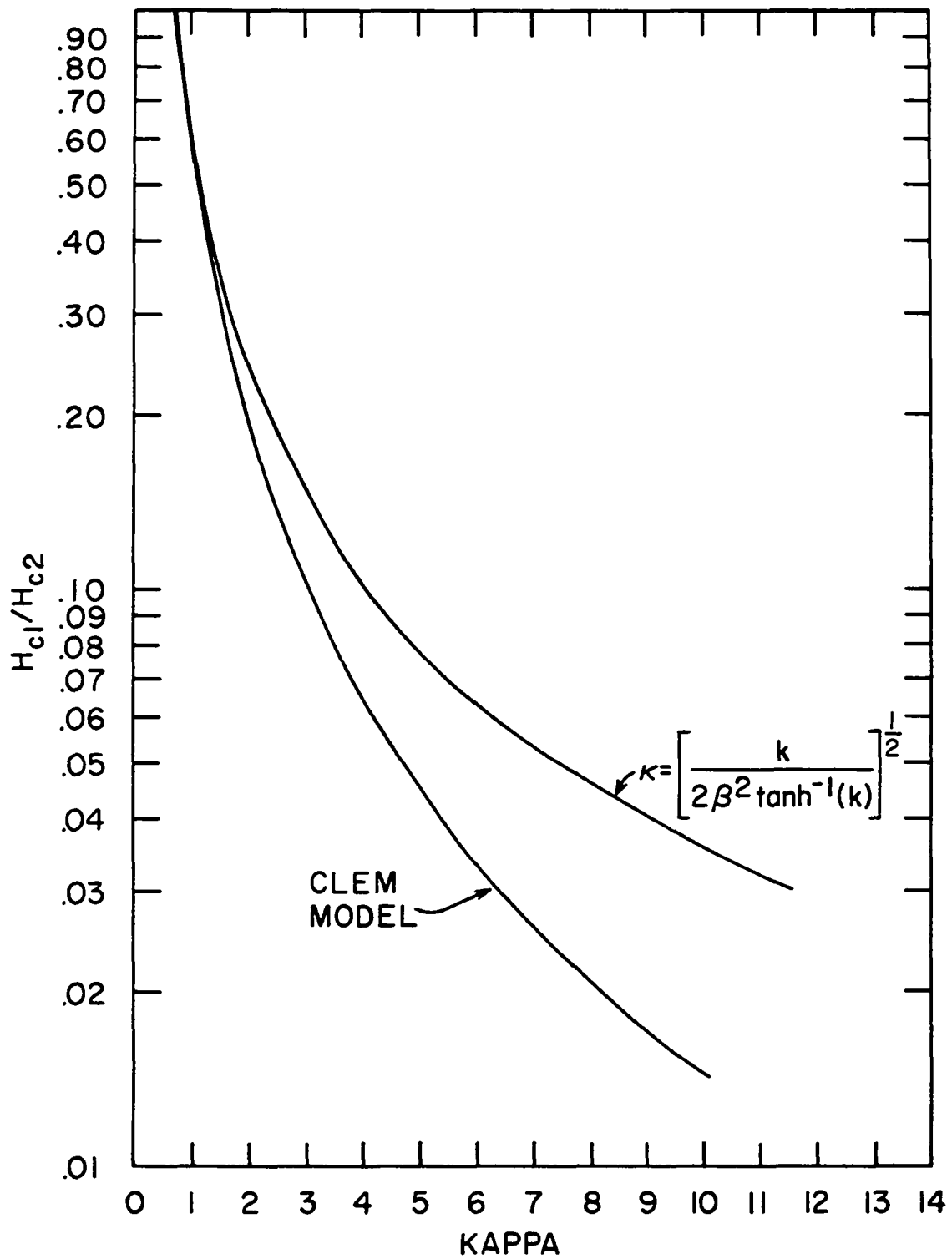


Figure 20. $\beta = H_{c1}/H_{c2}$ versus the Ginzburg-Landau parameter κ . Upper curve derives from Equation 2.31, and Clem model is described in Reference 39

function model for β versus κ . The important point is that Equations 2.31 and 2.24 should not be taken too seriously, as actual discrepancies with the true form of $H_{eq}(B)$ and $\kappa(\beta)$ are not important to the main thrust of this study.

F. Models for Surface Pinning

To incorporate the effects of surface pinning into our model, we consider a cylindrical specimen with an ideal surface immersed in a uniform axial field. As the field is slowly increased from zero, the first penetration of flux into the cylinder occurs when the applied field reaches a critical value H_S , termed the critical entry field. In general, the critical entry field is a function of the average magnetic induction near the surface of the sample; thus

$$H_S = H_{en}(B) \Big|_{B=0} \quad (2.32)$$

where $H_{en}(B)$ denotes the critical entry field as a function of B . In general, H_S is a material-dependent parameter greater than H_{c1} .

DeGennes (42) and Bean and Livingston (43) have considered the problem of calculating H_S ; their results show that

$$H_S = \frac{\phi_0}{4\pi\lambda(T)\xi(T)} \approx H_c \quad (2.33)$$

where ϕ_0 is the flux quantum. Clem (44) has shown that for high kappa materials,

$$H_{\text{en}}(B) \approx [H_s^2 + B^2]^{1/2} \quad . \quad (2.34)$$

In the same sense that there exists a critical entry field, there also exists a critical exit field, $H_{\text{ex}}(B)$, which represents the value of the surface field below which flux vortices will spontaneously pop out of the material. The critical exit field has meaning in the field-decreasing situation, and the critical entry field has meaning in the field-increasing case. Clem (44) has also shown that

$$H_{\text{ex}}(B) \approx B + \frac{\phi_0}{16\pi\lambda^2} \approx B \quad . \quad (2.35)$$

In order to contrive a simple model for $H_{\text{en}}(B)$ that is reasonably realistic, yet easy to use in a numerical computation, we note that the following boundary conditions must be satisfied:

$$H_{\text{en}}(B) \Big|_{B=0} = H_s \quad (2.36a)$$

and

$$H_{\text{en}}(B) \Big|_{B=H_{c2}} = H_{c2} \quad . \quad (2.36b)$$

To this end, we define the parameter δ according to

$\delta^2 = 1 - (H_S/H_{c2})^2$; thus if we express $H_{en}(B)$ as

$$H_{en}(B) = [H_S^2 + \delta^2 B^2]^{1/2} \quad (2.37)$$

it is clear that the requisite boundary conditions are satisfied. This form for $H_{en}(B)$ is similar to the model which we chose for the equilibrium field $H_{eq}(B)$, and lends itself nicely to numerical calculations in a one-parameter theory.

G. Weak Pinning Limit

1. Fields

Before examining detailed solutions to the fundamental equation for $\frac{dH}{d\rho}$, it is interesting to consider the special case of the weak pinning limit. Here, it is assumed that the critical current is small enough so that Equation 2.12 may be approximated as

$$dH/d\rho = - H/R_c(\rho) \quad (2.38)$$

or, in reduced units,

$$d\tilde{H}/d\tilde{\rho} = - \tilde{H}/\tilde{R}_c(\tilde{\rho}) \quad , \quad (2.39)$$

where we have defined $\tilde{H} = H/H_{c2}$, $\tilde{\rho} = \rho/a$, and $\tilde{R}_c = R_c/a$.

In the constant pitch model, Equation 2.39 becomes

$$d\tilde{H}/d\tilde{\rho} = - \tilde{H}\tilde{\rho}/[\tilde{\rho}^2 + \cot^2\alpha_s] \quad (2.40)$$

where α_s is the flux line pitch angle at the cylinder surface.

As mentioned earlier (see p. 48), the general solution to Equation 2.38 is

$$H(\rho) = H(0) \cdot \exp\left\{-\int_0^\rho dr \frac{\sin^2 \alpha(r)}{r}\right\}, \quad (2.41)$$

where we emphasize here that the weak pinning limit and the force-free model are essentially identical. When we impose the additional constraint of the constant pitch model, so that $R_c(\rho)$ has the specific form shown in Equation 2.40, Equation 2.41 reduces to

$$\tilde{H}(\tilde{\rho}) = \tilde{H}(0) \cdot |\cos \alpha(\tilde{\rho})| \quad (2.42)$$

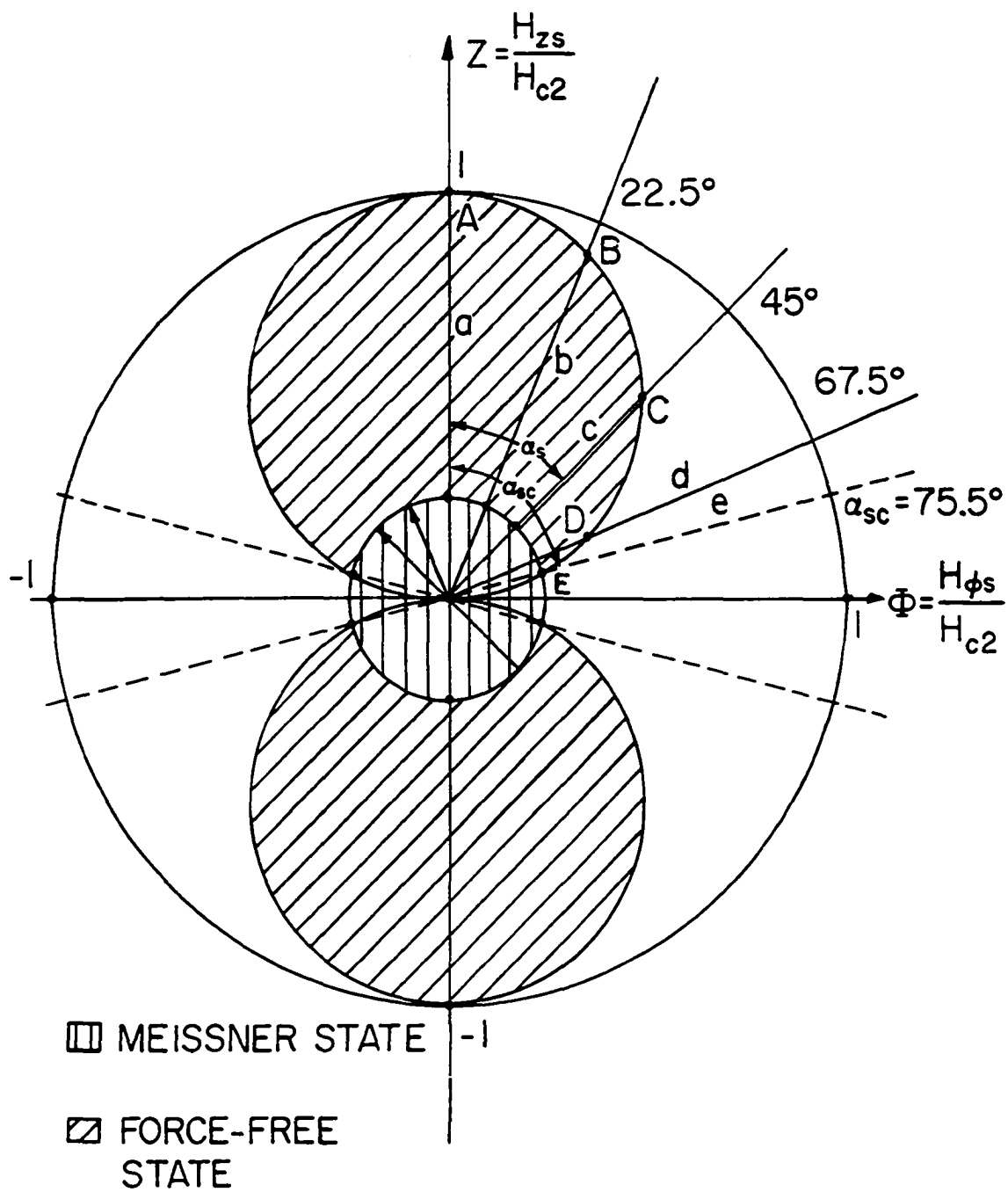
where

$$\cos \alpha(\tilde{\rho}) = [1 + \tilde{\rho}^2 \tan^2 \alpha_s]^{-1/2}. \quad (2.43)$$

Notice that $\alpha(0) = 0$ and $\alpha(1) = \alpha_s$, and that Equation 2.42 is easily obtained from 2.40.

The detailed behavior implicit in the result 2.42 contains many interesting subtleties which are nicely systematized via the phase diagram shown in Figure 21. The phase diagram is constructed in the following way: We consider a pair of orthogonal axes, corresponding to the axial and circumferential components of the field, labeled Z and $\bar{\theta}$

Figure 21. Phase diagram for constant pitch model with $\tilde{H}_{c1} = 0.25$, under the weak pinning assumption. Region inside vertically stripped circle represents Meissner state; region defined by angled stripes defines mixed state, and white region marks the breakdown of mixed state into either flux-flow regime or normal state. See text for full description



respectively. All field quantities are normalized to H_{c2} , so that

$$\tilde{H} = H/H_{c2} \ , \ \tilde{H}_z = H_z/H_{c2} \ , \text{ and } \tilde{H}_\varnothing = H_\varnothing/H_{c2} \ .$$

The large outer circle of radius one corresponds to having the magnitude of the field at the surface of the cylinder, H_s , equal to the upper critical field H_{c2} ; at any point on that circle, in reduced units, $\tilde{H}_s = 1$, so that

$$\tilde{H}_{s\varnothing}^2 + \tilde{H}_{sz}^2 = 1 \quad (2.44)$$

where the subscript s denotes surface ($\tilde{\rho} = 1$).

If we let $Z = H_{sz}$ and $\tilde{\varnothing} = H_s$, then Equation 2.44 is the same as

$$Z^2 + \tilde{\varnothing}^2 = 1 \quad (2.45)$$

Next, consider the physical situation arising when the field on the axis of the cylinder is exactly equal to H_{c2} . This would correspond to the maximum possible value of H throughout the cylinder. Then in reduced units, $\tilde{H}(0) = 1$, so that Equation 2.42 becomes

$$\tilde{H}(\tilde{\rho}) = |\cos\alpha(\tilde{\rho})| \quad (2.46)$$

and the orthogonal components of $\tilde{H}(\tilde{\rho})$ are

$$\tilde{H}_\varnothing = \tilde{H}(\tilde{\rho})\sin\alpha(\tilde{\rho}) \quad (2.47a)$$

$$H_z = \tilde{H}(\tilde{\rho}) \cos \alpha(\tilde{\rho}) \quad . \quad (2.47b)$$

On the surface, $\tilde{\rho} = 1$, $\alpha(\tilde{\rho}) = \alpha_s$, and we have

$$\tilde{H}_{s\theta} = |\cos \alpha_s| \sin \alpha_s = \bar{\theta} \quad (2.48a)$$

$$\tilde{H}_{sz} = |\cos \alpha_s| \cos \alpha_s = Z \quad . \quad (2.48b)$$

In this case, however, the magnitude of the surface field, \tilde{H}_s , is simply $|\cos \alpha_s|$, so that

$$\bar{\theta}^2 + Z^2 = |\cos \alpha_s|^2 = |Z| \quad . \quad (2.49)$$

Thus,

$$\bar{\theta}^2 + Z^2 - |Z| = 0 \quad . \quad (2.50)$$

If we momentarily restrict ourselves to the first quadrant where $\bar{\theta}$, Z are both positive, Equation 2.50 becomes

$$\bar{\theta}^2 + (Z - \frac{1}{2})^2 = (\frac{1}{2})^2 \quad (2.51)$$

which describes a circle of radius one-half centered at the point $\bar{\theta} = 0$, $Z = \frac{1}{2}$. In the fourth quadrant, where $Z < 0$, Equation 2.50 would yield

$$\bar{\theta}^2 + (Z + \frac{1}{2})^2 = (\frac{1}{2})^2 \quad (2.52)$$

which describes a circle of radius one-half centered at the point $\bar{\theta} = 0$, $Z = -\frac{1}{2}$. Thus, these two circles in the phase

diagram represent the magnitude of the surface field for various combinations of $\bar{\theta}$, Z , when the field on the axis is a maximum.

Next, we consider the lines labeled a, b, c, and d which represent four arbitrarily selected paths of constant surface pitch angle, α_s . (The particular choice of angles for the sketch, i.e., 0, 22.5, 45, 67.5 degrees, serves only for illustrative purposes.) Line e is at the critical angle, which we denote α_{sc} , and passes through the intersection point of the inner circle with the curve described by Equation 2.51. For ease of reference, we will call the curve of 2.51 the "upper loop". Thus, one may interpret the intersections of these rays with the upper loop (points A, B, C, D, and E) as yielding the coordinates $H_{s\theta}$, H_{sz} which give the maximum flux density at the axis. Since the $\bar{\theta}$ -coordinate represents $H_{s\theta}$, and hence is proportional to the current through the cylinder, we see that the 45° pitch angle yields a maximum in the transport current.

The small inner circle, whose radius is equal to \tilde{H}_{c1} , represents the pairs of values of $\tilde{H}_{s\theta}$ and \tilde{H}_{sz} which combine to yield a resultant field of magnitude \tilde{H}_{c1} on the surface. The line e, which goes through the intersection of the inner circle and the upper loop, represents the surface pitch angle which simultaneously gives \tilde{H}_{c2} on the axis and \tilde{H}_{c1} on the surface. That is, line e is at the critical angle.

Since the inner circle is described analytically by

$$\bar{\phi}^2 + Z^2 = \tilde{H}_{c1}^2 \quad (2.53)$$

and the upper loop is described by Equation 2.51, the simultaneous solution of Equations 2.51 and 2.53 yields

$$\bar{\phi}_c = \tilde{H}_{c1} [1 - \tilde{H}_{c1}^2]^{1/2} \quad (2.54a)$$

$$Z_c = \tilde{H}_{c1}^2 \quad (2.54b)$$

as the coordinates of point E, and yields for the critical angle

$$\begin{aligned} \alpha_{sc} &= \tan^{-1}[\bar{\phi}_c/Z_c] \\ &= \tan^{-1}[\sqrt{1 - \tilde{H}_{c1}^2} / \tilde{H}_{c1}] \quad . \end{aligned} \quad (2.55)$$

In the sketch of Figure 21, α_{sc} is 75.5° , and \tilde{H}_{c1} was arbitrarily given the value 0.25. So long as α_{sc} exceeds 45° , corresponding to $\tilde{H}_{c1} \leq 1/\sqrt{2}$, the maximum possible transport current will occur at $\alpha_s = 45^\circ$. If $\tilde{H}_{c1} \geq 1/\sqrt{2}$, the critical angle will be less than 45° and the maximum possible transport current will occur at the critical angle. Using Equation 2.54a and Ampere's law, this latter situation would imply that the maximum transport current would be

$$I_c = \frac{1}{2} c a H_{c2} \tilde{H}_{c1} [1 - \tilde{H}_{c1}^2]^{1/2} \quad (\tilde{H}_{c1} \geq 1/\sqrt{2}) \quad (2.56)$$

whereas, when $\alpha_{sc} < 45^\circ$, the maximum current possible is

$$I_{\max} = \frac{1}{4}caH_{c2} \quad (2.57)$$

and the maximum average current density would be

$$\begin{aligned} J_{\max} &= I_{\max}/\pi a^2 \\ &= cH_{c2}/4\pi a \quad . \end{aligned} \quad (2.58)$$

Figure 22 shows I_c/I_{\max} plotted as a function of the Ginzburg-Landau parameter κ .

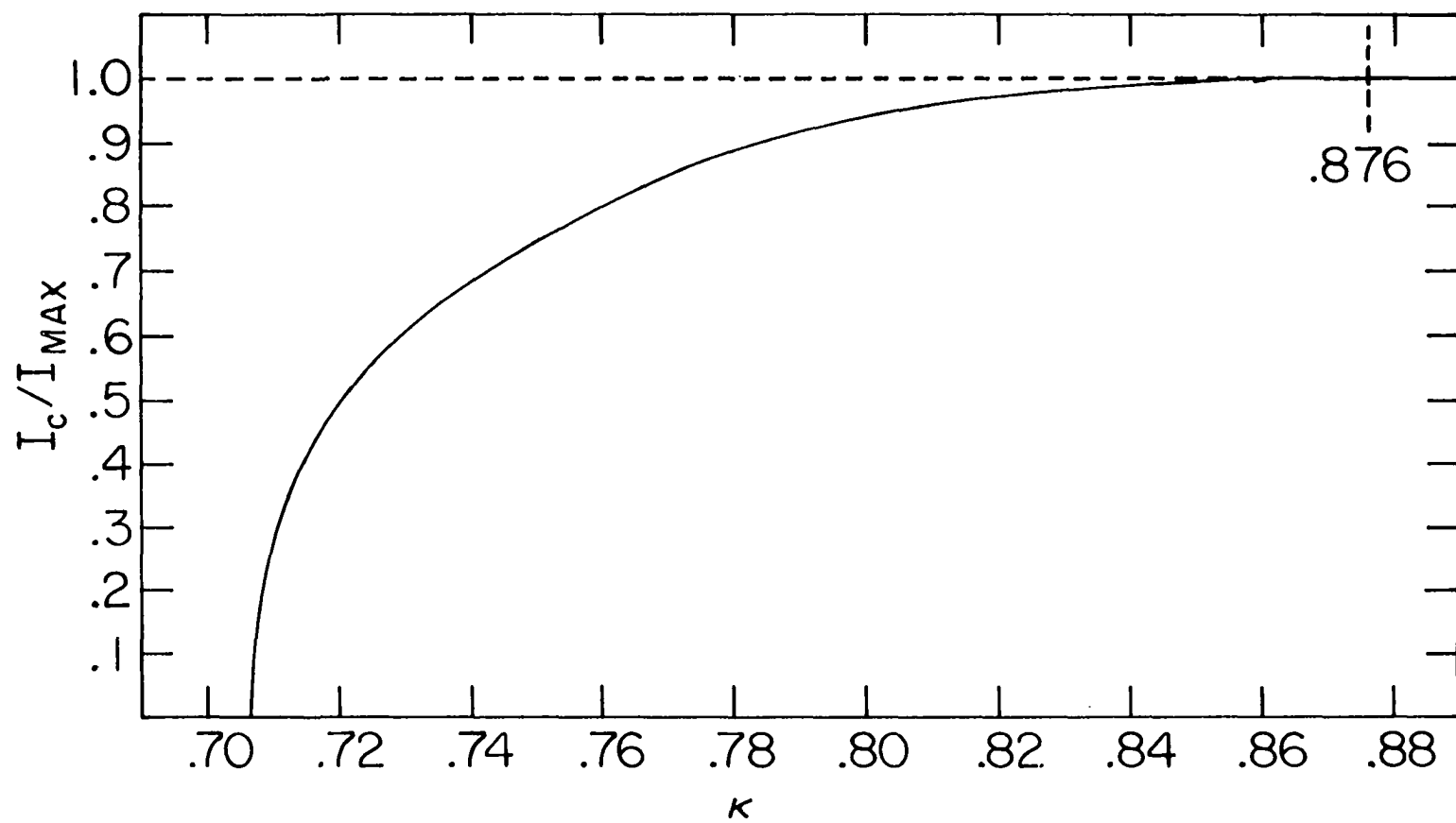
Thus, if one were seeking a weak pinning material which could carry the highest possible current, one would select a substance for which $H_{c1}/H_{c2} \leq 1/\sqrt{2}$; the best performance being defined by Equation 2.57. Using Figure 20, we see that such a material would have a Ginzburg-Landau parameter κ in excess of 0.88.

It is also interesting to look at some numerical values. As an example, suppose that we have a weak pinning material with a κ in excess of 0.88, so that $H_{c1}/H_{c2} < 0.707$. Operating at a surface pitch angle of 45° , we see that at maximum current,

$$H_{s\emptyset} = H_{sz} = \frac{1}{2}H_{c2} \quad (2.59)$$

and

Figure 22. Transport current in weak pinning model as a function of the Ginzburg-Landau parameter κ , normalized to the maximum possible current $I_{\max} = \frac{1}{4}caH_{c2}$. When κ exceeds 0.876, corresponding to $\tilde{H}_{c1} < 0.707$, maximum current remains equal to I_{\max} . The zero in I_c occurs at the κ corresponding to $H_{c1} = H_{c2}$



$$H_s = \frac{1}{\sqrt{2}} H_{c2} = 0.707 H_{c2} \quad . \quad (2.60)$$

If the upper critical field H_{c2} were 10^5 G and if the radius of the wire were $100 \mu\text{m}$ ($= 0.01 \text{ cm}$), Equation 2.57 would show that the maximum transport current would be about 2500 A, with a mean current density of about $8 \times 10^6 \text{ A/cm}^2$.

Equations 2.56 and 2.57 show that the total current is proportional to the wire radius, while the current density is inversely proportional to the radius. The current density is therefore limited to the minimum possible radius of the wire, which can be estimated by noting that the depairing current density is a probable upper bound on J_{max} . This is the current density at which Cooper pairs would begin to break up, destroying superconductivity. Since the depairing current density is approximately

$$J_d = cH_c / 4\pi\lambda \quad (2.61)$$

where λ is the magnetic penetration depth, and H_c is related to H_{c2} via

$$H_{c2} = \sqrt{2} \kappa H_c \quad , \quad (2.62)$$

Equations 2.58 through 2.62 show that the minimum value of the radius, a_{min} , is approximately

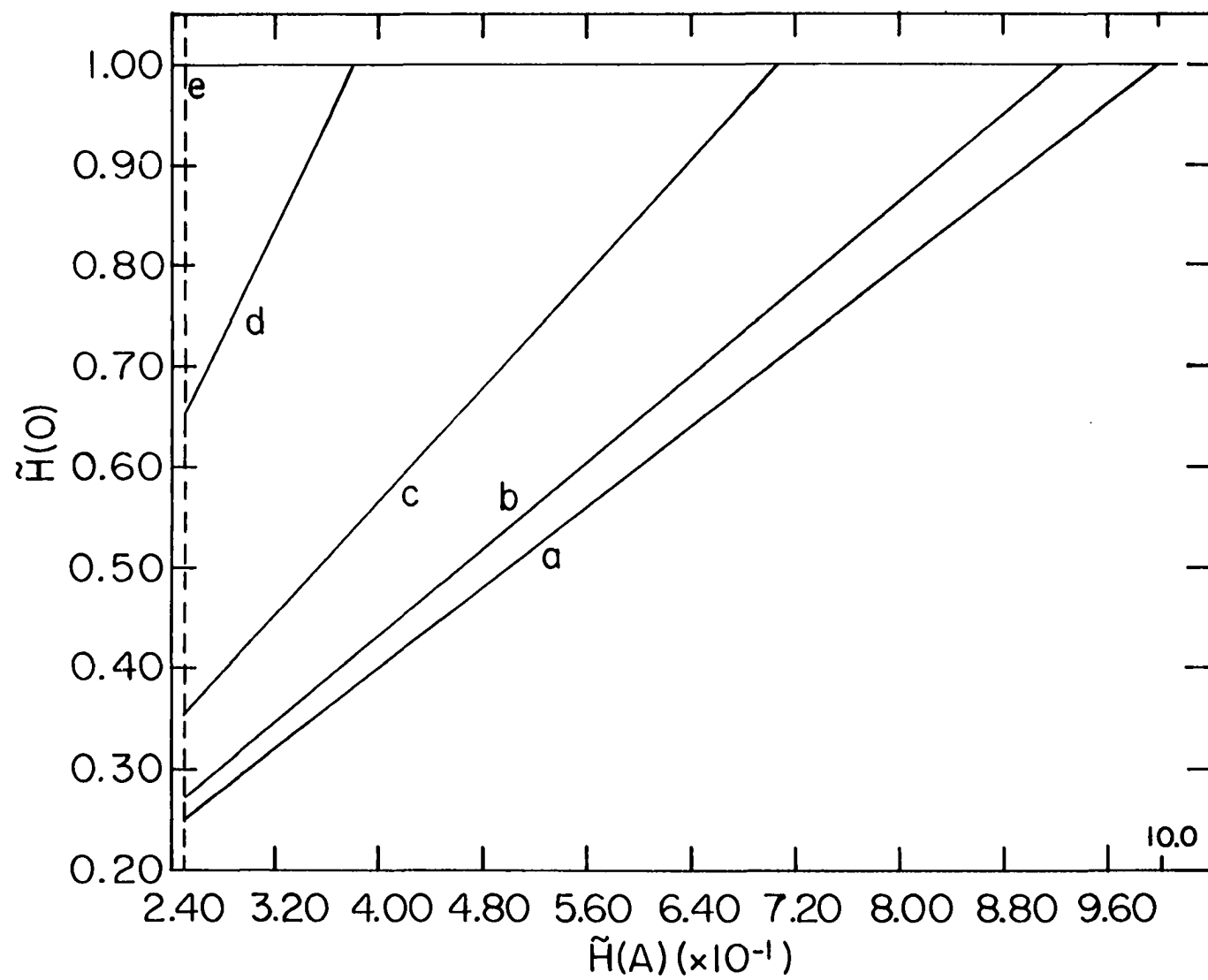
$$a_{\text{min}} \approx \sqrt{2} \lambda \kappa \quad . \quad (2.63)$$

Further understanding of the weak pinning limit may be obtained from Figures 23-26. In Figures 23 and 24, we plot $\tilde{H}(0)$ and $\tilde{B}(0)$ on the axis as a function of the reduced surface field H_s , for a specimen assumed to have $\tilde{H}_{c1} = 0.25$. The different curves labeled a, b, c, d and the point e, correspond to the five lines of constant pitch angle shown in Figure 21. We see that as the surface pitch angle is increased, there is a greater difference between the surface field and the field on the axis. At the critical angle these curves shrink to the point E, indicating that at that angle, the surface field is H_{c1} and the field on the axis is H_{c2} .

In Figures 25 and 26 are plotted the fields as functions of the radius, for each of five lines of constant surface pitch angle. In this case, the field at the surface is fixed at H_{c1} . Figures 27 and 28 show the same kind of ρ -dependence; however, here the field on the axis is fixed at H_{c2} .

In Figures 29 and 30 are five curves of $\tilde{H}(\tilde{\rho})$ versus $\tilde{\rho}$, all at the same surface pitch angle of 67.5° . Illustrated here is the way in which the flux profiles change as one progressively moves out along the 67.5° line of Figure 21.

Figure 23. Reduced field on the axis $\tilde{H}(0)$ as a function of the reduced surface field \tilde{H}_s for the constant pitch model in the weak pinning limit. $\tilde{H}_{c1} = 0.25$, and surface pitch angles α_s are (a) 0° , (b) 22.5° , (c) 45° , (d) 67.5° , and (e) $\alpha_{sc} = 75.5^\circ$. Also see Figure 21



.

Figure 24. Reduced flux density $\tilde{B}(0)$ on the axis as a function of the reduced surface field \tilde{H}_s for the constant pitch model in the weak pinning limit, under the same conditions as in Figure 23. Also see Figure 21

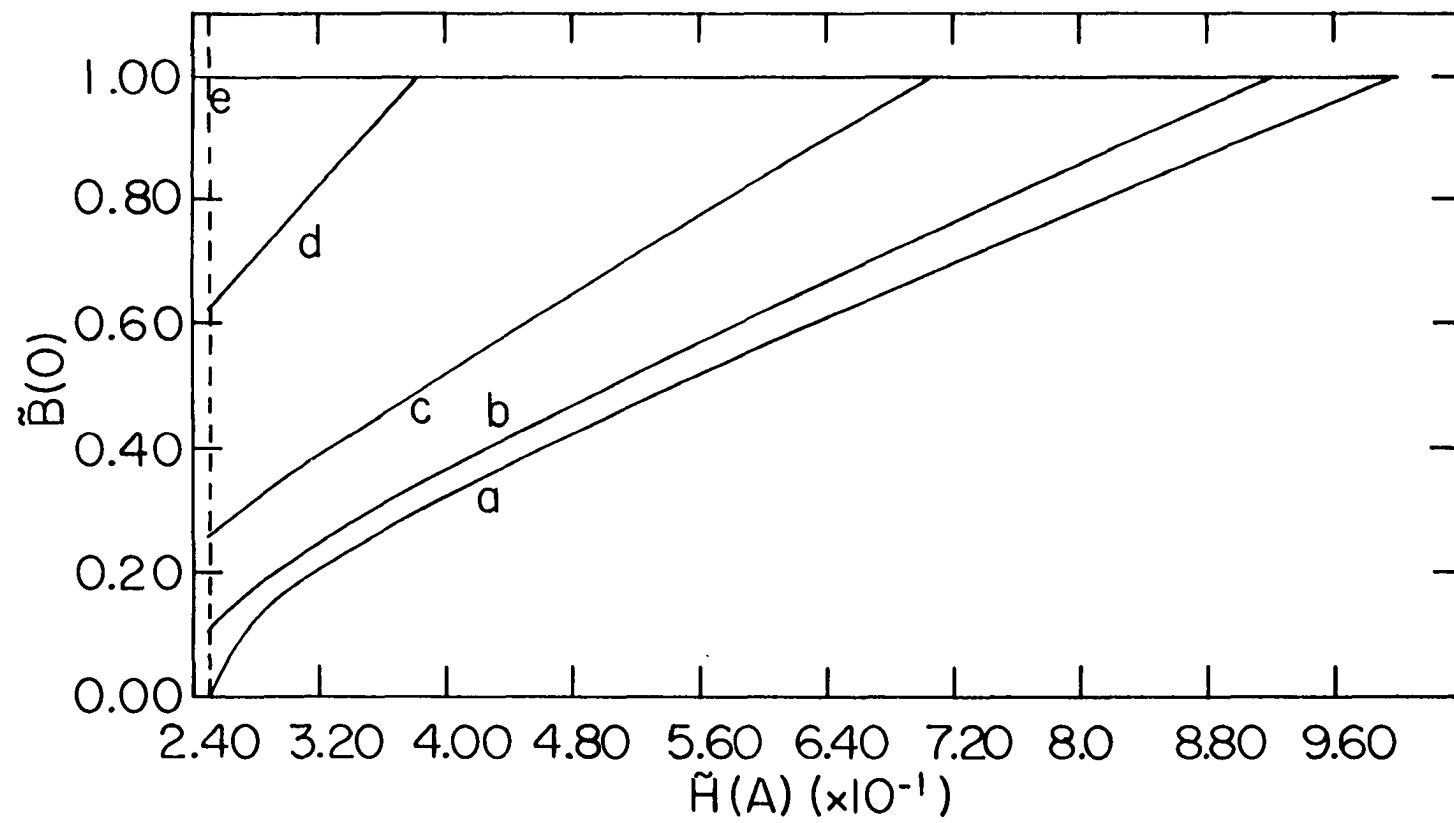
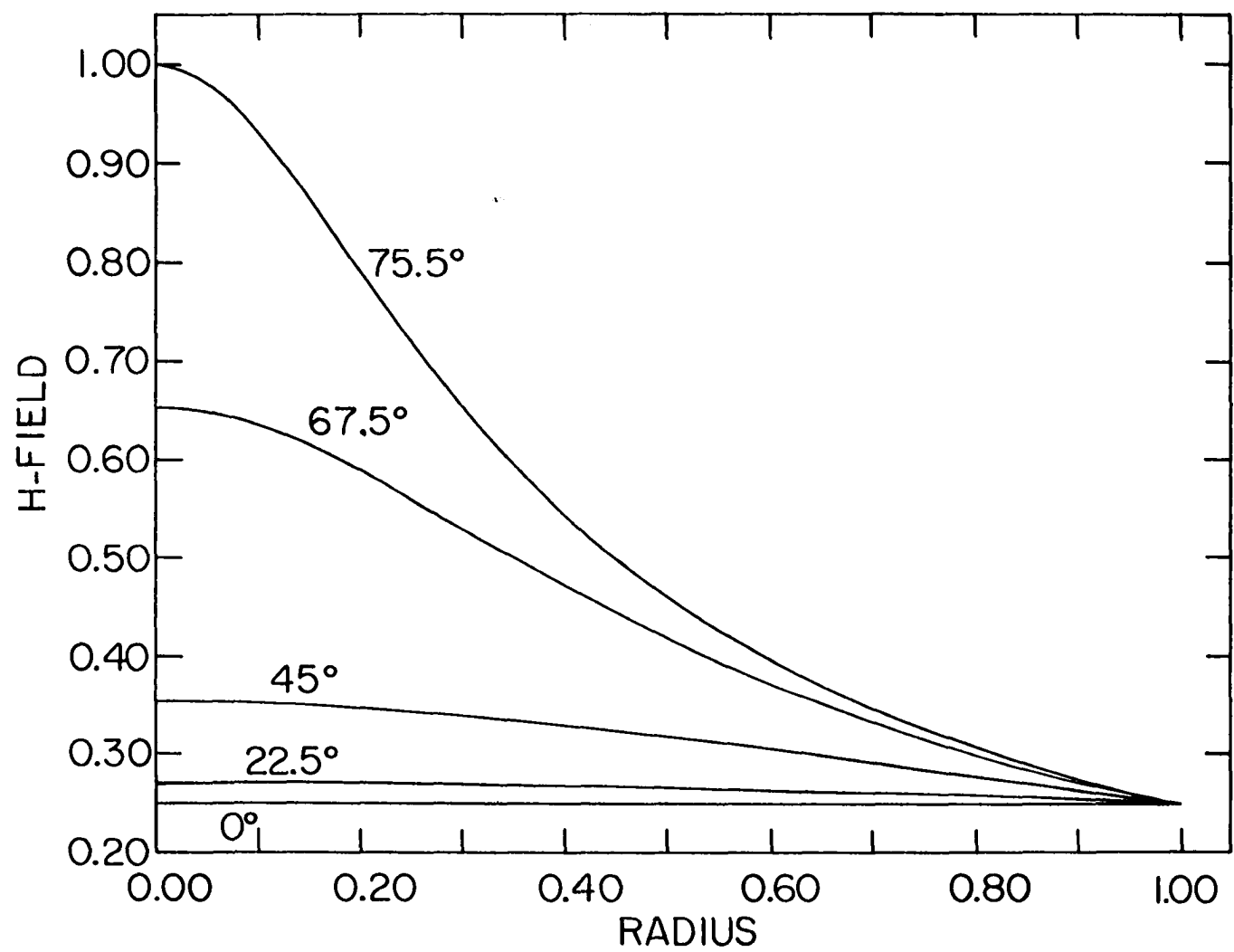


Figure 25. Reduced field \tilde{H} versus $\tilde{\rho}$ for the constant pitch model in the weak pinning limit, with reduced surface field $\tilde{H}_s = \tilde{H}_{c1} = 0.25$, for the surface pitch angles α_s shown. Also see Figure 21



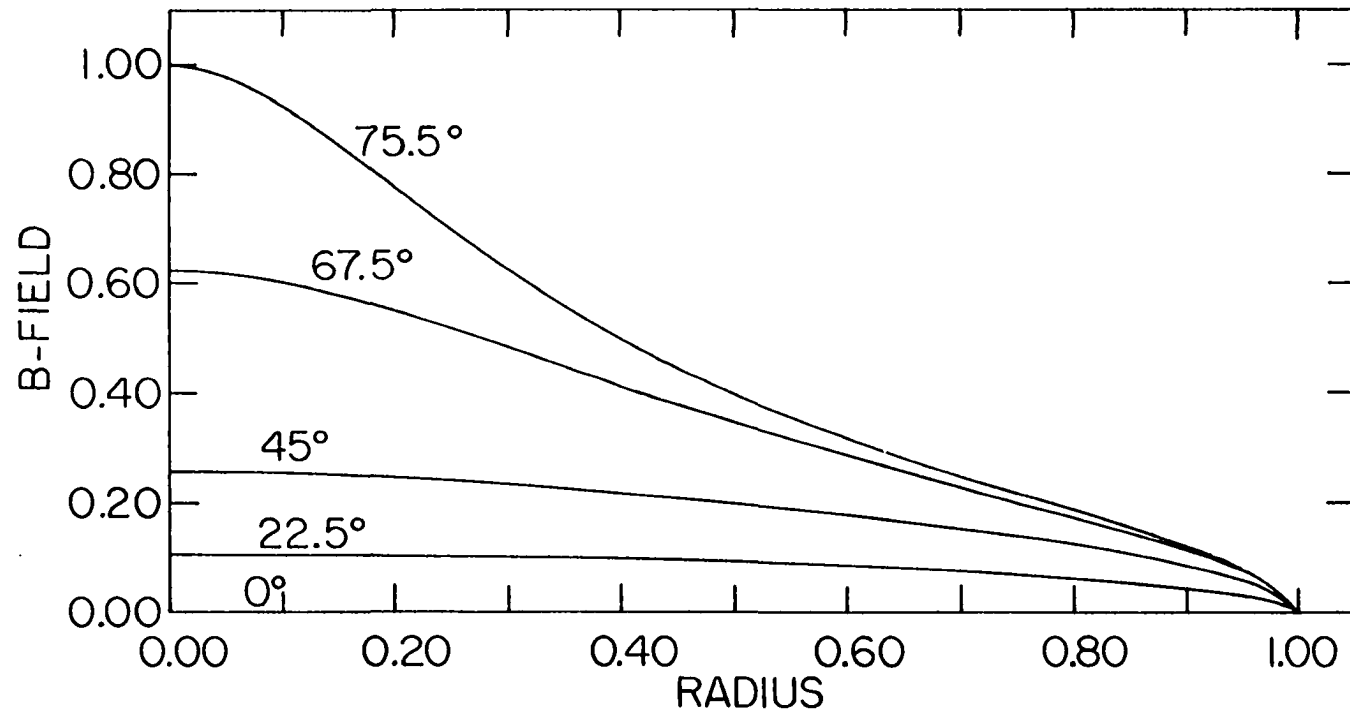
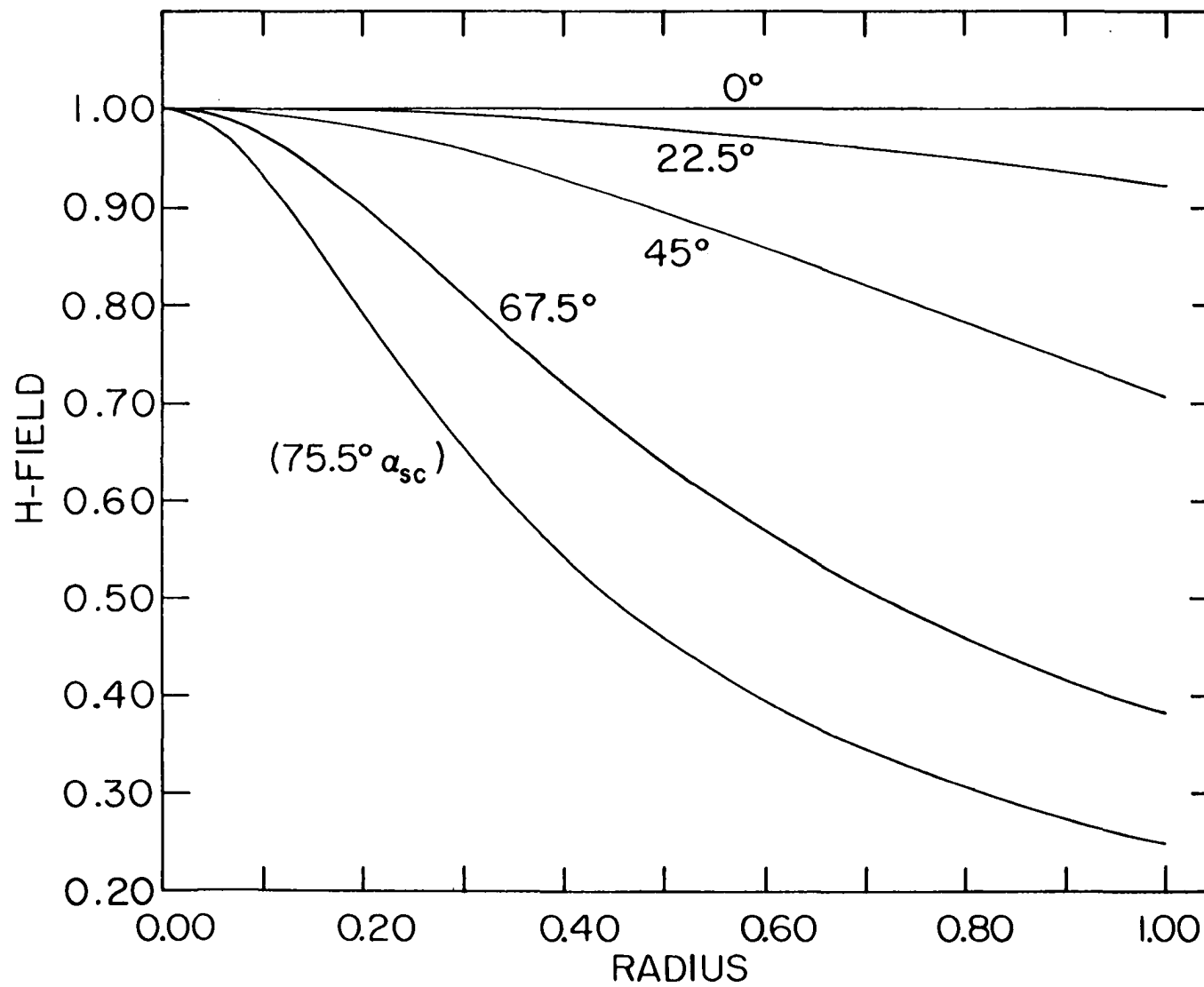


Figure 26. Reduced flux density \tilde{B} versus $\tilde{\rho}$ for the same conditions as in Figure 25. Also see Figure 21

Figure 27. Reduced field \tilde{H} versus $\tilde{\rho}$ for the constant pitch model with $\tilde{H}(0) = 1$ and $\tilde{H}_{c1} = 0.25$, and for the surface pitch angles α_s shown. The conditions correspond to points A, B, C, D, and E on Figure 21



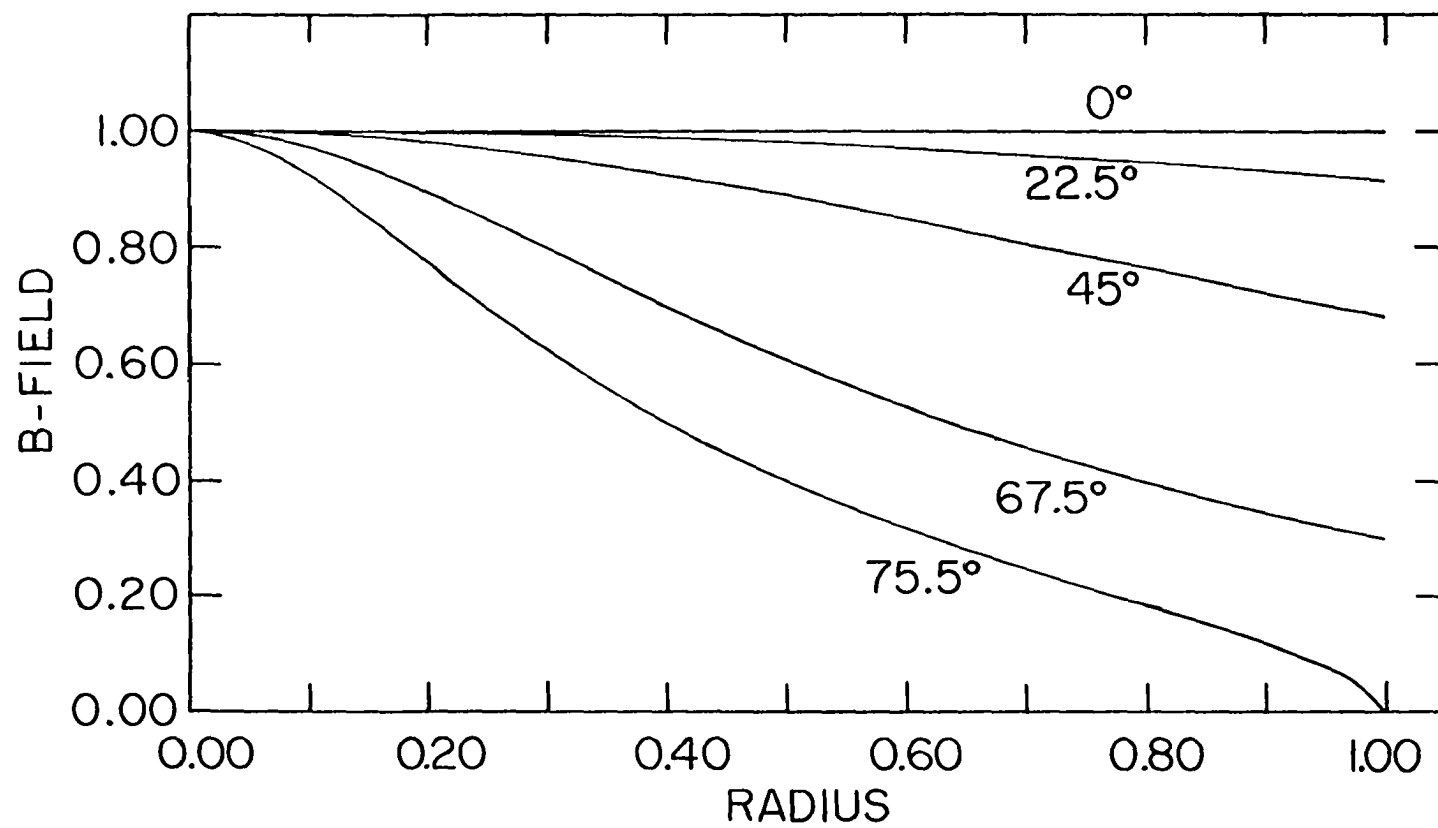
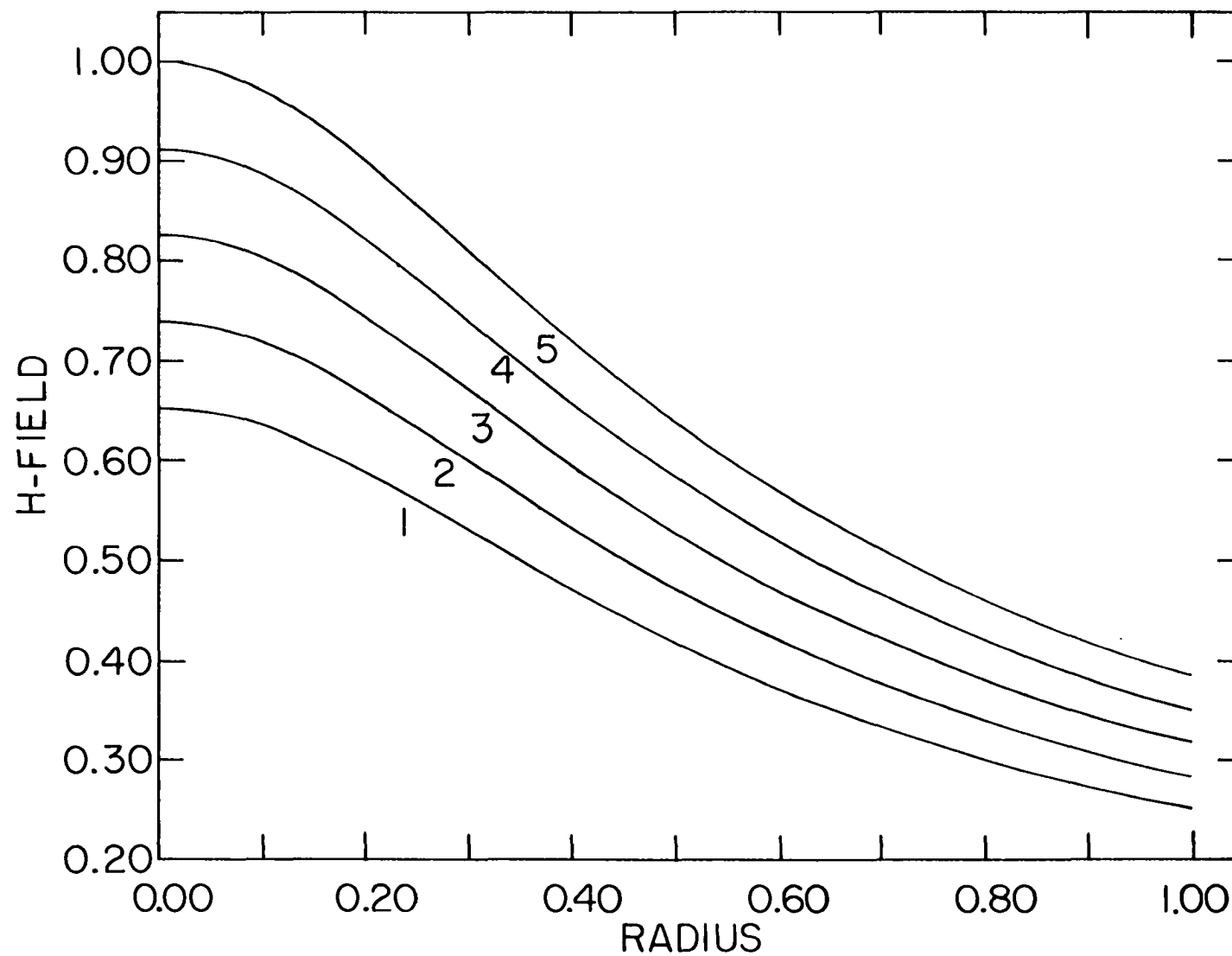


Figure 28. Reduced flux density \tilde{B} versus $\tilde{\rho}$ for the same conditions as Figure 27. Also see Figure 21

Figure 29. Reduced field \tilde{H} versus $\tilde{\rho}$ for the constant pitch model at fixed surface pitch angle $\alpha_s = 67.5^\circ$ for increasing values of the reduced surface field \tilde{H}_s . For curve 1, $\tilde{H}_s = 0.25 = \tilde{H}_{c1}$, and for curve 5, $\tilde{H}(0) = 1$. See Figure 21



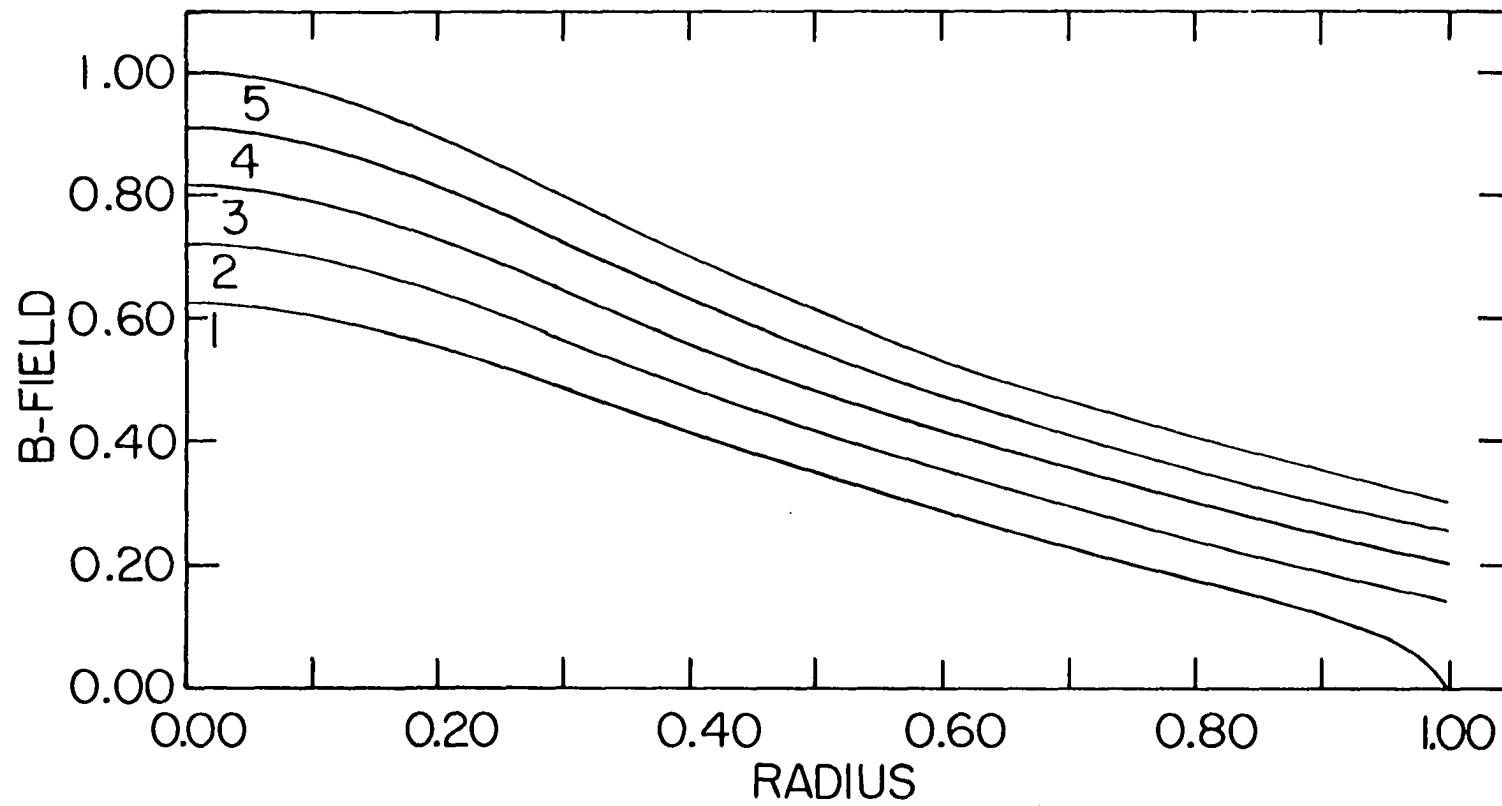


Figure 30. Reduced flux density \tilde{B} versus $\tilde{\rho}$ for the same conditions as Figure 29. Also see Figure 21

2. Currents

The thermodynamic current density is calculated from Ampere's law,

$$\vec{J} = \frac{c}{4\pi} \vec{\nabla} \times \vec{H} \quad , \quad (2.64)$$

which in component form is

$$J_{\varnothing} = - \frac{c}{4\pi} \frac{\partial H_z}{\partial \rho} \quad (2.65a)$$

$$J_z = \frac{c}{4\pi\rho} \frac{\partial}{\partial \rho} (\rho H_{\varnothing}) \quad . \quad (2.65b)$$

Using Equations 2.42 and 2.46 this becomes

$$J_{\varnothing} = \mp \frac{c}{4\pi} \frac{\partial}{\partial \rho} [H(0) \cos^2 \alpha(\rho)] \quad , \quad (2.66a)$$

$$J_z = \frac{c}{4\pi\rho} \frac{\partial}{\partial \rho} [\rho H(0) \cos \alpha(\rho) \sin \alpha(\rho)] \quad , \quad (2.66b)$$

where the upper sign applies when $0 < \alpha < \pi/2$, and the lower sign applies when $\frac{\pi}{2} < \alpha < \pi$. Taking the derivatives in Equation 2.66 yields

$$J_{\varnothing} = \pm \frac{cH(0)}{4\pi} [2\sin^2 \alpha(\rho) \cos^2 \alpha(\rho)] \quad (2.67a)$$

$$J_z = \frac{cH(0)}{4\pi\rho} [2\sin \alpha(\rho) \cos^3 \alpha(\rho)] \quad (2.67b)$$

after some algebra. In deriving 2.67 we make use of

$$\frac{\partial \alpha(\rho)}{\partial \rho} = \frac{\sin^2 \alpha(\rho)}{2\rho} \quad , \quad (2.68)$$

which follows from Equation 2.43. In reduced units \tilde{J}_\emptyset , \tilde{J}_z , defined by

$$\tilde{J}_\emptyset = J_\emptyset / (cH_c 2 / 4\pi a) \quad , \quad (2.69a)$$

$$\tilde{J}_z = J_z / (cH_c 2 / 4\pi a) \quad , \quad (2.69b)$$

we obtain

$$\tilde{J}_\emptyset = \pm 2\tilde{H}(0) \sin^2 \alpha(\tilde{\rho}) \cos^2 \alpha(\tilde{\rho}) \quad (2.70a)$$

$$\tilde{J}_z = 2\tilde{H}(0) \sin \alpha(\tilde{\rho}) \cos^3 \alpha(\tilde{\rho}) / \tilde{\rho} \quad (2.70b)$$

as the final result. One may show that $\tilde{J} = [\tilde{J}_\emptyset^2 + \tilde{J}_z^2]^{1/2}$ is given by

$$\tilde{J} = 2\tilde{H}(0) |\tan \alpha_s| / [1 + \tilde{\rho}^2 \tan^2 \alpha_s] \quad (2.71a)$$

or

$$J = \frac{cH(0)}{2\pi a} |\tan \alpha_s| / [1 + (\rho/a)^2 \tan^2 \alpha_s] \quad . \quad (2.71b)$$

The maximum magnitude of the current density occurs on the axis where $\rho = 0$, and has the value in reduced units,

$$\tilde{J}(0) = 2\tilde{H}(0) |\tan \alpha_s| \quad . \quad (2.72)$$

Figures 31-36 show the results of Equations 2.70 and

Figure 31. Reduced axial current density \tilde{J}_z versus $\tilde{\rho}$ for the same conditions as in Figure 25. Current density is normalized to $cH_{c2}/4\pi a = 1$

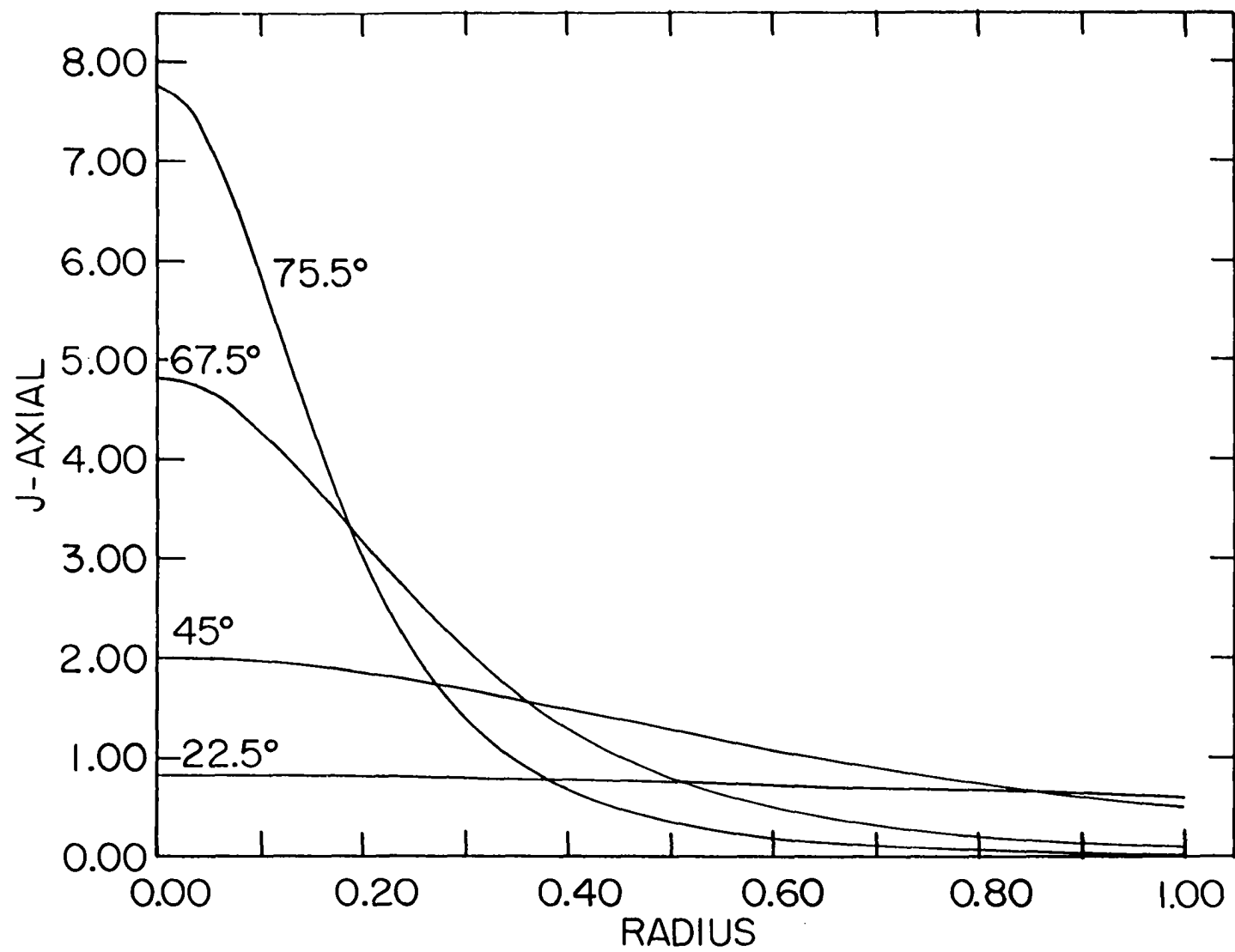


Figure 32. Reduced azimuthal current density \tilde{J}_θ versus $\tilde{\rho}$ for the same conditions as Figure 25. Current density is normalized to $cH_{c2}/4\pi a = 1$

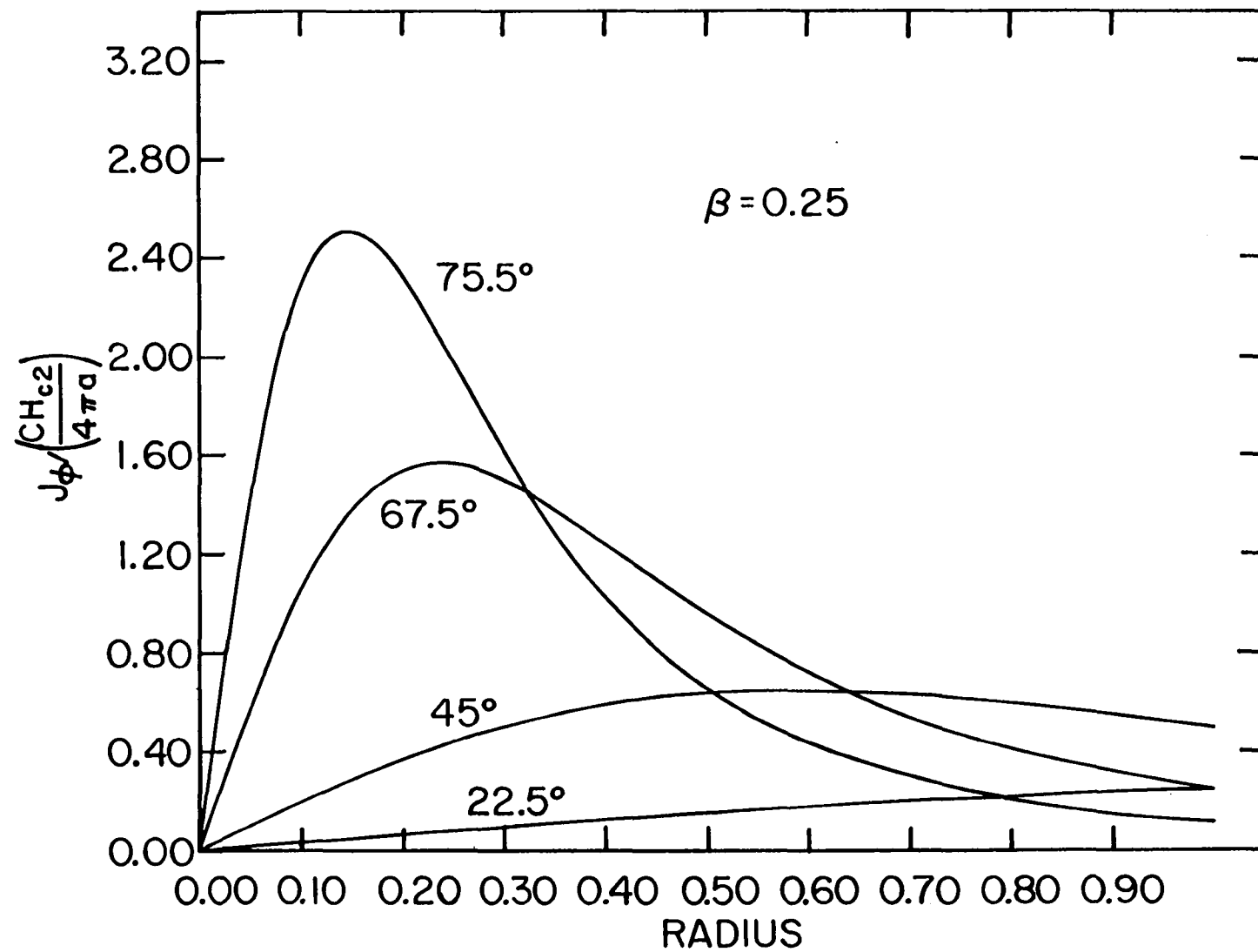


Figure 33. Magnitude of the reduced current density \tilde{J} versus $\tilde{\rho}$ for the same conditions as Figure 25. Here $\tilde{J} = [\tilde{J}_z^2 + \tilde{J}_\emptyset^2]^{1/2}$ where \tilde{J}_z and \tilde{J}_\emptyset are plotted in Figures 31 and 32 respectively

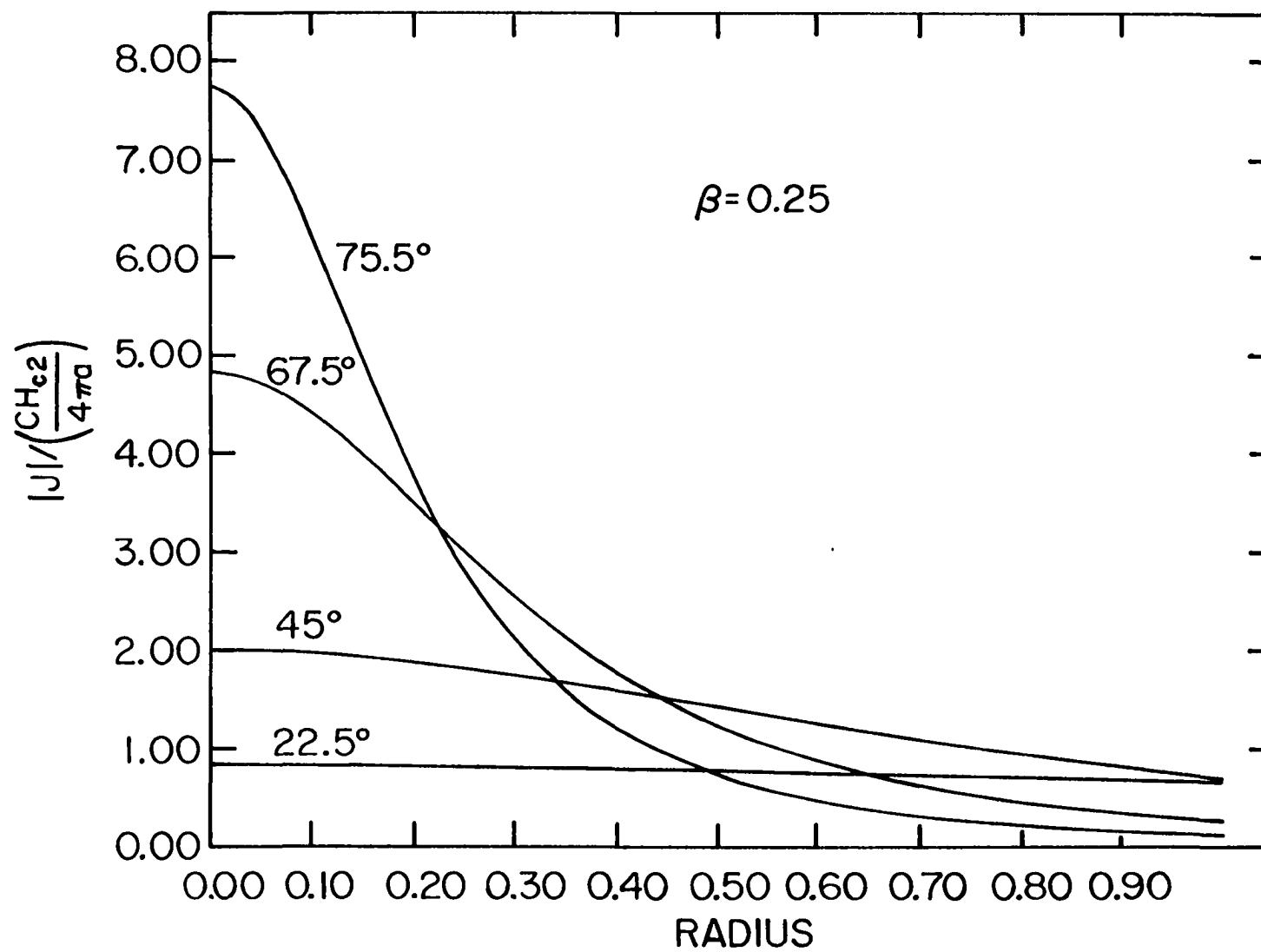


Figure 34. Reduced axial current density \tilde{J}_z versus $\tilde{\rho}$ for a surface pitch angle of 67.5° , under the same conditions as Figure 29. Curve labels 1, 2, ..., 5, correspond to the field profiles of the same numbers in Figure 29

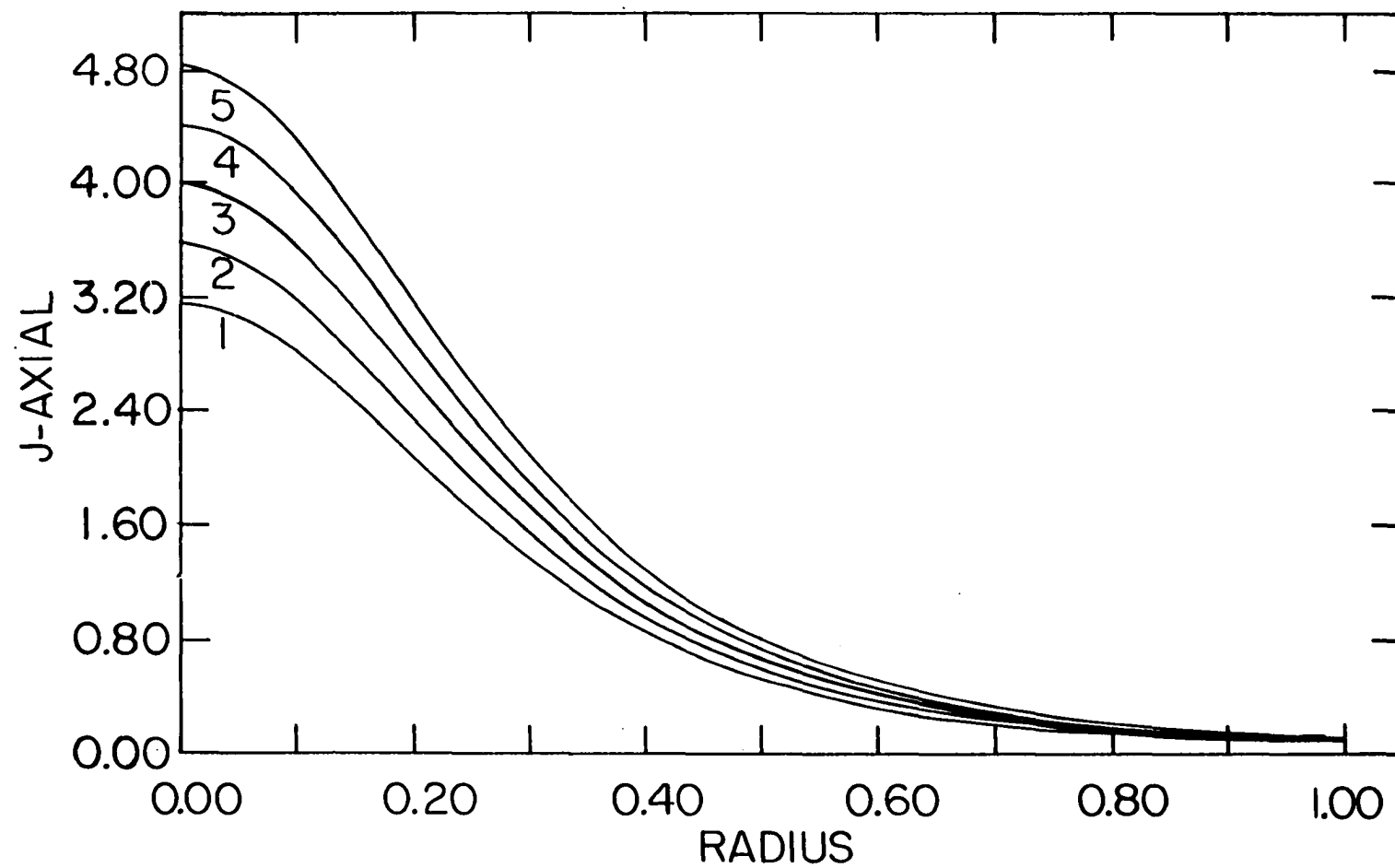


Figure 35. Reduced azimuthal current density \tilde{J}_θ versus $\tilde{\rho}$ for a surface pitch angle of 67.5° , under the same conditions as in Figure 29. Curve labels 1, 2, ..., 5 correspond to the same labels in Figure 29

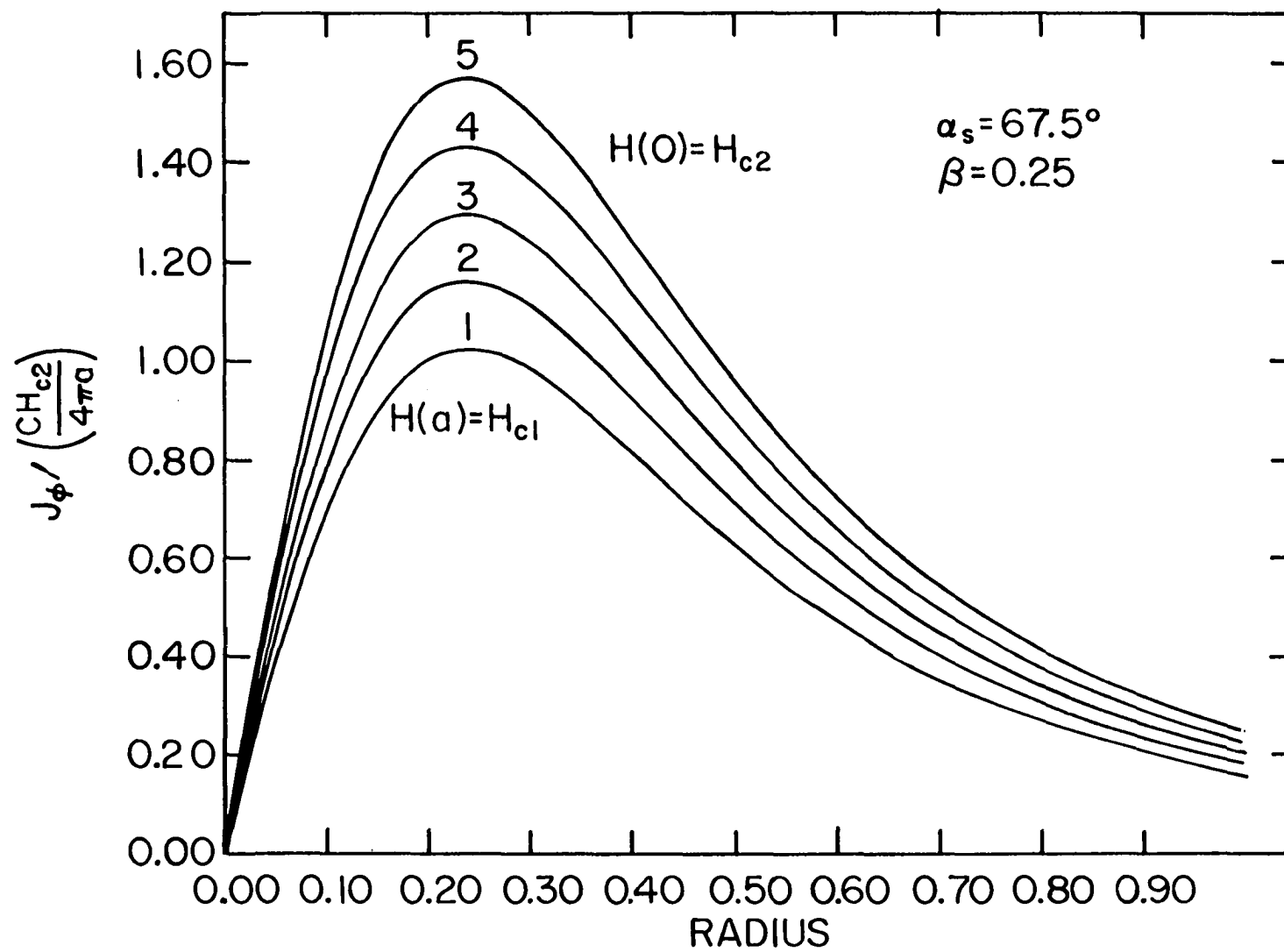
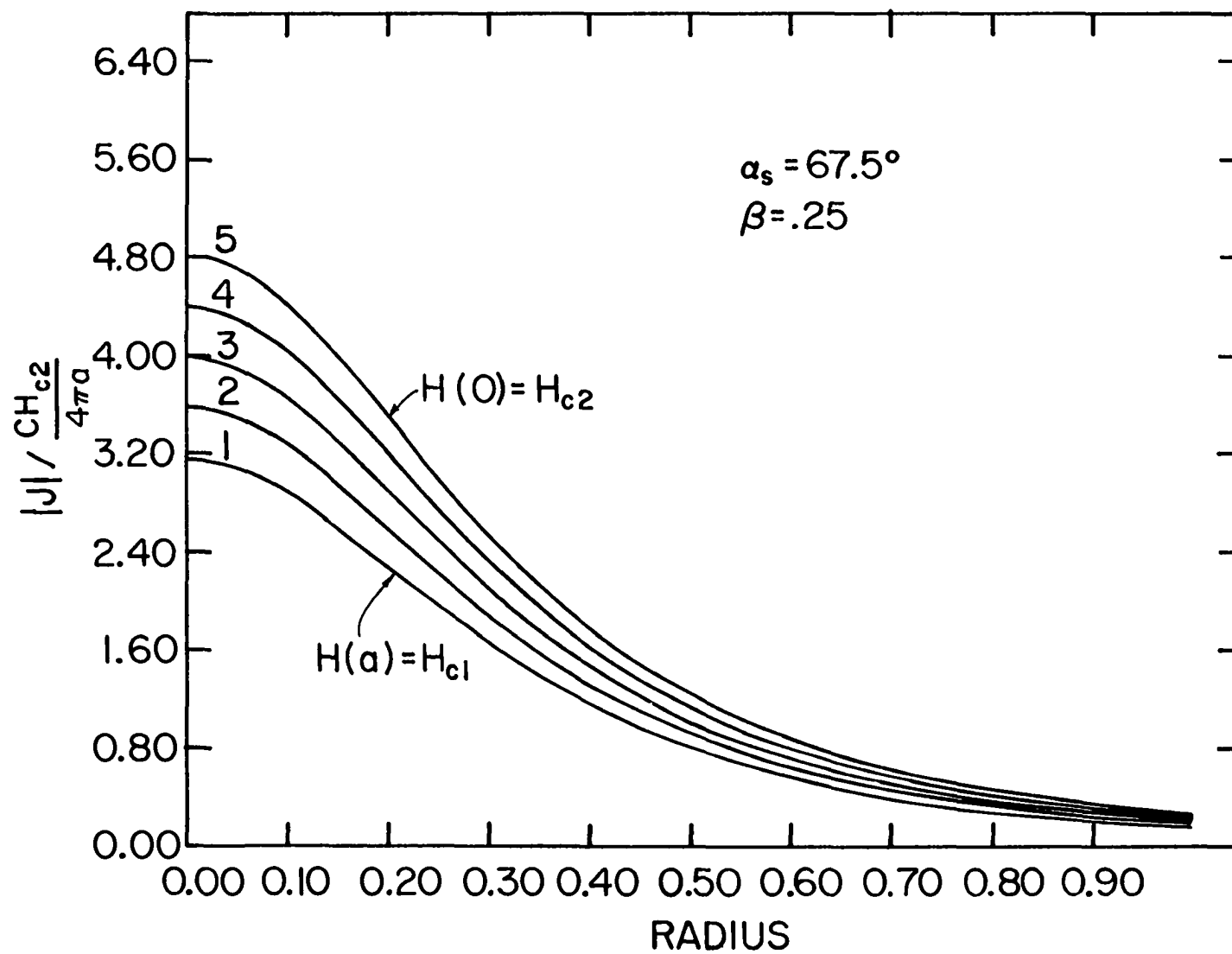


Figure 36. Magnitude of the reduced current density \tilde{J} versus $\tilde{\rho}$ for a surface pitch angle of 67.5° , under the same conditions as in Figure 29. $\tilde{J} = [\tilde{J}_z^2 + \tilde{J}_\theta^2]^{1/2}$ where \tilde{J}_z and \tilde{J}_θ are plotted in Figures 34 and 35 respectively



2.71. Figures 31-33 show the variations in \tilde{J}_z , \tilde{J}_θ , and \tilde{J} with the surface pitch angle, and Figures 34-36 show the variation of the current densities as the magnitude of the fields increase.

H. Finite, Nonzero Pinning

1. Descriptive

We describe here our investigations of the solutions to Equation 2.14,

$$\frac{\partial H}{\partial \rho} = \pm \frac{4\pi}{c} J_c(B) - \frac{H(B)}{R_c(\rho)} \quad (2.14)$$

in the very general case where $J_c(B)$ is nonzero. We restrict ourselves to the constant pitch assumption mentioned earlier, so that the vortex pitch angle as a function of radius is known through

$$\alpha(\rho) = \tan^{-1}[(\rho/a)\tan\alpha_s] \quad . \quad (2.68)$$

We also use the relationship for $H_{eq}(B)$ ($H(B)$ for short) as previously described in Equation 2.24; that is,

$$H(B) \equiv H_{eq}(B) = [k^2 B^2 + H_{c1}^2]^{1/2} \quad (2.69)$$

where

$$k^2 = 1 - [H_{c1}/H_{c2}]^2 \quad . \quad (2.70)$$

The analytical form for the critical current $J_c(B)$ is based on Urban's model (22) which we have discussed earlier; that is, we use

$$J_c(B) = J_c(0) \left[\frac{1 - B/H_{c2}}{1 + B/B_0} \right] \quad . \quad (2.71)$$

For ease of numerical computation, we have reduced these relationships to dimensionless form, consistent with earlier definitions. Specifically, the reduced quantities \tilde{B} , \tilde{H} , \tilde{J} , \tilde{R}_c , and $\tilde{\rho}$ are defined by

$$\begin{aligned} \tilde{B} &= B/H_{c2} \\ \tilde{H} &= H/H_{c2} \\ \tilde{R}_c &= R_c/a \\ \tilde{\rho} &= \rho/a \\ \tilde{J} &= J/(cH_{c2}/4\pi a) \quad . \end{aligned} \quad (2.72)$$

Our working equations in reduced form are

$$\frac{\partial \tilde{H}}{\partial \tilde{\rho}} = \pm \tilde{J}_c(\tilde{B}) - \tilde{H}(\tilde{B})/\tilde{R}_c(\tilde{\rho}) \quad (2.73a)$$

$$\alpha(\rho) = \tan^{-1}[\tilde{\rho} \tan \alpha_s] \quad (2.73b)$$

$$\tilde{H}(\tilde{B}) = [k^2 \tilde{B}^2 + \beta^2]^{1/2} \quad (2.73c)$$

$$\tilde{J}_c(\tilde{B}) = \tilde{J}_c(0) \cdot [(1 - \tilde{B})/(1 + \tilde{B}/\tilde{B}_0)] \quad (2.73d)$$

$$\tilde{R}_c(\tilde{\rho}) = \frac{\cot^2 \alpha_s + \tilde{\rho}^2}{\tilde{\rho}} \quad (2.73e)$$

where $\beta = H_{c1}/H_{c2} = \tilde{H}_{c1}$, and $\beta^2 + k^2 = 1$.

We also have a sixth equation to account for the effects of surface pinning, described earlier in Section F; that is,

$$H_{en}(B) = [H_S^2 + \delta^2 B^2]^{1/2} \quad (2.74a)$$

in the flux entering case, and

$$H_{ex}(B) = B \quad (2.74b)$$

in the flux exiting case. In reduced form these are

$$\tilde{H}_{en}(B) = [\tilde{H}_S^2 + \delta^2 \tilde{B}^2]^{1/2} \quad (2.75a)$$

$$\tilde{H}_{ex}(\tilde{B}) = \tilde{B} \quad (2.75b)$$

where δ is related to H_S according to

$$\delta^2 = 1 - (H_S/H_{c2})^2 \quad (2.76)$$

One should not confuse the surface barrier field H_S used in this expression with the magnitude H_S of the net magnetic field produced at the specimen's outer surface by the applied longitudinal field and the self-field of the current.

If we let $\gamma = H_S/H_{c2}$, then

$$H_{en}(B) = [\gamma^2 + \delta^2 B^2]^{\frac{1}{2}} \quad (2.77)$$

and

$$\gamma^2 + \delta^2 = 1 \quad . \quad (2.78)$$

Figure 37 shows qualitatively the relationship between $H(B)$ and $H_{en}(B)$. Notice that $H_{en}(B)$ is always at least as large as $H(B)$, and that $\gamma = \tilde{H}_S$ is always at least as large as $\beta = \tilde{H}_{c1}$. The utility of Equation 2.75 lies in relating the fields just inside the surface of the specimen to the fields just outside the surface.

Figure 38 shows qualitatively the relationship between $H_{en}(B)$ or $H_{ex}(B)$ and $H(B)$ at the surface, for three situations: a) where B is relatively small, b) where B is large, and c) where $B = H_{c2}$ is at its maximum.

2. Numerical methods

a. General method Solutions to Equation 2.73a were obtained by numerical integration on a digital computer, using a Runge-Kutta (RK) technique. We have used the following RK method, discussed by Scarborough (45). The equation which we are solving is a first-order differential equation of the general form

$$dy/dx = f(x,y) \quad . \quad (2.79)$$

We let (x_0, y_0) denote a known starting point, and let Δx

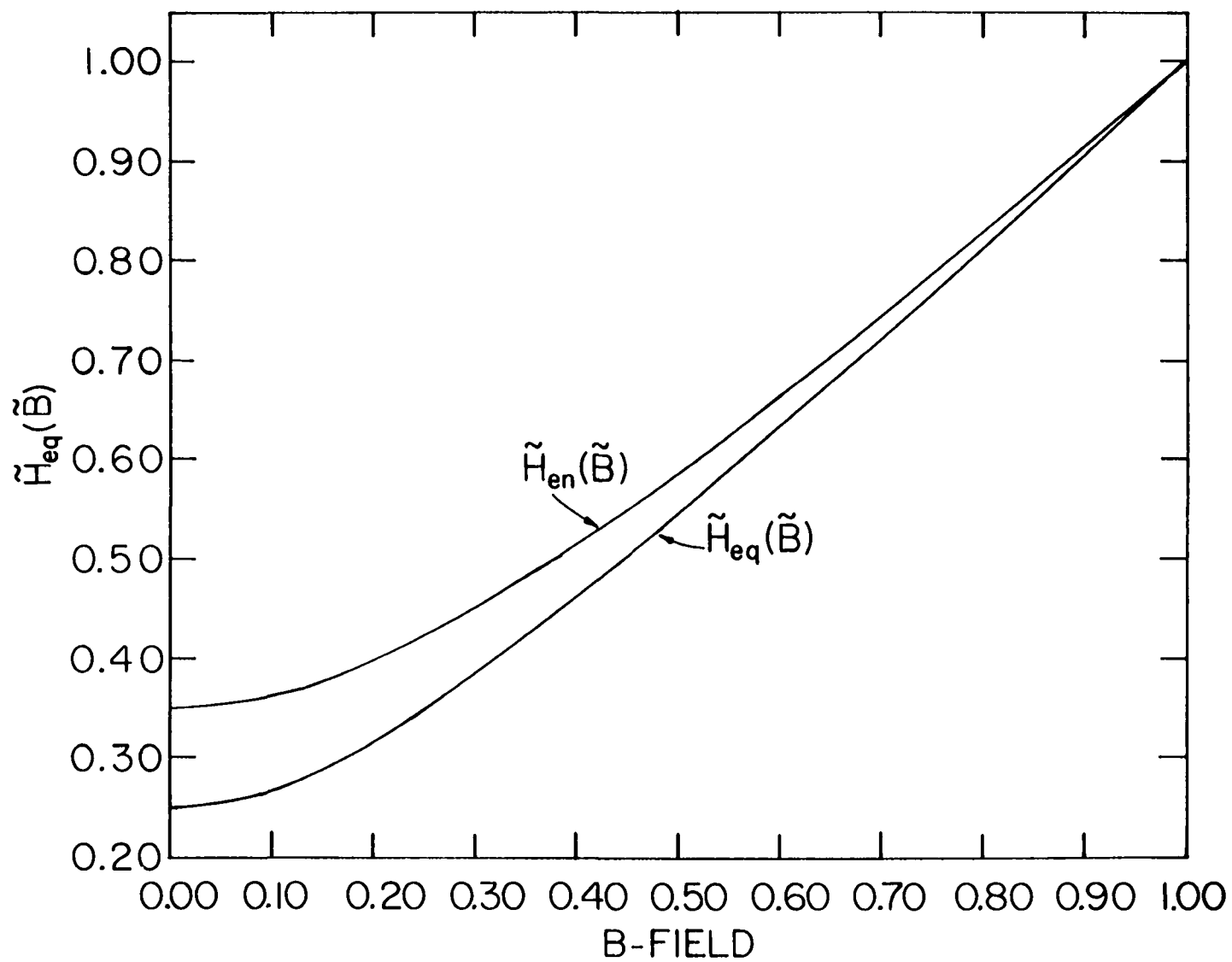
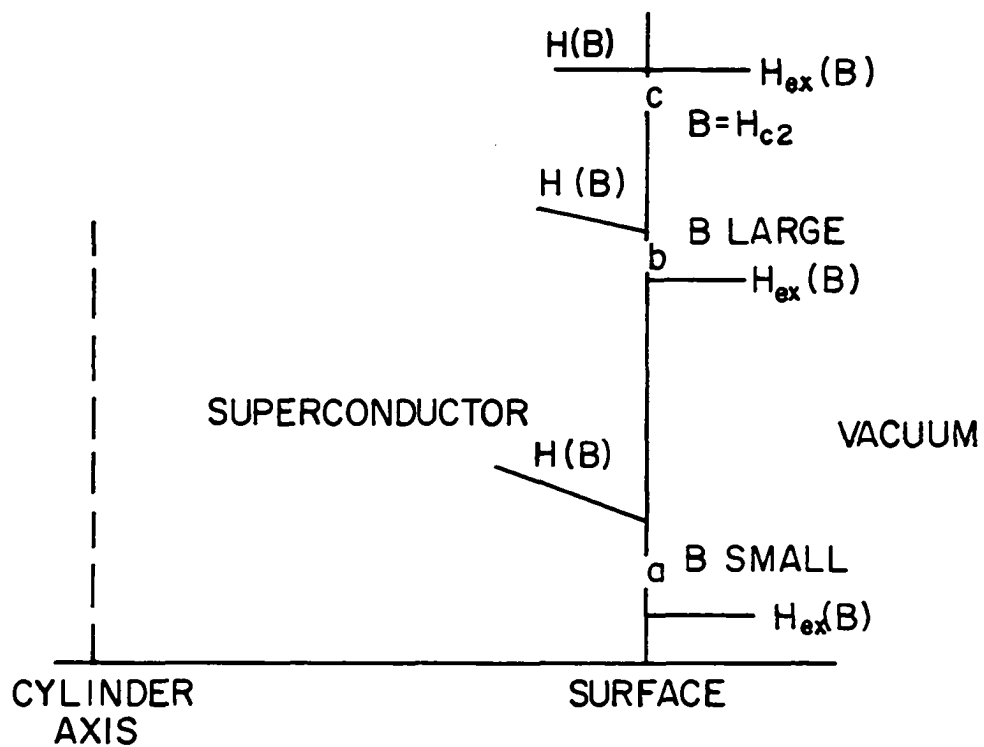
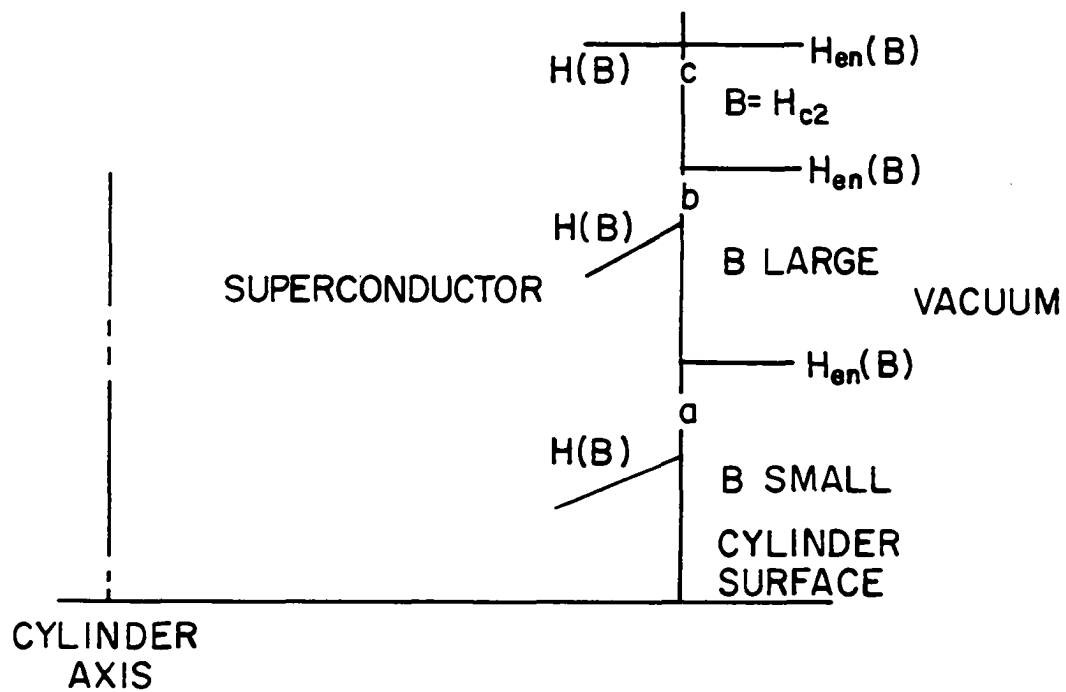


Figure 37. Model for $\tilde{H}_{eq}(\tilde{B})$ and $\tilde{H}_{en}(\tilde{B})$ versus \tilde{B} with $\tilde{H}_{c1} = 0.25$ and $\tilde{H}_S = 0.35$

Figure 38. Illustration of the way the surface field $H_{\text{en}}(B)$ or $H_{\text{ex}}(B)$ leads the internal field $H_{\text{eq}}(B)$. Upper figure applies in the flux-entering case, and lower figure applies in the flux-exiting case



denote the interval between the series of points $x_0, x_1, x_2, \dots, x_n$, at which we seek the corresponding ordinates $y_0, y_1, y_2, \dots, y_n$. We compute four quantities k_1, k_2, k_3 , and k_4 via

$$\begin{aligned} k_1 &= f(x_0, y_0) \Delta x \\ k_2 &= f(x_0 + \frac{1}{2} \Delta x, y_0 + \frac{1}{2} k_1 \Delta x) \Delta x \\ k_3 &= f(x_0 + \frac{1}{2} \Delta x, y_0 + \frac{1}{2} k_2 \Delta x) \Delta x \\ k_4 &= f(x_0 + \Delta x, y_0 + k_3 \Delta x) \Delta x \end{aligned} \quad (2.80)$$

and obtain Δy by averaging $k_1 \dots k_4$ through the weighting scheme

$$\Delta y = \frac{1}{6} \cdot [k_1 + k_4 + 2(k_2 + k_3)] \quad (2.81)$$

so that the new point (x_1, y_1) is given by

$$\begin{aligned} x_1 &= x_0 + \Delta x \\ y_1 &= y_0 + \Delta y \end{aligned} \quad (2.82)$$

The next point, (x_2, y_2) is obtained in exactly the same way, by replacing (x_0, y_0) by (x_1, y_1) in Equation 2.80, and so on. Thus, by proceeding in this manner, one may eventually obtain all the points $(x_1, y_1), \dots, (x_n, y_n)$ as the desired solution.

In solving for \tilde{H} as a function of $\tilde{\rho}$, we have used this routine with $\Delta x = 0.02$, so that the radius is divided into 50 equal intervals in the range from 0.0 to 1.0. The errors with this RK method are proportional to $(\Delta x)^5$, so that in these circumstances, a Δx of 0.02 is more than sufficiently accurate when compared with the other approximations used in the overall method. Eventually, we came to rely upon two computer programs, depending upon whether one wished to integrate from the surface inwards, or from the axis outwards.

An additional complication, which precluded the use of a canned RK routine, was the fact that special consideration was necessary at the zero(s) of $B(\rho)$. As will be shown in the next chapter, the slope of the H versus ρ curve at the flux front (i.e., where $H \approx H_{c1}$ and $B \approx 0$) determines the direction of the bulk force per unit volume on the vortex array. If the slope of the H versus ρ curve becomes negative at the flux front, then these bulk forces act inwards, precipitating a dramatic and irreversible collapse of flux spirals. (This startling result, which we have called the spiral collapse instability, is discussed in detail in the next chapter.) Thus, it was necessary to examine the derivative $\partial H / \partial \rho$ at the zero(s) of B to determine if the integration should be allowed to proceed, or be terminated. In actual practice, a zero in the slope $\partial H / \partial \rho$ was verified by

examining the second derivative $\partial^2 H / \partial \rho^2$ numerically, since the entire procedure was limited by the accuracy of the numerical method.

b. Magnetization The area under the curve of $B(\rho)$ versus ρ is related to the magnetization of the cylinder. From the usual electromagnetic results,

$$-4\pi\vec{M} = \vec{H} - \vec{B} \quad (2.83)$$

we have for the axial direction in the cylinder

$$\langle -4\pi M_z \rangle = H_{sz} - \langle B_z \rangle \quad (2.84)$$

where H_{sz} is the magnitude of the applied longitudinal field at the surface, and $\langle B_z \rangle$ is the mean axial field throughout the cylinder, defined as

$$\begin{aligned} \langle B_z \rangle &\equiv \frac{1}{\pi a^2} \int_0^a d\rho \, 2\pi \rho B_z(\rho) \\ &= \frac{2}{a^2} \int_0^a d\rho \, \rho B(\rho) \cos \alpha(\rho) \quad . \end{aligned} \quad (2.85)$$

The magnetization is said to be paramagnetic or diamagnetic according to whether $\langle -4\pi M_z \rangle$ is negative or positive, respectively. One could also define a mean circumferential magnetization per unit length, $\langle -4\pi M_\phi \rangle$, where

$$\langle -4\pi M_\emptyset \rangle = H_{s\emptyset} - \langle B_\emptyset \rangle \quad (2.86)$$

and

$$\begin{aligned} \langle B_\emptyset \rangle &\equiv \frac{1}{a} \int_0^a d\rho B_\emptyset(\rho) \\ &= \frac{1}{a} \int_0^a d\rho B(\rho) \sin \alpha(\rho) \quad . \end{aligned} \quad (2.87)$$

Equation 2.84 is most useful, since this is what the experimentalist can measure directly. We obtained numerical values for $\langle -4\pi M_z \rangle$ by performing the integration of Equation 2.85 numerically using Simpson's rule. Simpson's rule is appropriate when the function to be integrated does not have excessive curvature, and the number of ordinates in the integration is an odd number. The most general Simpson's rule formula is

$$\begin{aligned} \int f(x) dx &= \frac{1}{3} \Delta x [f_1 + 4f_2 + 2f_3 + 4f_4 + 2f_5 + 4f_6 \\ &\quad + \dots + 4f_{n-1} + f_n] \end{aligned} \quad (2.88)$$

where n is an odd integer, f_i denotes the i th ordinate, and all of the x_i are evenly spaced. In general, the multipliers on the right-hand side above follow the pattern

$$1, 4, 2, 4, 2, 4, 2, 4, 2, 4, \dots, 4, 1, \quad (2.89)$$

where in the special case of only three ordinates, the multipliers are simply 1, 4, and 1.

Any zeros of $B(\rho)$, which introduced an oddly spaced point, were accommodated by approximating the area about the zero point as a trapezoid. It is estimated that negligible error was introduced by this approximation.

3. Phase diagrams

We begin the analysis of the nonzero pinning case by examining phase diagrams analogous to Figure 21 for the weak pinning limit.

In order to make a comparison with the weak pinning limit, we selected a hypothetical material with the same lower critical field value, i.e., $H_{c1} = 0.25H_{c2}$. One such real substance would be vanadium. Using the Urban model for $\tilde{J}_c(\tilde{B})$,

$$\tilde{J}_c(\tilde{B}) = \tilde{J}_c(0) [(1 - \tilde{B}) / (1 + \tilde{B}/\tilde{B}_0)] \quad (2.90)$$

we arbitrarily selected a value for \tilde{B}_0 of 0.20, and proceeded to vary $\tilde{J}_c(0)$ through a wide range of values. Surface pinning was initially discounted for simplicity. This was effected by setting the surface pinning parameter H_S equal to H_{c1} .

Figures 39 through 44 show the influence of increasing the pinning strength, while Figure 45 shows the effect of a

modest amount of surface pinning. Since the curves have a vertical tangent at the maximum value of $H_{s\theta}$, we see that increasing pinning strength tends to increase the surface pitch angle at which the total current is a maximum, and also the magnitude of the maximum current. Also note that as the pinning strength increases, the surface field needed to produce a given $H(0)$ increases in magnitude, as evidenced by the merger of the two curves ($0.5H_{c2}$ and H_{c2}) at zero pitch angle. All curves in this series show a missing portion in the region where $H_{sz} \approx 0$, corresponding to pitch angles near 90° . The 90° case is radically different from the situations with lesser surface pitch angles, since flux spirals here degenerate into flux rings. As a result, it becomes increasingly more difficult to obtain values of $H_{s\theta}$ corresponding to a given field on the axis $H(0)$, because the integration may no longer be performed from the axis outwards, but rather, must be performed from the surface inwards. Thus, one must guess at an appropriate $H_{s\theta}$, and see what actually results by trial and error. As an additional complication, the sensitivity $dH(0)/dH_{s\theta}$ becomes enormous near 90° , making the guess for $H_{s\theta}$ that much more difficult. Finally, the spiral collapse instability (see next chapter) quite often assures that it is impossible to realize a given $H(0)$; i.e., the collapse drives the field on the axis above H_{c2} , causing destruction of the mixed state.

What is therefore missing from this survey are the details of the region of the phase diagram near $\alpha_s = 90^\circ$. Preliminary analysis indicates that the behavior near 90° is quite complex, and worthy of a detailed investigation in the future. An inherent feature of such a phase diagram would be a spiral collapse line delineating those regions subject to collapse from the noncollapse regions of the mixed state.

Figure 46 shows the influence of increasing pinning on the magnetization of the cylinder, while Figure 47 shows the change in the field profiles as the pinning strength is varied, all at a surface pitch angle of 15° . Figures 48 through 52 show similar field profiles at increasing surface pitch angles through 85° . Figure 52 reveals an interesting situation where portions of the curves of \tilde{H} versus $\tilde{\rho}$ for $\tilde{J}_c(0) = 1.0$ and 2.0 lie below \tilde{H}_{c1} . This indicates that, because of the spiral collapse instability, no static solutions are possible under these conditions.

Figures 53-55 show the product of the flux density B with the two orthogonal components of the current density $\langle \vec{j} \rangle$, and with the magnitude of $\langle \vec{j} \rangle$. Recalling that $\langle \vec{j} \rangle$ is derived from the curl of \vec{B} rather than the curl of \vec{H} , we see that singularities in $\langle \vec{j} \rangle$ are to be expected wherever $\partial B / \partial \rho$ changes abruptly, typically at the flux front. A smooth curve is obtained by plotting the product of B with $\langle \vec{j} \rangle$, although there is a sacrifice in the physical intuition for $\langle \vec{j} \rangle$.

Figure 39. Reduced surface field components $\tilde{H}_{s\theta}$ and \tilde{H}_{sz} required to yield a field on the axis equal to \tilde{H}_{c2} and $0.5\tilde{H}_{c2}$. Outer dashed lines define the minimum value of α_s ($= 63.44^\circ$) necessary for spiral collapse. (See discussion in Chapter III.) Inner dashed lines define sector where behavior is unknown, corresponding to $\alpha_s > 87.5^\circ$. $\tilde{J}_c(0) = 0.25$ corresponds to weak pinning material

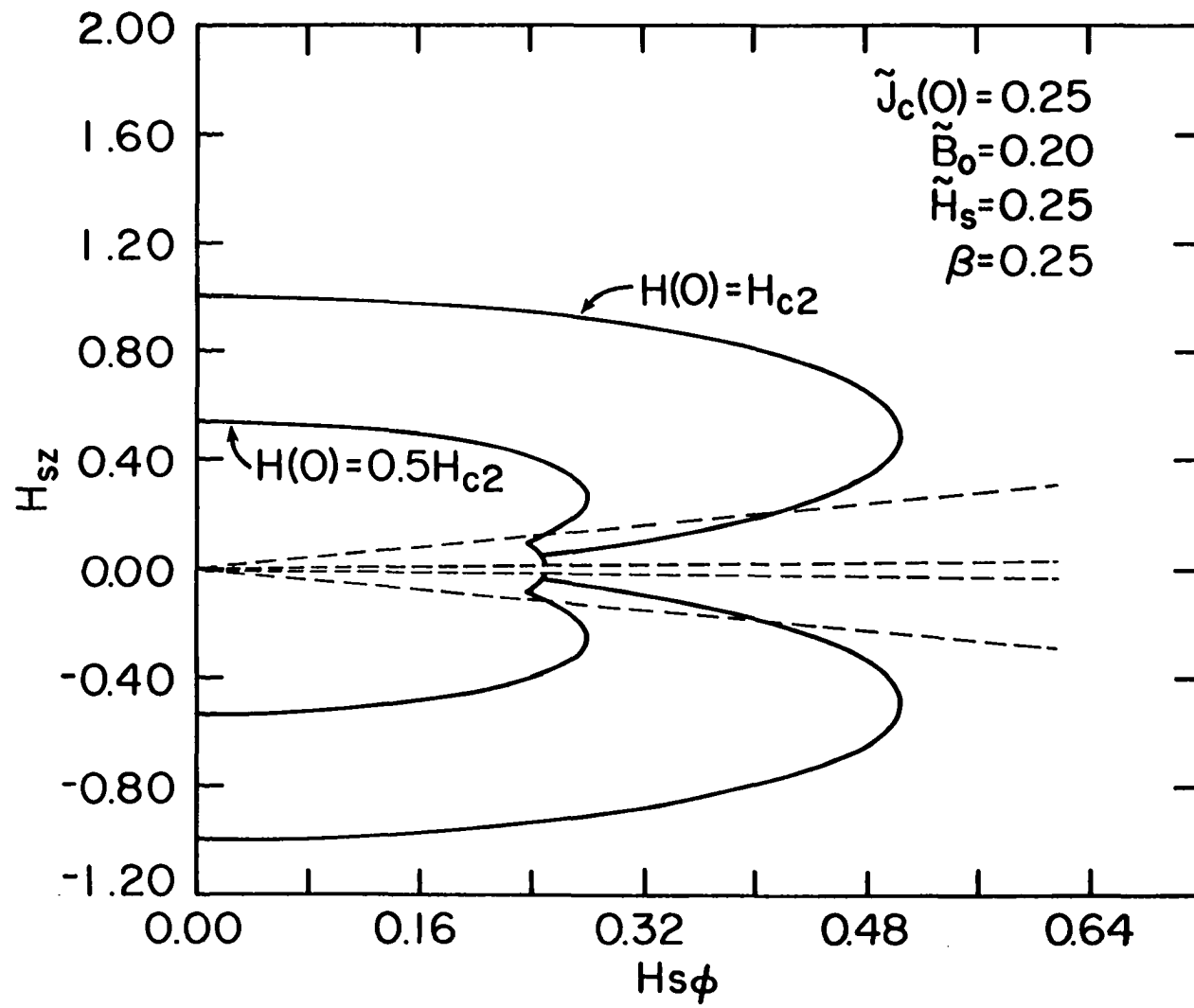


Figure 40. Reduced surface field components $\tilde{H}_{s\theta}$ and \tilde{H}_{sz} required to yield a field on the axis equal to \tilde{H}_{c2} and $0.5\tilde{H}_{c2}$. Dashed lines define the minimum value of α_s ($= 82.87^\circ$) necessary for spiral collapse. (See discussion in Chapter III.) Missing portions of the two curves indicate region where behavior is unknown ($\alpha_s > 87.5^\circ$)

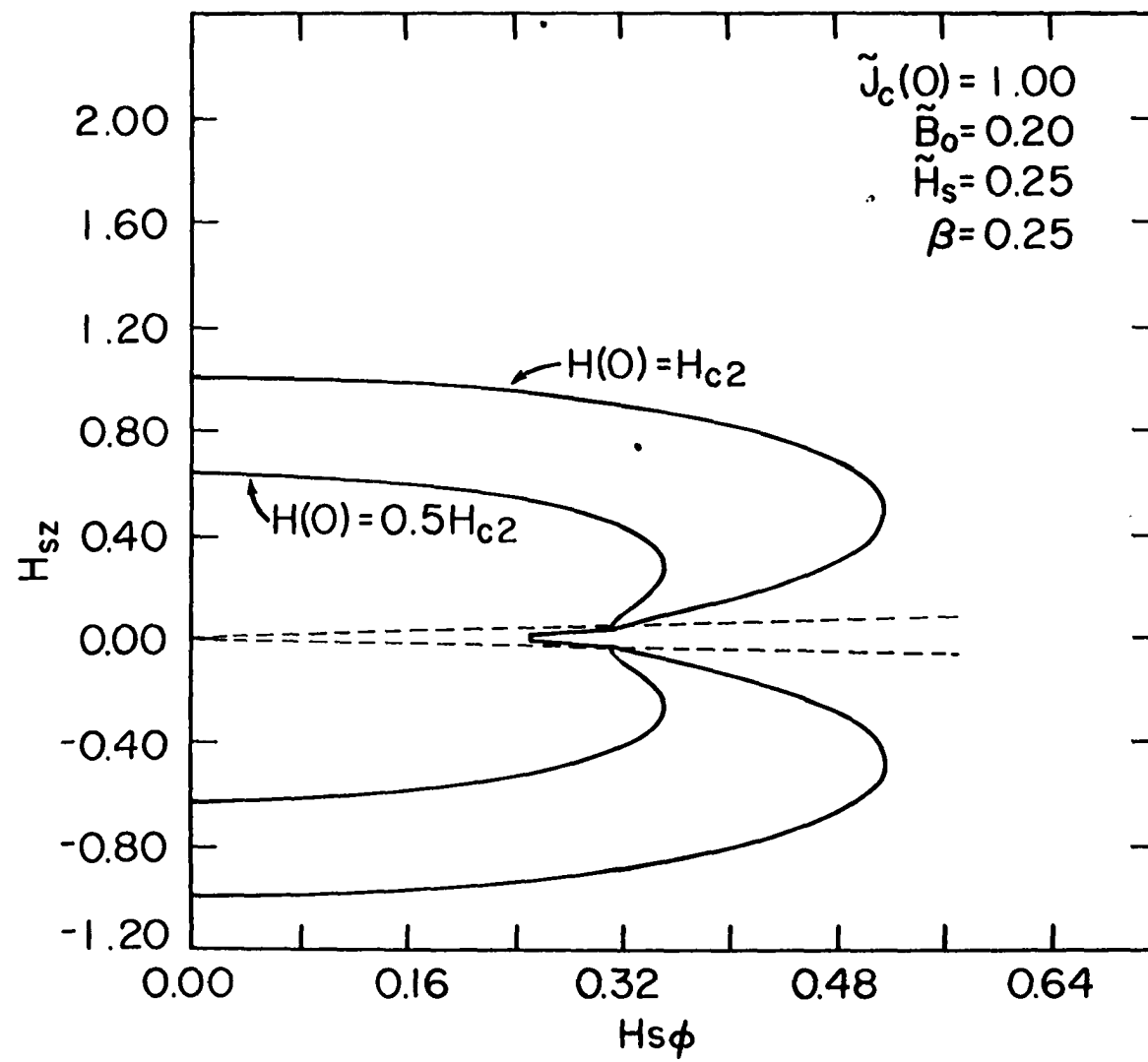


Figure 41. Reduced surface field components $\tilde{H}_{s\theta}$ and \tilde{H}_{sz} required to yield a field on the axis of \tilde{H}_{c2} and $0.5\tilde{H}_{c2}$. Dashed lines define the minimum value of α_s ($= 86.42^\circ$) necessary for spiral collapse. (See discussion in Chapter III.) Missing portions of the two curves indicate region where behavior is unknown ($\alpha_s > 87.5^\circ$). $\tilde{J}_c(0) = 2.0$ indicates a material with moderate pinning strength.

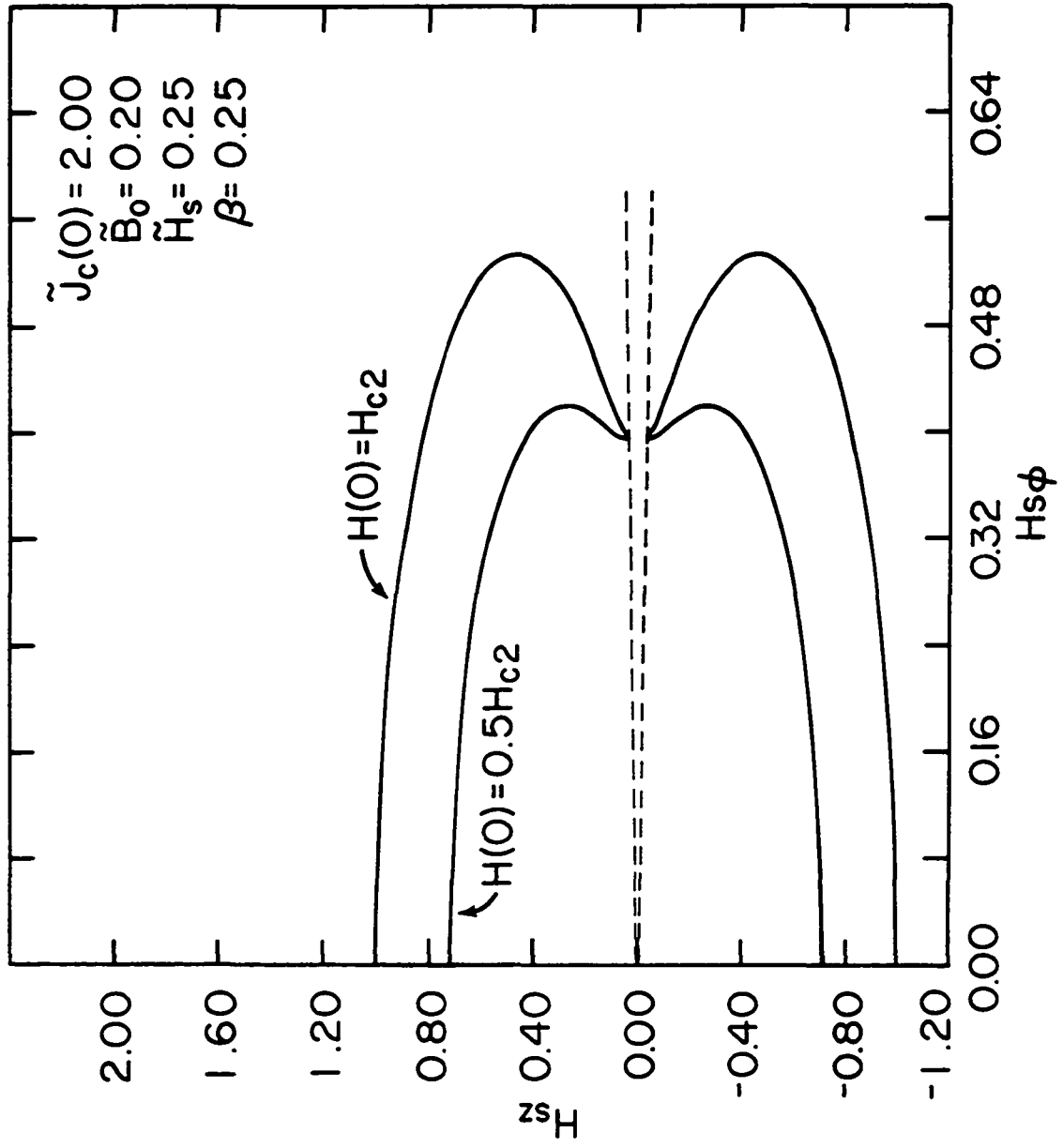


Figure 42. Reduced surface field components $\tilde{H}_{s\theta}$ and \tilde{H}_{sz} required to yield a field on the axis of \tilde{H}_{c2} and $0.5\tilde{H}_{c2}$. Missing section of curve at $\tilde{H}_{sz} \approx 0$ indicates region where behavior is unknown ($\alpha_s > 87.5^\circ$). $\tilde{J}_c(0) = 5.0$ indicates a material with moderately strong pinning strength

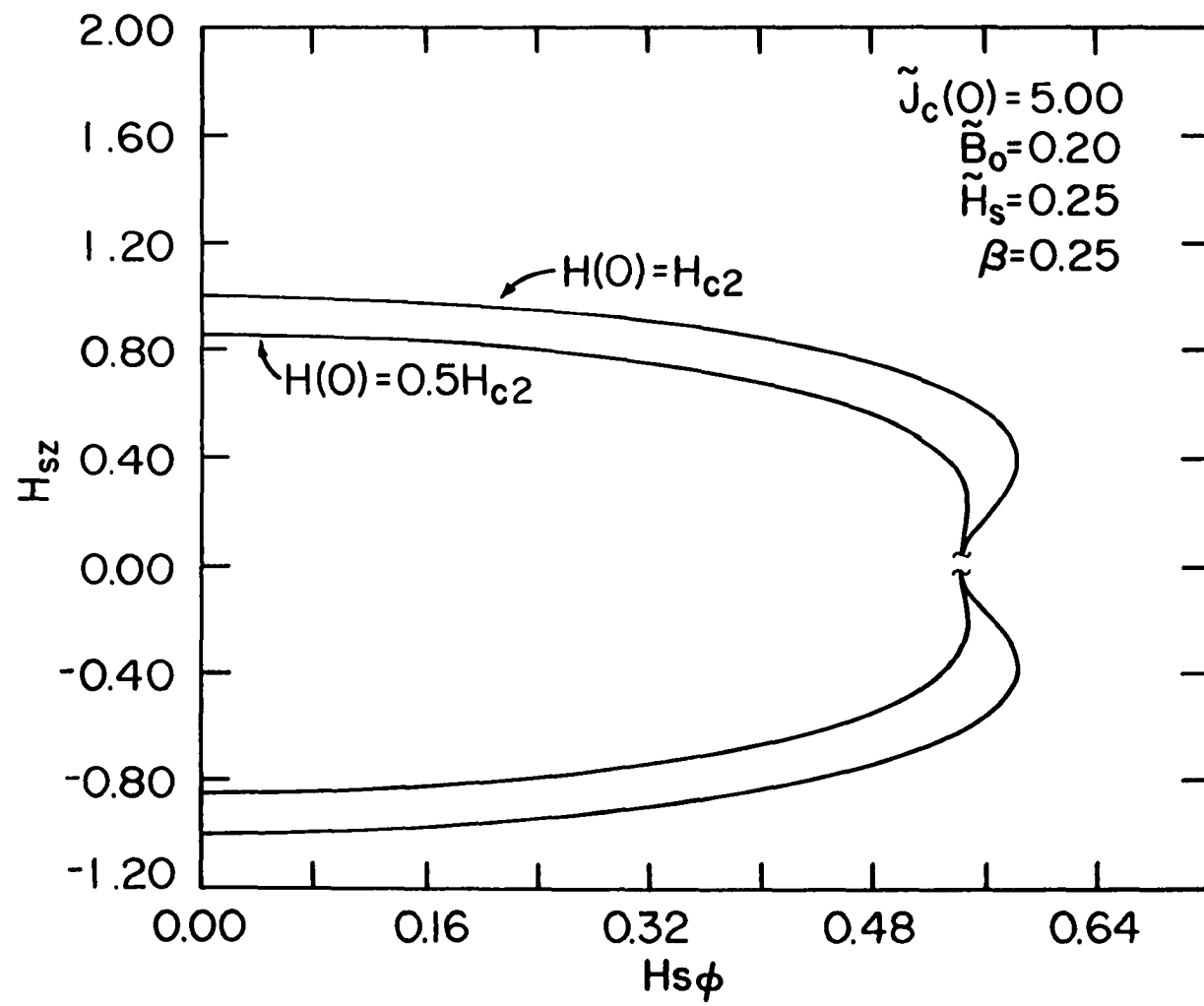


Figure 43. Reduced surface field components $\tilde{H}_{s\theta}$ and \tilde{H}_{sz} required to yield a field on the axis between $0.5\tilde{H}_{c2}$ and \tilde{H}_{c2} . Two curves are indistinguishable within the width of an ink line. Missing section at $\tilde{H}_{sz} \approx 0$ indicates region where behavior is unknown ($\alpha_s > 87.5^\circ$). $\tilde{J}_c(0) = 25.0$ indicates a very strong pinning material

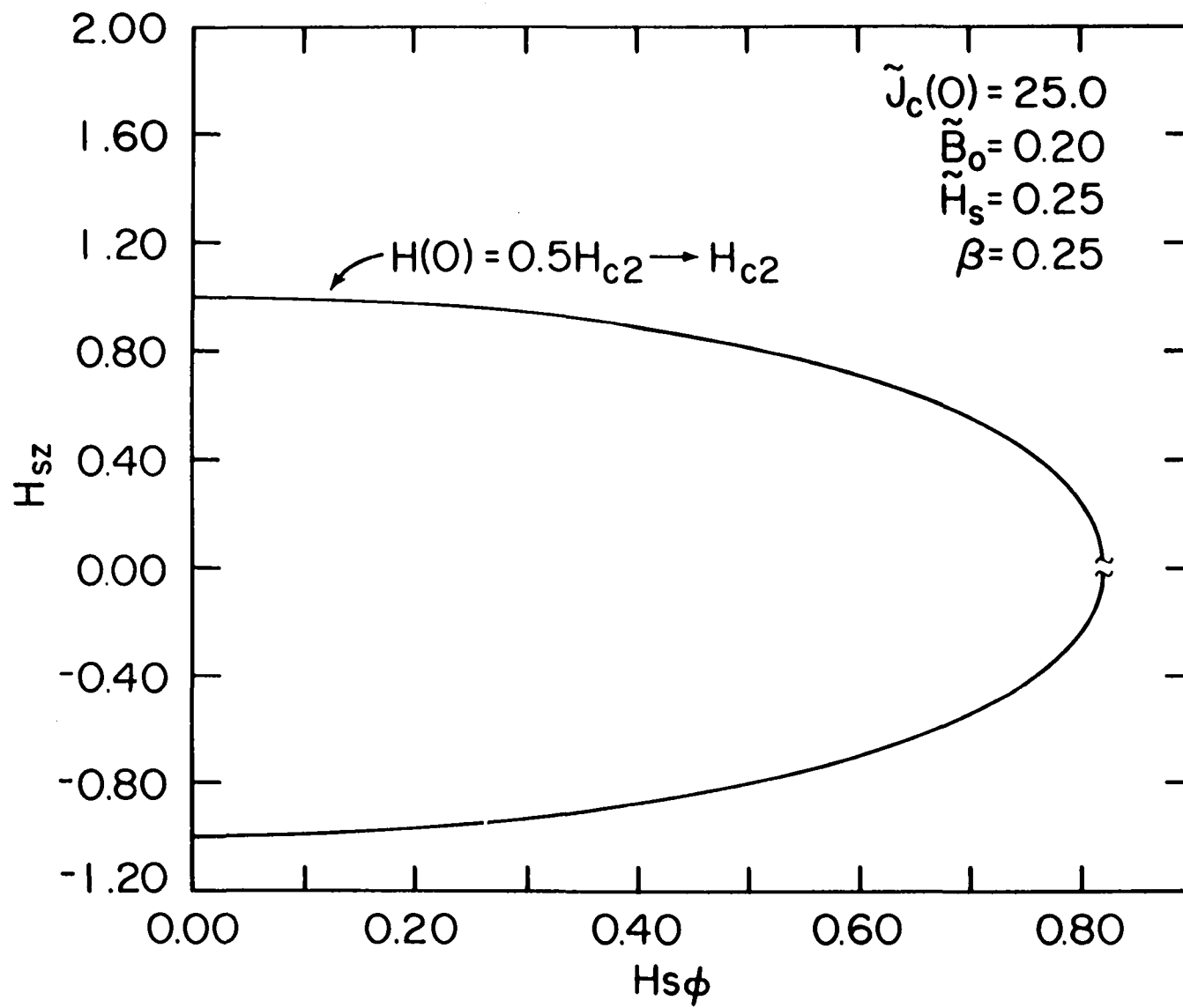


Figure 44. Summary of Figures 39-43, showing reduced surface field components required to yield a field on the axis of \tilde{H}_{c2} . Missing portions of each curve at $\tilde{H}_{sz} \approx 0$ indicate region where behavior is unknown

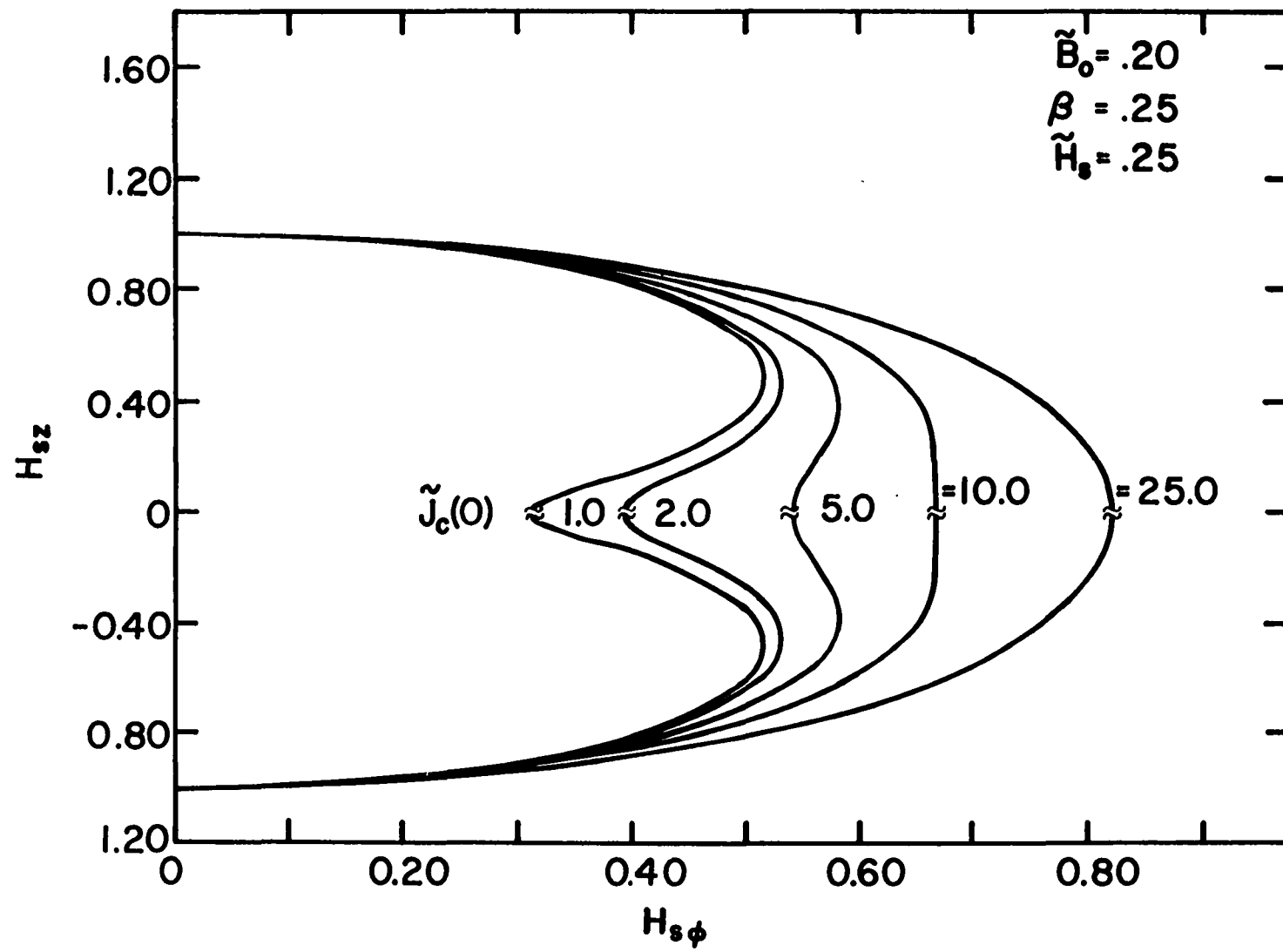


Figure 45. Influence of surface pinning on the reduced surface field components necessary to yield a field on the axis of \tilde{H}_{c2} . $\tilde{J}_c(0) = 1.0$, $\tilde{B}_0 = 0.20$, $\beta = 0.25$, and $\tilde{H}_S = 0.40$. Inner dashed circle represents a value of the surface field equal to \tilde{H}_{c1} ($= 0.25$). Outer solid circle represents a value of the surface field equal to \tilde{H}_S , the reduced surface barrier field ($= 0.40$). With the postulated amount of surface pinning, sample remains in Meissner state until $[H_{sz}^2 + H_{s0}^2]^{1/2}$ exceeds \tilde{H}_S . Region between lines a, b indicate region where behavior is unknown ($\alpha > 87.5^\circ$)

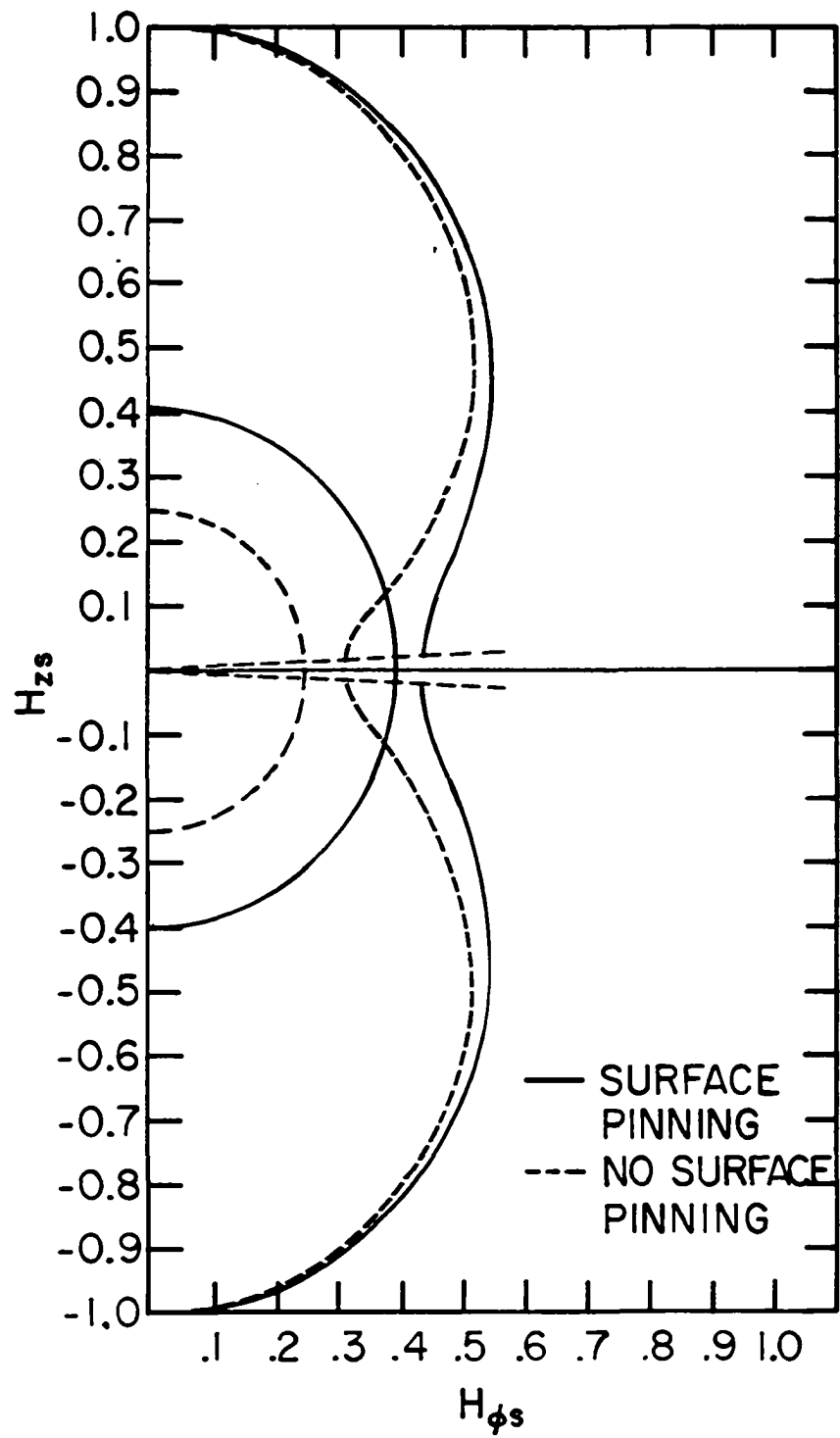


Figure 46. Reduced axial magnetization $\langle -4\pi\tilde{M}_z \rangle$ versus surface pitch angle α_s , for varying amounts of pinning strength. All curves apply to case where field on the axis is \tilde{H}_{c2} and therefore show greatest possible paramagnetic axial moment. Surface pinning was ignored. Relevant parameters are $\tilde{B}_0 = 0.20$, and $\beta = 0.25$

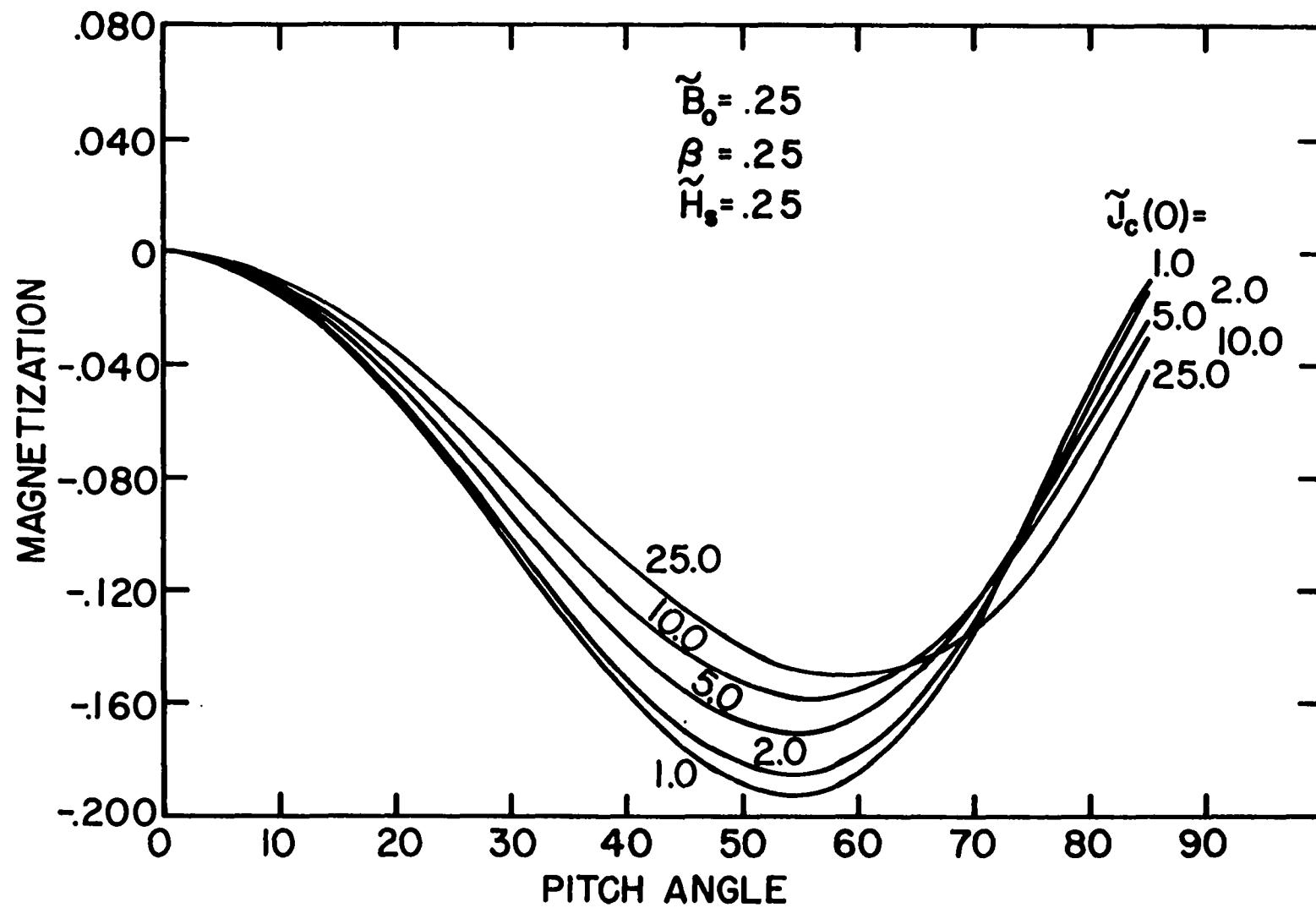


Figure 47. Field profiles \tilde{H} versus $\tilde{\rho}$ at a surface pitch angle of 15° , and at surface fields such that the field on the axis is \tilde{H}_{c2} . Five separate curves show the influence of varying amounts of bulk pinning strength. Surface pinning has been ignored, and $\beta = \tilde{H}_{c1} = 0.25$. These curves are the analog of Figure 27 for the weak pinning limit

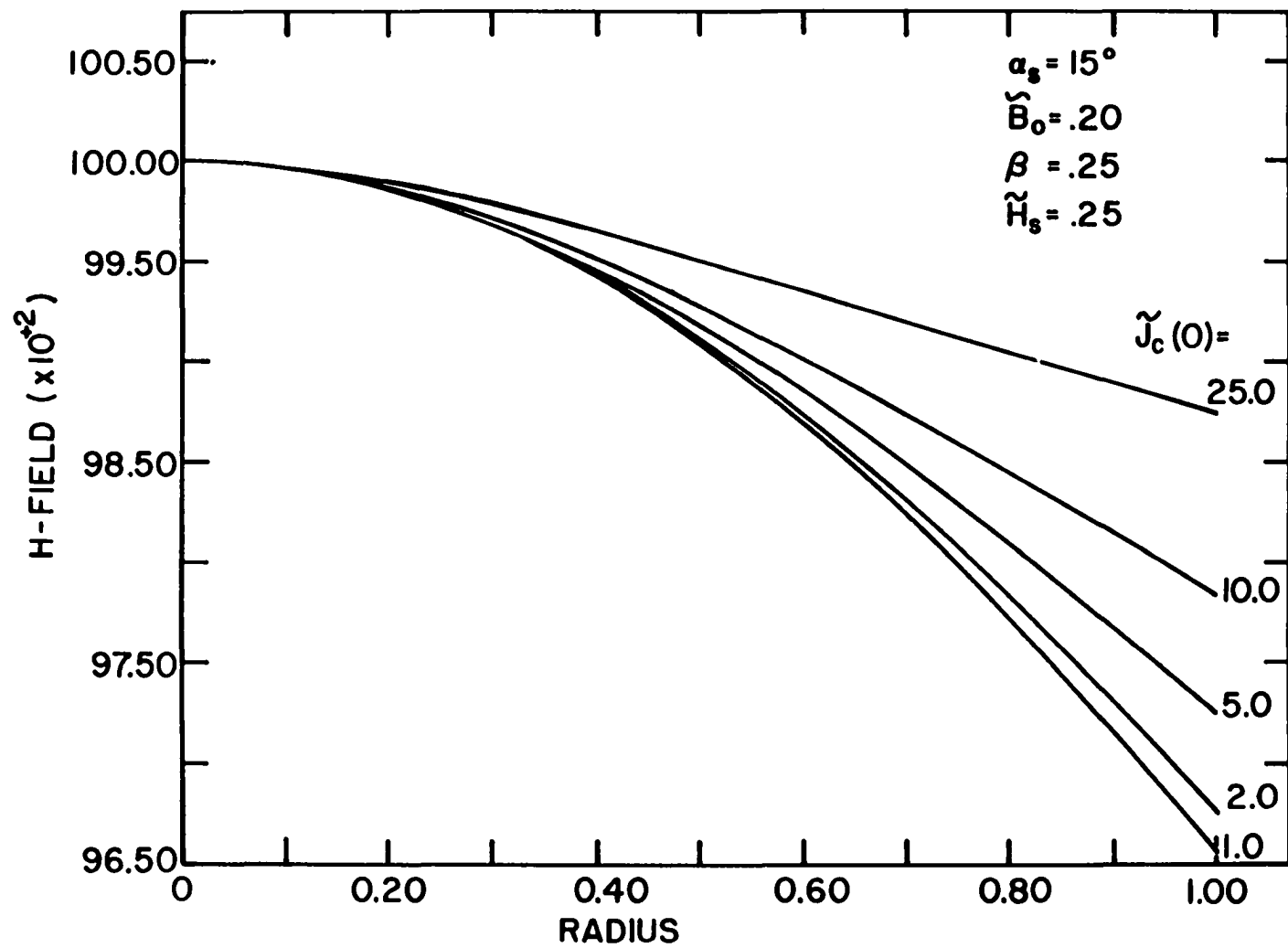


Figure 48. Reduced field profiles \tilde{H} versus $\tilde{\rho}$ at a surface pitch angle of 30° , and at surface fields such that the field on the axis is \tilde{H}_{c2} . Five separate curves show the influence of varying amounts of bulk pinning strength. Surface pinning has been ignored, and $\beta = \tilde{H}_{c1} = 0.25$. These curves are analogous to Figure 27 which describes the weak pinning limit. Also see Figure 47

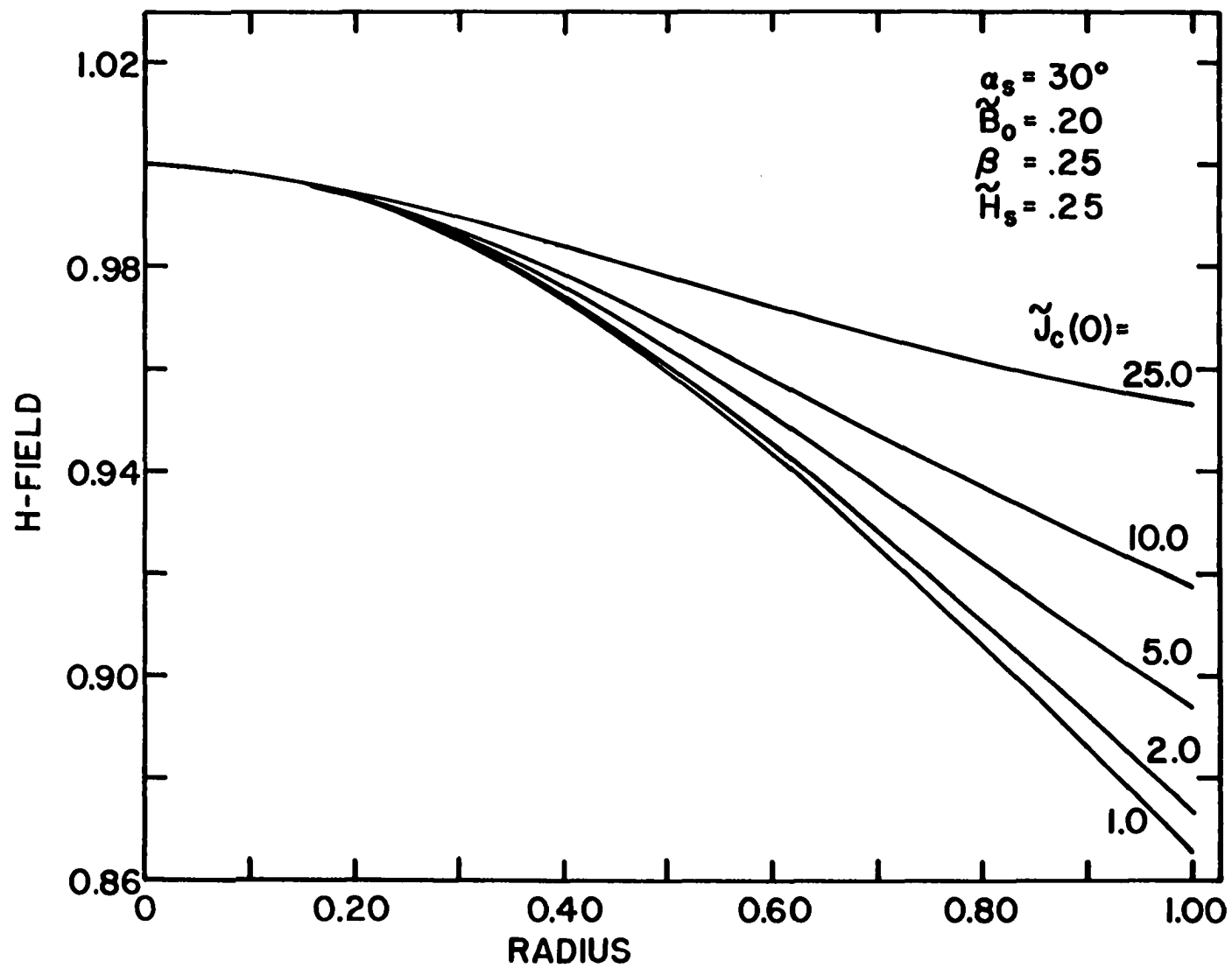


Figure 49. Reduced field profiles \tilde{H} versus $\tilde{\rho}$ at a surface pitch angle of 45° , and at surface fields such that the field on the axis is \tilde{H}_{c2} . Five separate curves show the influence of varying amounts of bulk pinning strength. Surface pinning has been ignored, and $\beta = \tilde{H}_{c1} = 0.25$. Also see Figures 47 and 48

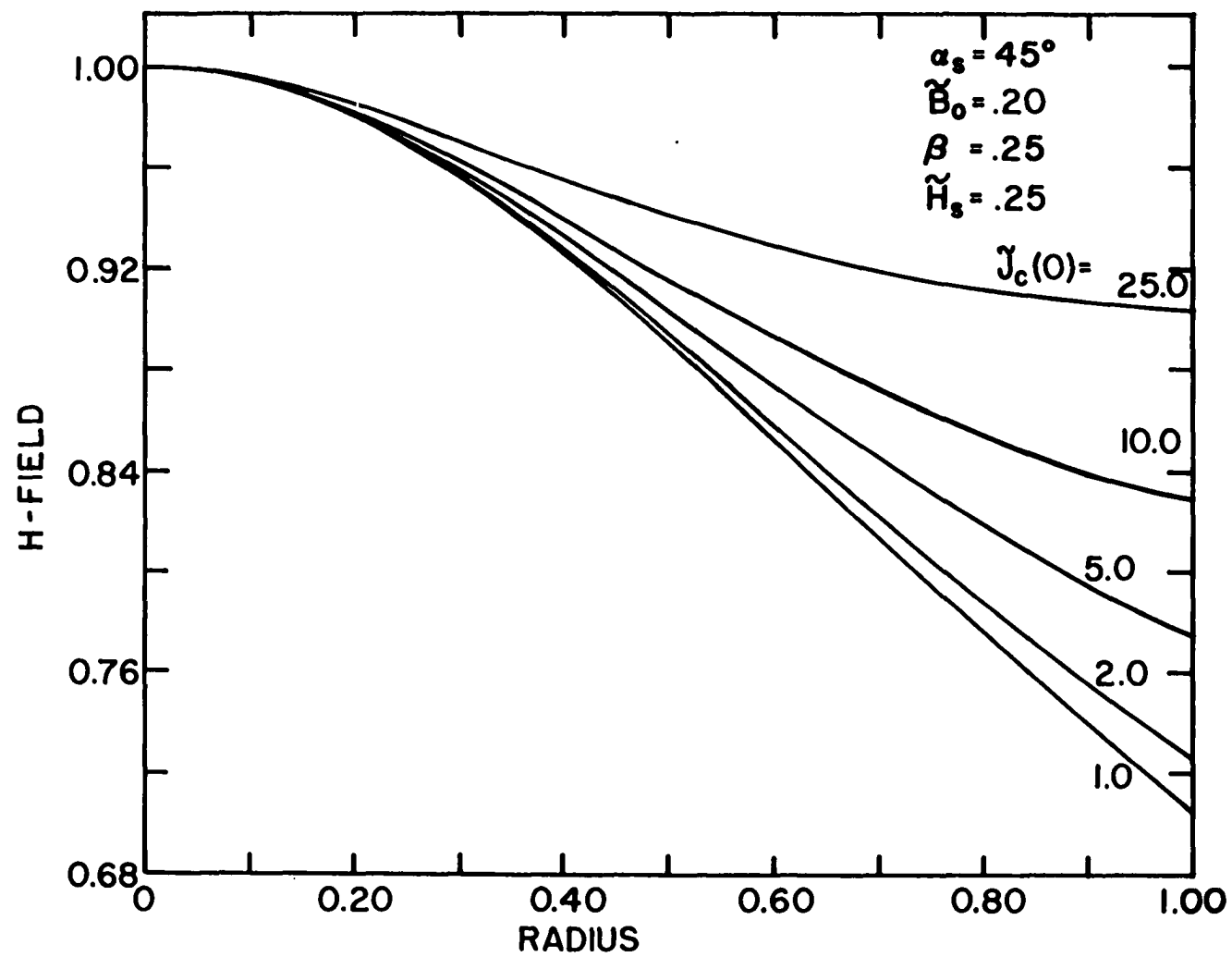


Figure 50. Reduced field profiles \tilde{H} versus $\tilde{\rho}$ at a surface pitch angle of 60° , and at surface fields such that the field on the axis is \tilde{H}_{c2} . Five separate curves show the influence of varying amounts of bulk pinning strength. Surface pinning has been ignored, and $\beta = \tilde{H}_{c1} = 0.25$. Also see Figures 47-49

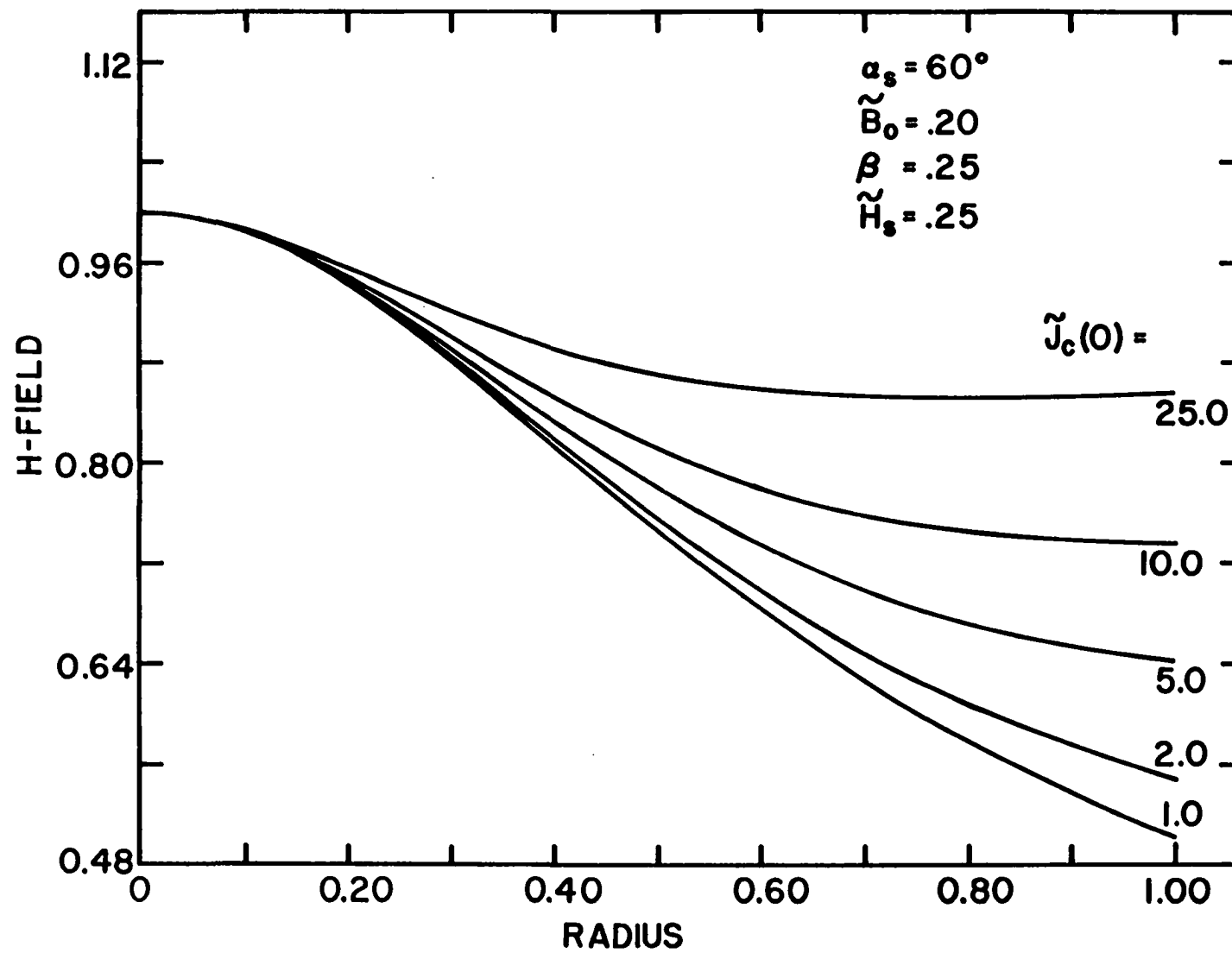


Figure 51. Reduced field profiles \tilde{H} versus $\tilde{\rho}$ at a surface pitch angle of 75° , and at surface fields such that the field on the axis is \tilde{H}_{c2} . Five separate curves show the influence of varying amounts of bulk pinning strength. Surface pinning has been ignored, and $\beta = \tilde{H}_{c1} = 0.25$. Also see Figures 47-50

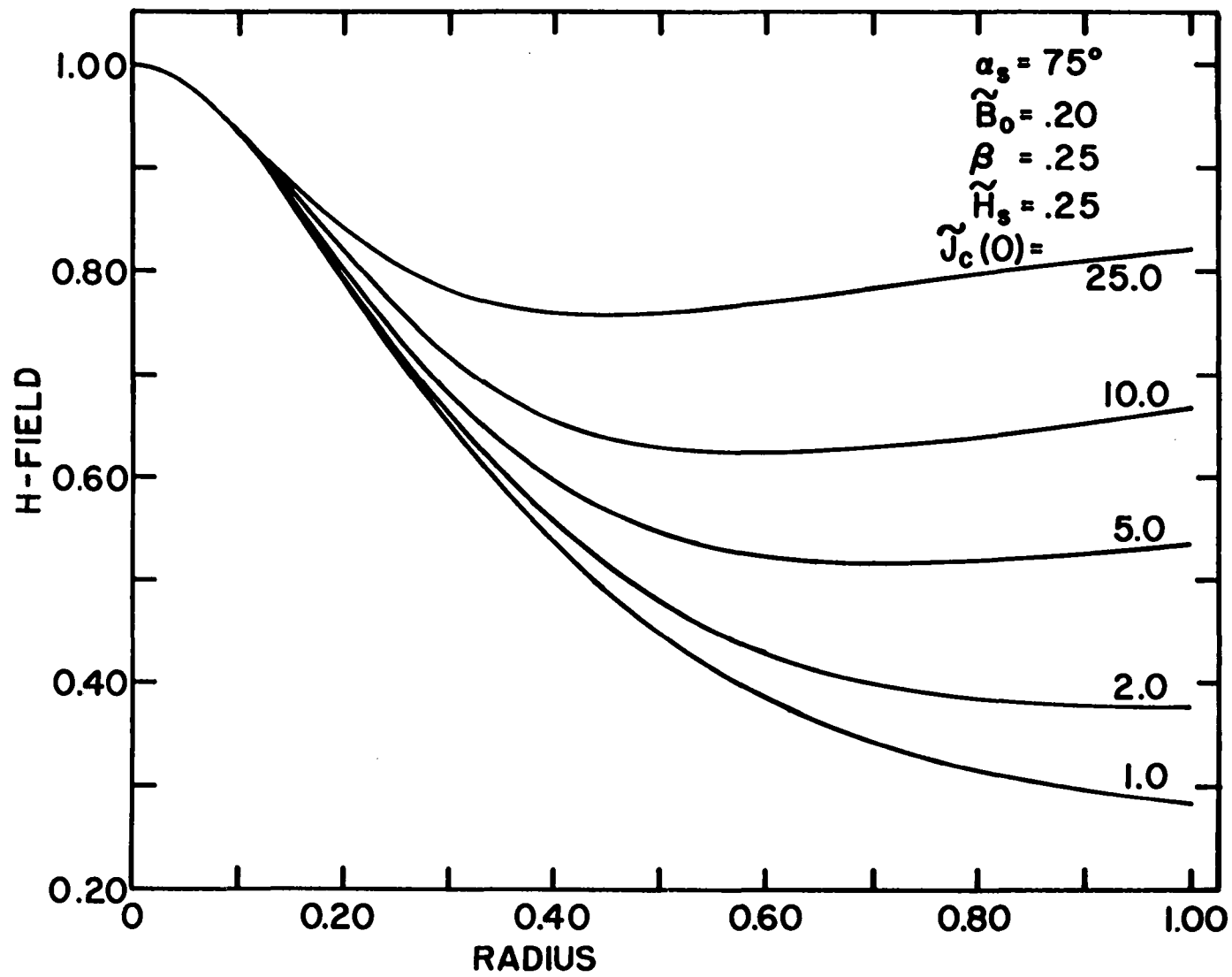


Figure 52. Hypothetical field profiles \tilde{H} versus $\tilde{\rho}$ at a surface pitch angle of 85° , analogous to Figures 47-51. Since portions of the curves for $\tilde{J}_c(0) = 1.0$ and 2.0 lie below \tilde{H}_{c1} , they indicate that because of spiral collapse (see Chapter III), no static solutions are possible. That is, spiral collapse instability would cause field to exceed H_{c2} , driving the sample into either the normal state, or into a flux-flow regime

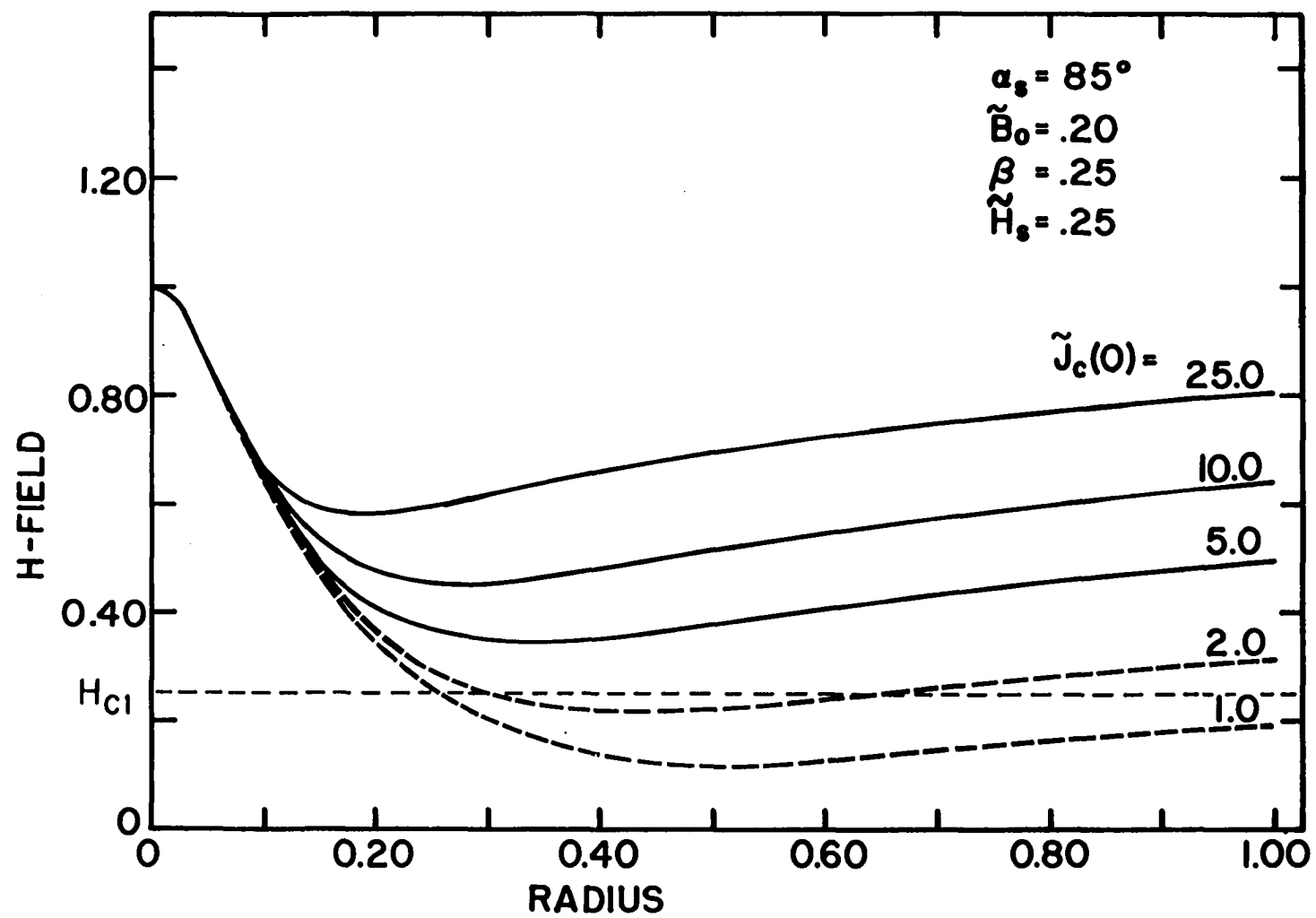


Figure 53. Reduced current density profiles showing the product $\tilde{B}\langle\tilde{j}_z\rangle$ versus $\tilde{\rho}$ at two different surface pitch angles, and at fields such that on the axis, $\tilde{H}(0) = \tilde{H}_{c2} = 1$. The five separate curves show influence of varying amounts of bulk pinning strength. Current density here is proportional to $\vec{\nabla}\times\vec{B}$ rather than $\vec{\nabla}\times\vec{H}$. Since $\partial\tilde{B}/\partial\tilde{\rho}$ is discontinuous at the flux front, $\langle\tilde{j}\rangle$ shows sharp spikes where $\tilde{B} \approx 0$. By plotting the product $\tilde{B}\langle\tilde{j}\rangle$, such singularities are removed, although at a sacrifice to the realization of the actual form of $\langle\tilde{j}\rangle$

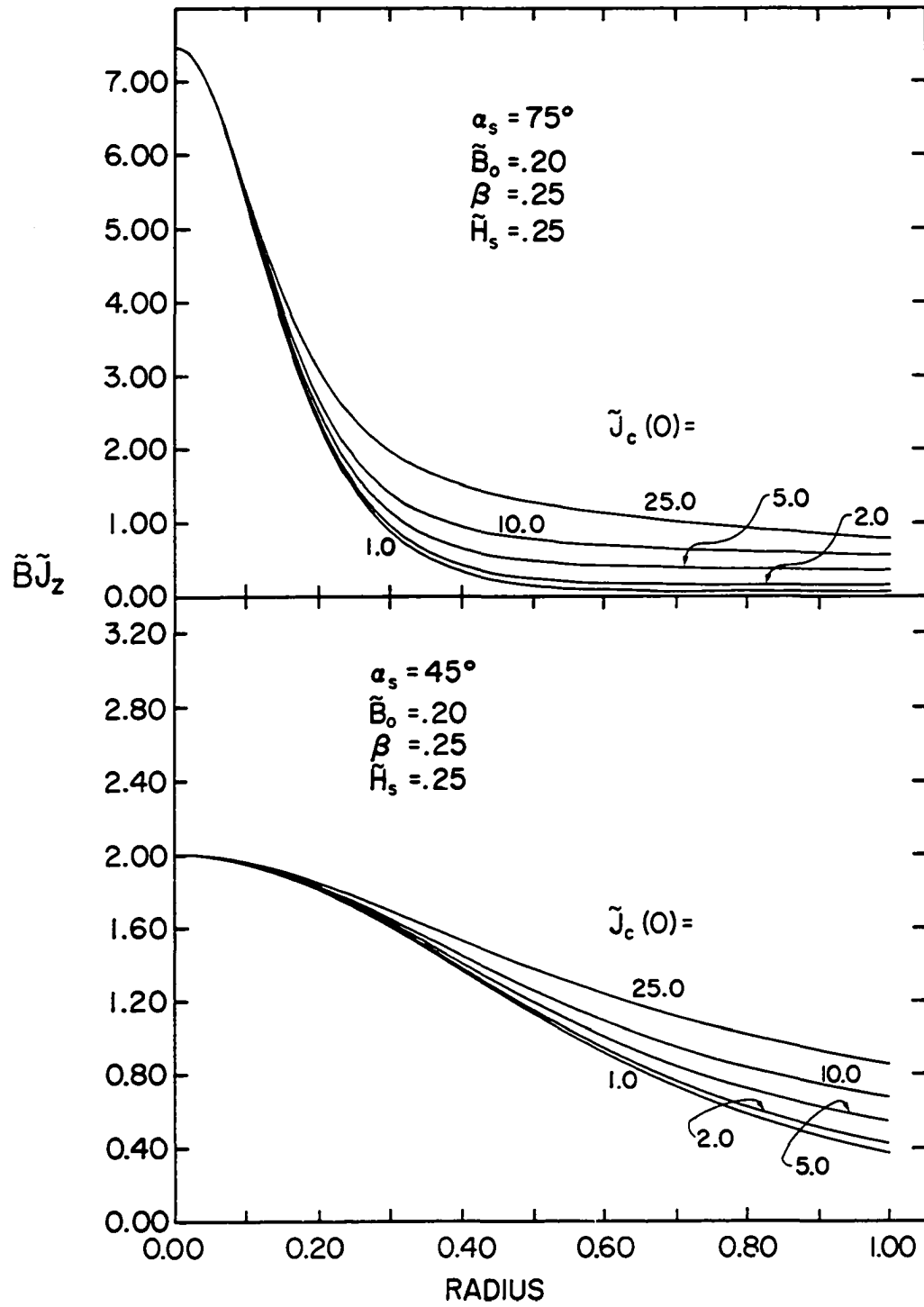


Figure 54. Reduced current density profiles showing the product $\tilde{B}\langle j_\theta \rangle$ versus $\tilde{\rho}$ at two different surface pitch angles, and at fields such that on the axis, $\tilde{H}(0) = \tilde{H}_{c2} = 1$. See caption for Figure 53

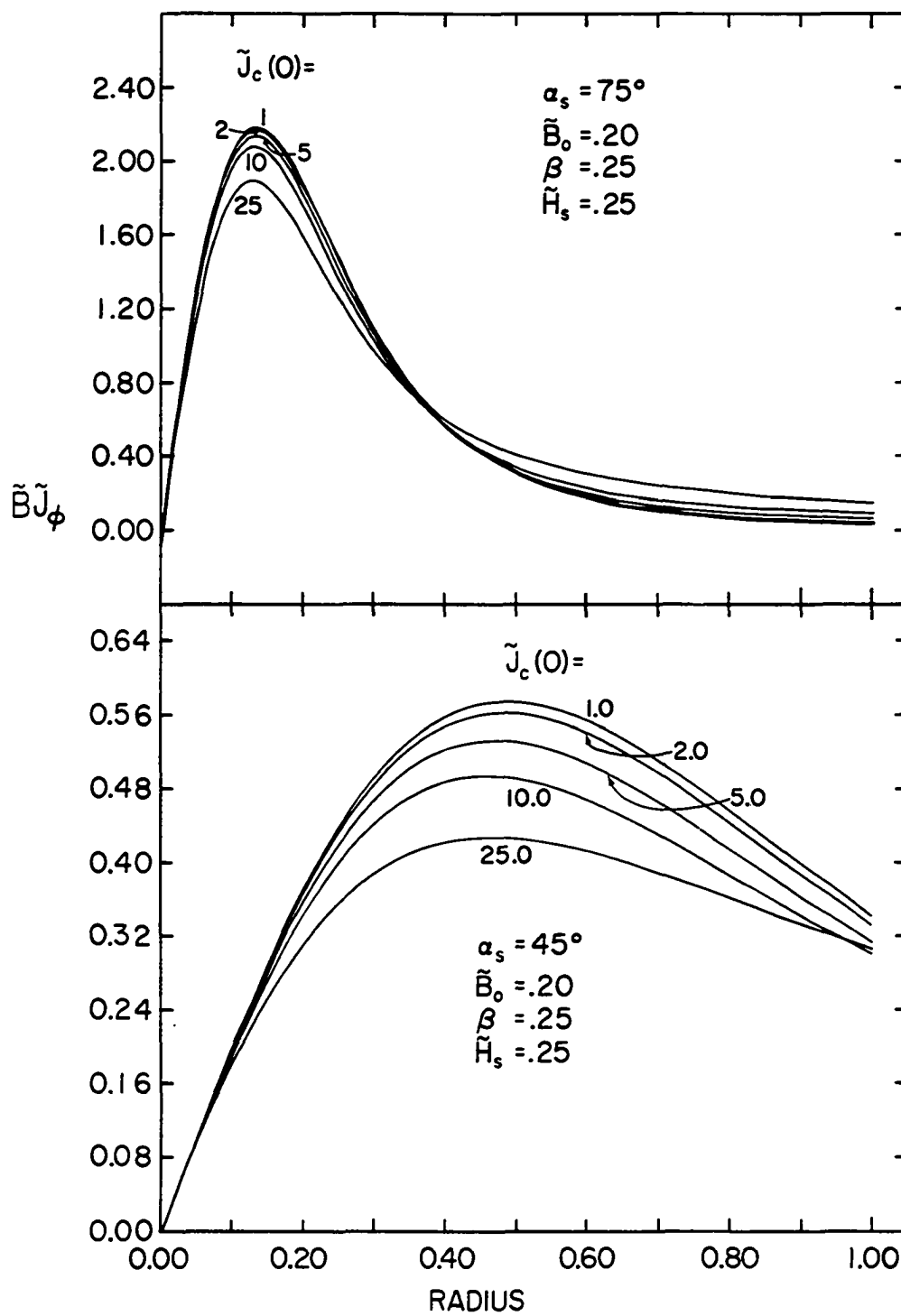
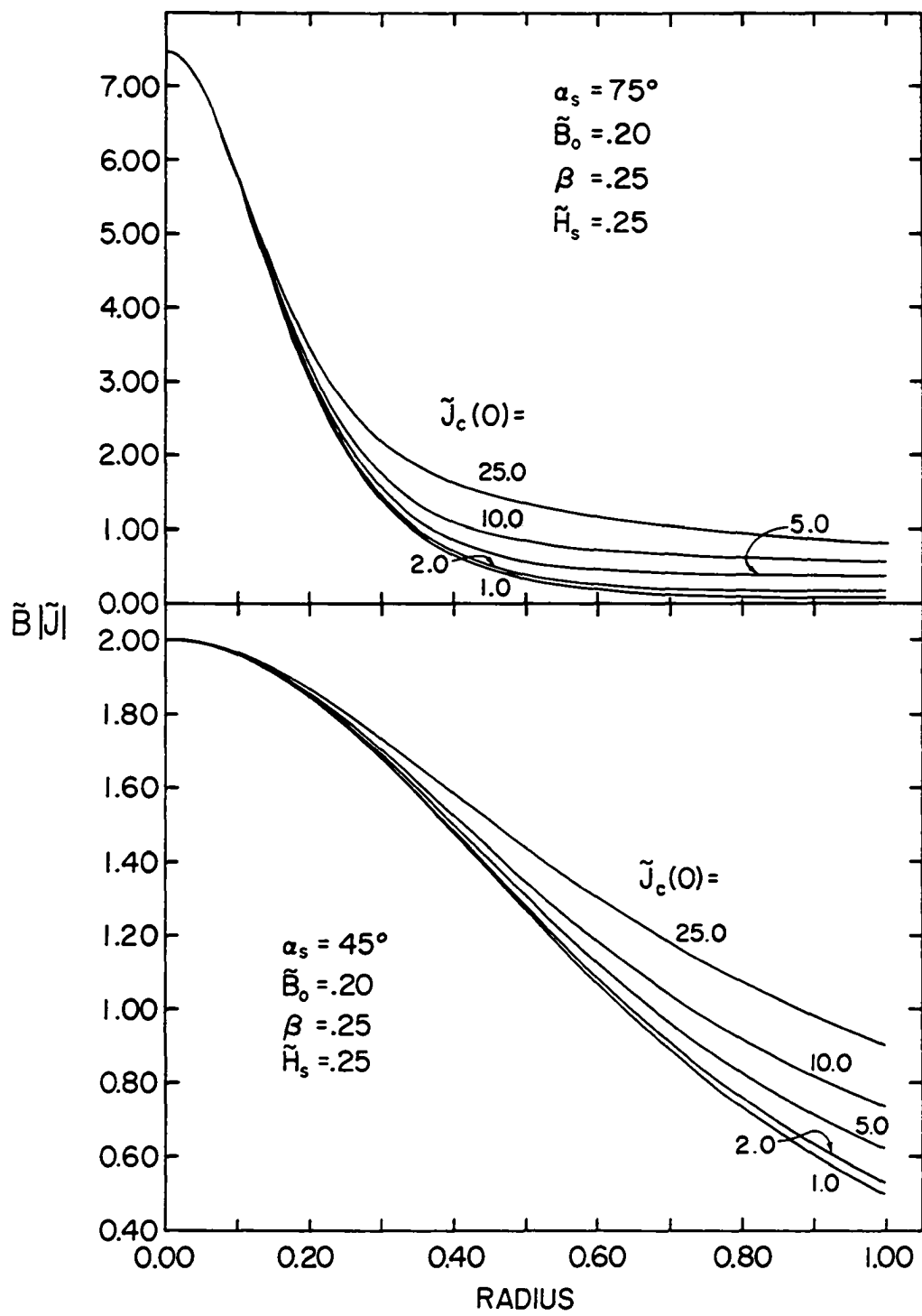


Figure 55. Reduced current density profiles showing the product of \tilde{B} and the magnitude of $\langle j \rangle$, at two different surface pitch angles, and at fields such that on the axis, $\tilde{H}(0) = \tilde{H}_{c2} = 1$. See Figures 53 and 54



The sharper curvature exhibited in the 75° case compared with the 45° case is indicative of the steeper flux gradients encountered in the former situation.

I. Comparison with Experiment

1. Magnetization

We compared our model to the published data of Timms and Walmsley (39), who obtained magnetization curves for two lead-bismuth cylinders under varying conditions of applied field and transport current. Their samples were Pb-56%Bi cast under vacuum in 3 mm inside diameter glass tubes. Axial field was supplied by a 0-6000 Oe superconducting solenoid, and a transport current was ramped from 0 to 1000 Amperes in synchronization with the source of the field. Surface pitch angle could be set to 2% accuracy in the ratio of H_ϕ/H_z . Figures 56 and 57 contain reproductions of their data for two samples with different histories of anneal, under conditions of zero transport current. We have labeled these Specimen #1 and Specimen #2. Figures 59 and 59 are reproductions of their data for the same two samples, under conditions of nonzero transport current. The symbol C on these curves represents the tangent of the surface pitch angle ($H_{s\phi}/H_{sz}$). We have superimposed our results on the above plots in order to compare their data and our model.

Figure 56. Reproduction of Timms and Walmsley (39) magnetization data for Specimen #1, together with calculated magnetization curve derived from two-parameter least-squares fitting of Timms and Walmsley data

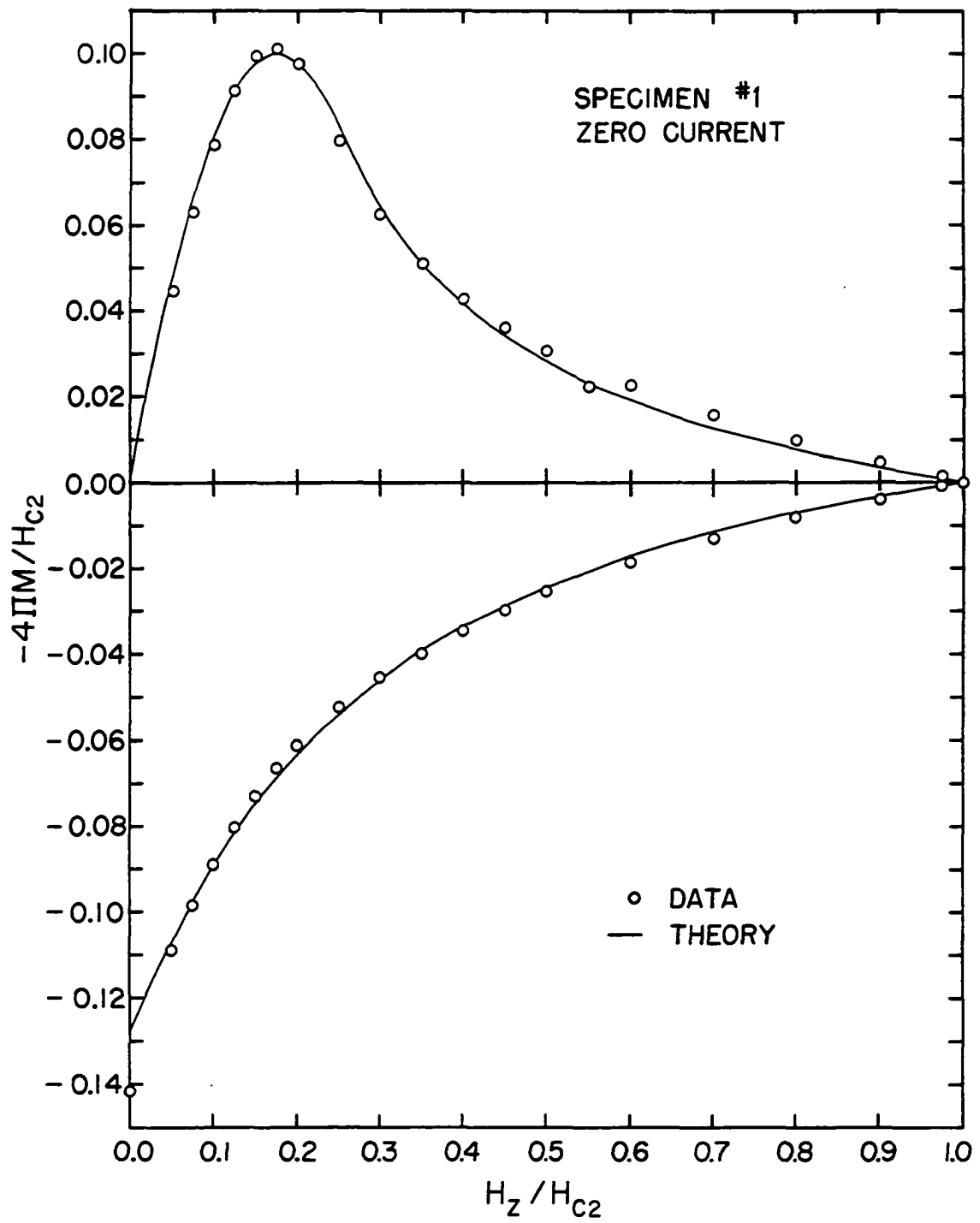


Figure 57. Reproduction of Timms and Walmsley (39) magnetization data for Specimen #2, together with calculated magnetization curve derived from two-parameter least-squares fitting of Timms and Walmsley data

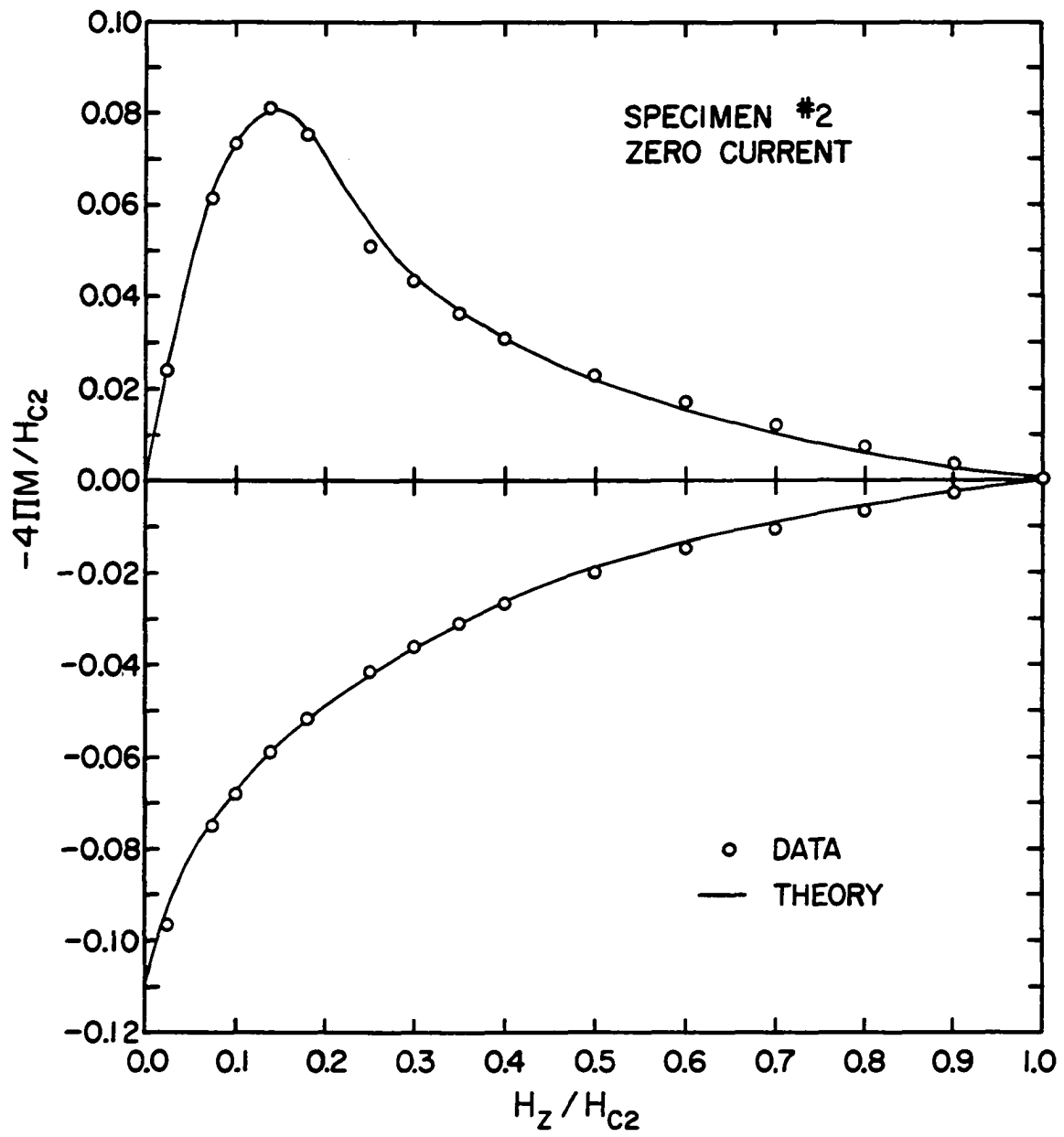


Figure 58. Reproduction of Timms and Walmsley (39) magnetization data for Specimen #1, together with calculated magnetization curve derived from three-parameter least-squares fitting of data in Figure 56. Various C values denote tangent of the surface pitch angle

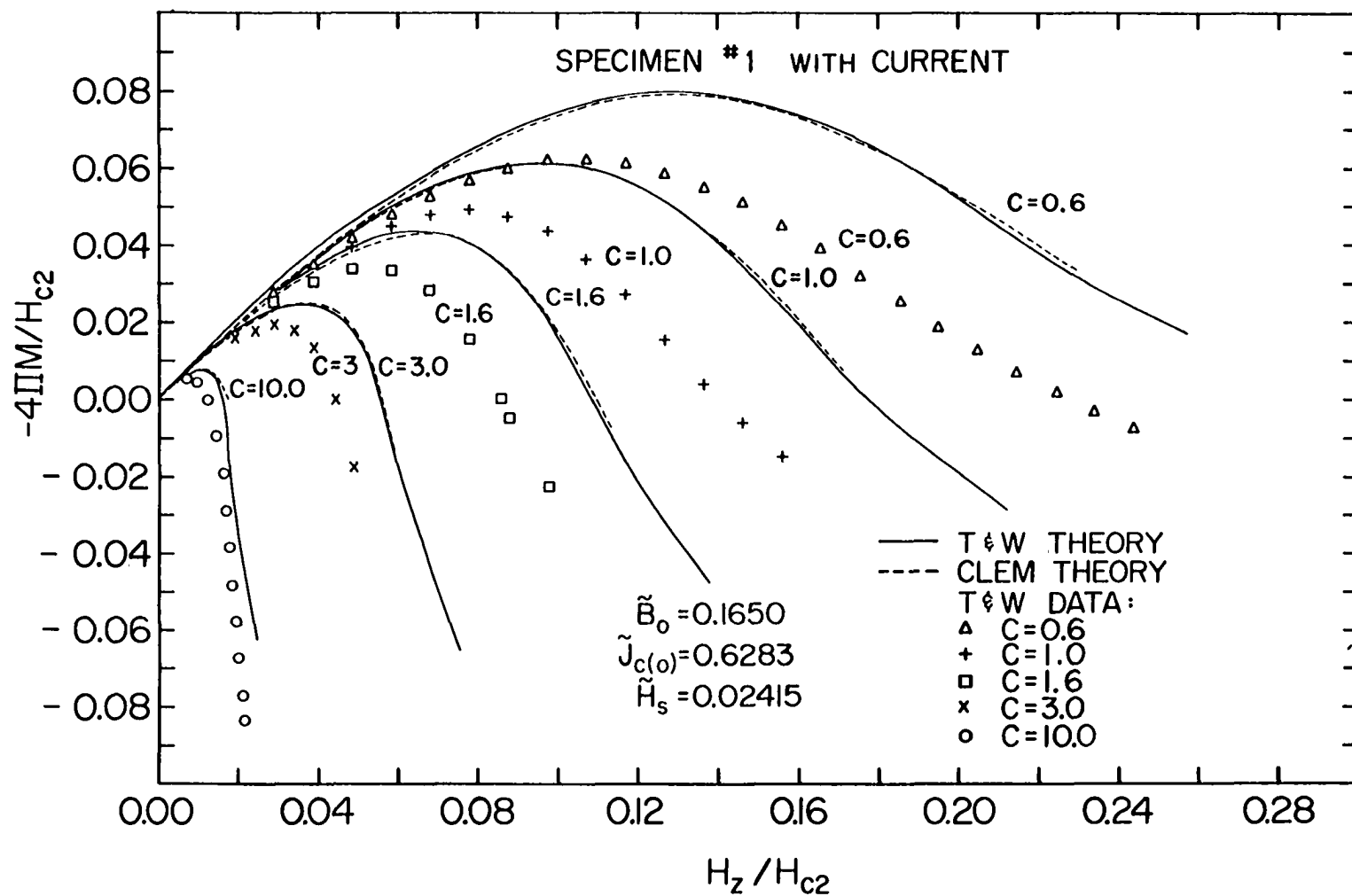


Figure 59. Reproduction of Timms and Walmsley (39) magnetization data for Specimen #2, together with calculated magnetization curve derived from three-parameter least-squares fitting of data in Figure 57. Various C values denote tangent of the surface pitch angle

Timms and Walmsley (39) give no measured value for the lower critical fields H_{c1} of the two samples, although H_{c2} was measured to be 5650 Oe, presumably for both samples. Voight (46) cites values for κ in lead-bismuth averaging about 14, which suggests a value for β ($= H_{c1}/H_{c2}$) of about 0.024, using our model for $\beta(\kappa)$.

In attempting to model their experimental results, our approach was to employ a fitting program to obtain appropriate values of $\tilde{J}_c(0)$ and \tilde{B}_0 for the critical current, using their zero current magnetization data (Figures 56 and 57). Later, we varied the third parameter, \tilde{H}_S , to account for surface pinning. Tables 2 and 3 show the magnetization values as read from Timms and Walmsley's (39) curves using a millimeter rule and appropriate scaling. The fitting program varied $\tilde{J}_c(0)$ and \tilde{B}_0 until the mean square difference between the calculated magnetization curves and the experimental magnetization curves were a minimum. The fitting was accomplished by regarding the flux-entering magnetization curve and the flux-exiting curve as one folded curve. Tables 4 and 5 show the results of the fitting, assuming zero surface pinning. In effecting the fitting, the surface field H_{SZ} was modeled by Equation 2.34 in the flux-entering portions, and by Equation 2.35 in the flux-exiting portion.

After the parameters $\tilde{J}_c(0)$ and \tilde{B}_0 were obtained, comparison was made with the Timms and Walmsley's (39) nonzero

current magnetization curves. Preliminary comparisons with their magnetization curves indicated a poor agreement with their results; it was therefore hypothesized that the discrepancies were due to surface pinning. We then attempted a three-parameter fit to the zero-current magnetization data, where now the surface pinning parameter \tilde{H}_S was a variable, along with $\tilde{J}_c(0)$ and \tilde{B}_0 . Tables 6 and 7 show the results of the three-parameter fittings, and Figures 58 and 59 summarize our model comparison with Timms and Walmsley's data. Under conditions of nonzero current, our model predicts a significantly greater value of $-4\pi M_z$ than is actually measured. The Walmsley and Timms' theory referred to in Figures 58 and 59 is based on a differential equation of the form

$$\tilde{B}d\tilde{B}/d\rho = \pm \omega R \tilde{B}^{1/2}[1 - \tilde{B}] \quad (2.91)$$

where ω is a pinning force density parameter and R is the cylinder radius. They assume a pinning force density relation of the form

$$F_p(\tilde{B}) = \omega \tilde{B}^{1/2}[1 - \tilde{B}] \quad (2.92)$$

and their model ignores surface barriers. The model of Equation 2.92 cannot be valid in the limit as \tilde{B} approaches zero, because it yields a pinning force per unit length which diverges as $\tilde{B}^{-1/2}$ in this limit.

Table 2. Timms and Walmsley's (39) data for Specimen #1

Point no.	Reduced applied field H_{sz}/H_{c2}	$-4\pi M/H_{c2}$ flux entering	$-4\pi M/H_{c2}$ flux exiting
1	0.0	0.0	-0.1415
2	0.05	0.0446	-0.1089
3	0.100	0.0787	-0.0890
4	0.125	0.0912	-0.0801
5	0.150	0.0993	-0.0730
6	0.175	0.1010	-0.0665
7	0.200	0.0976	-0.0612
8	0.250	0.0796	-0.0525
9	0.300	0.0628	-0.0458
10	0.350	0.0510	-0.0400
11	0.400	0.0428	-0.0348
12	0.450	0.0360	-0.0299
13	0.500	0.0307	-0.0257
14	0.600	0.0221	-0.0187
15	0.700	0.0154	-0.0130
16	0.800	0.0097	-0.0081
17	0.900	0.0046	-0.0039
18	0.975	0.0012	-0.0009

Table 3. Timms and Walmsley's (39) data for Specimen #2

Point no.	Reduced applied field H_{sz}/H_{c2}	$-4\pi M/H_{c2}$ flux entering	$-4\pi M/H_{c2}$ flux exiting
1	0.0	0.0	-0.1095
2	0.05	0.0443	-0.0851
3	0.075	0.0618	-0.0758
4	0.100	0.0735	-0.0683
5	0.125	0.0793	-0.0622
6	0.150	0.0801	-0.0575
7	0.175	0.0767	-0.0525
8	0.200	0.0700	-0.0482
9	0.250	0.0535	-0.0418
10	0.300	0.0435	-0.0362
11	0.350	0.0365	-0.0313
12	0.400	0.0310	-0.0271
13	0.450	0.0266	-0.0232
14	0.500	0.0228	-0.0200
15	0.600	0.0162	-0.0163
16	0.700	0.0112	-0.0112
17	0.800	0.0070	-0.0070
18	0.900	0.0032	-0.0032
19	0.975	0.0008	-0.0009

Table 4. Results of fitting theoretical curve to Timms and Walmsley's data Specimen #1, no surface pinning^a

Point no.	Applied field X_i	Experimental magnetization Y_i	Calculated magnetization Z_i
1	0.024	0.024	0.024
2	0.050	0.0446	0.0474
3	0.075	0.0630	0.0669
4	0.100	0.0787	0.0809
5	0.125	0.0912	0.0916
6	0.150	0.0993	0.0979
7	0.175	0.1010	0.1001
8	0.200	0.0976	0.0972
9	0.250	0.0796	0.0823
10	0.300	0.0628	0.0637
11	0.350	0.0510	0.0510
12	0.400	0.0428	0.0417
13	0.450	0.0360	0.0344
14	0.500	0.0307	0.0285
15	0.600	0.0221	0.0195
16	0.700	0.0154	0.0128
17	0.800	0.0097	0.0076
18	0.900	0.0046	0.0034
19	0.975	0.0012	0.0008

^aFinal values of variable parameters:

$$\tilde{B}_0 = 0.1663$$

$$\tilde{J}_c(0) = 0.6253 .$$

Values of fixed parameters:

$$\tilde{B}_s = 0.024$$

$$H_s = 0.024 .$$

Average of squared deviations:

$$0.0313 \times 10^{-4} = \frac{1}{38} \sum_{i=1}^{38} (Y_i - Z_i)^2 .$$

Table 4 (Continued)

Point no.	Applied field X_i	Experimental magnetization Y_i	Calculated magnetization Z_i
20	0.975	-0.0009	-0.0007
21	0.900	-0.0039	-0.0032
22	0.800	-0.0081	-0.0070
23	0.700	-0.0130	-0.0116
24	0.600	-0.0187	-0.0172
25	0.500	-0.0257	-0.0244
26	0.450	-0.0299	-0.0288
27	0.400	-0.0348	-0.0338
28	0.350	-0.0400	-0.0395
29	0.300	-0.0458	-0.0462
30	0.250	-0.0525	-0.0542
31	0.200	-0.0612	-0.0635
32	0.175	-0.0665	-0.0690
33	0.150	-0.0730	-0.0750
34	0.125	-0.0801	-0.0817
35	0.100	-0.0890	-0.0891
36	0.075	-0.0983	-0.0974
37	0.050	-0.1089	-0.1071
38	0.0	-0.1415	-0.1377

Table 5. Results of fitting theoretical curve to Timms and Walmsley's data Specimen #2, no surface pinning^a

Point no.	Applied field X_i	Experimental magnetization Y_i	Calculated magnetization Z_i
1	0.024	0.024	0.024
2	0.050	0.0443	0.0467
3	0.075	0.0618	0.0619
4	0.100	0.0735	0.0728
5	0.125	0.0793	0.0788
6	0.150	0.0801	0.0800
7	0.175	0.0767	0.0769
8	0.200	0.0700	0.0708
9	0.250	0.0535	0.0558
10	0.300	0.0435	0.0454
11	0.350	0.0365	0.0376
12	0.400	0.0310	0.0314
13	0.450	0.0266	0.0263
14	0.500	0.0228	0.0220
15	0.600	0.0162	0.0153
16	0.700	0.0112	0.0102
17	0.800	0.0070	0.0061
18	0.900	0.0032	0.0028
19	0.975	0.0008	0.0006

^aFinal values of variable parameters:

$$\tilde{B}_0 = 0.2274$$

$$\tilde{J}_c(0) = 0.3916 \quad .$$

Values of fixed parameters:

$$\beta = 0.024$$

$$\tilde{H}_s = 0.024 \quad .$$

Average of squared deviations:

$$0.0135 \times 10^{-4} = \frac{1}{38} \sum_{i=1}^{38} [Y_i - Z_i]^2 \quad .$$

Table 5 (Continued)

Point no.	Applied field X_i	Experimental magnetization Y_i	Calculated magnetization Z_i
20	0.975	-0.0009	-0.0006
21	0.900	-0.0032	-0.0026
22	0.800	-0.0070	-0.0056
23	0.700	-0.0112	-0.0093
24	0.600	-0.0163	-0.0138
25	0.500	-0.0200	-0.0194
26	0.450	-0.0232	-0.0228
27	0.400	-0.0271	-0.0267
28	0.350	-0.0313	-0.0311
29	0.300	-0.0362	-0.0362
30	0.250	-0.0418	-0.0421
31	0.200	-0.0482	-0.0492
32	0.175	-0.0525	-0.0532
33	0.150	-0.0575	-0.0576
34	0.125	-0.0622	-0.0626
35	0.100	-0.0683	-0.0680
36	0.075	-0.0758	-0.0743
37	0.050	-0.0851	-0.0816
38	0.0	-0.1095	-0.1084

Table 6. Results of fitting theoretical curve to Timms and Walmsley's data Specimen #1, with surface pinning^a

Point no.	Applied field X_i	Experimental magnetization Y_i	Calculated magnetization Z_i
1	0.050	0.0446	0.0474
2	0.075	0.0630	0.0669
3	0.100	0.0787	0.0810
4	0.125	0.0912	0.0917
5	0.150	0.0993	0.0980
6	0.175	0.1010	0.1002
7	0.200	0.0976	0.0973
8	0.250	0.0796	0.0824
9	0.300	0.0628	0.0638
10	0.350	0.0510	0.0510
11	0.400	0.0428	0.0417
12	0.450	0.0360	0.0344
13	0.500	0.0307	0.0285
14	0.600	0.0221	0.0194
15	0.700	0.0154	0.0127
16	0.800	0.0097	0.0076
17	0.900	0.0046	0.0034
18	0.975	0.0012	0.0008

^aFinal values of variable parameters:

$$\tilde{B}_0 = 0.1651$$

$$\tilde{J}_c(0) = 0.6283$$

$$\tilde{H}_s = 0.02415 \text{ .}$$

Value of fixed parameter:

$$\beta = 0.024 \text{ .}$$

Average of squared deviations:

$$0.0322 \times 10^{-4} = \frac{1}{37} \sum_{i=1}^{37} [Y_i - Z_i]^2 \text{ .}$$

Table 6 (Continued)

Point no.	Applied field X_i	Experimental magnetization Y_i	Calculated magnetization Z_i
19	0.975	-0.0009	-0.0007
20	0.900	-0.0039	-0.0032
21	0.800	-0.0081	-0.0070
22	0.700	-0.0130	-0.0115
23	0.600	-0.0187	-0.0172
24	0.500	-0.0257	-0.0244
25	0.450	-0.0299	-0.0288
26	0.400	-0.0348	-0.0337
27	0.350	-0.0400	-0.0395
28	0.300	-0.0458	-0.0462
29	0.250	-0.0525	-0.0542
30	0.200	-0.0612	-0.0636
31	0.175	-0.0665	-0.0691
32	0.150	-0.0730	-0.0751
33	0.125	-0.0801	-0.0817
34	0.100	-0.0890	-0.0891
35	0.075	-0.0983	-0.0975
36	0.050	-0.1089	-0.1072
37	0.0	-0.1415	-0.1379

Table 7. Results of fitting theoretical curve to Timms and Walmsley's data Specimen #2, with surface pinning^a

Point no.	Applied field X_i	Experimental magnetization Y_i	Calculated magnetization Z_i
1	0.050	0.0443	0.0468
2	0.075	0.0618	0.0620
3	0.100	0.0735	0.0730
4	0.125	0.0793	0.0790
5	0.150	0.0801	0.0805
6	0.175	0.0767	0.0771
7	0.200	0.0700	0.0710
8	0.250	0.0535	0.0558
9	0.300	0.0435	0.0453
10	0.350	0.0365	0.0375
11	0.400	0.0310	0.0313
12	0.450	0.0266	0.0262
13	0.500	0.0228	0.0220
14	0.600	0.0162	0.0152
15	0.700	0.0112	0.0101
16	0.800	0.0070	0.0060
17	0.900	0.0032	0.0027
18	0.975	0.0008	0.0006

^aFinal values of variable parameters:

$$\tilde{B}_0 = 0.2235$$

$$\tilde{J}_c(0) = 0.3946$$

$$\tilde{H}_s = 0.02446 \quad .$$

Value of fixed parameter:

$$\beta = 0.024 \quad .$$

Average of squared deviations:

$$0.0138 \times 10^{-4} = \frac{1}{37} \sum_{i=1}^{37} [Y_i - Z_i]^2 \quad .$$

Table 7 (Continued)

Point no.	Applied field X_i	Experimental magnetization Y_i	Calculated magnetization Z_i
19	0.975	-0.0009	-0.0006
20	0.900	-0.0032	-0.0026
21	0.800	-0.0070	-0.0056
22	0.700	-0.0112	-0.0093
23	0.600	-0.0163	-0.0138
24	0.500	-0.0200	-0.0194
25	0.450	-0.0232	-0.0227
26	0.400	-0.0271	-0.0266
27	0.350	-0.0313	-0.0310
28	0.300	-0.0362	-0.0361
29	0.250	-0.0418	-0.0420
30	0.200	-0.0482	-0.0491
31	0.175	-0.0525	-0.0532
32	0.150	-0.0575	-0.0576
33	0.125	-0.0622	-0.0626
34	0.100	-0.0683	-0.0681
35	0.075	-0.0758	-0.0744
36	0.050	-0.0851	-0.0817
37	0.0	-0.1095	-0.1087

2. Current

Timms and Walmsley (39) measured, for each specimen, the normalization current, defined to be the current at which the sample reverts to the normal state. Figure 60 shows a comparison between their experimental normalization currents and the predictions of our model, where both curves are normalized according to a unit of current defined to be

$$I_f = \frac{1}{4}caH_{c2} \quad . \quad (2.93)$$

With an H_{c2} of 5650 Oe and a sample radius of 1.5 mm, the unit of current I_f is 2119 A. We calculate the normalization current by determining the magnitude of the surface field, H_s , at which the field inside the cylinder first reaches H_{c2} . The normalization current is related to H_s via

$$2I_z/ca = H_s\theta = H_s \sin\alpha_s \quad ,$$

$$I_z = \frac{1}{2}caH_s \sin\alpha_s \quad , \quad (2.94)$$

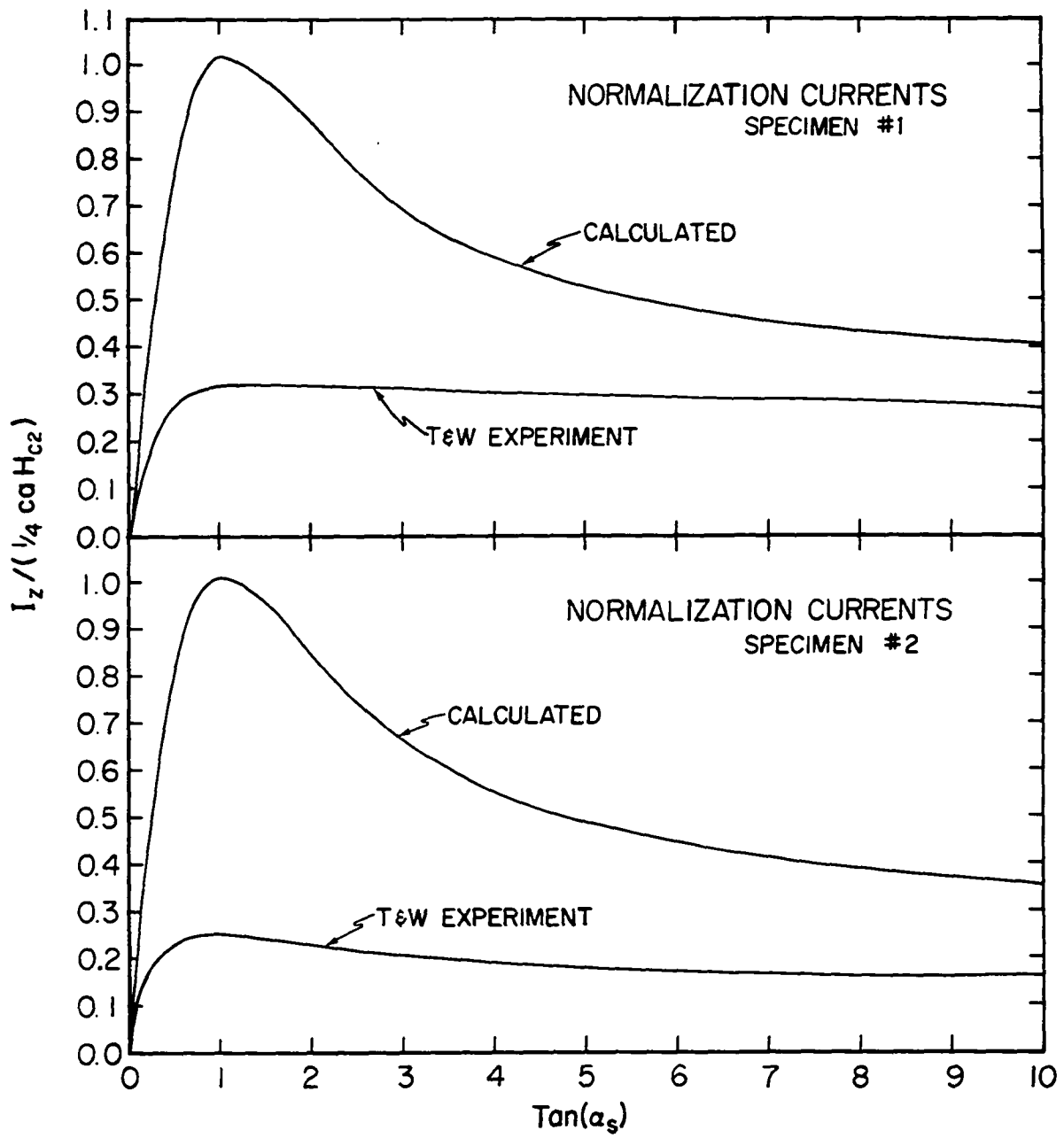
so that in reduced form,

$$\begin{aligned} \tilde{I}_z &= I_z/I_f \\ &= 2\tilde{H}_s \sin\alpha_s \quad . \end{aligned} \quad (2.95)$$

Figure 60 shows that the predicted values for the normalization current does not compare well with the measured

values. At present we have no reasonable explanation for the large discrepancies. However, one would expect reduced normalization currents if the applied current and field were brought to final values too quickly for the sample to remain at one temperature.

Figure 60. Experimental and theoretical reduced normalization currents versus tangent of the surface pitch angle, for the two specimens of Timms and Walmsley (39)



III. SPIRAL COLLAPSE INSTABILITY

A. Introduction

Our basic differential Equation 2.14 relating $H_{eq}(B)$ and the radius ρ displays an unusual feature when written in the form

$$\frac{\partial H}{\partial \rho} = H(B) \cdot [\rho_c^{-1}(B) - R_c^{-1}(\rho)] \quad , \quad (3.1)$$

where $\rho_c(B)$, defined as

$$\rho_c(B) = cH(B)/4\pi J_c(B) \quad , \quad (3.2)$$

may be called the field-dependent critical radius. We see immediately that a fortuitous combination of parameters might lead to the condition where $\rho_c(B) > R_c(\rho)$, resulting in $\partial H/\partial \rho$ less than zero. This is in marked contrast to the critical state model for straight vortex lines, which predicts that $\partial H/\partial \rho$ is always positive in the flux-entering case. As one may easily demonstrate, a negative $\partial H/\partial \rho$ is usually associated with a paramagnetic longitudinal moment, and can also lead to a sudden catastrophic collapse of flux spirals.

Before discussing the physical arguments describing the collapse, we first define two quantities, ρ_+ and ρ_- , which will be needed in that discussion. ρ_+ and ρ_- are those radii

where $\rho_c(B)$ and $R_c(\rho)$ are equal; i.e., where $\partial H/\partial \rho$ is zero. Because we are concerned with the behavior at the leading edge of the flux front, we evaluate Equation 3.2 with $B = 0$, resulting in

$$\rho_c(0) = cH_{c1}/4\psi J_c(0) \equiv \rho_c \quad , \quad (3.3)$$

so that from Equation 2.21 we have

$$\rho_c = R_c(\rho) = \rho + \frac{a^2}{\rho} \cot^2 \alpha_s \quad (3.4a)$$

or

$$\rho^2 + \rho_c \rho + a^2 \cot^2 \alpha_s = 0 \quad . \quad (3.4b)$$

The two solutions to Equation 3.4 are called ρ_+ and ρ_- :

$$\begin{aligned} \rho_+ &= \frac{1}{2}\rho_c + [(\frac{1}{2}\rho_c)^2 - a^2 \cot^2 \alpha_s]^{1/2} \\ \rho_- &= \frac{1}{2}\rho_c - [(\frac{1}{2}\rho_c)^2 - a^2 \cot^2 \alpha_s]^{1/2} \quad . \end{aligned} \quad (3.5)$$

We see that ρ_+ and ρ_- are real only if

$$\tan \alpha_s \geq 2a/\rho_c \quad (3.6)$$

and that

$$\rho_+ = \rho_- = \rho_c/2 \quad (3.7)$$

when $\tan \alpha_s = 2a/\rho_c$. Figure 61 shows qualitatively the

Figure 61. Comparison of fluxoid radius of curvature $R_c(\rho)$ and the fluxoid critical radius $\rho_c(B)$, for four hypothetical values of ρ_c . Minimum in $R_c(\rho)$ falls inside the cylinder, indicating that the surface pitch angle in this example exceeds 45°

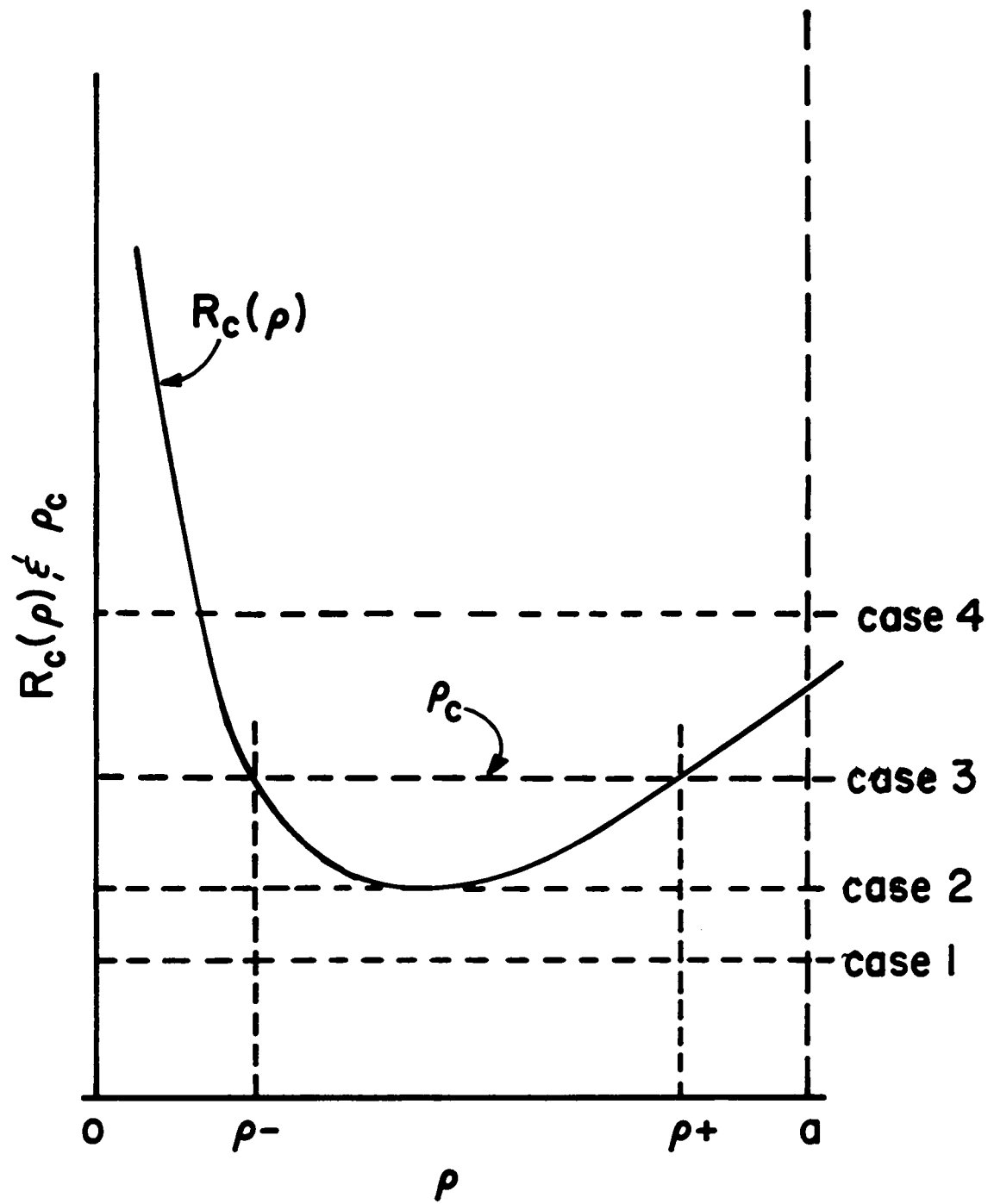
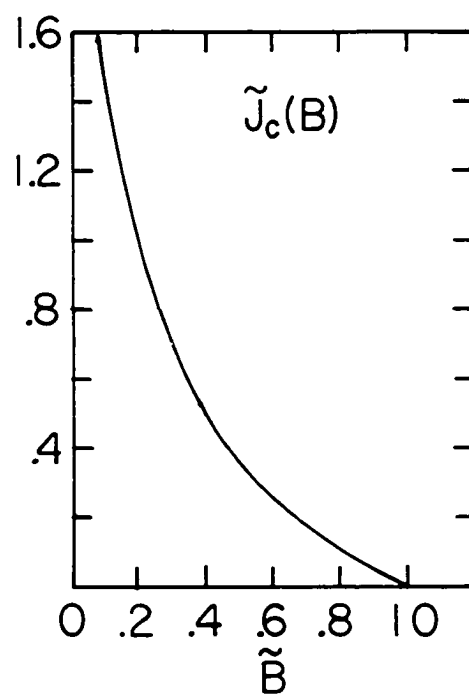
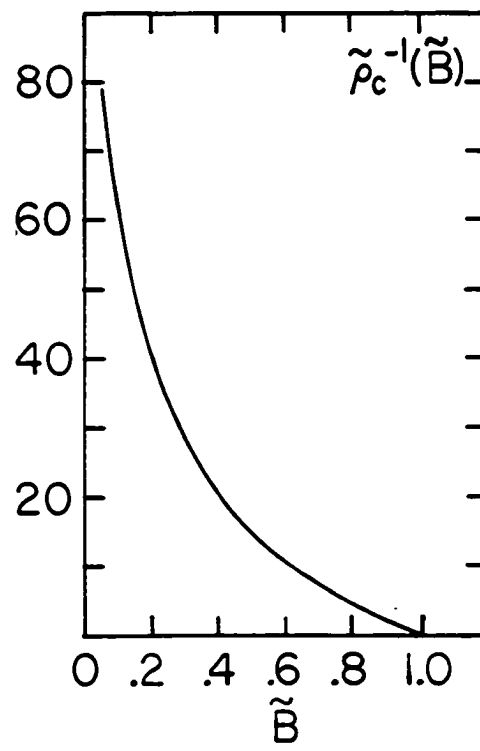
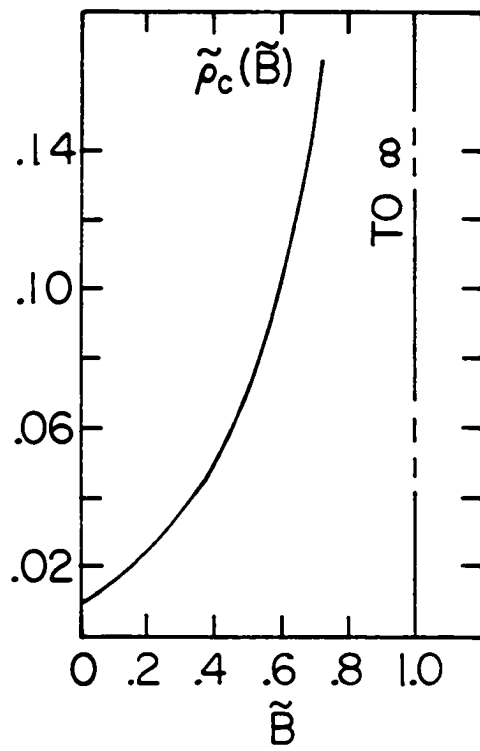


Figure 62. Typical behavior of $\tilde{\rho}_c(\tilde{B})$, $\tilde{\rho}_c^{-1}(\tilde{B})$, and $\tilde{J}_c(\tilde{B})$, here illustrated for $\beta = 0.024$, $\tilde{B}_0 = 0.20$, and $\tilde{J}_c(0) = 2.50$, such that $\tilde{\rho}_c(0) = 0.0096$ and $\tilde{\rho}_c^{-1}(0) = 104$



geometrical interpretation of Equation 3.5, and Figure 62 shows the behavior of $\tilde{\rho}_c(B)$, $\tilde{\rho}_c^{-1}(\tilde{B})$, and $\tilde{J}_c(\tilde{B})$. Both $\tilde{\rho}_c^{-1}(\tilde{B})$ and $\tilde{J}_c(\tilde{B})$ remain finite as \tilde{B} approaches zero.

B. Physical Argument

1. Force balance

In Equation 2.18 we had an expression for the force per unit volume f acting on a vortex array. This could also have been written as

$$f = (B/4\pi)\partial H/\partial \rho \quad (3.8)$$

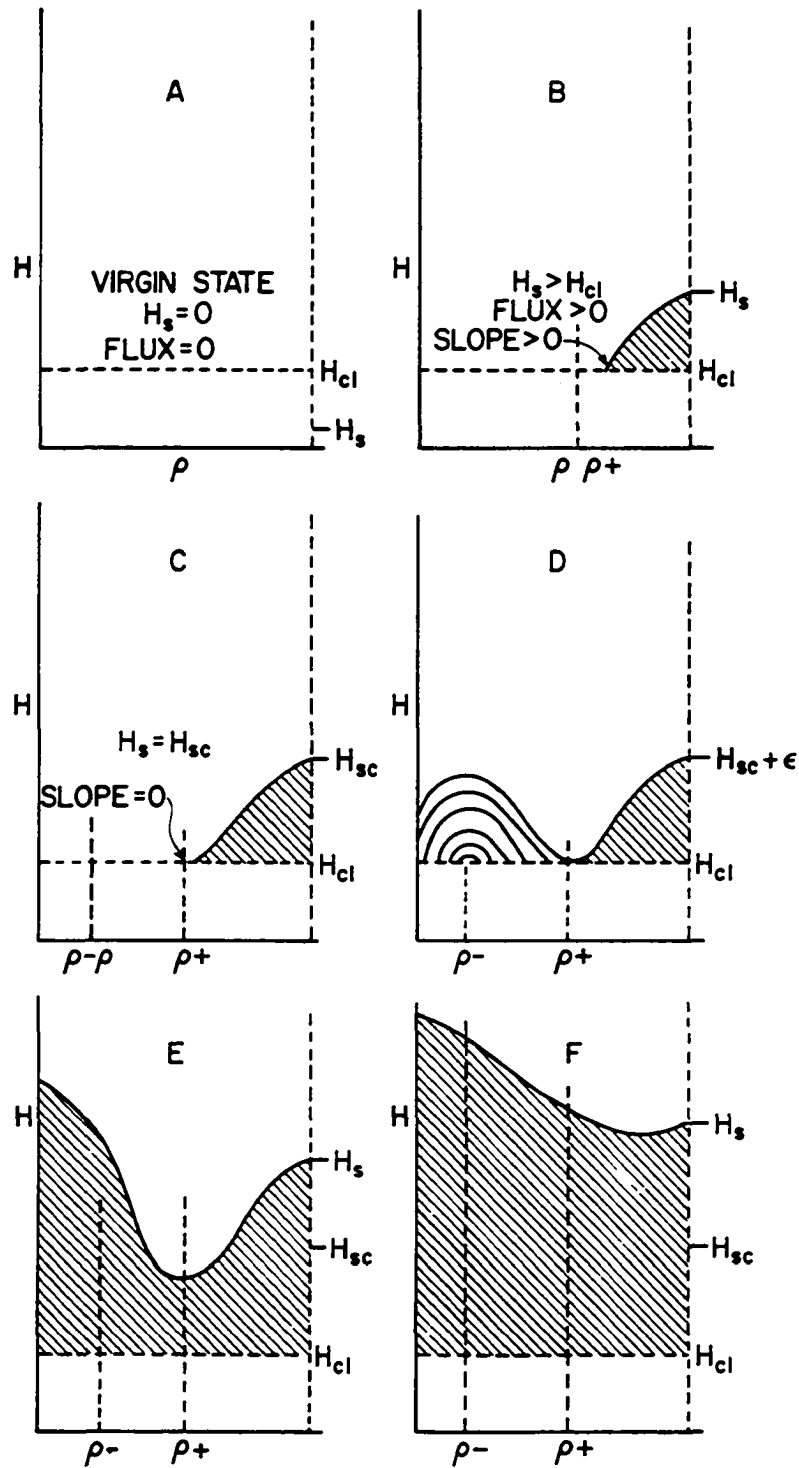
where we see immediately that the direction of f is determined by the algebraic sign of $\partial H/\partial \rho$. If f is zero, vortices near the flux front (ρ_+) are in a metastable equilibrium, and if $\partial H/\partial \rho$ is negative, the net force per unit volume acts inwards, resulting in an instability. Under this latter condition, vortices near the flux front will spontaneously collapse to the vicinity of ρ_- . At ρ_- , $\partial H/\partial \rho$ becomes positive again, so that an accretion of flux occurs in the neighborhood of ρ_- . Figuratively speaking, ρ_+ represents the crest of a free energy hill, and ρ_- represents the bottom of the trough.

2. Collapse sequence

We attempt to clarify the above discussion by narrating a possible collapse sequence (see Figure 63). We imagine a type-II cylinder in the virgin state (Figure 63A) and connected to some apparatus which can supply a transport current I_z and an axial surface field H_a . The resultant field at the surface will have magnitude $H_s = [H_a^2 + H_\phi^2]^{1/2}$, where H_ϕ is the field due to the current. We further assume that I_z and H_a may be regulated so as to maintain the ratio H_ϕ/H_z constant. This guarantees that the surface pitch angle α_s is always the same.

As H_a and I_z are slowly increased from zero, the sample remains flux-free until H_s reaches the lower critical field H_{c1} . As H_s then slowly exceeds H_{c1} , flux spirals start to penetrate the cylinder, resulting in a field profile similar to that of Figure 63B. For simplicity, we will assume that a surface barrier field does not exist. As H_s now increases, the position of the flux front, ρ_p , moves inwards, and more flux spirals penetrate the surface of the cylinder. At the same time, $\partial H / \partial \rho$ at the flux front grows smaller and smaller, until at some critical value of H_s , say H_{sc} , $\partial H / \partial \rho$ at ρ_p approaches zero, and ρ_p reaches the point ρ_+ (Figure 63C). The sample is now at the point where an instability is about to occur. We now increase H_s a minute amount ϵ above H_{sc} , and a flux collapse occurs. Flux spirals at the flux front

Figure 63. Sequence of events leading up to spiral collapse instability. H_s is the magnitude of the surface field, and H_{sc} is the critical value of the surface field, beyond which collapse occurs. ϵ is an infinitesimal increment in H_s



collapse to the vicinity of ρ_- (where once again $\partial H / \partial \rho$ becomes positive), and at the same time additional flux penetrates the cylinder, so that the region between ρ_+ and the surface maintains the same flux profile (Figure 63D). With H_s held fixed, additional flux cascades inwards, so that the cylinder assumes the sequence of field profiles shown in Figure 63D. Eventually the region between ρ_+ and ρ_- fills completely with flux. With further increases of H_s , we see profiles as in Figures 63E and F.

C. Energy and Heat

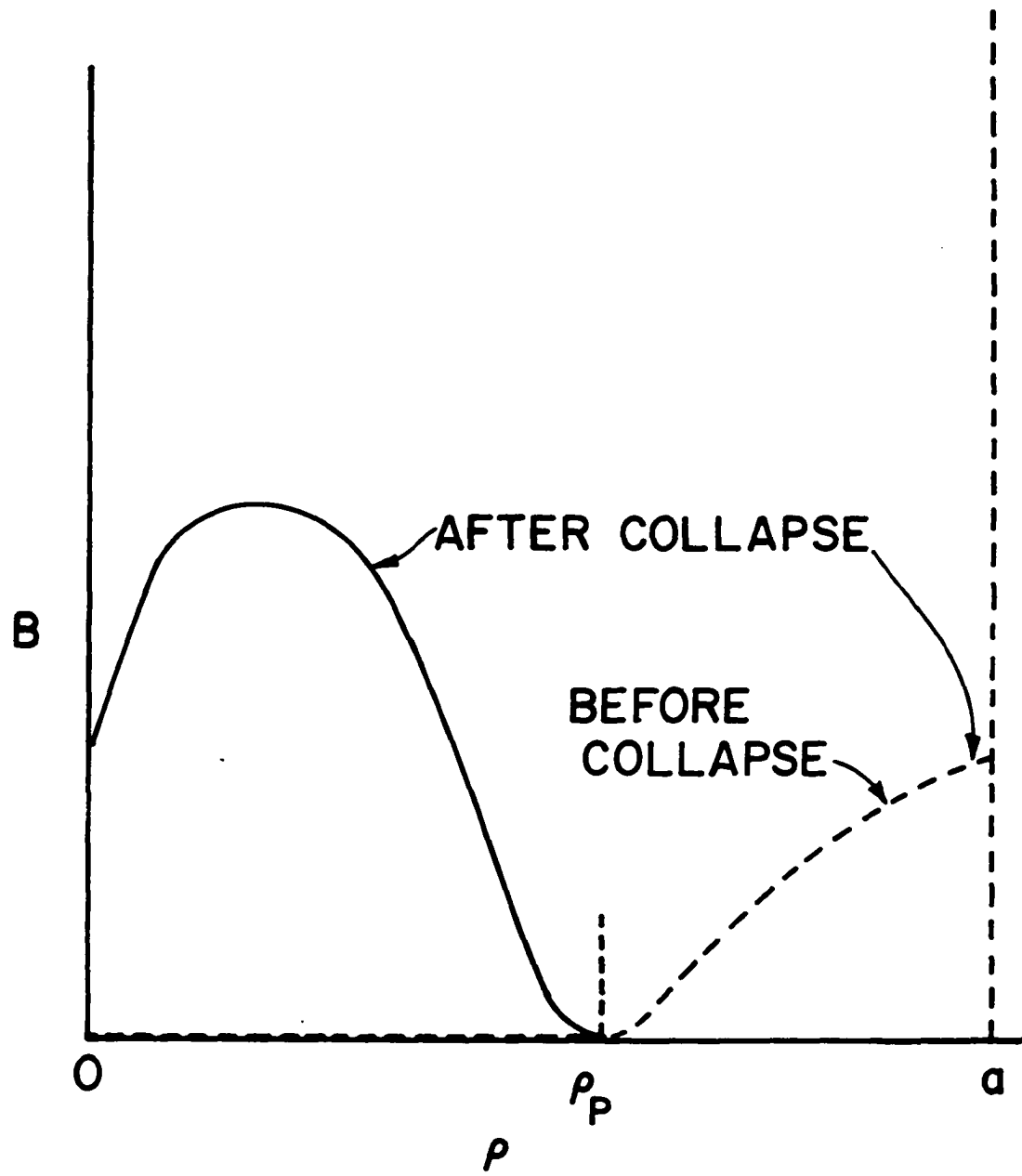
We may apply the first law of thermodynamics to determine the heat released during the collapse process. We write the first law in the form

$$Q' = \Delta W' - \Delta F' \quad (3.9)$$

where the primes denote "per unit length of cylinder", Q is the heat released, ΔW is the work done by the external currents and fields, and ΔF is the change in the Helmholtz free energy of the cylinder.

In Figure 64 we have a sketch of B versus ρ immediately before, and immediately after collapse has occurred. Notice that in the region $\rho_p < \rho < a$, the flux density is the same before and after collapse, and in the region $0 < \rho < \rho_p$, B is zero before collapse occurs. We may now calculate the change

Figure 64. Crude sketch of flux profiles before and after spiral collapse instability occurs, as used to calculate change in Helmholtz free energy during the collapse process



in the Helmholtz free energy, as follows.

Let F_a denote the free energy density after collapse, and let F_b denote the free energy density before collapse. Then the change in free energy per unit length of cylinder is

$$\begin{aligned}
 \Delta F' &= \int_0^a d^2\rho [F_a - F_b] \\
 &= \int_0^{\rho_p} d^2\rho F_a + \int_{\rho_p}^a d^2\rho F_a - \int_0^{\rho_p} d^2\rho F_b \\
 &\quad - \int_{\rho_p}^a d^2\rho F_b \quad . \quad (3.10)
 \end{aligned}$$

The third integral is zero since $B = 0$ for $\rho < \rho_p$ before collapse, and the second and forth integrals have equal magnitudes because the before and after flux profiles are identical in the region $\rho_p < \rho < a$. We are left with

$$\Delta F' = \int_0^{\rho_p} d^2\rho F_a = 2\pi \int_0^{\rho_p} d\rho \rho F[B(\rho)] \quad (3.11)$$

where the explicit dependencies of F upon B , and B upon ρ have been inserted. Although $B(\rho)$ versus ρ is obtained from numerical integration, $F(B)$ may be obtained analytically via

Equation 2.27. A plot of $F(B)$ is shown in Figure 65 for several values of the ratio H_{c1}/H_{c2} ($= \beta$), based on Equation 2.27. Knowledge of the flux profile $B(\rho)$ thus enables the integration of Equation 3.11 to be performed numerically.

Next, we consider the work done by the currents and fields. Using a familiar result from electromagnetism, we have that the energy crossing a unit area of cylinder surface per unit time is

$$\vec{S} = \frac{c}{4\pi} \vec{E}_s \times \vec{H}_s \quad (3.12)$$

where \vec{E}_s and \vec{H}_s are the electric and magnetic field vectors at the surface of the cylinder. In cylindrical coordinates, Poynting's vector becomes

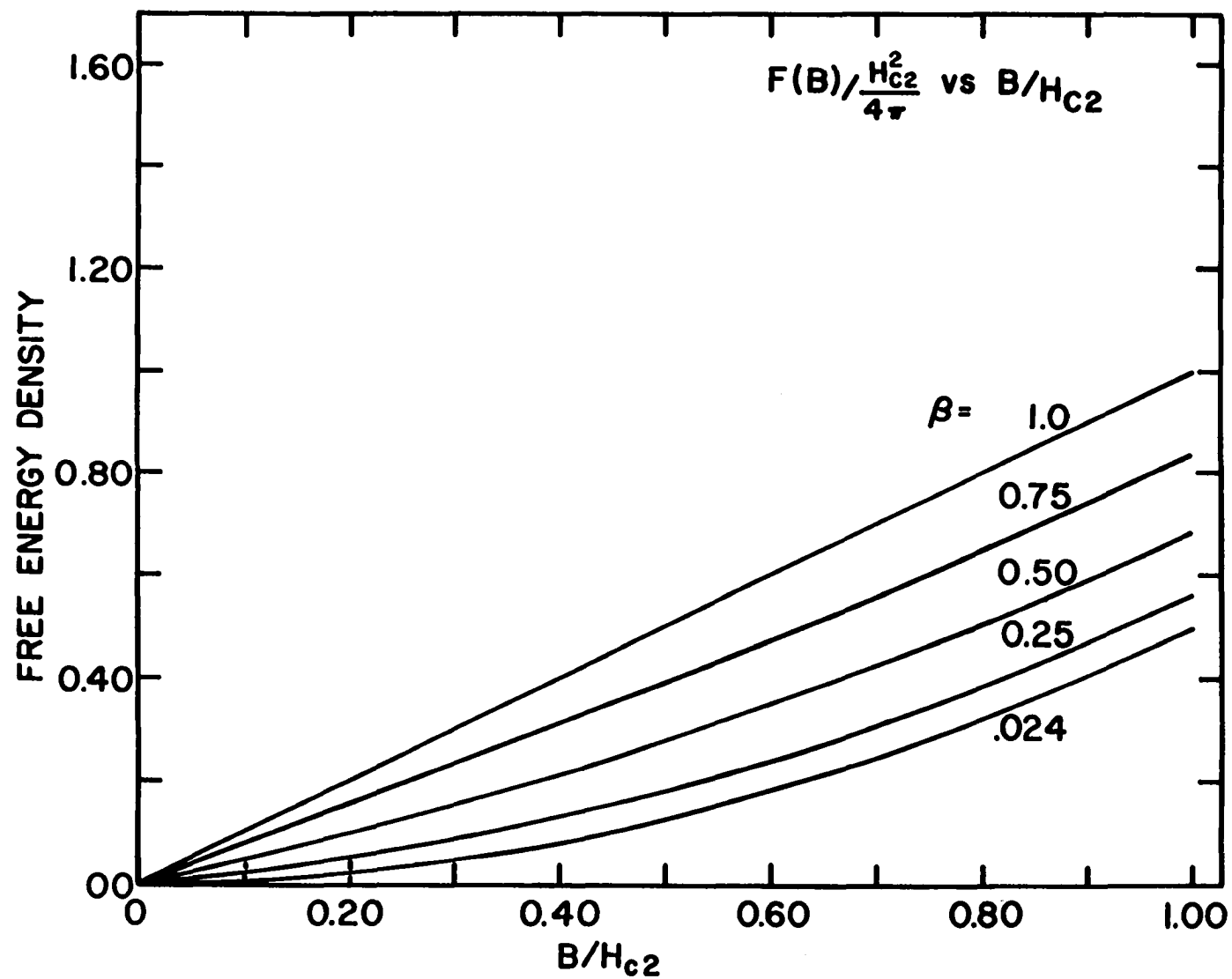
$$\vec{S} = (-\hat{\rho}) \frac{c}{4\pi} [E_{sz} H_{s\theta} - E_{s\theta} H_{sz}] \quad (3.13)$$

where the unit vector $(-\hat{\rho})$ indicates that energy is flowing into the cylinder in a radial direction. Next, we integrate \vec{S} over time to obtain the energy per unit of surface area, \vec{S}'' :

$$\vec{S}'' = (-\hat{\rho}) \frac{c}{4\pi} \int [E_{sz} H_{s\theta} - E_{s\theta} H_{sz}] dt \quad (3.14)$$

From Faraday's law, $\vec{\nabla} \times \vec{E} = -c^{-1} d\vec{B}/dt$, we obtain

Figure 65. Helmholtz free energy density, normalized to $\frac{1}{4}\pi H_{c2}^2$. Curves are derived from Equation 2.27. $\beta = H_{c1}/H_{c2}$



$$2\pi a E_{s\theta} = \int d\vec{A} \cdot \vec{\nabla} \times \vec{E} = -c^{-1} \int d\vec{A} \cdot \partial \vec{B} / \partial t = -c^{-1} d\bar{\Phi}_z / dt$$

$$E_{s\theta} = - [2\pi ca]^{-1} d\bar{\Phi}_z / dt \quad . \quad (3.15)$$

Also from Figure 66 we see that

$$\begin{aligned} E_{sz} &= - E_{s\theta} \tan \alpha_s \\ &= \frac{\tan \alpha_s d\bar{\Phi}_z / dt}{2\pi ca} \quad . \end{aligned} \quad (3.16)$$

Substituting Equations 3.15 and 3.16 into 3.14 we obtain

$$\begin{aligned} \vec{S}'' &= (-\hat{p}) \left[\frac{\tan \alpha_s}{8\pi^2 a} \int H_{s\theta} d\bar{\Phi}_z + \frac{1}{8\pi^2 a} \int H_{sz} d\bar{\Phi}_z \right] \\ &= (-\hat{p}) \left[\tan \alpha_s H_{s\theta} + H_{sz} \right] \frac{\Delta \bar{\Phi}_z}{8\pi^2 a} \quad . \end{aligned} \quad (3.17)$$

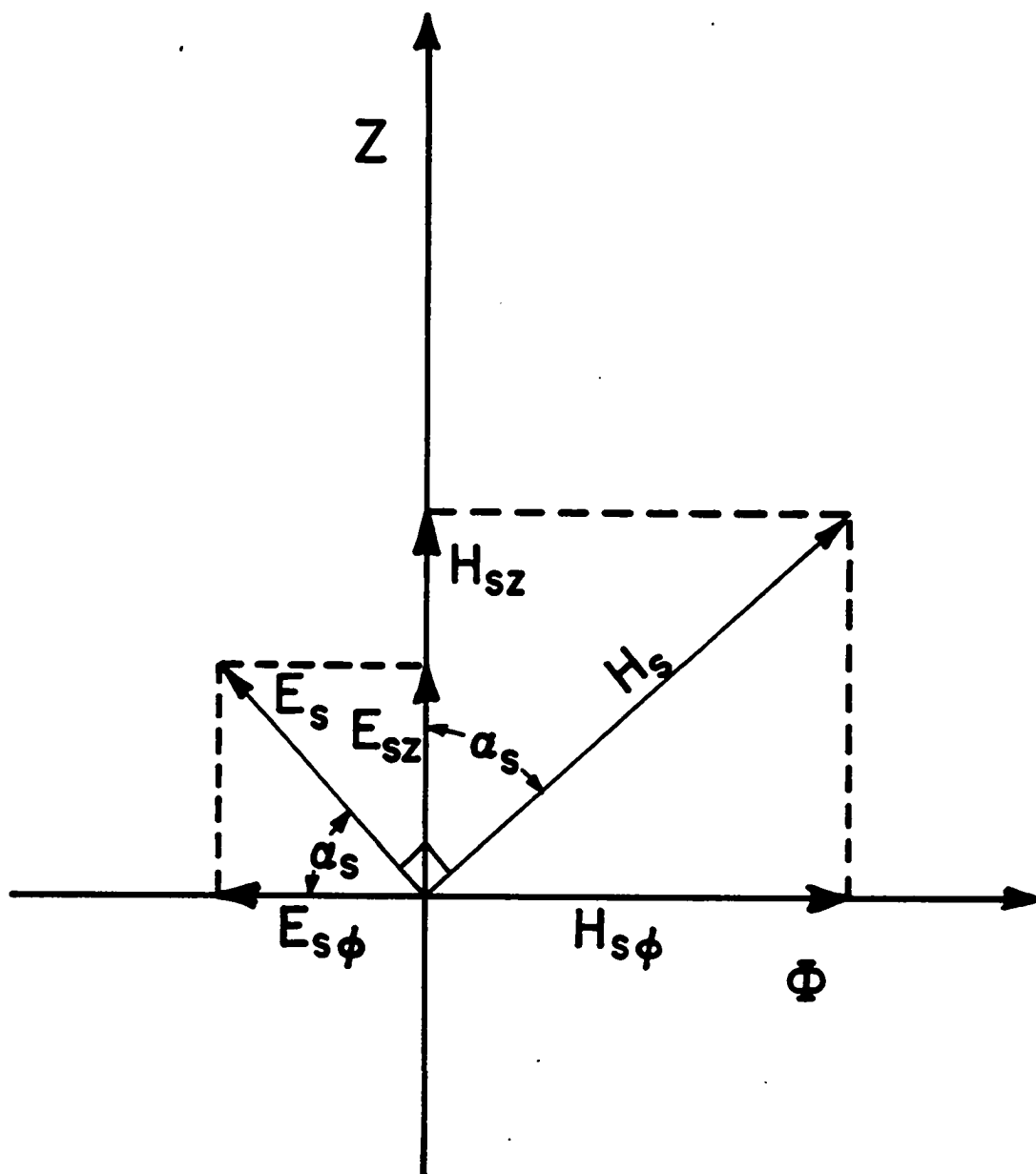
Since $H_{s\theta} = H_s \sin \alpha_s$ and $H_{sz} = H_s \cos \alpha_s$, Equation 3.17 reduces to

$$\begin{aligned} \vec{S}'' &= (-\hat{p}) \left[H_s \frac{\sin^2 \alpha_s}{\cos \alpha_s} + H_s \frac{\cos^2 \alpha_s}{\cos \alpha_s} \right] \frac{\Delta \bar{\Phi}_z}{8\pi^2 a} \\ &= (-\hat{p}) \frac{H_s \Delta \bar{\Phi}_z}{8\pi^2 a \cos \alpha_s} \quad . \end{aligned} \quad (3.18)$$

The work per unit length of cylinder is

$$\Delta W' = 2\pi a S'' = H_s \Delta \bar{\Phi}_z / 4\pi \cos \alpha_s \quad . \quad (3.19)$$

Figure 66. Vector diagram illustrating directions of the components of the electric and magnetic field vectors \vec{E} and \vec{H} , at the surface of the cylinder



Equation 3.18 shows that the fraction of the work contributed by the sources of the transport current is $\sin^2 \alpha_s$, and the fraction contributed by the sources of the axial field is $\cos^2 \alpha_s$.

Thus, the heat released during the collapse is

$$Q' = \frac{H_s \Delta \bar{\Phi}_z}{4\pi \cos \alpha_s} - 2\pi \int_0^{\rho_p} d\rho \rho F[B(\rho)] \quad . \quad (3.20)$$

Q' can be readily obtained by numerical methods. We note that $\Delta \bar{\Phi}_z$ represents the change in axial flux during collapse, and would be obtained by integration of $B_z(\rho)$ from $\rho = 0$ to $\rho = \rho_p$; i.e.,

$$\Delta \bar{\Phi}_z = 2\pi \int_0^{\rho_p} d\rho \rho B(\rho) \cos \alpha(\rho) \quad . \quad (3.21)$$

Hence, Equation 3.20 could be written as

$$Q' = \frac{H_s}{2 \cos \alpha_s} \int_0^{\rho_p} d\rho \rho B(\rho) \cos \alpha(\rho) - 2\pi \int_0^{\rho_p} d\rho \rho F[B(\rho)] \quad . \quad (3.22)$$

D. Experimental Verification of Collapse Modes

The existence of a collapse possibility depends upon the relative magnitudes of $R_c(\rho)$ and $\rho_c(B)$, and the surface pitch angle α_s . Specifically, we must have $\rho_c(0)$ exceed the minimum in $R_c(\rho)$, within the boundary of the cylinder ($0 < \rho < a$). Differentiating Equation 2.21 with respect to ρ and equating the result to zero, we find the minimum of $R_c(\rho)$ occurring where

$$\rho = \rho_{\min} = a \cot \alpha_s \quad (3.23)$$

with a corresponding value of $R_c(\rho_{\min})$ equal to

$$(R_c)_{\min} = 2a \cot \alpha_s \quad (3.24)$$

From Equation 3.23 we see that the minimum in $R_c(\rho)$ will lie within the cylinder whenever $\cot \alpha_s < 1$; i.e., whenever α_s exceeds 45° . If $\alpha_s < 45^\circ$, the minimum in $R_c(\rho)$ falls outside the cylinder. In this latter situation, we must compare $\rho_c(0)$ with $R_c(a)$, since $R_c(a)$ represents the smallest physically realizable value of $R_c(\rho)$. From Equation 2.21, $R_c(a)$ is just $a/\sin^2 \alpha_s$, so that in checking for a collapse possibility, we compare $\rho_c(0)$ with $a/\sin^2 \alpha_s$. Thus if

$$\frac{cH_{c1} \sin^2 \alpha_s}{4\pi a J_c(0)} > 1 \quad (3.25)$$

then collapse is possible. In reduced units Equation 3.25 is equivalent to

$$\frac{\beta \sin^2 \alpha_s}{\tilde{J}_c(0)} > 1$$

or

$$\alpha_s > \sin^{-1} \sqrt{\frac{\tilde{J}_c(0)}{\beta}} . \quad (3.26)$$

We note that in this case ($\alpha_s < 45^\circ$), ρ_+ lies outside the cylinder, so that collapse begins immediately when the surface field exceeds H_{c1} .

For situations where $\alpha_s > 45^\circ$, the minimum in $R_c(\rho)$ occurs within the cylinder, so that we need to compare $\rho_c(0)$ with $R_c(\rho_{\min})$. Thus, from Equations 3.3 and 3.24 we have that, if

$$\frac{cH_{c1} \tan \alpha_s}{8\pi a J_c(0)} > 1 \quad (3.27)$$

collapse is possible. In reduced units Equation 3.27 is equivalent to

$$\frac{\tan \alpha_s}{2J_c^*(0)} > 1$$

or

$$\alpha_s > \tan^{-1}[2\tilde{J}_c(0)/\beta] \quad . \quad (3.28)$$

The results expressed in Equations 3.27 and 3.28 indicate that the following conditions favor a collapse possibility:

1. large surface pitch angle α_s
2. low κ , implying high ratio H_{c1}/H_{c2}
3. low pinning material, implying low $J_c(0)$
4. small diameter sample.

It is interesting that requirements 2 and 3 are not difficult to simultaneously satisfy, since low pinning and low κ quite often occur together. For example, in the Pb-Bi material used in Timms and Walmsley's (39) experiments, where $\kappa \approx 14$ is relatively high, we may calculate that

$$\frac{cH_{c1}}{8\pi aJ_c(0)} \approx 0.02 \quad (3.29)$$

where $a = 1.5$ mm, $J_c(0) = 185$ A/cm², and $H_{c1} \approx 135$ G. Thus, in order for collapse to be possible, $\tan\alpha_s$ would have to exceed 50, implying that α_s would need to be in excess of 89° .

On the other hand, Wollan et al. (47) report data on vanadium and niobium which suggests that samples of these materials could show the collapse. Their vanadium measure-

ments show that $J_c(0)/H_{c1} \approx 7.3 \text{ A/cm}^2\text{Oe}$ on 0.23 diameter cylindrical samples. This gives

$$\frac{cH_{c1}}{8\pi aJ_c(0)} \approx 0.474 \quad (3.30)$$

suggesting that cylinders of this material would show the collapse as surface pitch angles in excess of 65° . The niobium sample was 3.0 mm in diameter with $J_c(0)/H_{c1} = 21 \text{ A/cm}^2\text{Oe}$. This yields

$$\frac{cH_{c1}}{8\pi aJ_c(0)} \approx 0.126 \quad (3.31)$$

requiring a surface pitch angle in excess of 82.8° for collapse.

The sudden collapse of vortices, and the accompanying rapid increase in axial flux $\Delta\Phi_z$, ought to be detectable in the laboratory. Since a common method of measuring magnetization in cylindrical samples employs a small pick-up coil wrapped around the sample near the midpoint, one would expect a sharp voltage spike in the coil output at the moment of collapse. For each turn in the pick-up coil, the voltage generated by a collapse should be approximately

$$v(\text{per turn}) = - \frac{1}{c} \frac{\Delta\Phi_z}{\Delta T} \quad (3.32)$$

where ΔT is the time interval over which the collapse

occurred. We have a numerical procedure to obtain the magnetization of the cylinder via the integration of $B(\rho)$ over the cylinder cross-section. Thus, we may estimate $\Delta\Phi_z$. In the following section, we will show a prediction for $\Delta\Phi_z$ for the vanadium samples of Wollan et al. (47) referred to on the previous page. To obtain ΔT for the collapse, we start with the magnetic diffusivity (48)

$$D(B) = c^2 \rho_f(B) / 4\pi (dB/dH) \quad (3.33)$$

which depends strongly upon B . Here, $\rho_f(B)$ is the superconductor resistivity in the flux-flow regime, and is related to the normal state resistivity ρ_n by (49)

$$\rho_f = \rho_n B/H_{c2} = \rho_n \tilde{B} \quad (3.34)$$

For a specimen of radius 'a', the characteristic diffusion time ΔT is approximately

$$\begin{aligned} \Delta T &= a^2 / 2D(B) \\ &= \frac{2\pi a^2 dB/dH}{c^2 \tilde{B} \rho_n} \end{aligned} \quad (3.35)$$

which is interpreted as the relaxation time required for the specimen to respond to a field or current change. The vanadium sample of Wollan et al. (47) had a resistivity ratio ($\rho_{300}/\rho_{4.2}$) of 1500, and Weast (50) gives a vanadium

resistivity at 20°C of 24.8-26 $\mu\Omega$ -cm. Taking ρ_{300} at 25 $\mu\Omega$ -cm, $\rho_{4.2} = \rho_n$ should be approximately $1.67 \times 10^{-8} \Omega$ -cm. With a sample radius of 0.115 cm, this gives a diffusion time of approximately

$$\Delta T \approx 5 \times 10^{-3} \cdot \left[\frac{1}{B} \cdot dB/dH \right] \text{ sec} \quad . \quad (3.36)$$

As a further approximation, we use our model relation

$$H(B) = [k^2 B^2 + \beta^2] \quad (3.37)$$

for calculating dB/dH at the surface of the cylinder, where $H = H_{sc}$ is the magnitude of the surface field at which collapse first occurs. From Equation 3.37 $dB/dH = H/k^2 B$ and $k^2 \sim 1$, so that at the surface of the cylinder

$$dB/dH = H_{sc}/B_{sc} \approx 1 \quad .$$

Thus, the diffusion time for collapse in Wollan's vanadium sample should be approximately

$$\Delta T \approx 5 \times 10^{-3} / \tilde{H}_{sc} \text{ sec} \quad (3.38)$$

or roughly 5 milliseconds.

E. Modeling Vanadium

1. Sample properties

We make a calculation here which predicts a spiral collapse possibility for the vanadium sample used by Wollan et al. (47). The relevant data as reported in (47) are

sample diameter: 0.23 cm

H_{c1} : 489 Oe @ 4.18 K

$J_c(0)/H_{c1}$: 7.3 A/cm²Oe @ 4.18 K .

This implies that $J_c(0) = 3570$ A/cm² and $a = 0.115$ cm. Haas (51) reports that H_{c2} for this sample was measured to be 751 Oe at 4.18 K, the relevant temperature in the above experiments. The reduced quantities derived from the above are

$$\tilde{J}_c(0) = J_c(0)/(cH_{c2}/4\pi a) = 0.688$$

$$\beta = H_{c1}/H_{c2} = 0.650$$

$$\tilde{\rho}_c(0) = cH_{c1}/4\pi aJ_c(0) = \tilde{H}_{c1}/\tilde{J}_c(0) = 0.9448$$

$$\frac{1}{2}\tilde{\rho}_c(0) = 0.4724 \quad . \quad (3.39)$$

There is some liberty in the selection of ρ_+ and ρ_- , as we need only insure that, for collapse to be possible,

$$\tan \alpha_s > [8\pi a J_c(0)/cH_{c1}] = 2.1169$$

$$\implies \alpha_s > 64.7^\circ \quad . \quad (3.40)$$

Arbitrarily, we selected $\alpha_s = 65^\circ$ so that from Equation 3.5

$$\tilde{\rho}_+ = 0.5479$$

$$\tilde{\rho}_- = 0.3969 \quad . \quad (3.41)$$

Because the shape of the critical current curve is unknown, a guess for the parameter \tilde{B}_0 of 0.20 was made. Finally, we assume negligible surface pinning, so that the parameter \tilde{H}_S of Equation 2.34 is equal to β .

2. Results

The choice of vanadium for illustrating the spiral collapse instability was especially fortuitous. As in the case of Figure 52, a stable mixed state configuration, wherein the entire cylinder was filled with flux ($\rho_p = 0$), proved impossible to achieve at the chosen surface pitch angle of 65° . As the magnitude of the surface field was increased beyond the critical entry field (here equal to \tilde{H}_{c1} , or 0.65), spiral collapse occurred at a penetration radius of 0.865, with a postcollapse field on the axis of $1.35H_{c2}$. Thus, the mixed state was destroyed before the entire cylinder could fill with flux.

We can therefore predict the following behavior for the vanadium sample of Haas (51): When the applied longitudinal field and axial transport current are gradually increased from zero, such that the surface pitch angle is maintained at a constant 65° , spiral collapse and subsequent destruction of the mixed state should occur when the magnitude of the surface field ($= [H_{s\theta}^2 + H_{sz}^2]^{1/2}$) reaches $0.650 H_{c2}$, or 488 G. This corresponds to an applied longitudinal field of 207 G and a transport current of 255 A.

Figures 67 through 70 depict the flux and current profiles predicted immediately after collapse. Since the mixed state is destroyed by the collapse, these figures do not represent physical reality.

F. Spiral Collapse in Hypothetical Material

1. General

We next discuss the collapse sequences of several hypothetical type-II materials operated under varying surface pitch angles. Our aim is to categorize the various possible ways in which collapsed flux may agglomerate as a function of the radius.

2. Surface pitch angle $> 45^\circ$

We begin with the case where the surface pitch angle exceeds 45° . In Section D we argued that this implies that

Figure 67. Flux profile for vanadium sample described in Section E of Chapter III. Profile illustrates collapse. Parameters used were $\tilde{J}_c(0) = 0.688$, $\tilde{B}_0 = 0.20$, and $\beta = \tilde{H}_{c1} = 0.650$

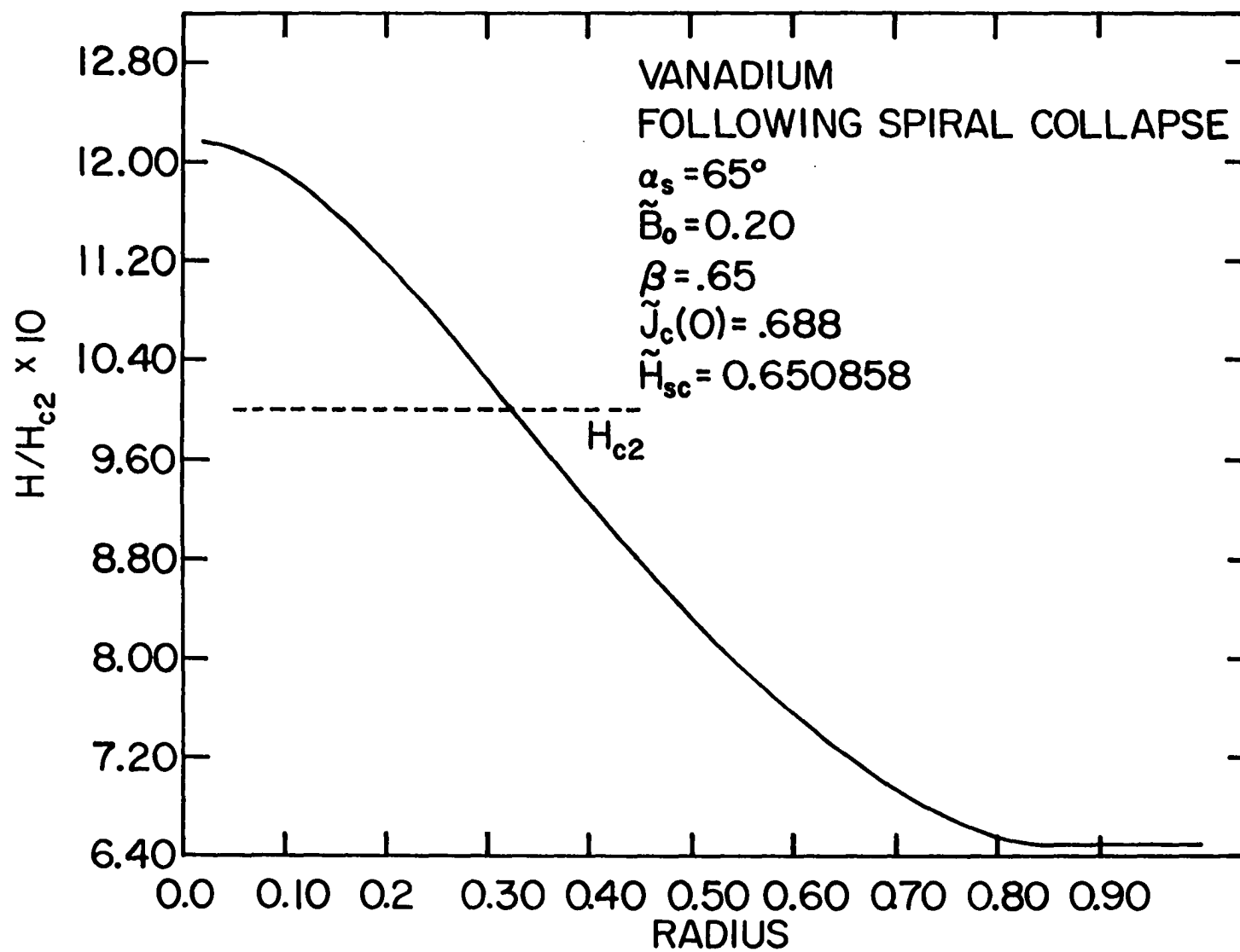


Figure 68. Reduced current density profile for vanadium sample described in Section E of Chapter III. Product $\tilde{B}\langle j_z \rangle$ versus reduced radius $\tilde{\rho}$ is shown, corresponding to reduced field profile shown in Figure 67. Current density here is proportional to $\vec{\nabla} \times \vec{B}$ rather than $\vec{\nabla} \times \vec{H}$. See Figure 53

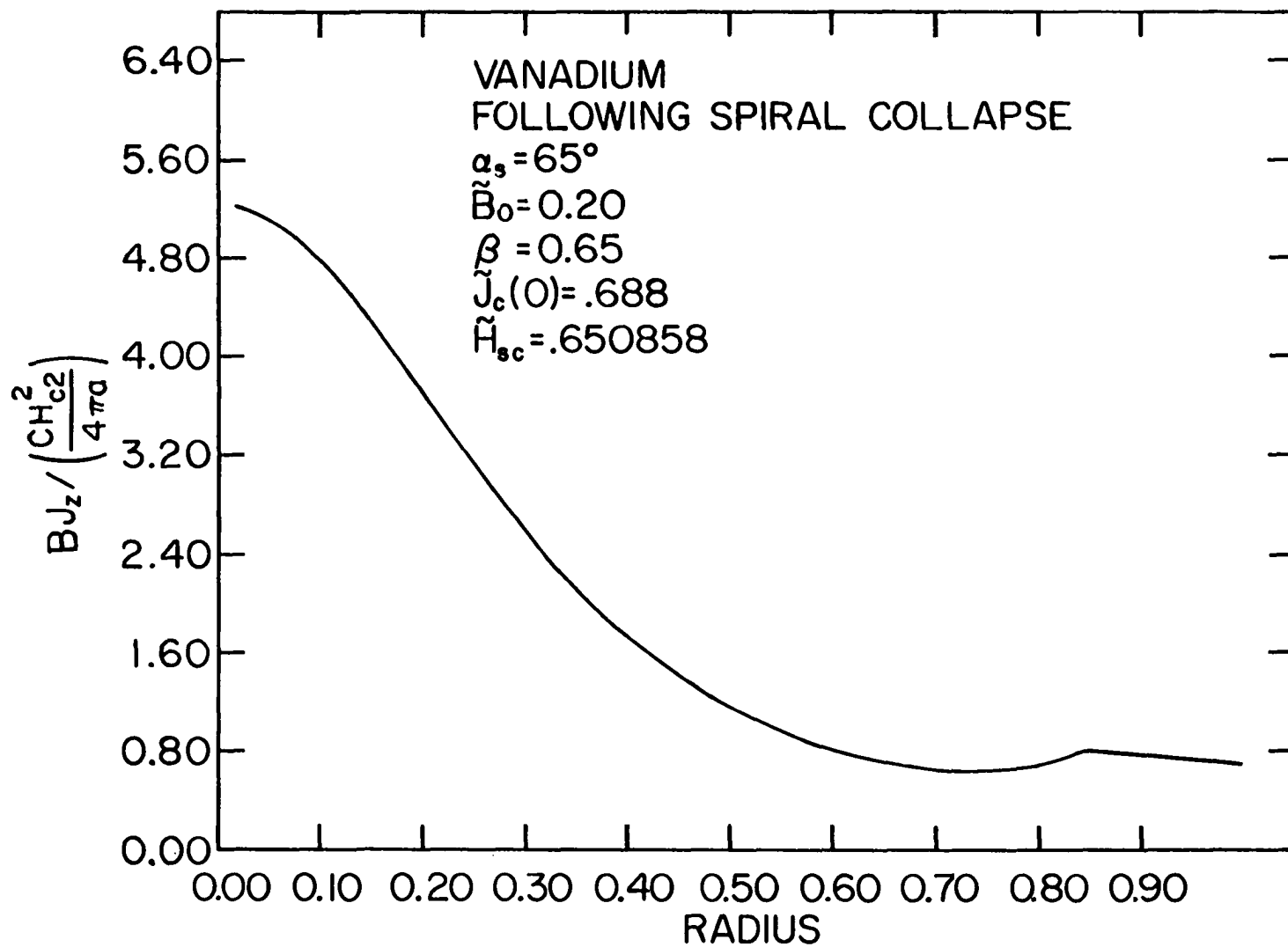


Figure 69. Reduced current density profile for vanadium sample described in Section E of Chapter III. Product $\tilde{B}\langle j_{\theta} \rangle$ versus reduced radius $\tilde{\rho}$ is shown, corresponding to reduced field profile of Figure 67. Current density here is proportional to $\vec{\nabla} \times \vec{B}$ rather than $\vec{\nabla} \times \vec{H}$. See Figure 68

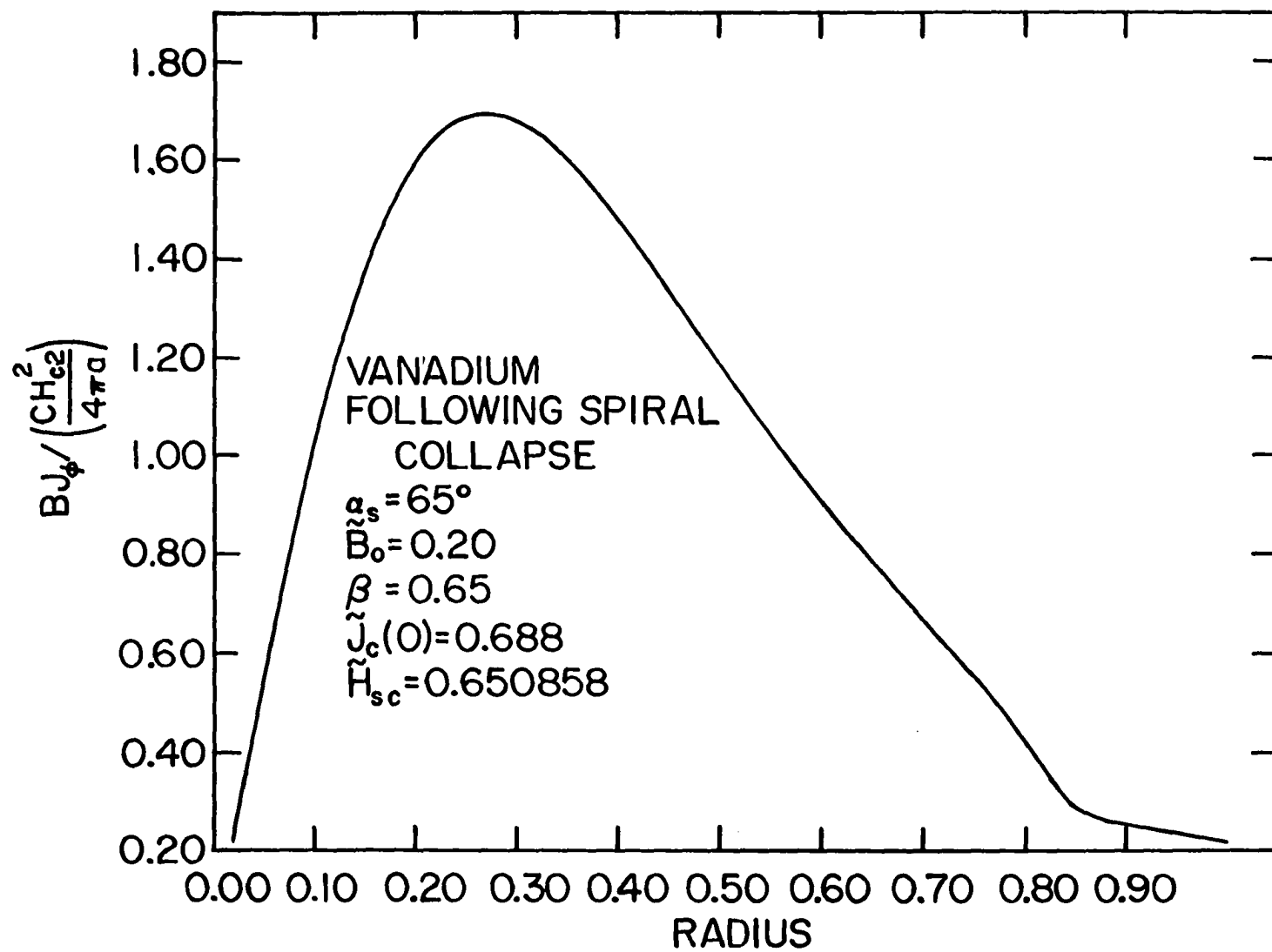
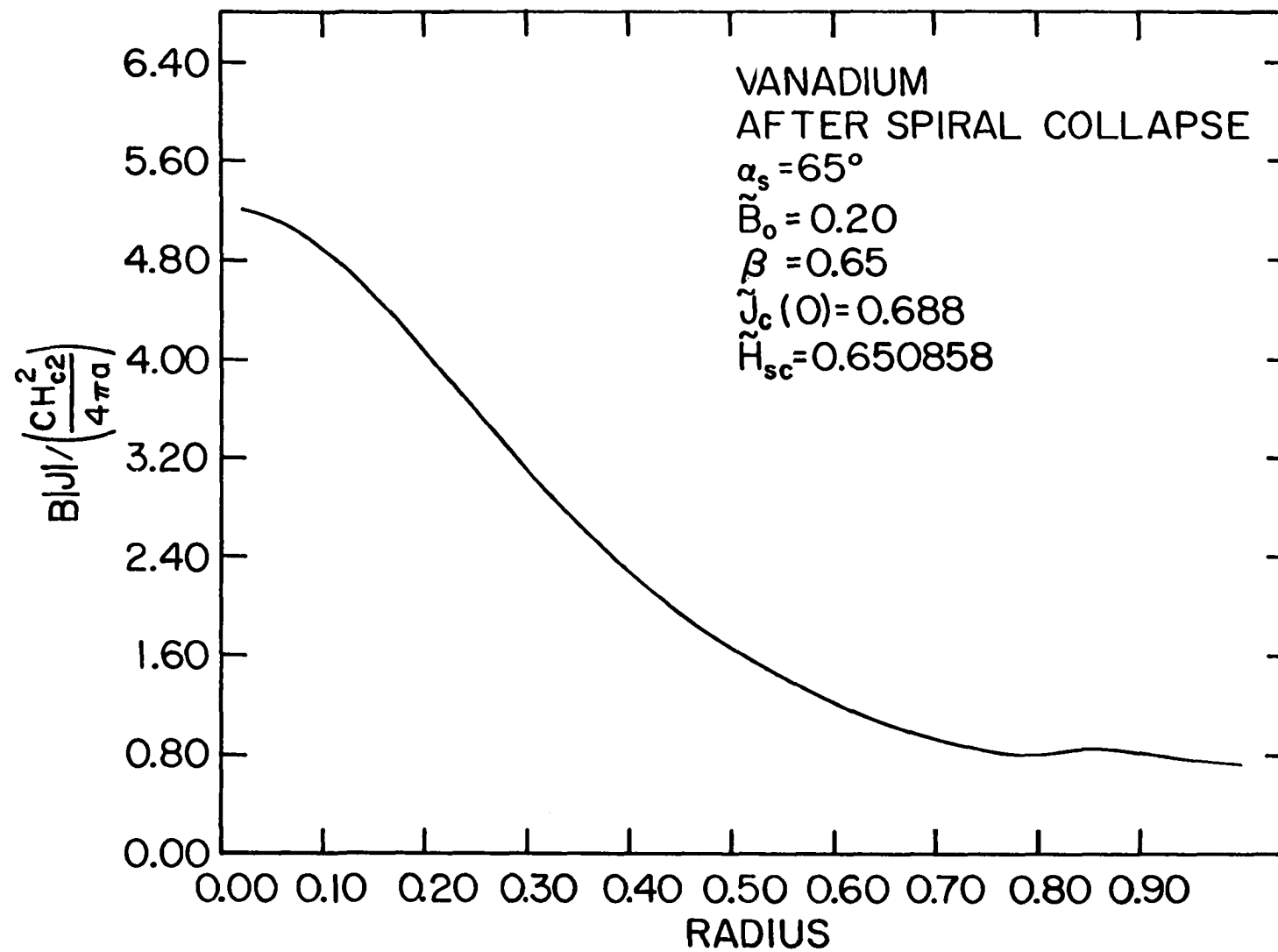


Figure 70. Reduced current density profile for vanadium sample described in Section E of Chapter III. Product of \tilde{B} and the magnitude of $\langle j \rangle$ versus the reduced radius $\tilde{\rho}$ is shown, where $\langle \tilde{j} \rangle = [\tilde{j}_z^2 + \tilde{j}_\theta^2]^{1/2}$



the minimum in $R_c(\rho)$ occurs within the cylinder. Accordingly, there are four distinct possibilities regarding the magnitude of $\tilde{\rho}_c(0) \equiv \rho_c$ with respect to $R_c(\rho)$. These possibilities are:

1. $\rho_c < R_c(\rho_{\min})$, implying that collapse cannot occur.
2. $\rho_c = R_c(\rho_{\min})$, implying that $\rho_+ = \rho_- = \frac{1}{2}\rho_c$. Collapse is possible here.
3. $\rho_c > R_c(\rho_{\min})$ but $\rho_c < R_c(a)$. Collapse is possible here, and ρ_+ and ρ_- are real and distinct. Because $\rho_c < R_c(a)$, collapse does not immediately occur with the first penetration of flux into the cylinder.
4. $\rho_c > R_c(\rho_{\min})$ and $\rho_c > R_c(a)$. Collapse is immediate with the first penetration of flux into the cylinder. Also, $\tilde{\rho}_+$ is greater than 1, so that $\tilde{\rho}_+$ is a virtual point lying outside the cylinder.

These four possibilities correspond to the lines labeled 1, 2, 3, and 4 in Figure 61.

3. Surface pitch angle $< 45^\circ$

When the surface pitch angle is less than 45° , the minimum in $R_c(\rho)$ lies outside the cylinder. That is, everywhere within the cylinder, $dR_c(\rho)/d\rho \leq 0$. Accordingly, there are

only two distinct possibilities of interest regarding the relative magnitudes of ρ_c and $R_c(a)$. These are

5. $\rho_c < R_c(a)$, implying that collapse is not possible.
6. $\rho_c \geq R_c(a)$, implying that collapse is possible and immediate with the first entry of flux into the cylinder.

4. Hypothetical material

We illustrate the above possibilities by assuming the existence of a hypothetical type-II material with all the required properties. We seek values of $\tilde{\rho}_c$, β , $\tilde{J}_c(0)$, and α_s which will illustrate all of the above six possibilities. We start with case #3, where $\alpha_s > 45^\circ$, and arbitrarily select $\frac{1}{2}\tilde{\rho}_c = 0.50$, $\tilde{\rho}_+ = 0.75$, and $\tilde{\rho}_- = 0.25$. Using Equation 3.5 we obtain the necessary surface pitch angle α_s according to

$$[(\frac{1}{2}\tilde{\rho}_c)^2 - \cot^2\alpha_s]^{\frac{1}{2}} = \tilde{\rho}_+ - \frac{1}{2}\tilde{\rho}_c = 0.25$$

$$\implies \alpha_s = 66.587^\circ \quad . \quad (3.42)$$

Noting that from Equation 3.3, $\tilde{\rho}_c = \beta/\tilde{J}_c(0)$, we see that in this case

$$\beta = \tilde{J}_c(0) \quad . \quad (3.43)$$

Arbitrarily we let $\beta = \tilde{J}_c(0) = 0.024$, so this represents a weak pinning, high κ material.

To illustrate case #2, where $\frac{1}{2}\tilde{\rho}_c = \tilde{\rho}_+ = \tilde{\rho}_-$, (and arbitrarily keep the same pitch angle $\alpha_s = 66.587^\circ$), we solve for $\frac{1}{2}\tilde{\rho}_c$ subject to the condition which will make the radical in Equation 3.42 disappear:

$$\begin{aligned}\frac{1}{2}\tilde{\rho}_c &= \cot\alpha_s \\ \Rightarrow \tilde{\rho}_c &= 0.866 \\ \Rightarrow \beta/\tilde{J}_c(0) &= 0.866 \quad .\end{aligned}\tag{3.44}$$

To illustrate case #1, where the surface pitch angle is still the same, we require $\tilde{\rho}_c < 0.866$.

Finally, to illustrate case #4, where $\tilde{\rho}_+$ lies outside the cylinder, we require $\tilde{\rho}_c$ to exceed $\tilde{R}_c(a)$. At the same pitch angle of 66.587° , $\tilde{R}_c(a) = \csc^2\alpha_s = 1.18750$ from Equation 3.4a, so that we require $\tilde{\rho}_c > 1.18750$, or

$$\beta/\tilde{J}_c(0) > 1.18750 \quad .\tag{3.45}$$

We may summarize the above quantities in Table 8.

Figure 71 illustrates the flux profiles obtained from operating the above hypothetical material under conditions favoring case #2. Relevant parameters are

$$\beta = 0.024$$

Table 8. Material parameters needed to establish a given collapse mode^a

Parameter	Case #1	Case #2	Case #3	Case #4
Type of action	No collapse	Verge of collapse	Collapse	Immediate collapse
$\tilde{\rho}_c$	<0.866	0.866	$0.866-1.18750$	>1.18750
$\frac{1}{2}\tilde{\rho}_c$	<0.433	0.433	$0.433-0.59375$	>0.59375
$\tilde{\rho}_+$	imaginary	0.433	$0.433-1.0$	>1.0
$\tilde{\rho}_-$	imaginary	0.433	$0.1875-0.433$	<0.1875
$\tilde{J}_c(0)$	$>\beta/0.866$	$\beta/0.866$	$\beta/1.1875-$ $\beta/0.866$	$<\beta/1.1875$

^aSurface pitch angle = 66.587° ; $\beta/\tilde{J}_c(0) = \tilde{\rho}_c$ where $\beta = H_{c1}/H_{c2}$.

$$\tilde{J}_c(0) = 0.02771$$

$$\tilde{\rho}_c = 0.866$$

$$\tilde{B}_0 = 0.20$$

$$\alpha_s = 66.587^\circ$$

$$\tilde{H}_S = 0.024 \text{ (no surface pinning) } .$$

Figure 72 illustrates the flux profiles obtained from operating a hypothetical material under conditions favoring case #3. Relevant parameters are

Figure 71. Field profile for hypothetical material illustrating case #2, spiral collapse. Reduced field is plotted versus the reduced radius. $\beta = \tilde{H}_{c1} = 0.024$, $\tilde{J}_c(0) = 0.02771$, $\tilde{B}_0 = 0.20$, and $\alpha_s = 66.587^\circ$. Surface pinning was ignored. With these parameters, $\rho_c = R_c(\rho_{\min})$, so that $\rho_+ = \rho_- = \frac{1}{2}\rho_c$, and the radical in Equation 3.5 vanishes

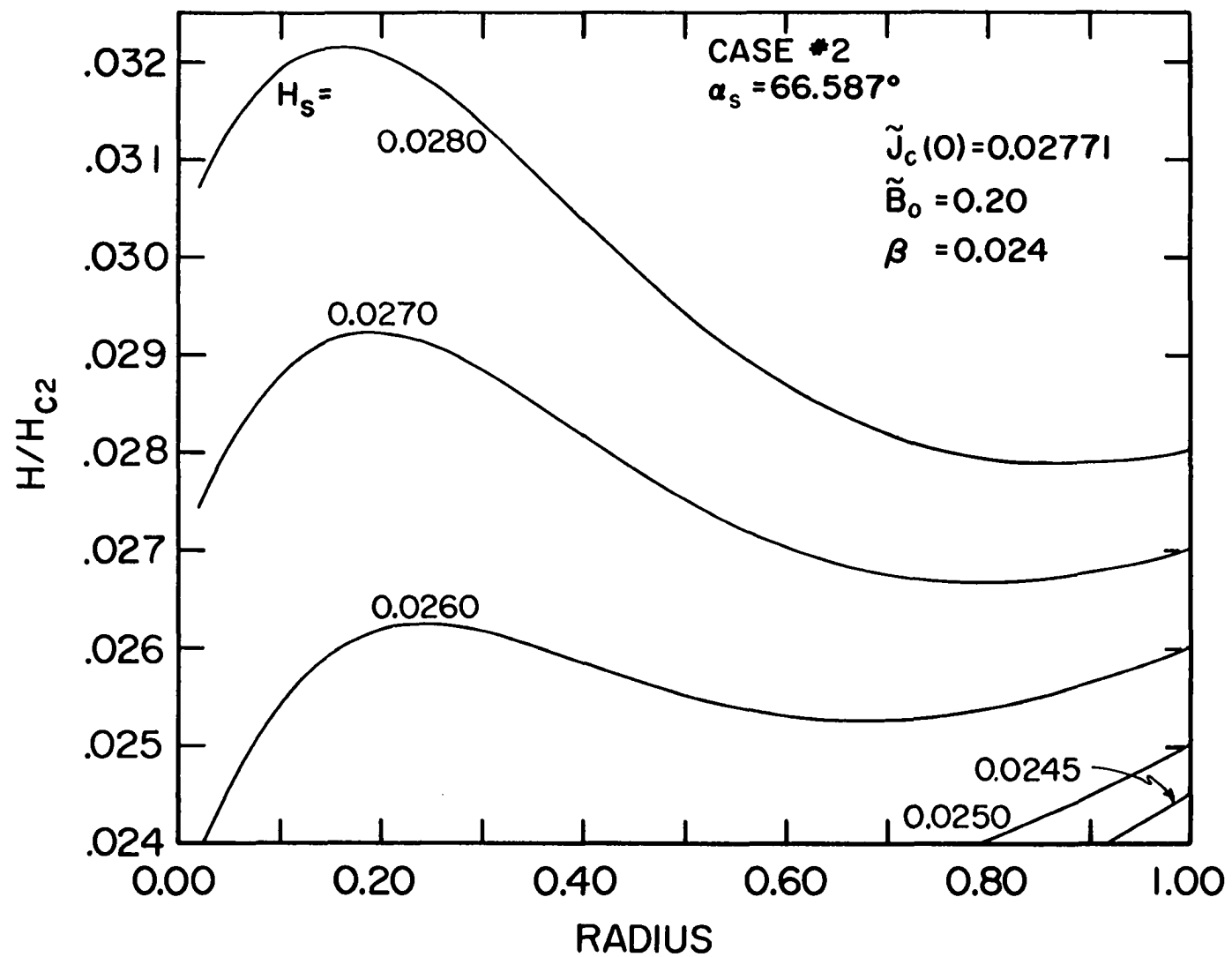
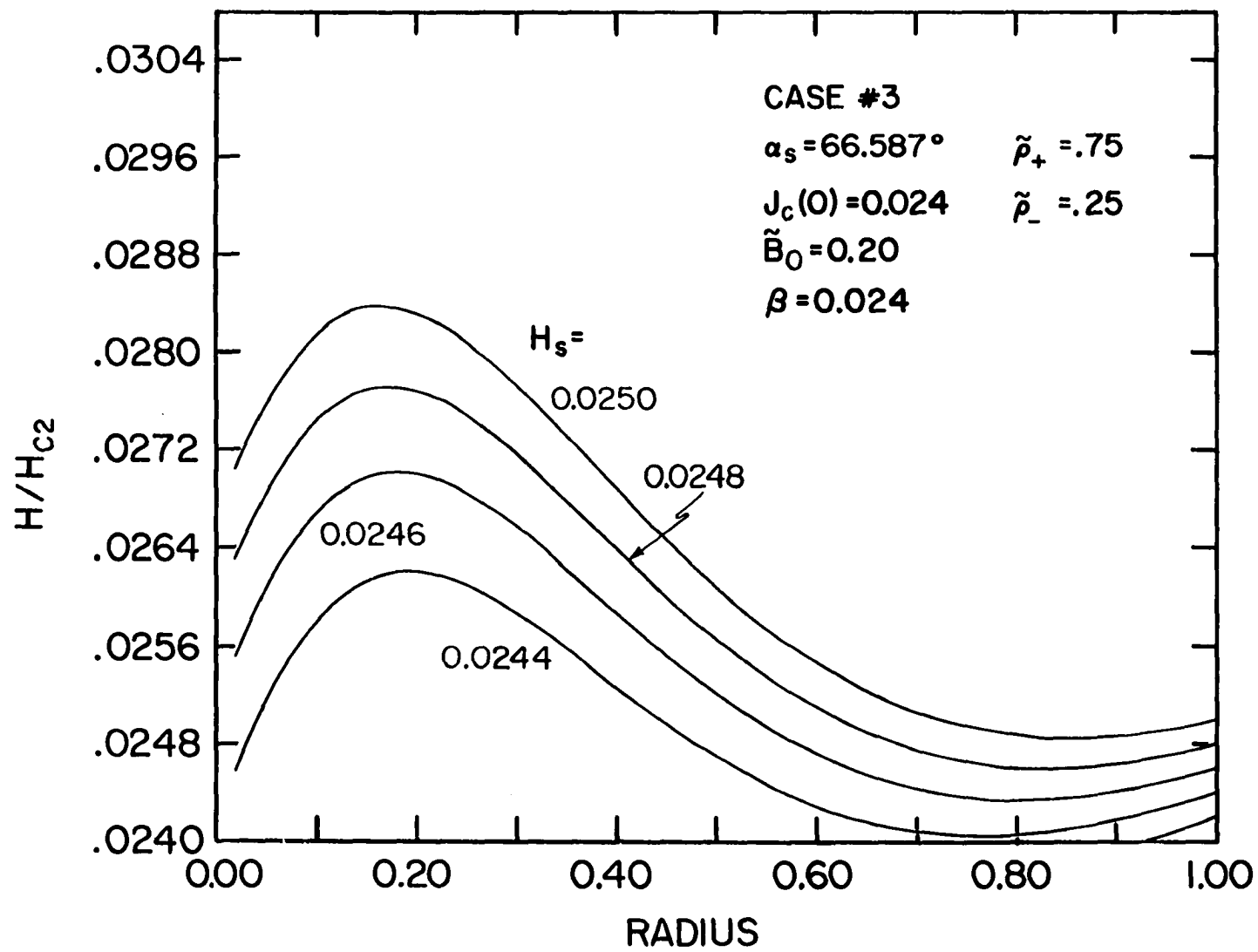


Figure 72. Reduced field profile for material illustrating case #3, spiral collapse, where ρ_+ falls inside the cylinder.
 $\beta = 0.024$, $\tilde{J}_c(0) = 0.024$, $\tilde{B}_0 = 0.20$, and $\alpha_s = 66.587^\circ$.
In this example, $\tilde{\rho}_c = 1.0$



$$\beta = 0.024$$

$$\tilde{J}_c(0) = 0.024$$

$$\tilde{B}_0 = 0.20$$

$$\alpha_s = 66.587^\circ$$

$$\tilde{\rho}_+ = 0.75$$

$$\tilde{\rho}_- = 0.25$$

$$\frac{1}{2}\tilde{\rho}_c = 0.50$$

$$H_S = 0.024 \text{ (no surface pinning) } .$$

Figure 73 illustrates the flux profile obtained from operating a hypothetical material under conditions favoring case #4. Relevant parameters are

$$\beta = 0.024$$

$$\tilde{J}_c(0) = 0.019$$

$$\tilde{B}_0 = 0.20$$

$$\alpha_s = 66.587^\circ$$

$$\tilde{\rho}_+ > 1.0$$

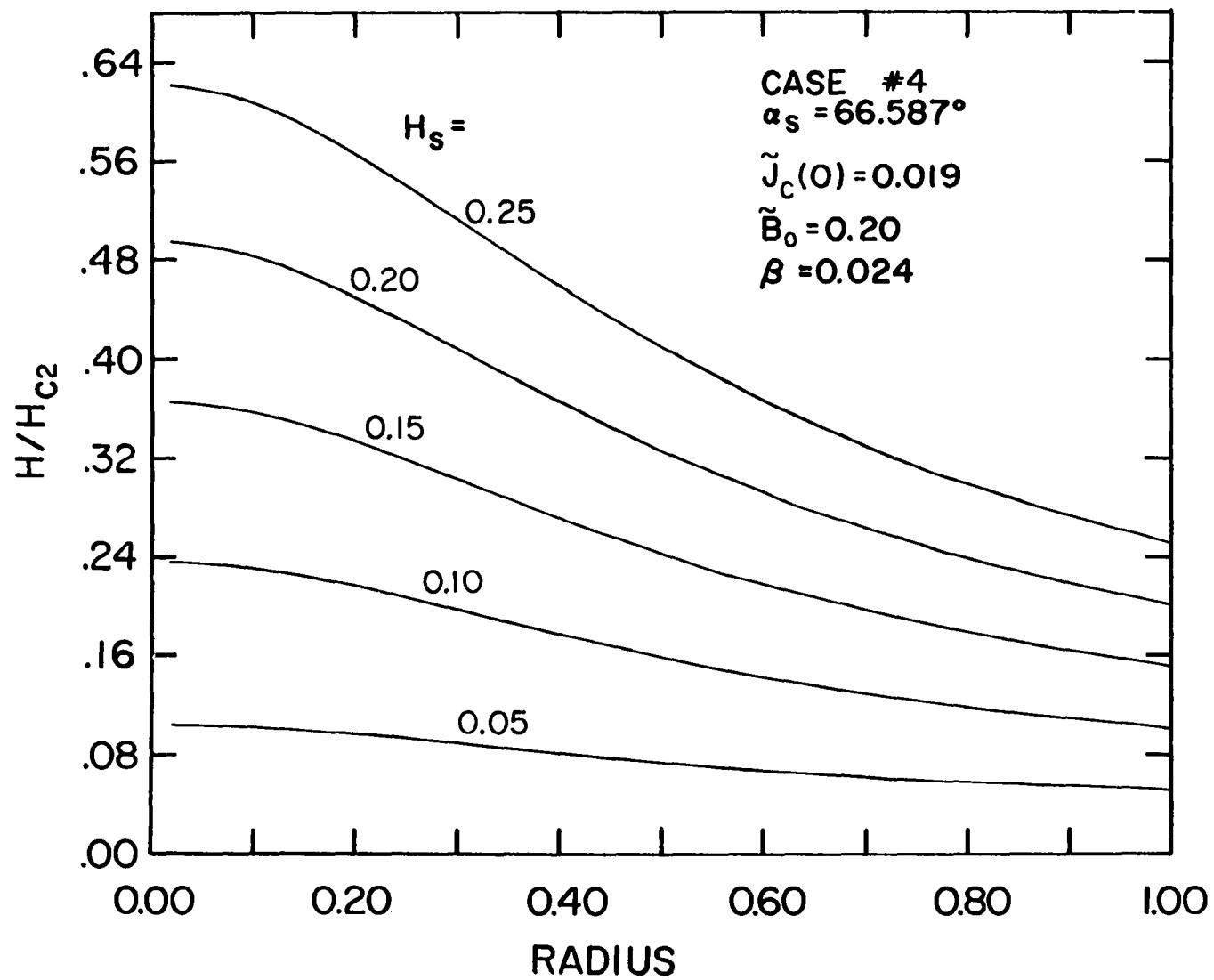
$$\tilde{\rho}_- = 0.1718$$

$$\frac{1}{2}\tilde{\rho}_c = 0.6316$$

$$\tilde{\rho}_c = 1.2632$$

$$\tilde{H}_S = 0.024 \text{ (no surface pinning) } .$$

Figure 73. Reduced field profile for material illustrating case #4, immediate spiral collapse. Here, ρ_+ falls outside the cylinder, so that flux spirals collapse immediately upon nucleation at the surface. $\beta = 0.024$, $\tilde{J}_c(0) = 0.019$, $\tilde{B}_0 = 0.20$, and $\alpha_s = 66.587^\circ$



Next, we consider cases #5 and #6, where $\alpha_s < 45^\circ$. Arbitrarily, we let $\alpha_s = 40^\circ$. Then

$$\tilde{R}_c(a) = \csc^2 40^\circ = 2.4203 \quad .$$

To insure against collapse, $\tilde{\rho}_c < \tilde{R}_c(a)$, so that we require

$$\tilde{\rho}_c = \beta / \tilde{J}_c(0) < 2.4203$$

or

$$\tilde{J}_c(0) > 0.4132\beta \quad .$$

If $\beta = 0.024$, then $\tilde{J}_c(0) > 0.00992$.

To illustrate case #6, where collapse is immediate, we require $\rho_c > R_c(a)$. Thus, we need $\tilde{J}_c(0) < 0.00992$.

Figure 74 illustrates the flux profiles obtained from operating a hypothetical material under conditions favoring case #5. Relevant parameters are

$$\beta = 0.024$$

$$\alpha_s = 40^\circ$$

$$\tilde{J}_c(0) = 0.015$$

$$\tilde{B}_0 = 0.20$$

$$H_S = 0.024 \text{ (no surface pinning)} \quad .$$

Figure 75 illustrates flux profiles obtained from operating a hypothetical material under conditions favoring case #6. Relevant parameters are

$$\beta = 0.024$$

$$\alpha_s = 40^\circ$$

$$\tilde{J}_c(0) = 0.008$$

$$\tilde{B}_0 = 0.20$$

$$\tilde{H}_S = 0.024 \text{ (no surface pinning) } .$$

Figure 74. Reduced field profile for material illustrating case #5, where spiral collapse does not occur. Here $\alpha_s = 40^\circ$ arbitrarily, $\beta = 0.024$, $\tilde{B}_0 = 0.20$, and $\tilde{J}_c(0) = 0.015$. The minimum in $\tilde{R}_c(\tilde{\rho})$ occurs outside the cylinder

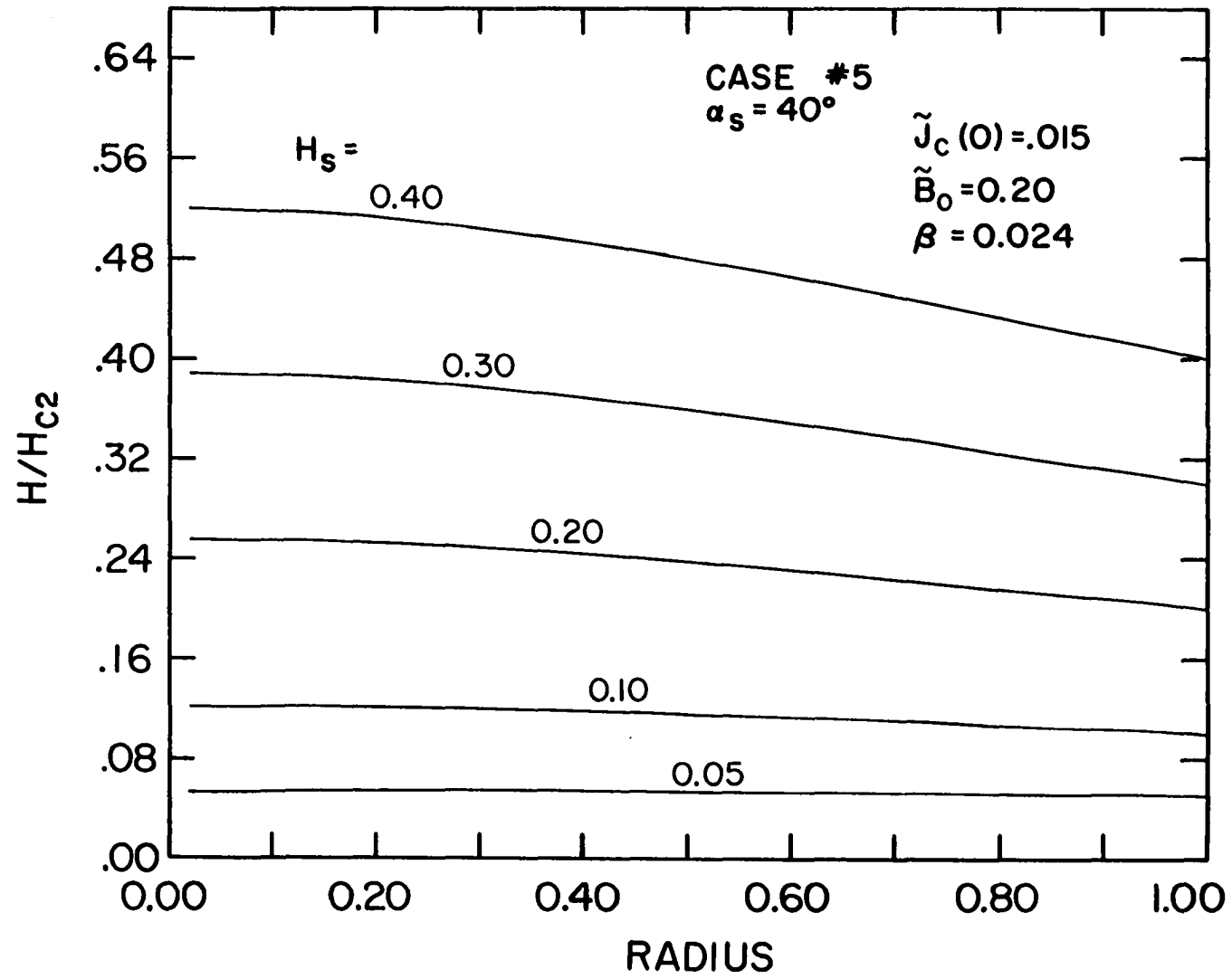
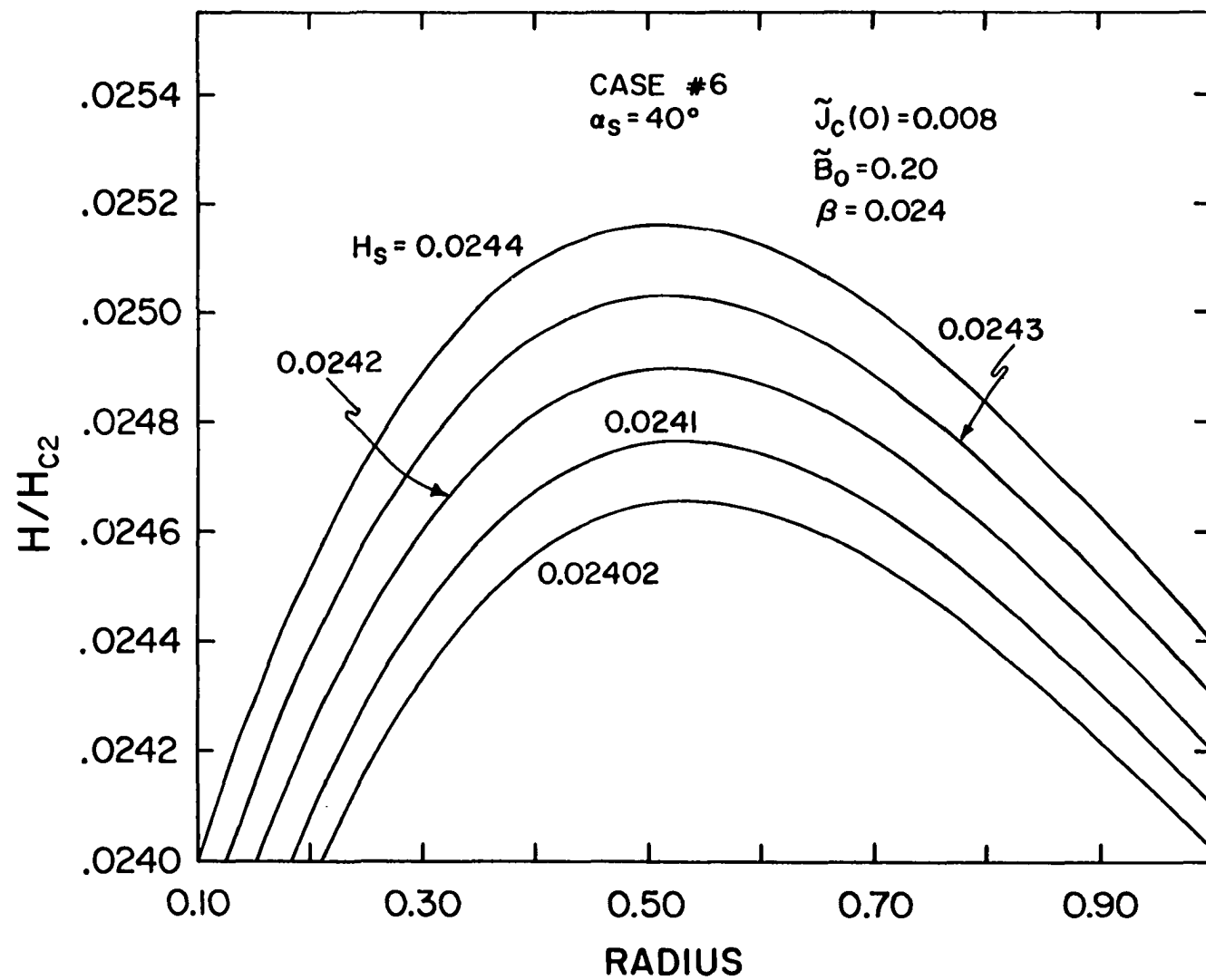


Figure 75. Reduced field profile for material illustrating case #6, where collapse is immediate with first nucleation of vortices at the surface of the cylinder. $\beta = 0.024$, $\alpha_s = 40^\circ$, $\tilde{J}_c(0) = 0.008$, and $\tilde{B}_0 = 0.20$. In this case, the minimum in $R_c(\rho)$ lies outside the cylinder, and $\rho_c(0)$ exceeds $R_c(a)$



IV. PROGRAMMED CURRENT AND FIELD

A. Introductory Remarks

Our previous calculations of the magnetic characteristics of type-II cylinders were based on the assumption that the surface pitch angle of nucleating vortices was always constant. That is, the applied longitudinal field H_{sz} and the azimuthal field $H_{s\phi}$ (due to the transport current) were always in a fixed ratio as the total surface field H_s varied in magnitude.

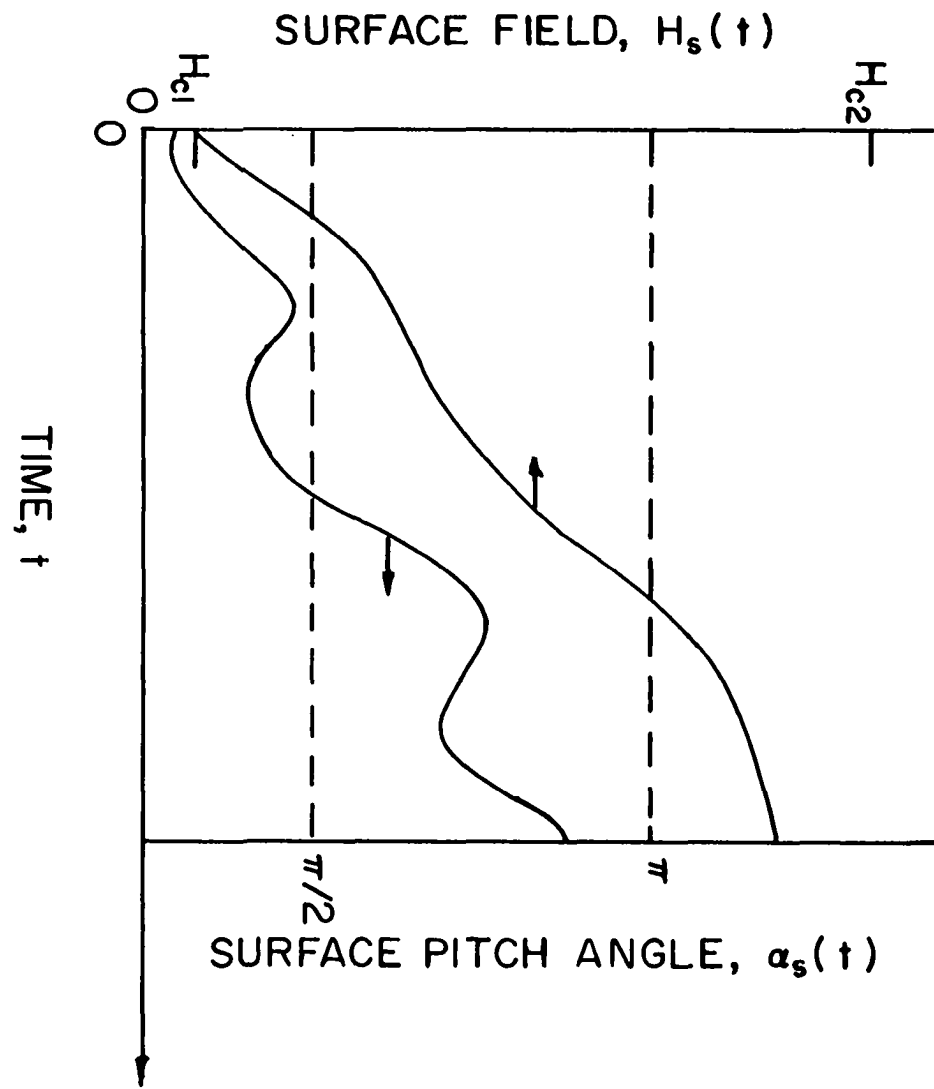
We wish to generalize this procedure to allow for a variation in the surface pitch angle. Specifically, we shall only require that the magnitude of the surface field, H_s , be a monotonically increasing function of time. Within that restriction, the surface pitch angle may vary arbitrarily between zero and 90° . The zero of time is taken to be the point at which flux first penetrates the sample. A sketch of this behavior is shown in Figure 76. The algebraic analysis which follows is due to J. R. Clem.

B. The Fields

In cylindrical coordinates, the surface field is characterized as

$$\vec{H}_s(t) = H_{sz}(t)\hat{z} + H_{s\phi}(t)\hat{\phi} \quad (4.1)$$

Figure 76. Sketch illustrating monotonically increasing magnitude of the surface field, and an arbitrarily changing surface pitch angle. Pitch angle is restricted to the range $0 \leq \alpha_s \leq \pi$, and H_s must not exceed H_{c2}



and the unit vector in the direction of $\vec{H}_S(t)$ is

$$\begin{aligned}\hat{\phi}_S(t) &= \vec{H}_S(t)/H_S(t) \\ &= \hat{z} \cos\alpha_S(t) + \hat{\phi} \sin\alpha_S(t) \quad .\end{aligned}\quad (4.2)$$

We regard the time t as merely a parameter related to the amount of flux that has entered the cylinder. That is, we are not concerned with the time dependence of flux entry, but rather, we solve for the current and flux distribution quasistatically. Here, time allows us to account for the order in which flux lines, at various pitch angles, entered the cylinder.

It is still necessary, however, to relate time with flux entry. Thus, we shall assume the magnitude of the electric field vector at the surface, $\vec{E}_S(t)$, to be constant, no matter how the field is varied. Then

$$E_S = \frac{\phi_0 v'}{c} = h v' / 2e \quad (4.3)$$

where v' is the rate per cm at which vortices, in the direction $\hat{\phi}_S(t)$, enter the cylinder, cutting through a line on the surface perpendicular to $\hat{\phi}_S$.

Referring to the vector diagram in Figure 66, we may also relate the electric field at the surface to the flux line velocity \vec{v} and the value of the field \vec{B} just inside the surface. Josephson (52) has demonstrated that \vec{E} , \vec{B} , and \vec{v}

are related via

$$\vec{E} = \vec{B} \times \vec{v} / c \quad . \quad (4.4)$$

Thus, if $\vec{B}(a,t)$ and $\vec{v}(a,t)$ denote the flux density and flux line velocity just inside the surface of the superconductor, we may write

$$\vec{B}(a,t) = B(a,t) \hat{\theta}_s(t) \quad (4.5a)$$

and

$$\vec{v}(a,t) = v(a,t) \hat{\rho} \quad (4.5b)$$

so that Equation 4.4 becomes

$$\vec{E}_s(t) = - \frac{B(a,t)v(a,t)}{c} \hat{e}_s(t) \quad (4.6)$$

where

$$\begin{aligned} \hat{e}_s(t) &= \vec{E}_s(t) / E_s(t) \\ &= - \hat{\theta} \cos \alpha_s(t) + \hat{z} \sin \alpha_s(t) \quad . \end{aligned} \quad (4.7)$$

As the flux front moves in towards the cylinder axis, the electric field at the penetration radius ρ_p ,

$$\vec{E}(\rho_p, t) = \vec{B}(\rho_p, t) \times \vec{v}(\rho_p, t) / c \quad , \quad (4.8)$$

is always zero, since either $B(\rho_p, t)$ or $v(\rho_p, t)$ must be zero. If $\rho_p > 0$, then $B(\rho_p, t) = 0$, or if the flux front reaches the

center, we have $\rho_p = 0$ and $v(0,t) = 0$.

We next consider the longitudinal flux, Φ_z . Starting with Faraday's law,

$$\vec{\nabla} \times \vec{E} = - \frac{1}{c} \frac{\partial \vec{B}}{\partial t} ,$$

we integrate both sides over the cross section of the cylinder, and apply Stokes' theorem. The result gives

$$E_{s\phi} = - \frac{1}{2\pi ca} \frac{d\Phi_z}{dt} \quad (4.9)$$

or, with the help of Equations 4.3 and 4.6,

$$d\Phi_z/dt = 2\pi a \phi_0 v' \cos \alpha_s(t) . \quad (4.10)$$

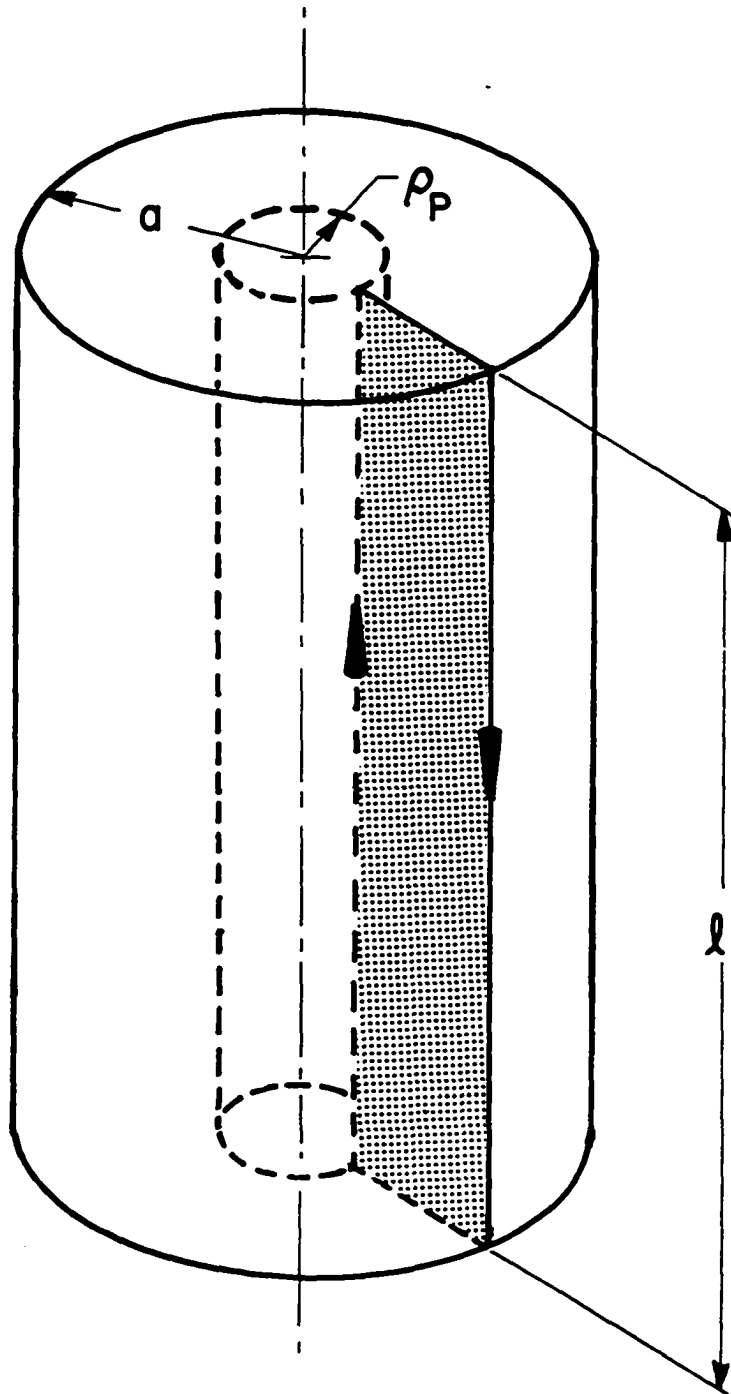
We next consider the aximuthal component of flux, Φ_ϕ . Again from Faraday's law,

$$\vec{\nabla} \times \vec{E} = - \frac{1}{c} \frac{\partial \vec{B}}{\partial t} \quad (4.11)$$

we compute the integral of $\vec{\nabla} \times \vec{E}$ over the path shown in Figure 77. Thus,

$$\begin{aligned} \int \int d\vec{s} \cdot \vec{\nabla} \times \vec{E} &= \oint d\vec{\ell} \cdot \vec{E} \\ &= \ell E_z(\rho_p, t) - \ell E_z(a, t) \\ &= - \frac{1}{c} \ell \frac{d}{dt} \int_{\rho_p}^a d\rho B_\phi(\rho, t) . \end{aligned} \quad (4.12)$$

Figure 77. Sketch illustrating the integration path for evaluating the surface integral of $\vec{\nabla} \times \vec{E}$ in Equation 4.12



Since $B = 0$ for $\rho \leq \rho_p$, and since $\vec{E}_\rho = 0$ everywhere, we obtain

$$E_z(a, t) = \frac{1}{c} \frac{d}{dt} \Phi_\emptyset(t) \quad (4.13)$$

where

$$\Phi_\emptyset = \int_0^a d\rho B_\emptyset(\rho, t) \quad . \quad (4.14)$$

From Equations 4.3 and 4.5 we obtain

$$\frac{d}{dt} \Phi_\emptyset = \emptyset_0 v' \sin \alpha_s(t) \quad . \quad (4.15)$$

We next define a parameter t' , which denotes the time of entry of a flux vortex. Let $\rho(t, t')$ denote the radial coordinate of the vortex at some time t , where $t \geq t'$. Thus, t' identifies a particular vortex. Also, let $L(t')$ denote the pitch length of the vortex which was nucleated at time t' . Then the pitch angle $\alpha(\rho, t)$, where $\rho = \rho(t, t')$, could also be denoted $\alpha'(t, t')$, and is related to the surface pitch angle $\alpha_s(t')$ at the time of entry. Note that at the time of entry, $t = t'$ and $\rho = a$. Also,

$$\alpha(a, t) = \alpha'(t, t) = \alpha_s(t) \quad . \quad (4.16)$$

Referring to the geometry of Figure 18, we may make the identifications

$$\begin{aligned}
L &\rightarrow L(t') \\
\alpha_s &\rightarrow \alpha_s(t') \\
\alpha &\rightarrow \alpha'(t, t') \quad .
\end{aligned} \tag{4.17}$$

Thus, using the trigonometric identifications developed earlier, we have

$$\begin{aligned}
\tan \alpha'(t, t') &= 2\pi \rho(t, t') / L(t') \\
\tan \alpha_s(t') &= 2\pi a / L(t') \\
\tan \alpha'(t, t') &= \frac{\rho(t, t')}{a} \tan \alpha_s(t') \quad .
\end{aligned} \tag{4.18}$$

Thus, using this nomenclature and the force balance equation developed earlier, we have

$$\frac{\partial H(\rho, t)}{\partial \rho} = \frac{4\pi}{c} J_c(\rho, t) - \frac{H(\rho, t) \sin^2 \alpha(\rho, t)}{\rho} \quad . \tag{4.19}$$

Note that $J_c(\rho, t)$ is related to $J_c(B)$ once we obtain a second differential equation relating ρ and t' .

1. Relating ρ , t , and t'

We began this description by assuming that the surface pitch angle is some specified function of time. At some time t , when the flux front has penetrated to some radius $\rho_p(t)$, the time of nucleation of the vortices at ρ_p is $t'(\rho_p, t) = 0$, since these were the first vortices to be nucleated. For any other $\rho \geq \rho_p$, the time of nucleation of the vortices at this

ρ is some function $t'(\rho, t)$. Thus, we may plot $t'(\rho, t)$ versus ρ and obtain something like the illustration in Figure 78a. Note that at the surface, $t'(\rho, t) = t'(a, t) = t$, since these vortices were the last ones nucleated.

Earlier we discussed the meaning of $\rho(t, t')$ as the radial coordinate, at time t , of a vortex that was nucleated at time t' . For example, if $t' = 0$, $\rho(t, 0)$ represents the radial coordinate of the vortex at the flux front, i.e., $\rho(t, 0) = \rho_p(t)$. Similarly, if $t' = t$, we are discussing the very latest vortex, so that $\rho(t, t) = a$. Thus, if $\rho(t, t')$ is plotted against t' (holding t fixed), we might obtain something like the figure sketched in Figure 78b. We see that Figure 78b is just the mirror image of Figure 78a, rotated 90° . In fact,

$$\left. \begin{array}{l} \rho(t, t') \\ t' = t'(\rho, t) \end{array} \right\} = \rho \quad (4.20a)$$

and

$$\left. \begin{array}{l} t'(\rho, t) \\ \rho = \rho(t, t') \end{array} \right\} = t' \quad (4.20b)$$

so that $\rho(t, t')$ may be regarded as the solution of $t'(\rho, t) = t'$, and $t'(\rho, t)$ as the solution of $\rho(t, t') = \rho$. Hence,

$$\frac{\partial t'(\rho, t)}{\partial \rho} = \left[\frac{\partial \rho(t, t')}{\partial t'} \right]^{-1} . \quad (4.21)$$

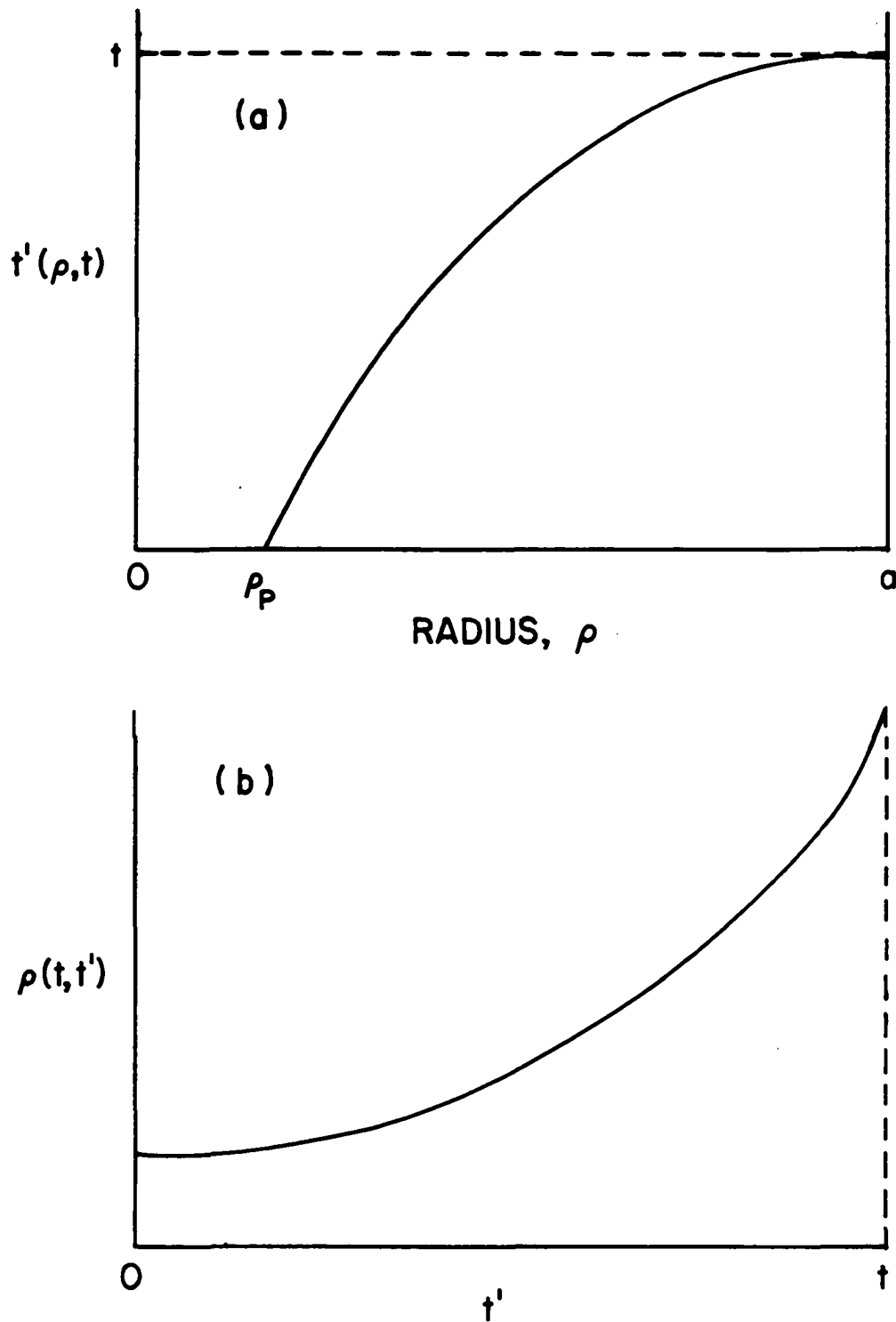


Figure 78. Sketch illustrating relationship of $t'(\rho, t)$ to ρ , and the relationship of $\rho(t, t')$ to t' (see Equation 4.21)

2. Relating t' , ρ , and H

We now seek to develop a relationship among t' , ρ , and H . We start by considering the axial flux contained in the region between ρ and $\rho + d\rho$ at a time t . Then

$$d\Phi_z = 2\pi\rho d\rho B_z(\rho, t) \quad . \quad (4.22)$$

This flux is related to the flux introduced into the specimen during the time interval $t'(\rho, t)$ to $t'(\rho + d\rho, t)$. This time interval has magnitude

$$\begin{aligned} dt' &= t'(\rho + d\rho, t) - t'(\rho, t) \\ &= d\rho \frac{\partial t'(\rho, t)}{\partial \rho} \quad . \end{aligned} \quad (4.23)$$

From Equation 4.10 we see that the flux $d\Phi_z$ introduced during the time interval t' to $t' + dt'$ is

$$d\Phi_z = 2\pi a \phi_0 v' \cos \alpha_s(t') dt' \quad . \quad (4.24)$$

Combining Equations 4.22, 4.23, and 4.24, we obtain

$$\rho B_z(\rho, t) = a \phi_0 v' \cos \alpha_s(t') \frac{\partial t'(\rho, t)}{\partial \rho} \quad . \quad (4.25)$$

We may do a similar operation on $B(\rho, t)$, obtaining

$$B_\theta(\rho, t) = \phi_0 v' \sin \alpha_s(t') \frac{\partial t'(\rho, t)}{\partial \rho} \quad . \quad (4.26)$$

We may now take Equations 4.25 and 4.26 and solve for $\frac{\partial t'(\rho, t)}{\partial \rho}$. The result is

$$\begin{aligned}
\frac{\partial t'(\rho, t)}{\partial \rho} &= \frac{\rho B_z(\rho, t)}{a \varnothing_0 v' \cos \alpha_s(t)} \\
&= \frac{B_\varnothing(\rho, t)}{\varnothing_0 v' \sin \alpha_s(t')} \quad .
\end{aligned} \tag{4.27}$$

Note that

$$\begin{aligned}
\frac{B_\varnothing(\rho, t)}{B_z(\rho, t)} &= \frac{\rho \varnothing_0 v' \sin \alpha_s(t')}{a \varnothing_0 v' \cos \alpha_s(t')} \\
&= \frac{\rho}{a} \tan \alpha_s(t') \\
&= \tan \alpha(\rho, t)
\end{aligned} \tag{4.28}$$

as was shown earlier.

Next, we use Equation 4.27 to express $B_\varnothing(\rho, t)$ as

$$B_\varnothing(\rho, t) = B(\rho, t) \sin \alpha(\rho, t) \tag{4.29}$$

and then obtain

$$\frac{\partial t'(\rho, t)}{\partial \rho} = \frac{B(\rho, t) \sin \alpha(\rho, t)}{\varnothing_0 v' \sin \alpha_s(\rho, t)} \quad . \tag{4.30}$$

The factor $\sin \alpha(\rho, t)$ may be removed from Equation 4.30 by use of the following trigonometric identity, which can be derived from Figure 18:

$$\begin{aligned}
\sin \alpha(\rho, t) &= \rho \sin \alpha_s(t') / [\rho^2 \sin^2 \alpha_s(t') \\
&\quad + a^2 \cos^2 \alpha_s(t')]^{1/2}
\end{aligned} \tag{4.31}$$

yielding

$$\frac{\partial t'(\rho, t)}{\partial \rho} = \frac{B(\rho, t)}{\emptyset_0 v'} \cdot \frac{\rho}{\sqrt{\rho^2 \sin^2 \alpha_s(t') + a^2 \cos^2 \alpha_s(t')}} \quad (4.32)$$

Similarly, using Equation 4.31 we may also reexpress Equation 4.19, the fundamental differential equation relating H and ρ , as

$$\frac{\partial H(\rho, t)}{\partial \rho} = \frac{4\pi}{c} J_c(\rho, t) - \frac{H(\rho, t) \sin^2 \alpha_s(t')}{\rho^2 \sin^2 \alpha_s(t') + a^2 \cos^2 \alpha_s(t')} \quad (4.33)$$

where it is understood that $t' = t'(\rho, t)$. Suppressing the time t to simplify the notation, we end up with the pair of simultaneous differential equations

$$\frac{\partial t'(\rho)}{\partial \rho} = \frac{\rho B(\rho)}{\emptyset_0 v'} [\rho^2 \sin^2 \alpha_s(t') + a^2 \cos^2 \alpha_s(t')]^{-1/2} \quad (4.34a)$$

$$\frac{\partial H(\rho)}{\partial \rho} = \frac{4\pi}{c} J_c[B(\rho)] - \frac{\rho H(\rho) \sin^2 \alpha_s(t')}{\rho^2 \sin^2 \alpha_s(t') + a^2 \cos^2 \alpha_s(t')} \quad (4.34b)$$

which may be numerically integrated to obtain $H(\rho)$ and $t'(\rho)$. See Figure 79.

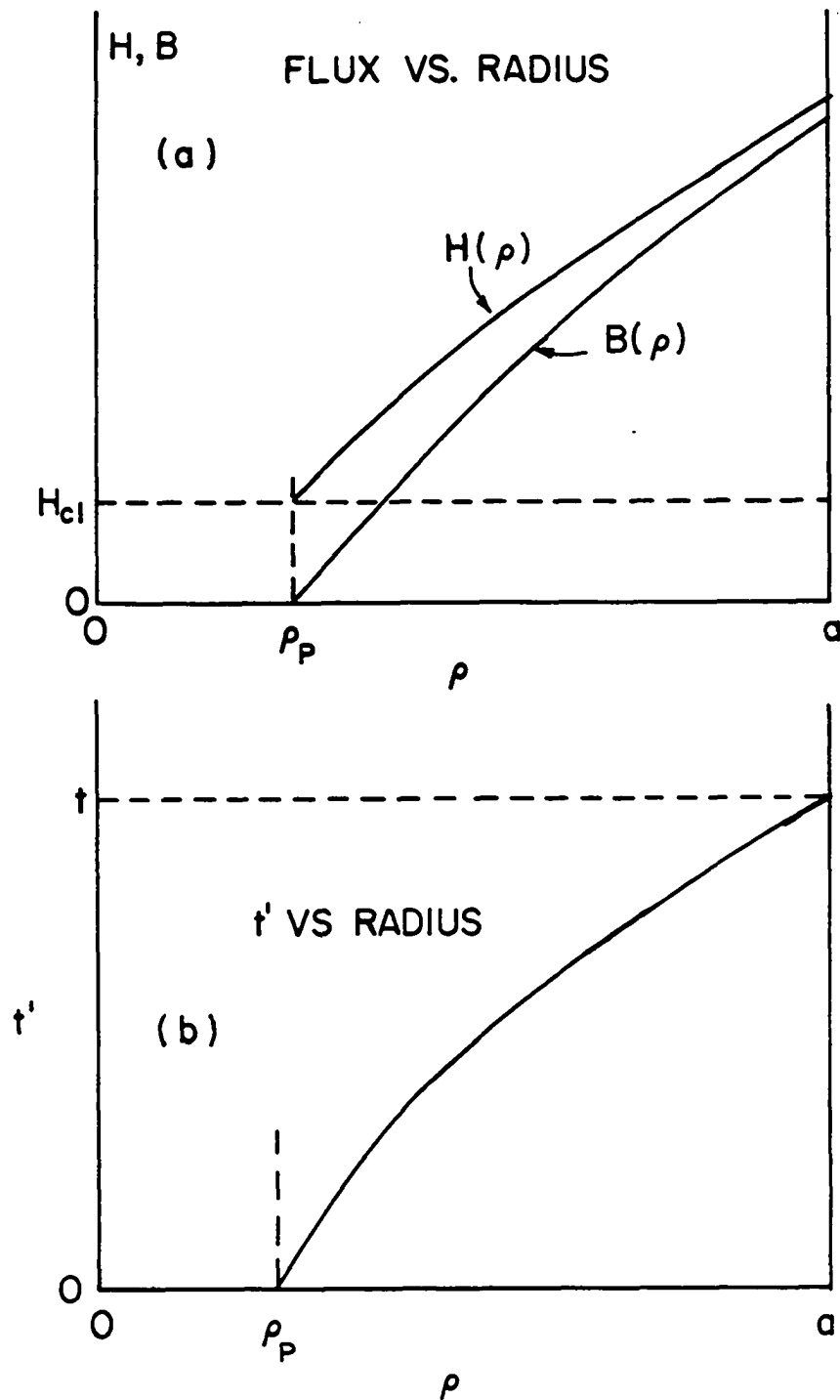


Figure 79. Sketch to illustrate hypothetical profiles of $H(\rho)$ versus ρ , and $t'(\rho)$ versus ρ , obtained from simultaneous integration of Equations 4.34

C. Instabilities

At the flux front with $\rho_p > 0$, where $B = 0$ and $H = H_{c1}$, a stable solution requires $\frac{\partial H}{\partial \rho} > 0$. That is, as seen from Equation 4.34, we must have

$$\frac{4\pi}{c} J_c(0) > \frac{H_{c1} \rho_p \sin^2 \alpha_s}{\rho_p^2 \sin^2 \alpha_{so} + a^2 \cos^2 \alpha_{so}}, \quad (4.35)$$

where α_{so} denotes the pitch angle of the very first vortices which had penetrated the sample. With $\rho_c = cH_{c1}/4\pi J_c(0)$, the above inequality may be rewritten as

$$\rho_p + \frac{a^2 \cot^2 \alpha_{so}}{\rho_p} > \rho_c. \quad (4.36)$$

For ρ_p decreasing toward zero, the left-hand side of this last inequality experiences a minimum at

$$\rho_p = a |\cot \alpha_{so}|. \quad (4.37)$$

Thus, the inequality required for stability will be satisfied for all values of ρ_p only if

$$2a |\cot \alpha_{so}| \geq \rho_c. \quad (4.38)$$

Typically, ρ_c is very small, and for such cases the inequality will be violated and an instability will occur only where $|\alpha_{so}| \sim \pi/2$.

D. Flux Accumulation and Reduced Quantities

The total axial flux $\bar{\Phi}_z(t)$ and azimuthal flux $\bar{\Phi}_\theta(t)$ are easily computed by integrating Equations 4.10 and 4.15:

$$\bar{\Phi}_z(t) = 2\pi a \theta_o v' \int_0^t dt' \cos \alpha_s(t') \quad (4.39)$$

and

$$\bar{\Phi}_\theta(t) = \theta_o v' \int_0^t dt' \sin \alpha_s(t') \quad . \quad (4.40)$$

These integrals are attainable, since we presumably know the variation of α_s with time.

To obtain reduced quantities, we consider the case where $\alpha_s = 0$, and denote t_{\max} as the time at which the axial flux is at the largest value of interest, $\rho a^2 H_{c2}$. Then Equation 4.39 yields

$$\pi a^2 H_{c2} = \bar{\Phi}_{z\max} = 2\pi a \theta_o v' t'_{\max} \quad (4.41)$$

so that

$$t'_{\max} = a^2 H_{c2} / 2\pi a \theta_o v' = a H_{c2} / 2\theta_o v' \quad . \quad (4.42)$$

Next, we define the reduced time \tilde{t}' as

$$\tilde{t}' = t' / t'_{\max} \quad . \quad (4.43)$$

Then Equations 4.34 may be expressed in reduced form as

$$\frac{\partial \tilde{t}'}{\partial \tilde{\rho}} = 2\tilde{\rho}\tilde{B}(\tilde{\rho})[\tilde{\rho}^2\sin^2\alpha_o(\tilde{t}') + \cos^2\alpha_s(\tilde{t}')]^{-1/2}$$

$$\frac{\partial \tilde{H}}{\partial \tilde{\rho}} = \tilde{J}_c - \frac{\tilde{\rho}\tilde{H}(\tilde{\rho})\sin^2\alpha_s(\tilde{t}')}{\tilde{\rho}^2\sin^2\alpha_s(\tilde{t}') + \cos^2\alpha_s(\tilde{t}')} \quad (4.44)$$

In solving Equation 4.44 simultaneously, we start with some assumed penetration radius, $\tilde{\rho}_p$. At this point, $\tilde{t}' = 0$ and $\tilde{H} = \tilde{H}_{c1}$. Integration proceeds via a Runge-Kutta numerical method (45), advancing $\tilde{\rho}$ from $\tilde{\rho}_p$ on out to $\tilde{\rho} = 1$. Along the way, we rely on tabulated values or functionally derived values of $\alpha_s(\tilde{t}')$. When the outer edge is reached, $\tilde{\rho} = 1$, $\tilde{t}' = \tilde{t}$, so that the choice of $\tilde{\rho}_p$ implicitly dictates \tilde{t} . Figure 79 illustrates a possible integration path in the \tilde{H} versus $\tilde{\rho}$ plane, and in the \tilde{t}' versus $\tilde{\rho}$ plane.

V. CONCLUSIONS AND PROBLEMS FOR FURTHER RESEARCH

A. Standardized Research Procedure

In all of the preceding, we have neglected end effects in order to obtain a simplified model with no z -dependencies. Within that limitation our model represents the best physically justifiable means of computing the macroscopic properties of a current-carrying type-II cylinder in an axial field.

The programmed current and field model (PCAF) is still in its infancy and remains to be proven. One difficulty in applying the PCAF model is that organized and collated data does not exist. It would be useful, then, to develop and ratify among a consensus of active experimenters a standardized experimental procedure for performing and recording magnetization experiments on type-II cylinders. Such a standard would follow in spirit the ASTM book of standard test procedures, as an example. In such a standardized procedure one might include the requirement for measurement of all the important material parameters, such as H_{c1} , H_{c2} , κ , critical current, and surface pinning qualities. In addition, this procedure would specify the surface field components $H_{s\phi}$ and H_{sz} at all phases of the experiment, since we are dealing with a history-dependent phenomenon. Also, the field-increasing situation ought to be carefully separated from the field-

decreasing case, since the behavior of the specimen is very much different in each case.

B. The Boundary Condition Problem

The flux exiting situation gives rise to a vexing problem with regard to the appropriate boundary conditions at the cylinder surface. To see this, suppose that a sample is filled with flux spirals, all of which entered at some well-defined surface pitch angle, α_s . Now change the current and axial field to produce a different surface pitch angle, and at the same time, reduce slowly the magnitude of the surface field. As the magnitude of the surface field is reduced, flux spirals will begin to exit from the sample. However, the exiting flux spirals will have a different pitch angle than the extant surface field, raising the question of how to resolve the discontinuity in the tangential component of \vec{H} that would occur. Clearly, there can be no discontinuity in the tangential components of \vec{H} , suggesting that either flux cutting, flux rotation, or some yet unpostulated mechanism of flux reorientation must occur very near to the surface.

C. The Critical Current Problem

From an experimental viewpoint, the critical current is that current at which a stable mixed state undergoes break-

down into either a flux-flow regime or the normal state. As was discussed in Chapter III, the present criterion for defining the critical current (i.e., when H_{c2} is first exceeded somewhere in the sample), when applied to the data of Timms and Walmsley (39), yields a critical current larger than that measured experimentally by a factor of approximately two. We do not at present understand the reason for this discrepancy.

Timms and Walmsley (39) used a modified form of the present theory in an attempt to calculate the critical current, and found a similar discrepancy with the measured values. They thus adopted the different theoretical criterion that the critical current is achieved when flux penetrates to the axis. They noted, however, that penetration to the axis is not necessarily a sufficient criterion for normalization. It appears that Timms and Walmsley's calculation of the penetration current is motivated by their feeling that the constant pitch model loses its applicability beyond this point. However, as we have shown in this work, the constant pitch model does retain its validity beyond the point where the flux front first reaches the cylinder axis. We thus see no physical justification for Timms and Walmsley's criterion for the critical current.

Gauthier (53, p. 4-23) has applied a constant-pitch model to his experimental conditions, and has found that our

criterion defining the critical current (i.e., when H_{c2} is first exceeded somewhere in the sample) yielded higher calculated critical current values than he observed experimentally.

Additional work remains before we may discover the reason for the discrepancy between the calculated and measured critical current values. Possibly fruitful areas for study are end effects, intermediate state structures, flux cutting, flux rotation, and instabilities.

VI. BIBLIOGRAPHY

1. C. J. Bergeron, Appl. Phys. Letters 3, 63 (1963).
2. C. J. Bergeron, S. T. Sekula, and R. W. Boom, Appl. Phys. Letters 2, 102 (1963).
3. B. S. Chandrasekhar, in Superconductivity, edited by R. D. Parks (Marcel Dekker, Inc., New York, 1969), vol. 1.
4. Z. M. Galasiewicz, Superconductivity and Quantum Fluids (Pergamon Press, London, England, 1970).
5. J. M. Blatt, Theory of Superconductivity (Academic Press, New York, 1964).
6. V. L. Newhouse, Applied Superconductivity (John Wiley and Sons, Inc., New York, 1964).
7. J. E. C. Williams, Superconductivity and its Applications (Pion Limited, London, England, 1970).
8. C. G. Kuper, An Introduction to the Theory of Superconductivity (Clarendon Press, Oxford, England, 1968).
9. E. A. Lynton, Superconductivity (Methuen and Company, Ltd., London, England, 1969), 3rd ed.
10. P. G. DeGennes, Superconductivity of Metals and Alloys (W. A. Benjamin, Inc., New York, 1966).
11. D. Saint James, E. J. Thomas, and G. Sarma, Type II Superconductivity (Pergamon Press, Oxford, England, 1969).
12. F. London, Superfluids (Dover Publications, Inc., New York, 1961), vol. 1, 2nd revised ed.
13. D. Shoenberg, Superconductivity (Cambridge University Press, Cambridge, England, 1965), 2nd ed.
14. H. K. Onnes, Leiden Comm. 1206, 1226 (1911), Suppl. 34, (1913); quoted in D. Shoenberg, Superconductivity (Cambridge, New York, 1952), p. 1.
15. D. J. Quinn III and W. B. Ittner III, J. Appl. Phys. 33, 748 (1962).

16. W. Meissner and R. Ochsenfeld, *Naturwissenschaften* 21, 787 (1933).
17. B. S. Deaver and W. M. Fairbank, *Phys. Rev. Letters* 7, 43 (1961).
18. R. Doll and M. Nabauer, *Phys. Rev. Letters* 7, 51 (1961).
19. V. L. Ginzburg and L. D. Landau, *Zh. Eksperim. i. Teor. Fiz.* 20, 1064 (1950).
20. A. A. Abrikosov, *Zh. Eksperim. i. Teor. Fiz.* 32, 1442 (1957) [English transl.: *Soviet Phys. - JETP* 2, 1174 (1957)].
21. A. M. Campbell and J. E. Evetts, *Critical Currents in Superconductors* (Taylor and Francis, Ltd., London, 1972), p. 15.
22. E. W. Urban, *J. Appl. Phys.* 42, 115 (1971).
23. C. P. Bean, *Phys. Rev. Letters* 8, 250 (1962).
24. H. London, *Phys. Letters* 6, 162 (1963).
25. Y. B. Kim, C. F. Hempstead, and A. R. Strnad, *Phys. Rev.* 129, 528 (1963).
26. P. W. Anderson, *Phys. Rev. Letters* 9, 309 (1962).
27. J. Friedel, *Appl. Phys. Letters* 2, 119 (1963).
28. J. Silcox and R. Rollins, *Appl. Phys. Letters* 2, 231 (1963).
29. K. Yasukochi, T. Ogasawara, U. Namubitsu, and S. Uskio, *J. Phys. Soc. Japan* 19, 1649 (1964).
30. F. Irie and K. Yamafuji, *J. Phys. Soc. Japan* 23, 255 (1967).
31. W. A. Fietz, M. R. Beasley, J. Silcox, and W. W. Webb, *Phys. Rev.* 136, A335 (1964).
32. J. H. Goedemoed, P. H. Kes, F. Th. A. Jacobs, and D. DeKlerk, *Physica* 35, 273 (1967).

33. T. H. Alden and J. D. Livingston, J. Appl. Phys. 37, 3551 (1966).
34. A. M. Campbell, J. E. Evetts, and D. Dew-Hughes, Phil. Mag. 18, 313 (1968).
35. H. T. Coffey, Phys. Rev. 166, 447 (1968).
36. Y. B. Kim, C. F. Hempstead, and A. R. Strnad, Phys. Rev. Letters 9, 306 (1962).
37. M. A. R. LeBlanc, B. C. Belanger, and R. M. Fielding, Phys. Rev. Letters 14, 704 (1965).
38. J. R. Clem, Dept. of Physics, Iowa State University, Ames, Iowa; unpublished.
39. W. E. Timms and D. G. Walmsley, J. Phys. F: Metal Physics 5, 287 (1975).
40. J. R. Clem, J. Low Temp. Phys. 18, 427 (1975).
41. L. Neumann and L. Tewordt, Z. Phys. 189, 55 (1966).
42. P. G. DeGennes, Solid State Comm. 3, 127 (1965).
43. C. P. Bean and J. D. Livingston, Phys. Rev. Letters 12, 14 (1964).
44. J. R. Clem, in Low Temperature Physics - LT13, vol. 3, edited by K. D. Timmerhaus, W. J. O'Sullivan, and E. F. Hammel (Plenum Publishing Corp., New York, 1974), pp. 102-6.
45. J. D. Scarborough, Numerical Mathematical Analysis (The Johns Hopkins Press, Baltimore, 1962), 5th ed., pp. 357-9.
46. H. Voight, Zeitschrift für Physik 213, 119 (1968).
47. J. J. Wollan, K. W. Haas, John R. Clem, and D. K. Finnemore, Phys. Rev. B 10, 1874 (1974).
48. J. R. Clem, H. R. Kerchner, and S. T. Sekula, Phys. Rev. B 14, 1893 (1976).

49. Y. B. Kim and M. J. Stephen, in Superconductivity, edited by R. D. Parks (Marcel Dekker, Inc., New York, 1969), vol. 2, p. 1138.
50. R. C. Weast, general editor, Handbook of Chemistry and Physics, (The Chemical Rubber Company, Cleveland, Ohio, 1972), 53rd ed., p. F145.
51. K. W. Haas, M. S. Thesis, unpublished, Iowa State University, Ames, Iowa, 1973.
52. B. D. Josephson, Phys. Letters 16, 242 (1965).
53. R. Gauthier, Ph.D. Thesis, unpublished, University of Ottawa, Ottawa, Canada, 1976.

VII. ACKNOWLEDGMENTS

The author is most pleased to acknowledge the debt he owes to his principal advisor, Professor John R. Clem. Without his patience, remarkable insight, and tireless energies, this work would not have come to fruition.

Thanks are also due to the personnel of the Ames Laboratory Computer Services Group, who rendered very generous and competent assistance with the numerous programming difficulties encountered during this research. In particular, the author would like to cite Dennis Jensen, Leonard Moon, Elaine Notis, and Tom Pinter.

The author also wishes to thank the personnel of the Ames Laboratory Graphics Department, who did such a fine job in drawing the numerous graphs and figures needed in this presentation. In particular, the author is most grateful to Miss Agnes K. Oh for her special efforts in this regard.

Warm thanks are also due to Mrs. Marlys Phipps of Ames, Iowa, who did such a very excellent job in the typing of the manuscript. Her careful attention to details and extreme patience with a very difficult text deserve recognition.

Finally, in no small way, the author would like to express his delight and appreciation for his wife Roberta, who put up with it all, and saw it through.

VIII. APPENDIX A. RADIUS OF CURVATURE
OF A FLUX SPIRAL

We compute the radius of curvature of a spiral of radius ρ , pitch L , and pitch angle with respect to the z -axis of α .

Let \vec{R} be a vector from the origin of coordinates to any point on the spiral. Then in rectangular coordinates \hat{i} , \hat{j} , \hat{k} ,

$$\vec{R} = \rho \cos \theta \hat{i} + \rho \sin \theta \hat{j} + k \theta \hat{k} \quad . \quad (\text{A.1})$$

In one turn about the spiral, the \hat{k} coordinate must change by an amount equal to the pitch length L , and the azimuthal coordinate changes by 2π radians. Thus,

$$2\pi k = L \quad (\text{A.2})$$

so that

$$k = L/2\pi = \rho \cot \alpha \quad . \quad (\text{A.3})$$

Now let \hat{T} be a unit vector tangent to the spiral at the point \vec{R} . Then

$$\hat{T} = d\vec{R}/ds \quad (\text{A.4})$$

where ds is an infinitesimal length of arch along the spiral.

Thus,

$$\hat{T} = d\vec{R}/ds = (-\rho \sin \theta \frac{d\theta}{ds}) \hat{i} + (\rho \cos \theta \frac{d\theta}{ds}) \hat{j} + k \frac{d\theta}{ds} \hat{k} \quad . \quad (\text{A.5})$$

Now

$$d\varnothing/ds = (d\varnothing/dc) \cdot (dc/ds) \quad (\text{A.6})$$

where c is the projection of the spiral onto the XY plane. Clearly, $d\varnothing/dc = \rho^{-1}$, and $dc/ds = \sin\alpha$, so that $d\varnothing/ds = \sin\alpha/\rho$. Then we may write \hat{T} as

$$\hat{T} = (-\sin\varnothing\sin\alpha)\hat{i} + (\cos\varnothing\sin\alpha)\hat{j} + \frac{k\sin\alpha}{\rho} \hat{k} . \quad (\text{A.7})$$

However,

$$k\sin\alpha/\rho = \cot\alpha\sin\alpha = \cos\alpha \quad (\text{A.8})$$

so that \hat{T} becomes

$$\hat{T} = (-\sin\varnothing\sin\alpha)\hat{i} + (\cos\varnothing\sin\alpha)\hat{j} + \cos\alpha \hat{k} \quad (\text{A.9})$$

and therefore

$$\begin{aligned} d\hat{T}/ds &= (-\sin\alpha\cos\varnothing \frac{d\varnothing}{ds})\hat{i} - (\sin\alpha\sin\varnothing \frac{d\varnothing}{ds})\hat{j} \\ &= (-\frac{\sin^2\alpha}{\rho} \cos\varnothing)\hat{i} - (\frac{\sin^2\alpha\sin\varnothing}{\rho})\hat{j} \\ &= -\frac{\sin^2\alpha}{\rho}[(\cos\varnothing)\hat{i} + (\sin\varnothing)\hat{j}] \\ &= (-\hat{\rho}) \frac{\sin^2\alpha}{\rho} \end{aligned} \quad (\text{A.10})$$

where $(-\hat{\rho})$ is a vector lying in the XY plane pointing from the spiral towards the axis. We recognize $d\hat{T}/ds$ as the rate

of change of the unit tangent, per unit change in arc, whose magnitude is the inverse of the radius of curvature. Thus,

$$1/R_c = \sin^2 \alpha / \rho \quad . \quad (A.11)$$

IX. APPENDIX B. LINE TENSION IN VORTEX RING

We compute here the force per unit length on a quantized vortex ring arising from line tension. Thermodynamics relates the energy per unit length ϵ of an isolated, singly quantized fluxoid, to the lower critical field H_{c1} via

$$\epsilon = \frac{\phi_0 H_{c1}}{4\pi} , \quad (B.1)$$

where ϕ_0 is the flux quantum. Thus, for a fluxoid in the shape of a ring of radius ρ , the total energy in the ring is

$$\begin{aligned} E &= \frac{\phi_0 H_{c1}}{4\pi} \cdot (2\pi \rho) \\ &= \frac{1}{2} \phi_0 H_{c1} \rho . \end{aligned} \quad (B.2)$$

A net force \vec{T} arising from line tension in the ring, which tends to collapse the ring, is related to the energy via

$$\begin{aligned} \vec{T} &= - \vec{\nabla} E \\ &= - \frac{1}{2} H_{c1} \phi_0 \hat{\rho} , \end{aligned} \quad (B.3)$$

where the minus sign indicates an inward-directed force.

Thus, the corresponding force per unit length of vortex \vec{t} is

$$\begin{aligned} \vec{t} &= - \frac{1}{2} \phi_0 H_{c1} \hat{\rho} / 2\pi \rho \\ &= - \frac{\phi_0 H_{c1}}{4\pi \rho} \hat{\rho} . \end{aligned} \quad (B.4)$$

The ring is stable against collapse whenever this force per unit length does not exceed the pinning forces per unit length, which tend to oppose the collapse. Thus, for stability against collapse, we require

$$J_c \phi_0 / c > \phi_0 H_{cl} / 4\pi \rho \quad (\text{B.5})$$

where the quantity $J_c \phi_0 / c$ represents the pinning force density per unit length. We see that the critical radius ρ_c , which is the smallest radius which the ring may have before collapse, is

$$\rho_c = c H_{cl} / 4\pi J_c \quad . \quad (\text{B.6})$$

X. APPENDIX C. DERIVATION OF BESSEL
FUNCTION SOLUTION

Derivation of the Bessel function solution from Equation 1.56. In the force-free state, we have that \vec{J} is parallel to \vec{H} , so that we may write

$$\vec{J} = \frac{ck(\rho)}{4\pi} \vec{H} \quad . \quad (C.1)$$

However, from Ampere's law,

$$\vec{J} = \frac{c}{4\pi} \vec{\nabla} \times \vec{H} \quad . \quad (C.2)$$

Combining Equations C.1 and C.2 we obtain

$$\begin{aligned} J_{\theta} &= \frac{ck(\rho)}{4\pi} H \sin \alpha \\ J_z &= \frac{ck(\rho)}{4\pi} H \cos \alpha \quad . \end{aligned} \quad (C.3)$$

Thus,

$$\begin{aligned} k(\rho) H \sin \alpha &= - \frac{\partial H_z}{\partial \rho} \\ k(\rho) H \cos \alpha &= \frac{1}{\rho} \frac{\partial}{\partial \rho} (\rho H_{\theta}) \end{aligned}$$

or

$$\begin{aligned} k(\rho) H \sin \alpha &= - \frac{\partial}{\partial \rho} (H \cos \alpha) \\ &= - \frac{\partial H}{\partial \rho} \cos \alpha + H \sin \alpha \frac{\partial \alpha}{\partial \rho} \quad . \end{aligned} \quad (C.4)$$

In the force-free limit, however,

$$\partial H / \partial \rho = - H \sin^2 \alpha / \rho \quad (\text{C.5})$$

so that we obtain Equation 1.55:

$$k(\rho) = \sin \alpha \cos \alpha / \rho + \frac{\partial \alpha(\rho)}{\partial \rho} \quad (\text{C.6})$$

In the case where $k(\rho) = k$, a constant, Equation C.6 yields

$$\frac{\partial \alpha(\rho)}{\partial \rho} + \frac{\sin \alpha(\rho) \cos \alpha(\rho)}{\rho} = k, \text{ a const.} \quad (\text{C.7})$$

A solution to Equation C.7 is

$$\alpha = \tan^{-1}[J_1(k\rho)/J_0(k\rho)] \quad , \quad (\text{C.8})$$

as may be seen from the following argument. Differentiate $\alpha(\rho)$ to obtain

$$\frac{\partial \alpha(\rho)}{\partial \rho} = k - \frac{J_0(k\rho)J_1(k\rho)}{\rho[J_0^2(k\rho) + J_1^2(k\rho)]} \quad (\text{C.9})$$

using the various relationships between Bessel function derivatives. Noting that

$$\sin \alpha = J_1(k\rho)/[J_0^2(k\rho) + J_1^2(k\rho)]^{1/2} \quad (\text{C.10})$$

and

$$\cos \alpha = J_0(k\rho)/[J_0^2(k\rho) + J_1^2(k\rho)]^{1/2} \quad (\text{C.11})$$

we have that

$$\sin\alpha\cos\alpha = J_0 J_1 / [J_0^2 + J_1^2] \quad . \quad (C.12)$$

Thus,

$$\begin{aligned} \frac{\partial \alpha(\rho)}{\partial \rho} &= k - \frac{\sin\alpha(\rho)\cos\alpha(\rho)}{\rho} \\ \Rightarrow \quad \frac{\partial \alpha(\rho)}{\partial \rho} + \frac{\sin\alpha(\rho)\cos\alpha(\rho)}{\rho} &= k \end{aligned} \quad (C.13)$$

which verifies the solution.

We may now show that Equation 1.58 is equivalent to Equation 1.56, in the following way: Let $r = k\rho$, so that the integral of Equation 1.56 becomes

$$\begin{aligned} I &\equiv - \int_0^{\rho} dr \frac{\sin^2 \alpha(\rho)}{r} \\ &= - \int \frac{dr}{r} \frac{J_1^2(r)}{J_0^2(r) + J_1^2(r)} \end{aligned} \quad (C.14)$$

after making use of Equation C.10. Now change variables:

Let

$$u = J_0^2(r) + J_1^2(r) \quad . \quad (C.15)$$

Then

$$du = - 2J_1^2 dr/r \quad (C.16)$$

and the integral becomes

$$\begin{aligned} I &= + \frac{1}{2} \int du/u \\ &= \frac{1}{2} \ln[J_0^2(r) + J_1^2(r)] \quad . \end{aligned} \quad (C.17)$$

Taking the logarithm of both sides of Equation 1.56 gives

$$\ln[H(\rho)/H(0)] = + \frac{1}{2} \ln[J_0^2 + J_1^2] \quad (C.18)$$

or

$$H(\rho) = H(0) \cdot [J_0^2(k\rho) + J_1^2(k\rho)]^{1/2} \quad (C.19)$$

as desired.